Post-selection-based Continuous Variable Quantum Information Processing

Jie Zhao

A thesis submitted for the degree of
Doctor of Philosophy in Physics
The Australian National University

Australian National University

July 2019

Declaration

This thesis is an account of research undertaken between May 2014 and January 2019 at The Department of Quantum Science, Research School of Physics and Engineering, The Australian National University, Canberra, Australia.

Except where acknowledged in the customary manner, the material presented in this thesis is, to my best knowledge, original and has not been submitted in whole or part for a degree in any university.

Jie Zhao
31 Mar 2019

To my beloved Mother and Father,
words are insufficient to express how much I am indebted to you.

Acknowledgments

The greatest thanks for the work in this thesis are owed to my supervisors Prof. Ping Koy Lam and Dr. Syed Assad, who are exceptional scientists. From them, I gained insights into some of the most fundamental pictures of quantum optics and optical experiments, learnt how to troubleshoot problems in the most effective way, and how to be a physicist always full of enthusiasm and curiosity in deciphering the fabulous and intricate nature of the world around us. The breadth of their knowledge has never failed to amaze me during my PhD, reminding me constantly of the wide range of possibilities in our research area. I would also like to thank Prof. Tim Ralph and Asso. Prof. Mile Gu, my PhD advisors, and Jayne Thompson. It has always been a great pleasure to discuss with them on various aspects of physics, especially when almost every discussion turned into a brainstorm. These discussions are undoubtedly valuable treasures of my PhD study. One of the most important lessons I learnt at ANU is the significance of collaborations between theorists and experimentalists.

I sincerely appreciate the opportunities I have had to work with many of my talented colleagues: Jiri Janousek, Oliver Thearle, Sara Hosseini, Alex Brieussel, Mark Bradshaw, Lorcan Conlon, Hao Jeng, Thibault Michel, and Biveen Shajilal from the quantum communication team, Ben Buchler, Geoff Campbell, Jesse Everett, Daniel Higginbottom, Anthony Leung, Sarah Lau, Karun Paul, and Aaron Trantor from the GEM team, Jiayi Qin, Jingyong Ma, Tobias Vogl, and Ming Gui from the optomechanical team, Ruvi Lecamwasam, and Jessica Eastman from the theory group and Junxiang Zhang, Cui Liang, and Kui Liu our visitors from China. Specifically, I would like to thank Jingyan, Jiao Geng, and Assad for teaching me many of the basic experimental skills and guiding me through experimental problems when I first joined the team. I also feel deeply grateful for having Giovanni Guccione as my dear colleague and one of my best friends. During the time we built the two squeezers together, we made numerous mistakes, but I believe we both learnt a lot from all the failures. Certainly, I have gained a lot of useful knowledge from his expertise in cavity alignment. I am indebted to you for helping me with the proofreading of both the amplification and the squeezing gate papers. I would like to thank Lorcan, Biveen, Sarah, Thibault, Ruvi, Oliver, Hao, and Min Jet for proofreading my thesis.

Without the technical support from the mechanical and electronic workshops, much of the work presented in this thesis would have been subject to serious delays. To Paul McNamara, Neil Devlin, Andrew Papworth, and Tristan Redman, thank you very much for almost always getting my requests done in time and your delightful sense of humor. My sincere thanks also goes to Lynne Christian and Amanda Haines for always being

kind and supportive.

I would like to acknowledge, in particular, Jingyan Haw for the work described in chapter 4 and 6, and Liu Kui and Hao Jeng for the work presented in chapter 7, 8, and 9. To Liu Kui, I will never forget how we assembled the new table frame all by ourselves and your tremendous help through the squeezing gate and teleportation projects during which we were confronted with countless problems.

I was extremely lucky to become a member of the ANU quantum optics group. Out of working hours, I sincerely appreciate the friendship I developed with many of the group members during my PhD study. Beside my ANU buddies, I would also like to thank my dear friends, Jing-nan, Jun, Lili, Xiaojun, Xiaying, Min Jet, Ye Dai, Joy, Duoduo, Mengman, and Haopeng for their enormous patience and considerate care for me during the past four and a half years, not to mention the occasional late night chats that offered me great help when I felt depressed and exhausted.

Thanks to Shiyin, Ya Zhang, Aaron, Geng Jiao, and Giovanni, my life in Canberra would have been so desolate without your company. Deep in my heart, I cherish every time we went travelling together, had dinner together, watched movies together, and went hiking together. Canberra itself, in my perspective, is hardly attractive, but it is the people I met here that makes it the place where I want to spend the rest of my life.

Most importantly I thank my parents for their unwavering faith in me, in all aspects, and for letting me pursue my life in my own way with their utmost support both emotionally and financially, although this has come at the price of me not spending as much time as I would like to spend in their company.

Abstract

Over the past three decades, there have been great advances in the burgeoning field of quantum information science, from the proposal of quantum key distribution that holds the promise of unconditionally secure communication, to quantum teleportation that harnesses entanglement to achieve communication that was previously confined to the realm of science fiction. Most of these possibilities were not foreseen before the union of quantum mechanics and the conventional information theory. The remarkable achievements emerged alongside the recognition that ultimate limits, such as the no-go theorem on noiseless linear amplification and the no-cloning theorem, exist on the performance of quantum devices. In practice, limited experimental resources also pose critical constraints on the benefits one can obtain from quantum mechanical systems over their classical counterparts.

In this thesis, we introduce various post-selection-based continuous variable (CV) quantum information protocols, showing that the aforementioned limitations can be efficiently surmounted by forgoing determinism. We demonstrate quantum information tasks with a finite success probability that would otherwise be impossible deterministically. Moreover, we showcase that the inclusion of such post-selection obviates the requirement for highly non-classical resources in a variety of quantum information processings–when benchmarked on the same criterion.

First, we heuristically study the properties of the post-selection filter that was originally proposed to emulate a noiseless linear amplifier (NLA). In particular, two equivalent implementations of NLA, i.e. the measurement-based NLA and the physical NLA, are investigated and compared in terms to their abilities to preserve the Gaussianity of an arbitrary input state and their success probability. The link between these two amplifiers is further clarified by integrating them into a measure-and-prepare setup. We conclude that the equivalence between the measurement-based and the physical approaches holds valid only when the effective parameters–the amplification gain, the cut-off, and the amplitude of the input state–are taken into account. We provide one concrete application of the measurement-based NLA as a 1-to-infinity cloner with fidelity surpassing its quantum limit.

The first application of the post-selection filter is concerned with quantum amplification. The noise properties of deterministic phase-insensitive amplifiers are discussed, whereby the signal to noise ratio inevitably degrades in compliance with the Heisenberg uncertainty principle. We demonstrate a noise-reduced quantum amplifier that circumvents this noise penalty at the expense of finite success probability. Here a measurement-based NLA is profitably combined with a deterministic linear amplifier, making it possible for the signal-to-noise ratio of an incoming optical signal to be enhanced phase

insensitively. The concatenation of the two amplifiers introduces the flexibility that allows one to tune between the regimes of high-gain or high noise-reduction, and control the trade-off between these performances and a finite heralding probability. We report amplification with a signal transfer coefficient of $\mathcal{T}_s > 1$ with no distortion of the output state. By partially relaxing the demand of output Gaussianity, we can obtain further improvement to achieve a $\mathcal{T}_s = 2.55 \pm 0.08$ with an amplification gain of 10.54. In addition, we construct a quantum cloning machine based on this hybrid linear amplifier for arbitrary coherent input states. We demonstrate the production of multiple clones (up to five) with fidelity of each clone consistently exceeding the corresponding the no-cloning limit.

Furthermore, we consider employing the post-selection algorithm in more general quantum information protocols where nonlinearities are involved. To this end, we develop two squeezers as optical parametric amplifiers, each producing fairly pure (best purity of 1.12) squeezed output up to 11 dB. We describe in detail the considerations made when designing the exact configuration of the squeezers. We experimentally characterize the pump threshold, escape efficiency, and the phase noise in presence of our system and conclude that the squeezers are capable of producing a high-magnitude of squeezing where the ultimate limit resides in the available optical coating techniques.

Additionally, we engineer a post-selection-based high-fidelity quantum squeezing gate. Such a squeezing gate is an indispensable building block for constructing a universal CV quantum computer. In comparison to the conventional squeezing gate, post-selection leads to a significant enhancement in fidelity regardless of the input state. Unity fidelity, that would require infinitely squeezed sources in the conventional scheme, now can be achieved with a modest level of ancillary squeezing. In particular, we report a squeezing fidelity of 98.49% for a target squeezing of -2.3dB, achieved with -6 dB of squeezed ancilla. This result would be impossible conventionally even if an infinitely squeezed state was at our disposal.

Finally, we propose and experimentally demonstrate a heralded CV quantum teleporter. Several appealing features of our teleportation scheme are analyzed. Firstly, as opposed to the conventional teleportation, high fidelity does not necessarily require highly squeezed resources. More remarkably, unity fidelity, that is conventionally unattainable, is achievable with imperfect EPR correlation. Secondly, our teleporter has the potential to resolve one of the long-standing problems of CV quantum teleportation: all existing experiments are confined to table-top demonstrations (a maximum of 30 m). This limit is ascribed to the fact that CV entanglement is extremely vulnerable to loss and noise. Thanks to the post-selection, our heralded teleporter works in analogy to an error-corrected channel able to compensate any loss incurred on the receiver's station. Unity fidelity is attainable regardless of the channel transmission, rendering the teleporter more resilient to channel imperfections. Thirdly, our teleporter, when operates in the non-unity gain regime, provides access to the operational region where the signal transfer coefficient $\mathcal{T}_q > 2$. This is forbidden conventionally in compliance with

the Heisenberg uncertainty principle. By employing the current teleportation scheme, telecloning and tele-amplification can be achieved with fidelity surpassing the corresponding quantum limit. We anticipate it to have numerous applications in quantum communication and computation, such as long-distance quantum networks and distributed quantum computation.

Contents

Chapter 1

Introduction

The discoveries of superposition and entanglement have spurred new perspectives for defining, encoding, manipulating, and transmitting information, which in turn has fostered a deeper understanding of the often counter-intuitive nature of quantum physics. These advances have given rise to an intriguing research field called quantum information, which lies at the intersection of quantum physics and conventional information theory. The unique properties of quantum mechanical systems are harnessed to realize information tasks that have no classical analogue [1, 2, 3, 4]. Its supremacy is evidenced in absolutely secure quantum communication [5, 6, 7, 8, 9], exemplified by quantum key distribution, that is otherwise impossible classically and also in quantum computation that has significantly higher operational speed over its classical counterpart [10, 11, 12, 13, 14, 15, 16]. Nevertheless, these appealing possibilities come at the price of fundamental limits, that in some scenarios, pose undesirable bounds on the performance of the quantum technologies. One such example is the well-known quantum no-cloning theorem incurred due to the linearity and unitarity of quantum mechanics [17]. It states that an unknown quantum state cannot be duplicated with arbitrarily high accuracy. The physics underlying such limitations resides in the argument that in principle one cannot carry out pefectly accurate measurement simultaneously on non-commuting observables or conjugate quadratures of an electromagnetic field [18, 19, 20]. However, post-selection was proposed recently as a way to overcome these limits [21, 22]: it was demonstrated that in various quantum information tasks, the fundamental quantum limits can be overcome by renouncing determinism. By employing conditional operations, the performance of quantum information systems can be enhanced substantially without requiring a corresponding increase in physical quantum resources. As such for resource intensive information tasks, the exploitation of post-selection allows one to really profit in practice from quantum supremacy. This thesis explicitly investigates post-selection as a novel approach to enhance the performance of continuous-variable (CV) quantum information processing. In particular, we explore the versatile applications of this post-selection algorithm, including entanglement distillation, noiseless amplification, quantum cloning, quantum computation and quantum teleportation. We envisage post-selection will become a useful component of the conventional Gaussian toolbox and hence be of great interest in continuous variable

quantum information and quantum metrology.

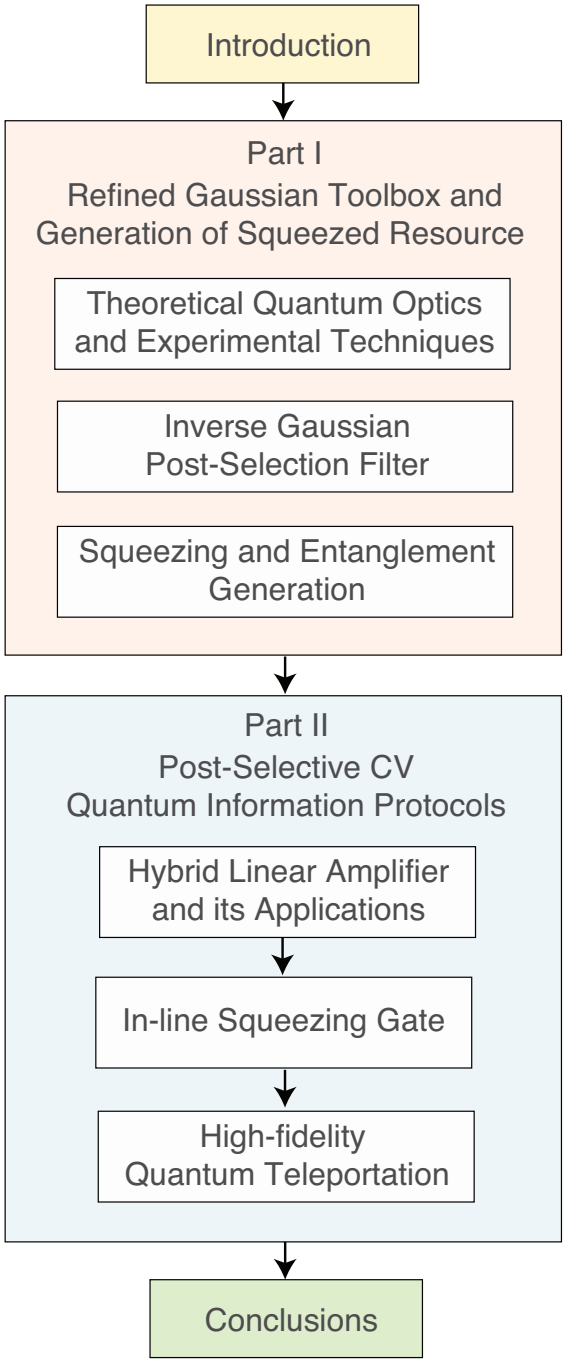

Figure 1.1: Thesis plans.

As illustrated in Fig. 1.1, this thesis comprises two main parts. In Part I, we first introduce some of the basic elements in the Gaussian toolbox for CV quantum information processing. We present the filter function that is used throughout the thesis and the construction of two squeezers that provide the nonlinear resources for some of the work in this thesis.

More specifically, we present in chapter 2 some of the fundamental light fields and

basic Gaussian operations that are relevant to the work in this thesis. In addition, we review briefly the quasi-probability distribution of these light fields.

Some experimental techniques that have been frequently used in the experiments during my PhD study are briefly discussed in chapter 3. In particular, we describe in detail the phasor diagram and sideband picture of various quantum states. We also analyze the outcome of the most commonly used Gaussian measurement, i.e. the homodyne measurement, and show how to extract error signals from the homodyne output to implement relative phase locking. Another frequently used locking technique, the Pound-Drever-Hall locking, is introduced as well.

We present, in chapter 4, an overview of a post-selection filter function that possesses an inverse Gaussian profile. This filter function serves as a crucial element in the second part of this thesis and provides a powerful tool to refine the aforementioned Gaussian toolbox. We examine thoroughly the behavior of this post-selection filter with respect to various figure of merits.

Finally, in chapter 5, we present how we designed and built a pair of doubly-resonant squeezers where squeezed vacuum is produced through optical parametric amplification. These squeezers provide the premier nonlinear resource for the work presented in the second part of this thesis. What follows in this chapter is a thorough characterization of the performance of the squeezers and the experimental results of our squeezing generation.

The second part of this thesis is concerned with applications of the filter function in various quantum communication and computation protocols.

As a concrete example to verify how the filter function can be utilized to facilitate quantum communication, we propose in chapter 6 a hybrid linear amplifier that concatenates a deterministic linear amplifier and a measurement-based noiseless linear amplifier. We experimentally demonstrate that this hybrid linear amplifier overcomes the inevitable degradation of signal-to-noise ratio (SNR) of a deterministic phase-insensitive linear amplifier. In particular, we report an SNR enhancement up to 4 dB with an amplitude gain of 10.54, equivalent to a power gain of 111.09. It is the first experimental demonstration of optical phase-insensitive amplification with enhanced signal-to-noise ratio with only linear optics. Moreover, we extend the amplification scheme to realize quantum cloning of arbitrary coherent states with unprecedented fidelity that significantly surpasses the no-cloning limit.

Chapters 7 and 8 provide, respectively, the theoretical modelling and experimental demonstration of a universal squeezing gate (SG). Thanks to the inclusion of post-selection, our SG is able to obtain high output fidelity without the conventional necessity of highly squeezed ancilla. Unity fidelity, that is impossible deterministically, is achievable via our SG scheme.

In chapter 9, we propose a heralded high-fidelity quantum teleportation protocol, which obviates two technical hurdles of the conventional teleporter. Firstly, near-unit fidelity is achievable via our scheme with a modest magnitude of squeezing that would

otherwise require perfect EPR correlation (equivalent to infinite squeezing) in a conventional CV teleporter. Secondly, our heralded teleporter is capable of correcting loss on the receiver's station: regardless of the channel transmission, unit fidelity is always obtainable at the expense of reduced success probability. The teleporter becomes resilient to channel loss and hence the distance of teleportation can be extended to arbitrary lengths.

Finally, the main results of this thesis are summarized in chapter 10, where we provide an outlook on future projects in light of the work presented in this thesis.

A large portion of the content of this thesis has been published in, or submitted to international peer-reviewed journals or conference proceedings. The following is a list of related publications:

1. J. Zhao J. Y. Haw, S. M. Assad, T. Symul, and P. K. Lam. *Characterization of measurement-based noiseless linear amplifier and its applications.* Physical Review A **96**, 012319, (2017).

2. J. Zhao, J. Dias, J. Y. Haw, T. Symul, M. Bradshaw, R. Blandino, T. Ralph, P. K. Lam, and S. Assad. *Quantum enhancement of signal-to-noise ratio with a heralded linear amplifier*, Optica **4**, 1421, (2017).

3. J. Zhao, J. Dias, J. Y. Haw, T. Symul, M. Bradshaw, R. Blandino, T. Ralph, P. K. Lam, and S. Assad. *Quantum enhancement of signal-to-noise ratio for arbitrary coherent states using heralded linear amplifier*, 2017 Conference On Lasers and Electro-Optics Pacific Rim (CLEO-Pr), IEEE, (2017).

4. J. Y. Haw, J. Zhao, J. Dias, S. M. Assad, M. Bradshaw, R. Blandino, T. Symul, T. C. Ralph, and P. K. Lam. *Surpassing the no-cloning limit with a heralded hybrid linear amplifier*, Nature Communications **7**, 13222, (2016).

5. J. Zhao, K. Liu, J. Hao, M. Gu, J. Thompson, S. M. Assad, and P. K. Lam. *High-fidelity squeezing gate for continuous-variable quantum light field*, Unpublished manuscript.

Part I

Refined Gaussian Toolbox and Generation of Squeezed Resource

Chapter 2

Theoretical Quantum Optics

This chapter provides an overview of some fundamental knowledge about quantum optics that constitutes the theoretical basis of this thesis. In particular, we describe briefly the quantization of the electromagnetic field which leads to the invention of the creation and annihilation operators. We also introduce the quadrature operators that are extensively used to characterize a quantum light field. Various optical states that are related to the work in this thesis are presented. The final section is concerned with the quasi-probability representations for these states, among which we focus ourselves on the Wigner function and the Husimi Q function. Further details on a comprehensive description of quantum optics theory can be found in many textbooks, such as [23, 24, 25, 26].

2.1 Fundamental Quantum Optical Fields

2.1.1 Quantization of Electromagnetic Field

The classical behaviour of an electromagnetic field can be elegantly described by the Maxwell's equations, whereby the electric field that is restricted to a certain volume of space is given by [24]

$$\mathbf{E}(\mathbf{r},t) = \mathbf{i}\sum_{k}\left(\frac{\hbar\omega_k}{2\varepsilon_0}\right)^{1/2}\left[\alpha_k\mathbf{u}_k(\mathbf{r})e^{-i\omega_k t} - \alpha_k^*\mathbf{u}_k^*(\mathbf{r})e^{i\omega_k t}\right]. \tag{2.1}$$

Here the normalization factor $(\hbar\omega_k/2\varepsilon_0)^{1/2}$ is chosen such that the Fourier amplitudes α_k and α_k^* are dimensionless, where ω_k refers to the mode angular frequency, $\hbar$ the reduced Plank constant and ε_0 the free space permittivity. The vector mode functions $\mathbf{u}_k$ form a base set for expanding the electric field and their exact expression depends on the boundary condition of the volume under consideration. The fact that these vector modes are non-interacting and orthogonal simplifies the analysis of the overall electric field. Because each mode is independent of one another, the full statistical description of the entire electromagnetic field can be treated as product of the distribution function for each individual mode. Consequently, the corresponding total energy, namely the

Hamiltonian, of the electromagnetic field can be derived

$$\mathcal{H} = \frac{1}{2}\int (\varepsilon_0 \mathbf{E}^2 + \mu_0 \mathbf{H}^2) d\mathbf{r} = \sum_k \hbar\omega_k \left(\alpha_k^* \alpha_k + \frac{1}{2}\right), \tag{2.2}$$

where $\mathbf{H}$ and μ_0 denote the magnetic field and the magnetic permeability of free space respectively.

Quantization of the electromagnetic field is then accomplished by transforming the complex amplitudes α_k and α_k^* into a pair of mutually adjoint operators $\hat{a}_k$ and $\hat{a}_k^\dagger$ known as the creation and annihilation operators of the electromagnetic field. Note that $\hat{a}_k$ and $\hat{a}_k^\dagger$ should satisfy the boson commutation relations,

$$\left[\hat{a}_k, \hat{a}_{k'}^\dagger\right] = \delta_{kk'}, \quad [\hat{a}_k, \hat{a}_{k'}] = \left[\hat{a}_k^\dagger, \hat{a}_{k'}^\dagger\right] = 0, \tag{2.3}$$

due to the fact that photons are bosons. The quantized electromagnetic field can be expressed in terms of the creation and annihilation operators

$$\mathbf{E}(\mathbf{r}, t) = \mathbf{i}\sum_k \left(\frac{\hbar\omega_k}{2\varepsilon_0}\right)^{1/2} \left(\hat{a}_k e^{-i\omega_k t} - \hat{a}_k^\dagger e^{i\omega_k t}\right). \tag{2.4}$$

Accordingly, the Hamiltonian in Eq. (2.2) now becomes

$$\hat{\mathcal{H}} = \sum_k \hbar\omega_k \left(\hat{a}_k^\dagger \hat{a}_k + \frac{1}{2}\right), \tag{2.5}$$

which is the sum of energy in each mode k with respect to the number of photons contained in the mode and the vacuum fluctuation $1/2\hbar\omega_k$. This represents the intrinsically unavoidable noise associated with all measurements that is imposed by quantum mechanics and is often termed the *quantum noise limit*. Equation (2.5) implies that the electromagnetic field can be regarded as an ensemble of modes, each representing a simple harmonic oscillator.

Quantization of the electromagnetic field also gives rise to a particularly intriguing quantum state: the Fock state or photon number state, $|n_k\rangle$, being the eigenstate of the quantized Hamiltonian $\hat{\mathcal{H}}$ in (2.5). Here, n_k denotes the number of photons in mode k. Such quantum state has no classical analogue and it forms a complete orthonormal basis

$$\langle n_k | m_k \rangle = \delta_{nm}, \quad \sum_{n_k=0}^{\infty} |n_k\rangle\langle n_k| = 1, \tag{2.6}$$

and hence can be utilized for representing other quantum states. With the photon number state being defined, the physical interpretation of the creation and annihilation op-

erators becomes apparent. Application of the operators $\hat{a}_k$ and $\hat{a}_k^\dagger$ to $|n_k\rangle$ yields

$$\hat{a}_k|n_k\rangle = \sqrt{n_k}|n_k - 1\rangle, \quad \hat{a}_k^\dagger|n_k\rangle = \sqrt{n_k + 1}|n_k + 1\rangle. \tag{2.7}$$

This means by applying $\hat{a}_k$ or $\hat{a}_k^\dagger$ on a photon number state, one quanta of energy $\hbar\omega_k$ is added or subtracted from the state. In addition, we introduce the photon number operator $\hat{n}_k$

$$\hat{n}_k = \hat{a}_k^\dagger \hat{a}_k. \tag{2.8}$$

The action of $\hat{n}_k$ upon a Fock state $|n_k\rangle$ yields the mean photon number of the state: $\hat{n}_k|n_k\rangle = n_k|n_k\rangle$.

2.1.2 Quadrature Operators and Heisenberg Uncertainty Relation

In quantum mechanics, operators must be Hermitian to represent physically measurable quantities. As the creation and annihilation operators are non-Hermitian, they do not correspond to any measurable observables. We therefore define the following quadrature operators for electromagnetic fields, which are analogous to the in-phase and in-quadrature components of a classical electronic signal defined in the rotating frame [25],

$$\hat{X}_{+_k} = \hat{a}_k + \hat{a}_k^\dagger, \quad \hat{X}_{-_k} = -i(\hat{a}_k - \hat{a}_k^\dagger). \tag{2.9}$$

Here, $\hat{X}_{+_k}$ and $\hat{X}_{-_k}$ indicate the amplitude and phase quadratures of the electromagnetic field, respectively. Substituting Eq. (2.9) into Eq. (2.3), we find that these quadrature operators satisfy the following commutation relation,

$$\left[\hat{X}_+, \hat{X}_-\right] = 2i. \tag{2.10}$$

In accordance with the Heisenberg uncertainty principle, Eq. (2.10) implies that the multiplication of the quadrature fluctuations, $\Delta\hat{X}_+$ and $\Delta\hat{X}_-$, must be larger than 1 (the convention $\hbar = 2$ is used here) :

$$\Delta\hat{X}_+ \Delta\hat{X}_- \geq 1. \tag{2.11}$$

This shows that the amplitude and phase quadratures of an electromagnetic field cannot be determined simultaneously with perfect precision regardless of the measurement device that is employed. More generally, this uncertainty relation holds valid for any conjugate quadratures, that can be represented by rotations of $\hat{X}_+$ and $\hat{X}_-$, of an electromagnetic field.

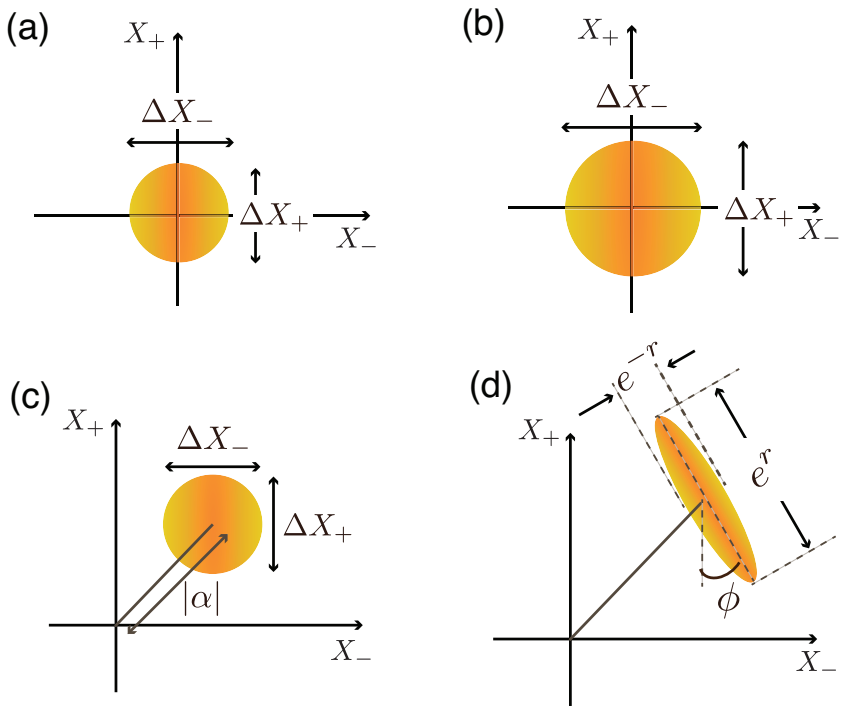

Figure 2.1: Phase space diagram showing the noise contours at half maximum of the full 2-dimensional Wigner function (see Sec. 2.2.1) of (a) vacuum state, (b) thermal state, (c) coherent state, and (d) squeezed state.

2.1.3 Coherent States and Displacement Operator

Quantum states where the product of uncertainty in its amplitude and phase saturates the inequality (2.11) are typically called minimum-uncertainty states. One such example is the so called coherent state $|\alpha\rangle$ where $\Delta X_+ = \Delta X_-$, as illustrated in Fig. 2.1 (a). It is of great practical relevance as it approximates the direct output of a highly stabilized laser operating above threshold. In this regard, it is typically referred to as a quasi-classical state, but the distinctive uncertainty associated with its quadrature amplitudes can still be utilized in a broad range of quantum information protocols, such as the CV quantum key distribution [27, 28, 29, 30], random number generation [31, 32], and quantum cloning as will be discussed in chapter 6.4.

Coherent states are the eigenstates of the annihilation operator

$$\hat{a}|\alpha\rangle = \alpha|\alpha\rangle, \tag{2.12}$$

and can be obtained by applying a displacement operation $\hat{D}$ upon a vacuum state

$$|\alpha\rangle = \hat{D}(\alpha)|0\rangle = \exp\left(\alpha\hat{a}^\dagger - \alpha^* a\right)|0\rangle. \tag{2.13}$$

A coherent state can be expanded in terms of Fock states as

$$|\alpha\rangle = \sum |n\rangle\langle n|\alpha\rangle = \mathrm{e}^{-|\alpha|^2/2} \sum \frac{\alpha^n}{(n!)^{1/2}} |n\rangle. \tag{2.14}$$

The number of photons contained in a coherent state $|\alpha\rangle$ follows a Poissonian distribution,

$$P_n = |\langle n|\alpha\rangle|^2 = \frac{|\alpha|^{2n} e^{-|\alpha|^2}}{n!}, \tag{2.15}$$

with the mean and standard deviation of photon number being $\langle\alpha|\hat{n}|\alpha\rangle = |\alpha|^2$ and $\Delta\hat{n} = |\alpha|$, respectively, where $\hat{n}$ refers to the photon number operator defined in Eq. (2.8).

Like Fock states, coherent states also form a complete (overcomplete in fact) basis that can be used to represent arbitrary quantum states despite the fact that coherent states are non-orthogonal:

$$\mathbf{I} = \frac{1}{\pi} \int |\alpha\rangle\langle\alpha| \mathrm{d}^2\alpha, \quad \langle\alpha|\beta\rangle = \exp\left(-\frac{1}{2}|\alpha|^2 - \frac{1}{2}|\beta|^2 - \alpha^*\beta\right), \tag{2.16}$$

where $\mathrm{d}^2\alpha = \mathrm{d}(\mathrm{Re}\{\alpha\})\mathrm{d}(\mathrm{Im}\{\alpha\})$ and $\mathbf{I}$ is the identity operator. Expanding a density operator of an electromagnetic field, $\hat{\rho}$, in terms of coherent states gives the *P representation* of the light field

$$\hat{\rho} = \int P(\alpha)|\alpha\rangle\langle\alpha| \mathrm{d}^2\alpha. \tag{2.17}$$

This was first introduced independently by Glauber [33] and Sudarshan [34]. $P(\alpha)$ in Eq. (2.17) is a quasi-probability distribution of α, because for light fields that exhibit non-classical properties, $P(\alpha)$ may take on negative values or become highly singular. One prominent example is the Fock state, of which the P function possesses a singularity point at origin and is zero over the entire complex plane spanned by $|\alpha\rangle\langle\alpha|$. For squeezed states and quantum states exhibitting photon anti-bunching phenomena, the P function appears to be negative [35, 25, 24]. In these situations, it is not possible to interprete the P function as a conventional probability distribution. Nevertheless, in spite of the mathematical problems arising in such situations, the P function indeed provides a fairly illuminating way to manifest the exotic quantum nature of a light field.

Thermal States

Unlike coherent states which are coherent superposition of Fock states, thermal states result from the mixture of Fock states and therefore are considered as classical states. Its

density operator is diagonal in the Fock state basis

$$\hat{\rho}_{\rm th}(\bar{n}_{\rm th}) = \sum_{n=0}^{\infty} \frac{\bar{n}_{\rm th}^{n}}{(\bar{n}_{\rm th}+1)^{n+1}} |n\rangle\langle n|, \tag{2.18}$$

where $\bar{n}_{\rm th}$ denotes the average photon number of the state. A thermal state is regarded as the most fundamental Gaussian state since every Gaussian state can be decomposed into thermal states [35]. It also maximizes the von Neumann entropy $S = -\mathrm{Tr}(\hat{\rho}\log\hat{\rho})$ [35]. The covariance matrix of a thermal state is given by $\mathbf{V}_{\rm th} = (2\bar{n}_{\rm th}+1)\mathbf{I}$, where $\mathbf{I}$ is the 2×2 identity matrix.

2.1.4 Squeezed States and Squeezing Operator

As sketched in Fig. 2.1 (d), imagine a stretching force and a compressing force are applied, respectively, on the two conjugate quadratures of the ball representing a coherent state, we obtain consequently another minimum-uncertainty state, that is the pure squeezed state. In contrast to a coherent state with equal uncertainty in the conjugate quadratures, the noise in the squeezed quadrature is suppressed, while the noise in the anti-squeezed quadrature is amplified accordingly to adhere to the uncertainty relation (2.11).

A squeezed vacuum $|0,\varepsilon\rangle$ may be generated by applying the unitary squeezing operator $\hat{S}(\varepsilon)$ on vacuum,

$$|0,\varepsilon\rangle = \hat{S}(\varepsilon)|0\rangle = \exp\left(\frac{\varepsilon^* a^2 - \varepsilon a^{\dagger 2}}{2}\right), \tag{2.19}$$

where $\varepsilon = re^{2i\phi}$ and r is called the *squeezing factor*; ϕ represents the angle of the squeezed state, as illustrated in Fig. 2.1 (d). The noise suppression in the squeezed quadrature emerges from the pairing effect that is encapsulated in $\hat{S}(\varepsilon)$: the action of the squeezing operation always creates or eliminates a pair of photons simultaneously that, as a consequence, correlates the upper and lower sidebands of the carrier field. In this way the uncertainty in one particular quadrature is reduced even below the standard quantum noise at the expense of an increased uncertainty in the conjugate quadrature.

The amount of noise suppression of a squeezed state is characterized by the squeezing factor r as follows

$$\Delta X_{+_s} = e^{-r}, \quad \Delta X_{-_s} = e^{r}. \tag{2.20}$$

The asymmetry in the uncertainties reaches its ultimate limit when $r \to \infty$. For this infinitely squeezed state, its squeezed quadrature is measurable with perfect accuracy; meanwhile, the information about its anti-squeezed quadrature is completely lost. We will show in chapter 5 that the squeezing operator $\hat{S}(\varepsilon)$ is equivalent to the unitary operator for time evolution of a degenerate parametric amplifier (OPA) in the interaction

picture [24] and it is this close connection that advices OPA as a promising candidate for experimental squeezing generation.

Alternatively by displacing a squeezed vacuum, one can obtain the bright squeezed state, that is $|\alpha, \varepsilon\rangle = \hat{D}(\alpha)\hat{S}(\varepsilon)|0\rangle$. Because $\hat{D}(\alpha)$ and $\hat{S}(\varepsilon)$ are non-commuting operators, the two operations can only be swapped if $\hat{D}(\alpha)$ is replaced by $\hat{D}(\beta)$ where $\beta = \alpha \cosh r + \alpha^* e^{i\phi} \sinh r$.

Squeezing Purity

Other than the squeezing factor r, purity is often used as another important figure of merit to quantify the squeezing quality. It is defined as the product of the variances of the squeezed and anti-squeezed quadratures

$$\mathcal{P}_s = \langle (\Delta X_{+_s})^2 \rangle \langle (\Delta X_{-_s})^2 \rangle. \tag{2.21}$$

The impurity of a squeezed state therefore denotes it is no longer a minimum-uncertainty state. In practice, any optical loss experienced by the squeezed state would deteriorate its purity; therefore, special precautions need to be taken to minimize losses in the experimental system.

2.1.5 Two-mode Squeezed States and Its Covariance Matrix

The two-mode squeezed state is of paramount importance for CV quantum information, for it exhibits the Einstein-Podolski-Rosen (EPR) correlation that is an unique feature of quantum states. More specifically, for such a state, its conjugate quadratures, $\hat{X}_{\pm}$, of one mode can be precisely and simultaneously determined better than that is allowed by the Heisenberg uncertainty principle, based on a full knowledge of $\hat{X}_{\pm}$ of the other mode, although the two modes are spacelike separated so any measurement on one mode should have no effect on the other mode. Similar correlation was described between the momentum and position of two remotely located particles in the seminal work of Einstein, Podolski, and Rosen [36], and was later referred to as entanglement. The authors argued that this spooky action at a distance is only possible if information can transfer faster than the speed light and hence the quantum wave function does not provide a complete description of reality. The so called "local hidden variable" theory was then proposed to account for this bewildering behavior of the entangled particles. To verify whether or not entanglement exists turned out to be an extremely difficult technical challenge. Therefore, the argument was left open for more than 50 years until recent loophole-free Bell test experiments successfully observe a contradiction with local realism [37, 38, 39].

The two-mode squeezed state can be expressed mathematically as [35]

$$|r\rangle_{\rm EPR} = \sqrt{1-\lambda^2}\sum_{n=0}^{\infty}(-\lambda)^n|n\rangle_a|n\rangle_b, \tag{2.22}$$

where $\lambda = \tanh r \in [0,1]$ characterizes how strong is the correlation between the two modes a, b. The generation of a two-mode squeezed state is accomplished through the unitary two-mode squeezing operator

$$\hat{S}_2(r) = \exp\left[r(\hat{a}\hat{b} - \hat{a}^\dagger\hat{b}^\dagger)/2\right]. \tag{2.23}$$

Acting on the two-mode vacuum, it gives $\hat{S}_2(r)|0\rangle_{\rm a}|0\rangle_{\rm b} = |r\rangle_{\rm EPR}$. Similar photon pairing embedded in the one-mode squeezing operator appears here between the two interacting modes. Thus, a correlation resembling the original EPR paradox is established between the modes' quadrature amplitudes.

In practice, $\hat{S}_2(r)$ can be directly achieved via a non-degenerate parametric amplifier (NOPA) [40]. This can be readily seen by the Hamiltonian describing an NOPA system in the interaction picture,

$$\hat{\mathcal{H}}_{\rm NOPAI} = i\hbar\chi\left(\hat{a}_1^\dagger\hat{a}_2^\dagger e^{-2i\omega t} - \hat{a}_1\hat{a}_2 e^{2i\omega t}\right), \tag{2.24}$$

which corresponds explicitly to $\hat{S}_2(r)$ where $r = \hbar\chi/2$. $\hat{a}_1$ and $\hat{a}_2$ in Eq. (2.24) denote the annihilation operators for the signal and idler modes respectively. Apart from using NOPA, an alternative approach (passive method) to produce the two-mode squezed state is to mix two single-mode squeezed states that are out of phase on a 50:50 beamsplitter [41]. We adopt this indirect method to prepare entanglement for the teleportation experiment that shall be presented in chapter 9 in this thesis.

Covariance Matrix of the Two-mode Squeezed State

Any Gaussian state can be fully characterized by its coherent amplitudes, $\langle\hat{X}_+\rangle$ and $\langle\hat{X}_-\rangle$, and its covariance matrix. The remaining section is devoted to study the covariance matrix of the two-mode squeezed state. We shall consider in particular the two-mode squeezed vacuum. The conventional definition of a covariance matrix is given by [35]

$$\mathbf{V}_{ij} = \frac{1}{2}\langle\{\Delta\hat{X}_i, \Delta\hat{X}_j\}\rangle = \frac{1}{2}\langle\hat{X}_i\hat{X}_j + \hat{X}_j\hat{X}_i\rangle - \langle\hat{X}_i\rangle\langle\hat{X}_j\rangle. \tag{2.25}$$

where $\Delta\hat{X} := \hat{X} - \langle\hat{X}\rangle$ and $\{,\}$ is the anticommutator. It provides a complete description of the second moments of an arbitrary quantum state. The variances of quadrature operators are denoted by its diagonal elements which are sufficient for characterizing single-mode quantum states. The complementary non-diagonal elements instead denote the statistical correlations between different modes which are significant for un-

derstanding the non-classicality of a multi-mode quantum state. So the full knowledge of a Gaussian state can be obtained.

We first calculate the variance of the amplitude quadrature $\hat{X}_+$ of the two modes a and b

$$\begin{aligned}\mathbf{V}_{11} = \mathbf{V}_{33} &= \langle(\Delta\hat{X}_{+a})^2\rangle = \langle\hat{X}_{+a}^2\rangle - \langle\hat{X}_{+a}\rangle^2 \\ &(1-\lambda^2)\sum_{n=0}^{\infty}\lambda^{2n}\left[\langle n,n|(\hat{a}_a+\hat{a}_a^\dagger)|n,n\rangle^2 + \langle n,n|(\hat{a}_a+\hat{a}_a^\dagger)^2|n,n\rangle\right] \\ &(1-\lambda^2)\sum_{n=0}^{\infty}\lambda^{2n}\left[0 + \langle n,n|2\hat{a}_a^\dagger\hat{a}_a+1|n,n\rangle\right] \\ &(1-\lambda^2)\sum_{n=0}^{\infty}\lambda^{2n}(2n+1) = \frac{1+\lambda^2}{1-\lambda^2} = \cosh(2r).\end{aligned} \tag{2.26}$$

Here we have used Eq. (2.9) in the above derivation. Similarly, for the phase quadrature $\hat{X}_-$, we have

$$\mathbf{V}_{22} = \mathbf{V}_{44} = \cosh(2r). \tag{2.27}$$

The correlation between the conjugate quadratures of the two modes can be obtained similarly,

$$\begin{aligned}\mathbf{V}_{12} &= \frac{1}{2}\left(\langle\hat{X}_{+a}\hat{X}_{-a}\rangle + \langle\hat{X}_{-a}\hat{X}_{+a}\rangle - 2\langle\hat{X}_{+a}\rangle\langle\hat{X}_{-a}\rangle\right) \\ &= (1-\lambda^2)\sum_{n=0}^{\infty}\lambda^{2n}\left[i\langle n,n|\left((\hat{a}_a^\dagger)^2-\hat{a}_a^2+1\right)|n,n\rangle + i\langle n,n|\left((\hat{a}_a^\dagger)^2-\hat{a}_a^2-1\right)|n,n\rangle\right] - 0 \\ &= \frac{1}{2}(i-i) = 0.\end{aligned} \tag{2.28}$$

Indeed, there is alwasys no correlation being observed between conjugate quadratures regardless of which mode do they belong to, i.e.

$$\mathbf{V}_{14} = \mathbf{V}_{21} = \mathbf{V}_{23} = \mathbf{V}_{32} = \mathbf{V}_{34} = \mathbf{V}_{41} = \mathbf{V}_{43} = 0. \tag{2.29}$$

In addition, we calculate the correlation between the same quadrature of the two modes, which turns out to be

$$\begin{aligned}\mathbf{V}_{13} &= \frac{1}{2}\left(\langle\hat{X}_{+a}\hat{X}_{+b}\rangle + \langle\hat{X}_{+b}\hat{X}_{+a}\rangle - 2\langle\hat{X}_{+a}\rangle\langle\hat{X}_{+b}\rangle\right) = \langle\hat{X}_{+a}\hat{X}_{+b}\rangle \\ &= \langle\hat{a}_a\hat{a}_b\rangle + \langle\hat{a}_a\hat{a}_b^\dagger\rangle + \langle\hat{a}_a^\dagger\hat{a}_b\rangle + \langle\hat{a}_a^\dagger\hat{a}_b^\dagger\rangle = \langle\hat{a}_a\hat{a}_b\rangle + \langle\hat{a}_a^\dagger\hat{a}_b^\dagger\rangle.\end{aligned} \tag{2.30}$$

where

$$\begin{aligned}\langle \hat{a}_a^\dagger \hat{a}_b^\dagger \rangle &= (1-\lambda^2)\sum_{n=0}^{\infty}\lambda^{2n}\langle n,n|\sum_{m=0}^{\infty}\lambda^m(m+1)m+1,m+1\rangle \\ &= (1-\lambda^2)\sum_{n'=0}^{\infty}\lambda^{n'+1}\sum_{m=0}^{\infty}\langle n'+1,n'+1|\lambda^m(m+1)|m+1,m+1\rangle \\ &= (1-\lambda^2)\sum_{n'=0}^{\infty}\sum_{m=0}^{\infty}\lambda^{n'+m+1}\delta_{n',m} \\ &= (1-\lambda^2)\sum_{m=0}^{\infty}\lambda^{2m+1}(m+1) = \frac{\lambda}{1-\lambda^2} = \cosh(2r)\sinh(2r).\end{aligned} \tag{2.31}$$

Follow the similar steps, we find

$$\langle \hat{a}_a \hat{a}_b \rangle = \cosh(2r)\sinh(2r). \tag{2.32}$$

Substituting Eq. (2.31) and (2.32) into (2.30) gives $\mathbf{V}_{13} = \sinh(2r)$. The covariance matrix of the two-mode squeezed vacuum is obtained that takes the form

$$\mathbf{V}_{\text{EPR}} = \begin{pmatrix} \cosh r\mathbf{I} & \sinh r\mathbf{Z} \\ \sinh r\mathbf{Z} & \cosh r\mathbf{I} \end{pmatrix}, \tag{2.33}$$

where $\mathbf{I}$ is the identity matrix and $\mathbf{Z} := \text{diag}(1,-1)$. Consider the joint quadrature operators $\hat{q}_- := (\hat{X}_{+a} - \hat{X}_{+b})/\sqrt{2}$ and $\hat{p}_+ := (\hat{X}_{-a} + \hat{X}_{-b})/\sqrt{2}$, their variances can be deduced

$$\langle (\Delta\hat{q}_-)^2 \rangle = \langle (\Delta\hat{p}_+)^2 \rangle = e^{-2r}. \tag{2.34}$$

This coincides with the EPR correlation, thereby implying the presence of bipartite entanglement in a two-mode squeezed vacuum. In particular, as the squeezing factor increases $r \to \infty$, perfect EPR correlation is obtained: $\hat{X}_{+a} = \hat{X}_{+b}$ and $\hat{X}_{-a} = -\hat{X}_{-b}$, indicating that the uncertainty of the quadrature amplitudes of mode b are diminished (including quantum shot noise) once the quadrature amplitudes of mode a are ascertained.

We also note that the measure of entanglement in a two-mode squeezed state is of great significance for quantifying its non-classicality, but is outside the scope of this thesis. This topic has attracted considerable attentions and so far various entanglement measures have been proposed. For a more in-depth description see, for example, the von Neumann entropy [42], inseperability criterion [43], entanglement of formation [44], logarithmic negativity [45], and EPR steering [46].

2.2 Representations of Quantum Light Fields

2.2.1 Quasi-Probability Distribution: Wigner Function and Husimi Q Function

We have described two representations of the electromagnetic field: expanding its density operator in terms of Fock states (see Sec. 2.1.1) reveals its photon number distribution which, however, conceals the information about its quadrature amplitudes; on the other hand, the Glauber-Sudarshan P representation (see Sec. 2.1.3) maps the operators in an infinite-dimensional Hilbert space to probability distribution well adapted to classical mathematical analysis. However, a number of mathematical problems arise once non-classical light fields are considered. As such there remains an incentive to introduce more general framework for representing quantum optical systems. To this end, two quasi-probability distributions relevant to the work in this thesis are explored in the following.

Wigner Function

The first quasi-probability distribution introduced to quantum mechanics was the so called *Wigner function* [47], which is also the most accessible distribution function from the experimental viewpoint. The Wigner function of a general density operator is defined as

$$W(q,p) = \frac{1}{\pi\hbar}\int_{-\infty}^{\infty} \mathrm{d}x \langle q-x|\hat{\rho}|q+x\rangle e^{\left(\frac{2ipx}{\hbar}\right)}, \tag{2.35}$$

where q and p are the eigenvalues of the quadrature operators $\hat{X}_+$ and $\hat{X}_-$ in Eq. (2.9). In particular for an N-mode Gaussian state with mean quadrature vector $\mathbf{x} = (\hat{X}_{+1}, \hat{X}_{-1}, \ldots, \hat{X}_{+N}, \hat{X}_{-N})$ and covariance matrix $\mathbf{V}$ (see Eq. (2.25)), its Wigner function can be more succinctly expressed as [35]

$$W(\mathbf{x}) = \frac{\exp\left[-(1/2)(\mathbf{x}-\bar{\mathbf{x}})^T\mathbf{V}^{-1}(\mathbf{x}-\bar{\mathbf{x}})\right]}{(2\pi)^N\sqrt{\det[\mathbf{V}]}}, \tag{2.36}$$

where $\bar{\mathbf{x}} := (\langle\hat{X}_{+1}\rangle, \langle\hat{X}_{-1}\rangle, \ldots, \langle\hat{X}_{+N}\rangle, \langle\hat{X}_{-N}\rangle)$ is the mean of the quadrature vector, and $\det[\mathbf{V}]$ stands for the determinant of the matrix $\mathbf{V}$. Note that although the Wigner function is always positive and well behaved for Gaussian states, it exhibits negativity for some non-Gaussian states, such as Fock states.

Husimi Q Function

An alternative function is the *Husimi Q function* that is the direct projection of the density operator on a coherent state

$$Q(\alpha) = \frac{\langle\alpha|\hat{\rho}|\alpha\rangle}{\pi}. \tag{2.37}$$

It is therefore positive since the density operator is a positive operator and is bounded by $Q(\alpha) < 1/\pi$. Physically the Q function represents the probability distribution for obtaining α when an optimal simultaneous measurement is conducted on $\hat{X}_+$ and $\hat{X}_-$. Due to the non-commuting feature of $\hat{X}_+$ and $\hat{X}_-$, one unit of shot noise is added to the width of the distribution that would otherwise be obtained if the two quadratures are measured individually. For example, the Q function of a coherent state is given by

$$Q(\beta) = \frac{|\langle\alpha|\beta\rangle|^2}{\pi} = \frac{-|\alpha-\beta|^2}{\pi}, \tag{2.38}$$

which is a Gaussian distribution centred at $(\mathrm{Re}(\beta), \mathrm{Im}(\beta))$. It has a variance of 2, which is twice that of what we found when individual measurements of the conjugate quadratures are performed instead. Note that the P function is accessible via dual-homodyne detection or heterodyne detection.

The three quasi-probability distributions are closely related: Wigner function is obtainable via a Gaussian convolution of the P function, while the Husimi Q function is the Gaussian convolution of Wigner function. Other representations also exist, such as the generalized P function [48] and R representation [24].

The quasi-probability representations provide a way to define Gaussian states which are CV states that have a Wigner representation in terms of Gaussian functions [35]. Together with Gaussian operations which denote the transformations between Gaussian states, they constitute the primary elements in the Gaussian toolbox for analyzing CV quantum information systems. Note that for a Gaussian state, the first two moments of its quadrature amplitudes, namely their expectation values and the covariance matrix, are sufficient for a complete characterization of the state [49].

Chapter 3

Gaussian Toolbox and Its Experimental Realization

This chapter describes some elementary operations in the Gaussian toolbox for continuous variable quantum information and their corresponding experimental implementations. The operations are formulated mathematically and explained as to provide readers an insight in the underlying physics. We start with the linearization of field operators, which forms the basis for analyzing the amplitude and phase modulations detailed in the following section. This sideband modulation offers a way to realize the displacement operation. Based on it, we obtain two equivalent pictorial representations of quantum fields, namely the phasor diagram and sideband models. Moreover, we give a brief overview of the output of a homodyne detection which is the most commonly used Gaussian measurement. We describe in detail how its output can be utilized to extract error signals to facilitate phase locking. The rest of this chapter is devoted to the PDH locking technique that is frequently used throughout this thesis.

3.1 The Quantum Sideband Modulations

We have presented the rigorous mathematical description of a state of light using quasi-probability distributions (see Sec. 2.2), which however does not provide a physically intuitive interpretation for the properties of a light field. Besides, the general distribution function describing a free-propagating light field needs to be derived from the complex stochastic differential equations in the Shrödinger picture [24, 25]. However, the mathematical difficulty in this situation outweighs its generality. In this section, we introduce an alternative route for representing a state of light in the Heisenberg picture by means of linearization of field operators [50, 51]. This consequently gives rise to two particularly useful avenues to visualize an optical system, namely the sideband picture and the phasor diagram (equivalent to the ball-on-stick picture) [52, 53, 25].

3.1.1 Linearization of Operators

As we shall show, linearization of the field operators serves as a building block for developing theoretical models for many concepts in quantum optical experiments. This includes the analysis of loss, detections, and unitary Gaussian operations. More explicitly, in situations where the modulations and fluctuations of interest are relatively small compared to the amplitude of the laser beam, we can decompose the annihilation operator of a light field into two components,

$$\hat{a}(t) \approx \alpha + \delta\hat{a}(t). \tag{3.1}$$

The c-number component represents the steady-state expectation value of the operator and is hence independent of time, and $\delta\hat{a}(t)$ describes the time-varying fluctuation of the operator. The decomposition assumes the following conditions that are well suited for most of the CV optical experiments

$$\langle \delta\hat{a}(t) \rangle = 0, \quad |\delta\hat{a}(t)| \ll |\alpha|. \tag{3.2}$$

The former indicates the fluctuation of the light field has no net contribution to the field amplitude, while the latter signifies that fluctuation is negligible compared to the average intensity of the light field. As a result, the higher order fluctuation terms are neglected. Using Eq. (2.9), the linearized quadrature operators can be obtained

$$\delta\hat{X}_+(t) = \delta\hat{a}(t) + \delta\hat{a}^\dagger(t), \quad \delta\hat{X}_-(t) = \, i\left(\delta\hat{a}^\dagger(t) - \delta\hat{a}(t)\right). \tag{3.3}$$

Note that the fluctuation operators $\delta\hat{X}_\pm$ are equivalent to $\Delta\hat{X}_\pm$ defined in the previous chapter.

3.1.2 Sideband Picture: Classical Phasor diagram and Sideband models

Historically, it was originally elucidated by Caves that any state of light can be represented by a phasor diagram of the quadrature operators of the light field [52, 53, 25]. This quantum phasor diagram can actually be obtained by applying a conventional quantization on the classical phasor diagram that has been well developed. Thus in the following, the classical phasor diagram and sideband picture are introduced first, which are subsequently extended to the quantum regime.

Consider a classical optical field of frequency ω_0 that is normally referred to as the *carrier*,

$$\alpha(t) = \alpha_0 e^{i\omega_0 t}. \tag{3.4}$$

As shown in Fig. 3.1, it can be represented by a complex phasor in a coordinate system that is defined by its real and imaginary components and rotates at carrier frequency ω_0.

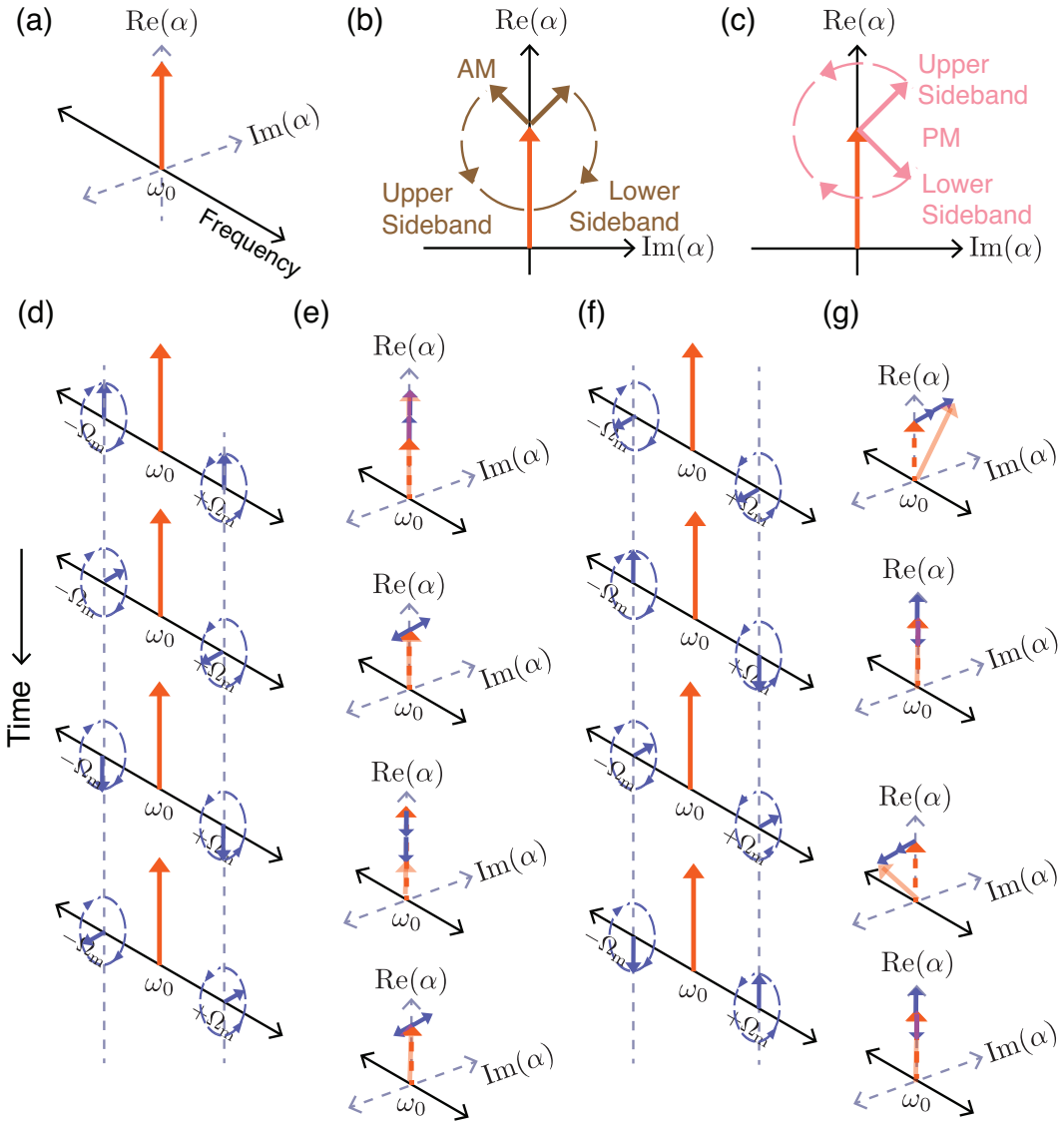

Figure 3.1: Phasor diagram of the carrier (a), the amplitude (b) and phase (c) modulations. (d) and (f) illustrate, respectively, the sidebands' evolutions involved in the amplitude and phase modulations. The corresponding phasor evolutions are shown in (e) and (g).

This pictorial representation of light field is known as the *rotating frame* where the carrier phasor becomes a stationary reference and the time-dependent sideband modulations can be visualized as rotating vectors on top of the carrier field, resulting in a final output field being the sum of all the vectors.

Applying an amplitude modulation of frequency Ω_{m} on the carrier field gives

$$\begin{aligned}\alpha(t) &= \alpha_0 e^{i\omega_0 t}\left(1 - M\cos(\Omega_{\mathrm{m}} t)\right) \\ &= \alpha_0\left[e^{i\omega_0 t} - \frac{M}{2}\left(e^{i(\omega_0-\Omega_{\mathrm{m}})t} + e^{i(\omega_0-\Omega_{\mathrm{m}})t}\right)\right],\end{aligned} \tag{3.5}$$

where M refers to the modulation depth. Note that the amplitude modulation creates

two sideband frequency components at $\omega_0+\Omega_\mathrm{m}$ and $\omega_0-\Omega_\mathrm{m}$, depicted as small blue phasors on Fig. 3.1 (d). The two sideband phasors are perfectly correlated: the upper and lower sidebands have the same amplitudes and their rotations relative to the carrier are synchronized, which means the phase components produced by individual sideband are completely cancelled out with each other such that pure amplitude modulation is attained.

Following the same methodology, we obtain a phase modulated light field that is described by

$$\begin{aligned}\alpha(t) &= \alpha_0 e^{i\omega_0} e^{iM\cos(\Omega_\mathrm{m}t)} \\ &= \alpha_0 e^{i\omega_0 t}\left(1 + iM\cos(\Omega_\mathrm{m}t) - \frac{M^2}{2}\cos^2(\Omega_\mathrm{m}t) + \cdots\right) \\ &= \alpha_0 e^{i\omega_0 t} - \frac{\alpha_0 M^2}{4} e^{i\omega_0 t} + i\alpha_0\frac{M}{2}\left(e^{i(\omega_0-\Omega_\mathrm{m})t} + e^{i(\omega_0+\Omega_\mathrm{m})t}\right) \\ &- \frac{\alpha_0 M^2}{8}\left(e^{i(\omega_0-2\Omega_\mathrm{m})t} + e^{i(\omega_0+2\Omega_\mathrm{m})t}\right) + \cdots .\end{aligned} \tag{3.6}$$

Two distinctions are drawn here between the amplitude and phase modulations by comparing Eq. (3.5) and (3.6). First, unlike the amplitude modulation where only a single-frequency sideband is created, the phase modulated field can be decomposed into the carrier field and an infinite set of sidebands, equally spaced at Ω_m. Second, apart from the phase modulation attributed from the sideband components $\pm\Omega_\mathrm{m}$, $\pm 3\Omega_\mathrm{m}$, there are amplitude modulation introduced as well owing to the sideband components $\pm 2\Omega_\mathrm{m}$, $\pm 4\Omega_\mathrm{m}$. These residual amplitude modulaitons contaminate the purity of the phase modulation and implies that no absolutely pure phase modulation is in principle achievable. However, in situations where the modulation depth is small, i.e. $M \ll 1$, the higher-order sidebands including the undesirable amplitude remnant can be neglected. Hence Eq. (3.6) can be faithfully approximated by

$$\alpha(t) \approx \alpha_0\left[e^{i\omega_0 t} + i\frac{M}{2}\left(e^{i(\omega_0+\Omega_\mathrm{m})t} + e^{i(\omega_0-\Omega_\mathrm{m})t}\right)\right]. \tag{3.7}$$

Likewise, we present the sideband picture of phase modulated beam in Fig. 3.1 (f). The first-order upper and lower sidebands, shown as blue phasors, are rotating in clockwise and anti-clockwise, respectively, at frequency Ω_m relative to the carrier. In addition, the phasor diagram for phase modulation in the complex plane is depicted in Fig. 3.1 (g), where the dashed red phasor denotes the original input beam whilst the light red vector stands for the output beam.

Before we leave the discussion of sideband modulations, there is one more thing we need to point out. Aside from the small angle expansion applied above in Eq. (3.6), an alternative complete expression of the phase modulation is given by the Bessel function

as follows [54]

$$\alpha(t) = \alpha_0 e^{i\omega_0} \left(J_0(M) + \sum_{l=1}^{\infty} J_l(M) \left(e^{il\Omega_{\rm m} t} + e^{-il\Omega_{\rm m} t} \right) \right), \tag{3.8}$$

where $J_l(M)$ are the Bessel functions of the first kind.

3.1.3 Phasor diagram and Sideband Picture of Quantum States

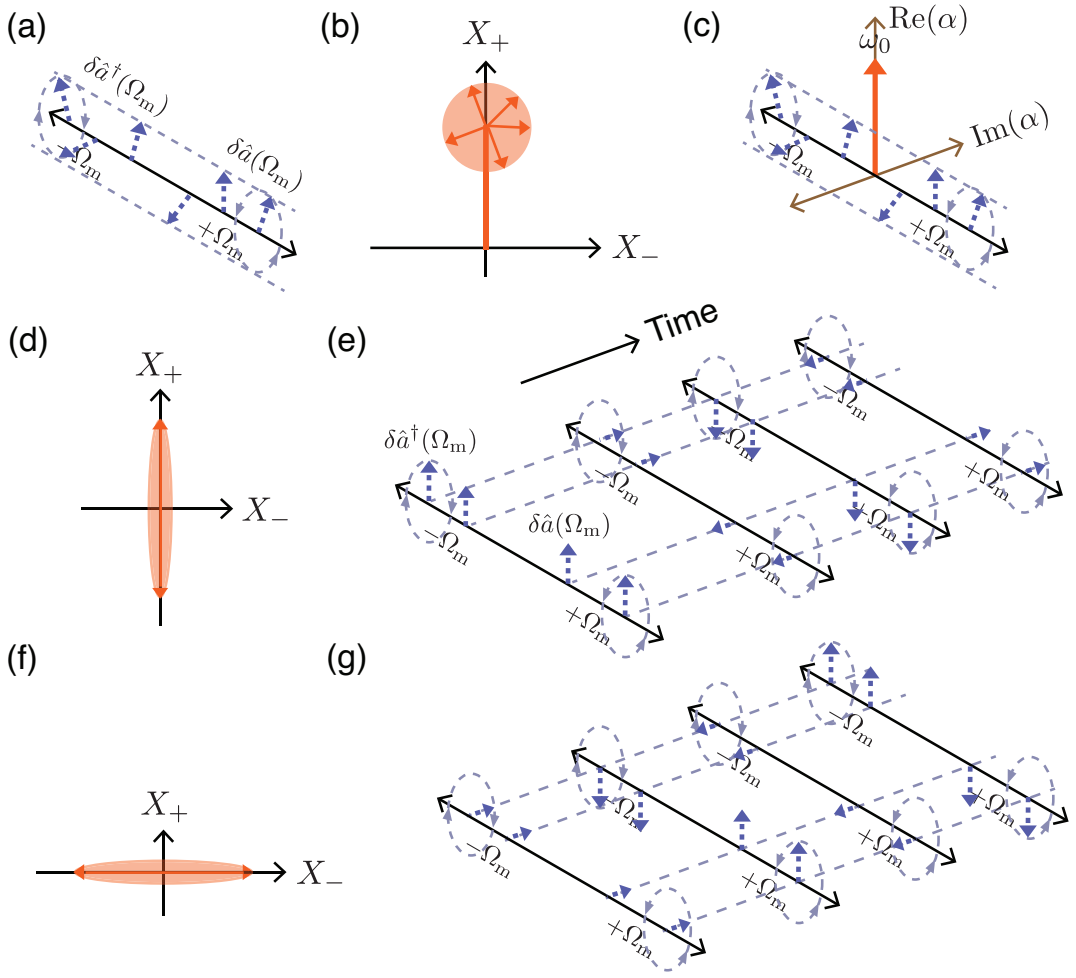

Figure 3.2: (a) Sideband picture for the vaccum state where the tiny dashed blue phasors represent the fluctuation operator $\delta\hat{a}(t)$ in Eq. (3.1); phasor diagram (b) and sideband picture (c) for a coherent state. (d) shows the phasor diagram for an infinitely phase squeezed vacuum, whilst (e) illustrates the corresponding time evolution of its correlated upper and lower sidebands. Similarly, we present the phasor diagram and sidebands evolution of an infinitely amplitude squeezed vacuum, respectively, in (f) and (g).

In the previous section, we introduced the linearization of quantum mechanical operators, where $\hat{a}$ ($\hat{a}^\dagger$) are decomposed into a steady-state component, α, and a frequency dependent fluctuation operator, $\delta\hat{a}(\omega)$ ($\delta\hat{a}^\dagger(\omega)$). This enables the description of quantum optical fields in the sideband picture directly in analogy to its classical counter-

part: α here corresponds to the carrier field at frequency ω_0 whilst $\delta\hat{a}(\omega)$ and $\delta\hat{a}^\dagger(\omega)$ are analogues to the upper and lower sidebands of the classical optical field [53, 55], as shown in Fig. 3.2. This correspondence is revealed by a direct comparison between Eq. (2.1) and (2.4). Formalism derived in Sec. 2.1.2 remains valid in this sideband picture, where the amplitude fluctuation remains fluctuations in the amplitude quadrature, *i.e.* $\delta X_+ = \delta\hat{a} + \delta\hat{a}^\dagger$ and phase fluctuation is simply the fluctuation in the phase quadrature, *i.e.* $\delta X_- = i(\delta\hat{a}^\dagger - \delta\hat{a})$.

Quantum noise (QN), as depicted in Fig. 3.2 (a), is represented by sideband phasors rotating randomly with respect to each other and the carrier at all frequencies; a combined modulation at every quadrature is created as a net effect. The length of the QN phasor vectors are determined by vacuum fluctuation, which on average should create a field strength of $\sqrt{\hbar\omega_0/2}$. Note that although the QN phasors are very tiny compared to the carrier due to $\hbar \simeq 1.055 \times 10^{-34}$ J·s, their existence highlights the fundamental quantum nature of an electromagnetic field, in stark contrast to its classical representation in Fig. 3.1.

The uncorrelated fluctuation operators shown in Fig. 3.2 (a) can also be equivalently represented in quadrature space (X_+, X_-) as Fig. 3.2 (b). The upper and lower sidebands QN phasors here constitute various non-deterministic, time-varying amplitude/ phase uncertainty vectors. In particular for a coherent state, due to the equal uncertainty in the amplitude and phase quadratures, the uncertainty vectors comprise an uncertainty circle that can be emulated as an circular shading area in Fig. 3.2 (b). Together with a stationary phasor, it illustrates the phasor diagram of a coherent state. It is a hybrid diagram that embodies both the quantum and classical properties of the coherent state.

With the help of phasor diagram and sideband model, the non-classical squeezing generation can be intuitively interpreted as the occurrence of correlation between the upper and lower sidebands. The squeezing factor r in Eq. (2.20) determines how well the correlation is. For example, a squeezed vacuum that is infinitely squeezed in phase quadrature can be intuitively visualized as sidebands being parallel and rotating in phase to each other and the carrier (see Fig. 3.2 (e)). These perfectly correlated sidebands create amplitude modulation alone and the lack of phase modulation results in a perfect noise reduction in the phase quadrature.

3.1.4 Experimental Realization of Amplitude and Phase Modulations

In our laboratory, we exploit the commercial products from Newport, namely 4104NF and 4004, to realize amplitude and phase modulation, respectively. These modulators employ the Pockels effect, also referred to as the electro-optic effect, of the $LiNbO_3$ birefringent crystal. By applying an alternating electric field on the crystal, its refractive index along a particular optical axis (which axis is affected is determined by the property of the nonlinear crystal) changes in proportional to the applied electric field, which

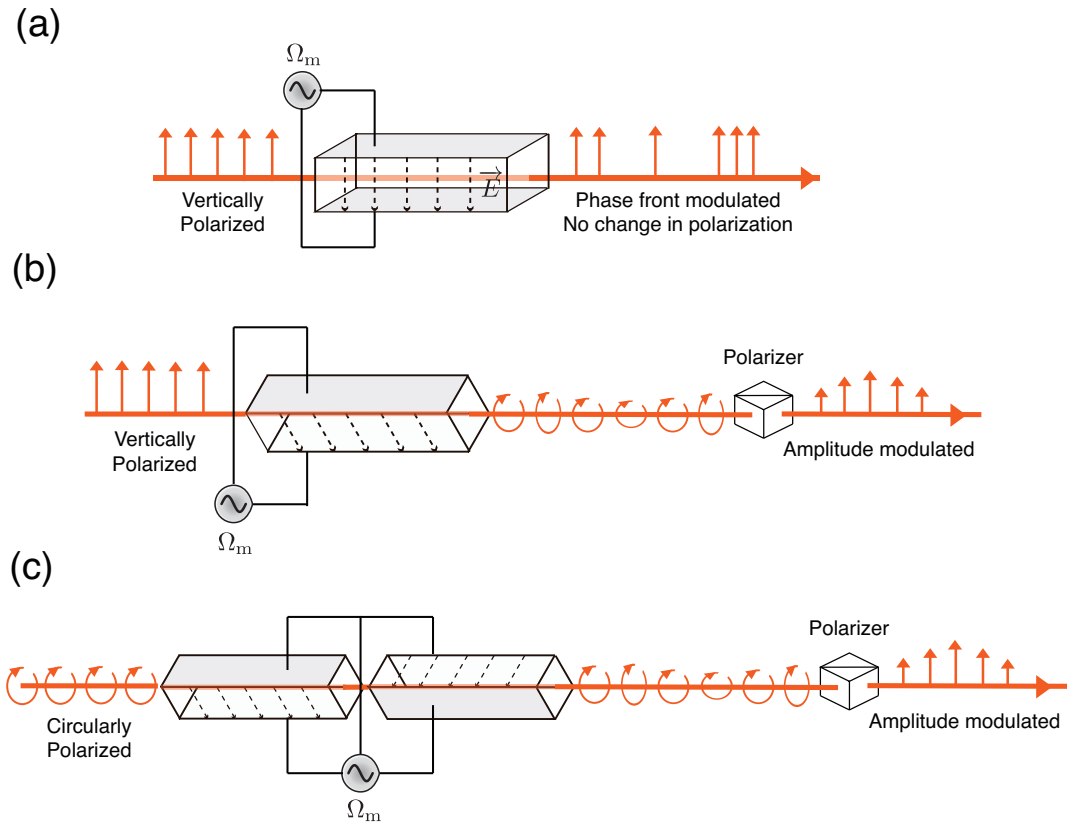

Figure 3.3: (a) and (b) illustrate, respectively, the experimental realization of phase and amplitude modulations using birefringent crystals, whilst (c) shows the actual configuration of the amplitude modulation in our laboratory.

in turn incurs an additional phase shift on the polarization component of the incident beam parallel to that optical axis. The change of refractive index is typically very small,

$$n \to n + \Delta n = n - \frac{1}{2}\varsigma n^3 E = n - \frac{1}{2}\varsigma n^3 E(0)\cos(\Omega_m t), \tag{3.9}$$

due to the small Pockels coefficient, ς, which typically lies in the range 10^{-12} to 10^{-10} m/V [56]. Here E refers to the external electric field and Ω_m the modulation frequency. Nevertheless, the accumulated phase change can be significant if the beam travels a distance substantially exceeding its wavelength.

The experimental realizations of amplitude and phase modulation are depicted in Fig. 3.3 (b) and (a), respectively. A single *anisotropic* $LiNbO_3$ crystal is utilized for phase modulation, with its orientation being configured such that a vertically polarized beam passing through the crystal maintains its polarization, but experiences a sinusoidal phase change due to the change of refractive index along the direction of the electric field. Amplitude modulation, on the other hand, can be realized by rotating the nonlinear crystal by $45°$, as shown in Fig. 3.3 (b). The polarization of the incoming beam is then decomposed into two orthogonal components, one being parallel and the other perpendicular to the optical axis of the crystal. These two orthogonally polarized components

are subject to different phase shifts due to the change of refractive index enforced by the external electric field. In this situation, the nonlinear crystal works equivalently to a polarization retarder with retardation varying at $\cos(\Omega_m t)$. Consequently, an elliptically polarized beam is produced which is subsequently fed through a polarizer selecting either the vertical or horizontal polarization component, and henceforth intensity modulation ensues. Here we realize the amplitude modulation in an alternative way (see Fig. 3.3 (c)): two of the same crystals as that being utilized in the phase modulator are mounted in series with their optical axis at 90°. This arrangement stabilizes the performance of the crystal, reducing the fluctuation of refractive index cause by ambient temperature changes (less than $1\text{mrad}/^\circ\text{C}$). Another advantage of such dual crystal setup lies in its flexibililty that allows for simultaneous amplitude and phase modulations, as well as single sideband modulations. Which particular modulation is implemented is dependent upon the input polarization and the external electric field applied on each crystal [57].

We also point out that other than utilizing the electo-optical effect, a common alternate is to employ the acousto-optical effect [56, 25] to implement sideband modulations and the corresponding devices are called acousto-optical modualtors (AOM). The idea is rooted in the observation that a proportional perturbation of the refractive index of a crystal is incurred by a standing acoustic wave created through the external electric field. When light passes through the crystal, it experiences the Bragg diffraction with the diffraction angle being modulated by the electric field. The intensity of the reflected beam that is proportional to the intensity of the sound wave is modulated as the result.

Rules for aligning the Amplitude and Phase Modulators

The alignment of the amplitude and phase modulators comply exactly with the working mechanism of the nonlinear crystal illustrated in Fig. 3.3 (a) and (c).

The incoming light beam is prepared to be vertically polarized. To preclude any wavefront distortion, the light beam needs to be collimated to possess a beam waist lying in the range $100 \sim 250$ μm. It is then fed through a Glan-Thompson to purify its polarization. We align both the horizontal and vertical position of the phase modulator to maximally retain the polarization purity of the incident beam so as to ensure the polarization of the output beam is still vertical. Precautions need to be taken meanwhile to ensure no distortion appears on the beam's spatial mode. The amplitude modulator is aligned following the same procedures and lastly a quarter wave plate is placed in between the phase and amplitude modulators and rotated to maximize the transmitted power of the end polarizer.

Ideally, the amplitude modulator should be only producing amplitude modulations, and likewise for the phase modulator provided that the modulation depth is small. However, there is cross-talk between the two modulations in practice. The worse the alignment of the modulators are, the more significant the cross-talk is. Such cross-talk

deteriorates the purity of the modulation and in turn affects adversely any phase locking relying on the modulation signals. We exploit a balanced homodyne detection to measure the cross-talk, as shown in Fig. 3.4 (a). By locking the homodyne consecutively to amplitude and phase, we are able to measure the residual modulation coming from the modulation on the conjugate quadrature. Figure 3.4 (b) showcases the experimental results where cross-talk cancellation of 41.7 dB for phase and 40.3 dB for amplitude are observed, respectively. For typical quantum information experiments, a cross-talk cancellation above 35 dB should be satisfactory.

3.2 Displacement Operation

In Sec. 2.1.3, we introduced coherent state as resulting from applying the displacement operator, $\hat{D}(\alpha) = \exp\left(\alpha\hat{a}^\dagger - \alpha^* a\right)$, upon a vacuum state (see Eq. (2.13)). In spite of this elegant mathematical expression, one would ask what is the realistic device to implement such a transformation. One way to realize $\hat{D}(\alpha)$ is to apply sideband modulations as detailed in the previous section. Consider a carrier field, $\alpha(t)$, it was shown that amplitude/phase modulation with modulation depth $M \ll 1$ equivalently performs the role of the displacement operator $\hat{D}(M\alpha/\sqrt{2})/\ \hat{D}(iM\alpha/\sqrt{2})$ [25]. Therefore, a direct correspondence between amplitude/phase modulation and amplitude/phase displacement is established.

Another way to experimentally emulate a displacement operator is to combine the target signal beam with a bright coherent beam on a beamsplitter (BS) with transmissivity approaching 1. As shown in Fig. 3.5, consider an arbitrary single-mode quantum state ρ_{in}, pure or mixed, couple it with an auxiliary bright coherent state, $|\beta = \beta_x + i\beta_y\rangle$, on a BS with transmissivity η. Once the following conditions are fulfilled

$$|\beta| \to \infty, \quad 1 - \eta \to 0, \tag{3.10}$$

so $|\beta|\sqrt{1-\eta}$ is approximately constant, it has been proved that evolution of the input signal is governed by [58]

$$\hat{\rho}_{\text{out}} = \text{Tr}_\beta \left[\hat{U}\rho_{\text{in}} \otimes |\beta\rangle\langle\beta|\hat{U}^\dagger\right] = \hat{D}(\beta')\hat{\rho}_{\text{in}}\hat{D}^\dagger(\beta'), \tag{3.11}$$

obtained as a partial trace over the auxiliary mode. $\beta' = \beta\sqrt{1-\eta}$ denotes the modulation enforced on the signal beam that is transferred from the original modulation on the auxiliary beam. The operator $\hat{U}$ refers to the BS operator in the interaction picture

$$\hat{U}(\eta) = \exp\left[\arccos(\sqrt{\eta})(\hat{a}^\dagger\hat{b} - \hat{a}\hat{b}^\dagger)\right]. \tag{3.12}$$

A better approximation to $\hat{D}$ is attained by attenuating the transmissivity η, which, however, would require an auxiliary beam with higher intensity.

Whilst the transformation in Eq. (3.11) holds for general single-mode signal beam, its

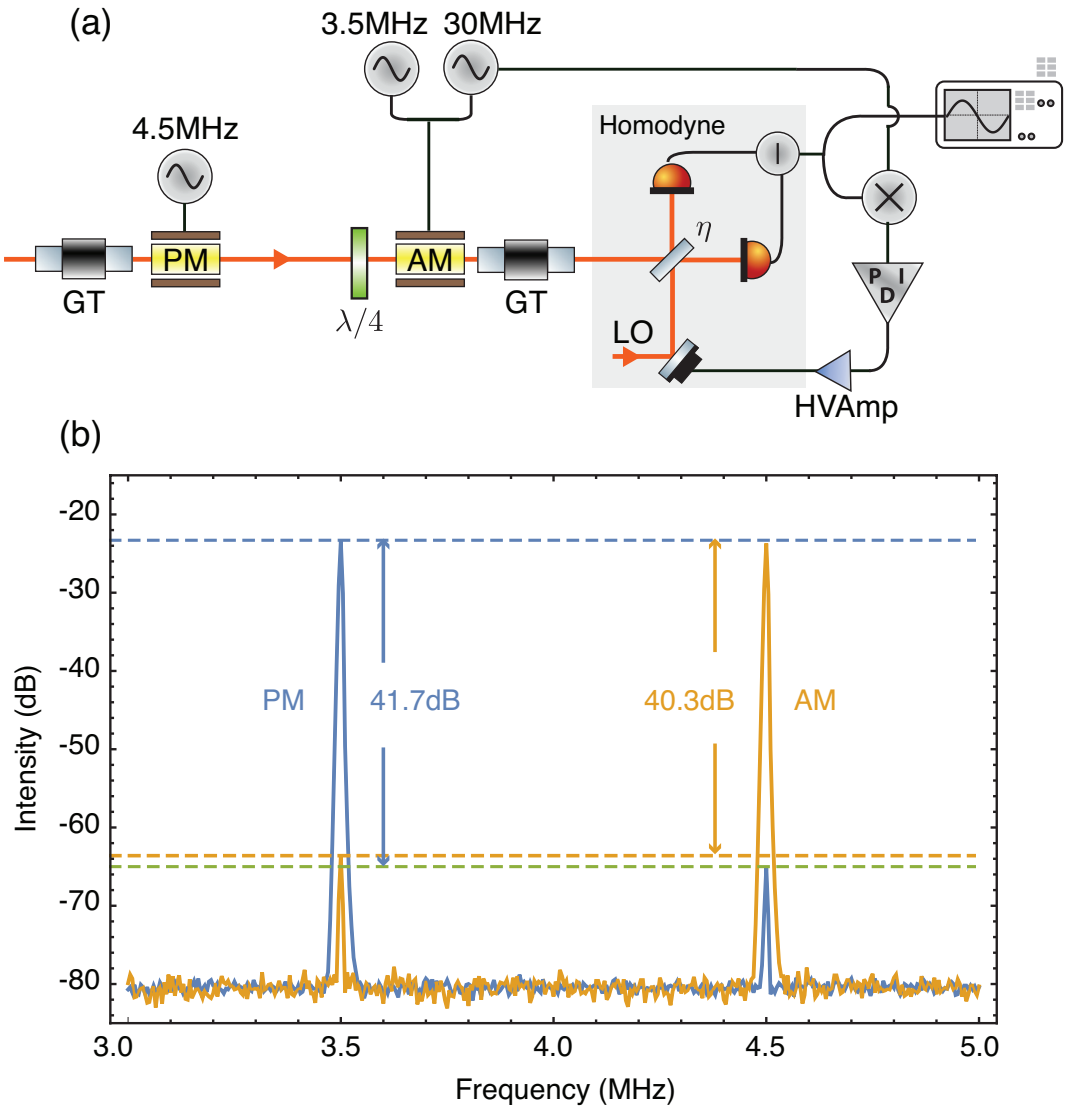

Figure 3.4: (a) Experimental layout for measuring the cross-talk between amplitude and phase modulations; LO: local oscillator, GT: glan-thompson polarizer, HVAmp: high voltage amplifier, PID: PID servo controller, and η: transmissivity of the beamsplitter for the homodyne detection, which is set to be 50:50 here in order to realize a balanced homodyne measurement. Demodulation is carried out by mixing down the subtracted photocurrent with the same modulation signal and low-pass filtering out the high frequency components. The encoded sideband information is extracted via demodulation and hence an error signal is obtained. The error signal is fed through a field programmable gate arrays (FPGA) system where a digital PID controller is executed. The resultant signal, after passing through a high-voltage amplifier, is sent back to the piezoelectric actuator (PZT) attached to one mirror on the LO to lock it in-phase to the signal beam. (b) Experimental results for cross-talk measurement between the amplitude and phase modulations that are displayed on an electronic spectrum analyzer (SA). The SA settings are: resolution bandwidth (RBW): 10 kHz; video bandwidth (VBW): 10 kHz; sweep time: 4.07×10^{-2} s.

validity can be intuitively verified by concerning ourselves with a coherent signal beam and the input-output relation for quadrature operators in this diagram (see Fig. 3.5).

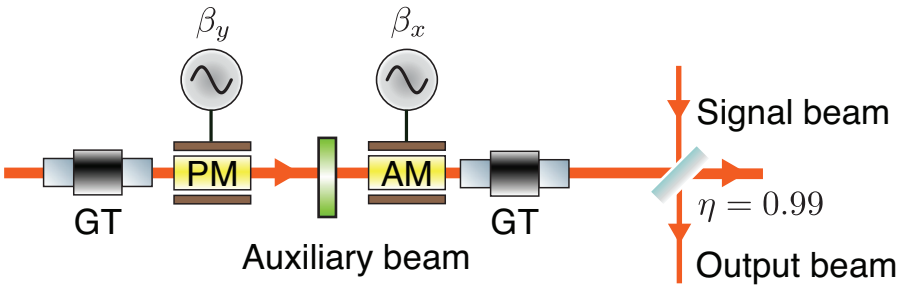

Figure 3.5: Emulating a displacement operation by combining a bright auxiliary beam and the target signal beam on a highly biased beamsplitter.

Under the action of a BS with transmissivity η, the quadrature operators of its input modes, $\hat{\mathbf{x}} := (\hat{X}_{+a}, \hat{X}_{-a}, \hat{X}_{+b}, \hat{X}_{-b})$, are transformed via the symplectic map

$$\hat{\mathbf{x}} \to \begin{pmatrix} \sqrt{\eta}\mathbf{I} & \sqrt{1-\eta}\mathbf{I} \\ -\sqrt{1-\eta}\mathbf{I} & \sqrt{\eta}\mathbf{I} \end{pmatrix} \hat{\mathbf{x}}, \tag{3.13}$$

where $\mathbf{I}$ denotes the 2×2 identity matrix. We thus obtain the quadrature operators of the output mode exiting the BS

$$\hat{X}_{+\text{out}} = \sqrt{\eta}\hat{X}_{+\text{in}} + \sqrt{1-\eta}\hat{X}_{+\text{aux}}, \quad \hat{X}_{-\text{out}} = \sqrt{\eta}\hat{X}_{-\text{in}} + \sqrt{1-\eta}\hat{X}_{-\text{aux}}, \tag{3.14}$$

where the subscripts in and aux stand for the input and the auxiliary beam, respectively. Recall that a displacement operator $\hat{D}(\beta)$ with $\beta = \beta_x + i\beta_y$ implements the translation

$$\hat{\mathbf{x}} \to \hat{\mathbf{x}} + \mathbf{d}_\beta, \tag{3.15}$$

where $\mathbf{d}_\beta = (\beta_x, \beta_y)$. Because a displacement $\hat{D}(\beta)$ is enacted upon the bright auxiliary beam in vacuum, its quadrature operators can be written as

$$\hat{X}_{+\text{aux}} = \beta_x + \delta\hat{X}_{+\text{aux}}, \quad \hat{X}_{-\text{aux}} = \beta_y + \delta\hat{X}_{+\text{aux}}. \tag{3.16}$$

Since both the signal and auxiliary beams are coherent states, $\langle(\delta\hat{X}_{\pm\text{in}})^2\rangle = \langle(\delta\hat{X}_{\pm\text{aux}})^2\rangle = 1$. By substituting Eq. (3.16) into (3.14), one can notice that a faithful approximation to $\hat{D}(\beta')$ on the signal beam is achievable by satisfying $\eta \to 1$ and $\beta = \beta'/\sqrt{1-\eta}$.

3.3 Gaussian Measurements

Directly detecting a light field with a single photodetector suffices for the purpose of probing simply the intensity noise of the light beam. However, this direct detection is not capable of differentiating between quadratures. Especially for investigating the quadrature variances of quantum states possessing non-symmetric Wigner functions in

phase space, a reference beam is required to interrogate an arbitrary quadrature amplitude. A device that is designed to this end is called *homodyne detection* [59] and its schematic is plotted in Fig. 3.4 (a). Homodyne detection is the most commonly used Gaussian measurement in CV quantum information processing. The reason resides in the observation that its outcome reveals exactly the quasi-probability distribution of the quadrature of interest, i.e. the marginal integral of the two-dimensional Wigner function (see Eq. (2.35)) over the conjugate quadrature [60]

$$P(\hat{X}_+) = \int W(q,p)\mathrm{d}p, \quad P(\hat{X}_-) = \int W(q,p)\mathrm{d}q. \tag{3.17}$$

In addition, its significance is due in part to the recognition that repeatitive homodyne detection in different quadratures enables the full tomography for any quantum state [61, 62, 63], and in part to the fact that concatenation of two homodyne measurements in conjugate quadratures, often called *dual homodyne detection*, provides us an access to the simultaneous estimation of both quadrature amplitudes.

3.3.1 Homodyne Detection

Consider an optical field of interest, $\hat{a}_{\mathrm{in}}$, interfering with a reference beam on a BS with transmissivity of η. The reference beam is commonly termed the *local oscillator* (LO) and its intensity is significantly higher than that of the signal beam. The input mode undergoes the linear unitary Bogoliubov transformation

$$\begin{pmatrix} \hat{a}_{\mathrm{o}1} \\ \hat{a}_{\mathrm{o}2} \end{pmatrix} \to \begin{pmatrix} \sqrt{\eta} & \sqrt{1-\eta} \\ -\sqrt{1-\eta} & \sqrt{\eta} \end{pmatrix} \begin{pmatrix} \hat{a}_{\mathrm{in}} \\ e^{i\theta}\,\hat{a}_{\mathrm{LO}} \end{pmatrix}, \tag{3.18}$$

where θ denotes the relative phase between the LO and the signal beam; $\hat{a}_{\mathrm{o}1}$, $\hat{a}_{\mathrm{o}2}$, are the two output modes emerging from the BS.

In terms of balanced homodyne detection where $\eta = 0.5$ (it is otherwise called unbalanced homodyne), photocurrents of the two detectors are given by

$$\begin{aligned}
i_{\mathrm{o}1}(t) &= \frac{g_{\mathrm{D}}}{2}\hat{a}^{\dagger}_{\mathrm{o}1}(t)\hat{a}_{\mathrm{o}1}(t) = \frac{g_{\mathrm{D}}}{2}\left(\alpha^{*}_{\mathrm{o}1} + \delta\hat{a}^{\dagger}_{\mathrm{o}1}(t)\right)\left(\alpha_{\mathrm{o}1} + \delta\hat{a}_{\mathrm{o}1}(t)\right) \\
&= \frac{g_{\mathrm{D}}}{2}\left(\alpha^2_{\mathrm{in}} + \alpha^2_{\mathrm{LO}} + 2\alpha_{\mathrm{in}}\alpha_{\mathrm{LO}}\mathrm{cos}\theta + \alpha_{\mathrm{in}}\left(\delta\hat{X}_{+\mathrm{in}}(t) + \delta\hat{X}^{-\theta}_{\mathrm{LO}}(t)\right)\right. \\
&\left.+\alpha_{\mathrm{LO}}\left(\delta\hat{X}_{+\mathrm{LO}}(t) + \delta\hat{X}^{\theta}_{\mathrm{in}}(t)\right)\right), \\
i_{\mathrm{o}2}(t) &= \frac{g_{\mathrm{D}}}{2}\hat{a}^{\dagger}_{\mathrm{o}2}(t)\hat{a}_{\mathrm{o}2}(t) \\
&= \frac{g_{\mathrm{D}}}{2}\left(\alpha^2_{\mathrm{in}} + \alpha^2_{\mathrm{LO}} - 2\alpha_{\mathrm{in}}\alpha_{\mathrm{LO}}\mathrm{cos}\theta + \alpha_{\mathrm{in}}\left(\delta\hat{X}_{+\mathrm{in}}(t) - \delta\hat{X}^{-\theta}_{\mathrm{LO}}(t)\right)\right. \\
&\left.+\alpha_{\mathrm{LO}}\left(\delta\hat{X}_{+\mathrm{LO}}(t) - \delta\hat{X}^{\theta}_{\mathrm{in}}(t)\right)\right).
\end{aligned} \tag{3.19}$$

Here we applied Eq. (2.9), (3.1) and (3.18) and omitted the higher-order terms, e.g. $\hat{a}_{\rm in}\hat{a}_{\rm in}$. Here, $g_{\rm D}$ is the amplification gain of the photodetectors that is defined as [64]

$$g_{\rm D} = \frac{\eta_{\rm diode} e}{h\nu}, \tag{3.20}$$

where e denotes the electronic charge, h Planck's constant, ν (Hz) the optical frequency and $\eta_{\rm diode}$ the photodiodes efficiency. $\hat{X}_\theta$ in Eq. (3.19) stands for the generalized quadrature operator

$$\hat{X}^\theta = \cos\theta\hat{X}_+ + \sin\theta\hat{X}_-, \qquad \theta \in [0, 2\pi]\,. \tag{3.21}$$

Taking the sum and subtraction of these photocurrents, we obtain

$$\begin{aligned} i_{\rm sum}(t) &= g_{\rm D}\left(\alpha_{\rm in}^2 + \alpha_{\rm LO}^2 + \alpha_{\rm in}\delta\hat{X}_{+\rm in}(t) + \alpha_{\rm LO}\delta\hat{X}_{+\rm LO}(t)\right), \\ i_{\rm sub}(t) &= g_{\rm D}\left(2\alpha_{\rm in}\alpha_{\rm LO}\cos\theta + \alpha_{\rm in}\delta\hat{X}^\theta_{\rm LO}(t) + \alpha_{\rm LO}\delta\hat{X}^\theta_{\rm in}(t)\right). \end{aligned} \tag{3.22}$$

Neglecting the terms scaled by $\alpha_{\rm in}$ because $|\alpha_{\rm in}| \ll |\alpha_{\rm LO}|$, Eq. (3.22) simplifies to give

$$\begin{aligned} i_{\rm sum}(t) &= g_{\rm D}\left(\alpha_{\rm LO}^2 + \alpha_{\rm LO}\delta\hat{X}_{+\rm LO}(t)\right), \\ i_{\rm sub}(t) &= g_{\rm D}\left(2\alpha_{\rm in}\alpha_{\rm LO}\cos\theta + \alpha_{\rm LO}\delta\hat{X}^\theta_{\rm in}(t)\right). \end{aligned} \tag{3.23}$$

In practice, the subtracted photocurrent is considered as the output of the balanced homodyne, consisting of a DC component and an alternating (time-dependent) AC component that carries the noise spectrum of the signal beam. Equation (3.23) gives great insights into the importance of a bright local oscillator beam: it amplifies the quantum attributes of the light field under interrogation which may otherwise be disguised in the electronic noise of the probing device, i.e. electronic noise of the detector itself and the spectrum analyzer.

The efficiency of the homodyne detection is normally quantified by the fringe visibility for the interference between the signal and LO. More precisely, the total detection efficiency, $\eta_{\rm D}$, is then given by

$$\eta_{\rm D} = \eta_{\rm diode}{\rm VIS}^2 = \eta_{\rm diode}\left(\frac{i_{\max} - i_{\min}}{i_{\max} + i_{\min}}\right)^2 = \eta_{\rm diode}\left(\frac{\alpha_{\rm in}\alpha_{\rm LO}}{\alpha_{\rm in}^2 + \alpha_{\rm LO}^2 + \alpha_{\rm in}\alpha_{\rm LO}}\right)^2, \tag{3.24}$$

where $\eta_{\rm diode}$ refers to the quantum efficiency of the detector photodiodes. Any imperfect situation with ${\rm VIS} < 1$, that may arise from the mismatch of LO to the signal beam either in terms of spatial modes or polarization modes, would result in an additional coupling between the LO and the modes orthogonal to signal that are occupied by vacuum. As a result, the output photocurrent of the homodyne detector in Eq. (3.19) now contains

two items

$$i_{\mathrm{o1}}(t) = \frac{g_{\mathrm{D}}}{2}\left(\sqrt{1-\eta_{\mathrm{D}}}\hat{a}_{\mathrm{o1}}^{\dagger} + \sqrt{\eta_{\mathrm{D}}}\hat{a}_{v}^{\dagger}\right)\left(\sqrt{1-\eta_{\mathrm{D}}}\hat{a}_{\mathrm{o1}} + \sqrt{\eta_{\mathrm{D}}}\hat{a}_{v}\right), \tag{3.25}$$

where $\hat{a}_v$ represents the uncorrelated vacuum fluctuation. Equation (3.24) implies that by enhancing the mode-matching between the signal and LO, a higher detection efficiency is attainable. This can be achieved by adjusting the lens configurations to ensure the shape of the LO's spatial mode coincides with that of the signal beam. On the other hand, the alignment mirrors need to be carefully tuned to ensure their beam waists lie at the same position. These two alignments complement each other and result in an enhanced overlap between the two modes. Any inefficiency involved in the homodyne detection would be considered as loss. Thus, enhancement of the homodyne efficiency is particularly crucial for the squeezing measurement that will be discussed in chapter 5 of this thesis. An elegant analysis on this topic can be found in Prof. Ping Koy Lam's thesis [53].

3.4 Locking Techniques

Feedback control, as opposed to the open-loop control, is extensively used in classical engineering to continuously correct the behavior of a dynamical system [65]. The correction is achieved by comparing the actual and desired outputs of the system, where the deviation is typically referred to as *error signal*. Through modification of the error signal, e.g. via the Proportional-Integral-Derivative (PID) controller, and adjustment of system parameters based on the modified error signal, the action of the system under control tends to reduce the deviation to zero. We can, by the same token, actively control and stabilize the performance of a quantum optical system in order to lock it to a desired operating condition.

Among all types of locking techniques, here we present two most regularly used locking methods in quantum optical experiments. One is phase locking to maintain the relative phase between two interfering beams, and the other is the Pound-Drever-Hall locking [66, 67, 68], used to keep optical cavities on resonance.

3.4.1 Relative Phase Locking

Recall the homodyne and feedback setup presented in Fig. 3.4 (a), and suppose the signal beam is only phase modulated at frequency Ω_{m}. Photocurrent for either of the outgoing modes of the BS is given by (see Eq. (3.19))

$$\begin{aligned} i_{\mathrm{o1}}(t) = \frac{g_{\mathrm{D}}}{2}\Big(&\alpha_{\mathrm{in}}^2 + \alpha_{\mathrm{LO}}^2 + 2\alpha_{\mathrm{in}}\alpha_{\mathrm{LO}}\cos\theta + \delta\hat{X}_{+\mathrm{in}}(t)\left(\alpha_{\mathrm{in}} + \alpha_{\mathrm{LO}}\cos\theta\right) \\ &+\delta\hat{X}_{-\mathrm{in}}(t)\alpha_{\mathrm{LO}}\sin\theta + \delta\hat{X}_{+\mathrm{LO}}(t)\left(\alpha_{\mathrm{LO}} + \alpha_{\mathrm{in}}\cos\theta\right) + \delta\hat{X}_{-\mathrm{LO}}(t)\alpha_{\mathrm{in}}\sin\theta\Big), \end{aligned} \tag{3.26}$$

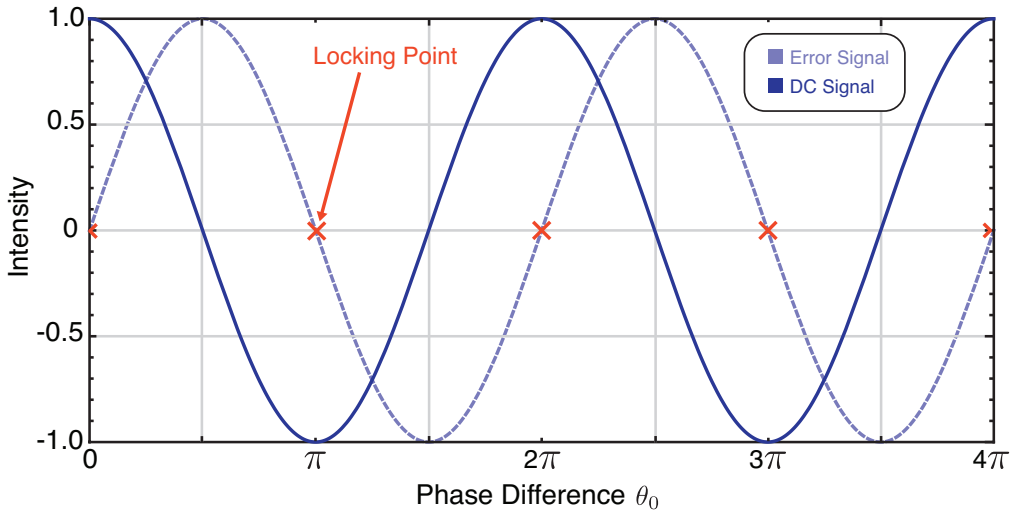

Figure 3.6: The error signal extracted from the output of a homodyne detection superimposed by the DC output of the detectors.

which results in an output noise power,

$$\langle|\delta i_{o1}|^2\rangle = \frac{g_D^2}{4}\Big(\langle(\delta\hat{X}_{+in})^2\rangle\left(\alpha_{in}^2 + 2\alpha_{in}\alpha_{LO}\cos\theta + \alpha_{LO}^2\cos^2\theta\right) + \langle(\delta\hat{X}_{-in})^2\rangle\alpha_{LO}^2\sin^2\theta$$
$$+\langle(\delta\hat{X}_{+LO})^2\rangle\left(\alpha_{in}^2\cos^2\theta + 2\alpha_{in}\alpha_{LO}\cos\theta + \alpha_{LO}^2\right) + \langle(\delta\hat{X}_{-LO})^2\rangle\alpha_{in}^2\sin^2\theta\Big). \tag{3.27}$$

Using the substitution $\langle(\delta\hat{X}_{\pm in})^2\rangle = \langle(\delta\hat{X}_{\pm LO})^2\rangle = 1$, since the signal beam and LO are shot noise limited, the variance of the photocurrent can thus be simplified as

$$\langle|\delta i_{o1}|^2\rangle = \frac{g_D^2}{2}\left(\alpha_{in}^2 + \alpha_{LO}^2 + 2\alpha_{in}\alpha_{LO}\cos\theta\right). \tag{3.28}$$

Owing to the cosine phase modulation applied on the signal beam, the relative phase between LO and signal are varying as a function of time, i.e. $\theta = \theta_0 + M\cos(\Omega_m t)$, where θ_0 denotes the average phase and M is the modulation depth. For the case of a small modulation depth ($M \ll 1$), the following approximation holds valid

$$\cos(\theta) = \cos\left(\theta_0 + M\cos(\Omega_m t)\right) = \cos\theta_0\cos\left[M\cos(\Omega_m t)\right] - \sin\theta_0\sin\left[M\cos(\Omega_m t)\right]$$
$$\approx \cos\theta_0 - \sin\theta_0 M\cos(\Omega_m t). \tag{3.29}$$

Substituting Eq. (3.29) into Eq. (3.28) gives

$$\langle|\delta i_{o1}|^2\rangle = \frac{g_D^2}{2}\left[\alpha_{in} + \alpha_{LO}^2 + 2\alpha_{in}\alpha_{LO}\left(\cos\theta_0 - \sin\theta_0 M\cos(\Omega_m t)\right)\right]. \tag{3.30}$$

The sideband error signal can then be recovered by demodulating Eq. (3.30), which is mathematically described by multiplication of the signal by a cosine function oscillating

at the same frequency $\Omega_{\rm m}$, i.e.

$$\left[\frac{g_{\rm D}^2}{2}\left(\alpha_{\rm in}^2+\alpha_{\rm LO}^2\right)+g_{\rm D}^2\alpha_{\rm in}\alpha_{\rm LO}{\rm cos}\theta_0\right]{\rm cos}(\Omega_{\rm m}t)-g_{\rm D}^2\alpha_{\rm in}\alpha_{\rm LO}{\rm sin}\theta_0 M\left(\frac{{\rm cos}(2\Omega_{\rm m}t)+1}{2}\right). \tag{3.31}$$

Physically, the demodulation is equivalent to shifting all frequency components up and down by $\Omega_{\rm m}$ based on the convolution theorem. Applying further a low pass filter on the demodulated signal to select only the DC component, we obtain the phase locking error signal

$$\xi_{\rm ES,PM}=g_{\rm D}^2 M\alpha_{\rm in}\alpha_{\rm LO}\frac{{\rm sin}\theta_0}{2}, \tag{3.32}$$

which is plotted in Fig. 3.6 along with the DC output of the homodyne detectors. Notice that the zero crossings of the error signal lie at every $\theta_0 = N\pi$, $N \in \mathbf{Z}$, implying that with phase modulated signal beam, the LO and signal will always be locked in phase. So far we have used only one of the outgoing modes of the BS to derive the error signal. In practice, however, subtraction of the two photocurrents is more commonly utilized

$$\langle|\delta i_{o1}|^2\rangle-\langle|\delta i_{o2}|^2\rangle=2g_{\rm D}^2\alpha_{\rm in}\alpha_{\rm LO}{\rm cos}\theta. \tag{3.33}$$

Following the methodology detailed above, the same error signal would be obtained after demodulation and filtering.

Amplitude Modulation

Applying instead amplitude modulation on the signal beam, that is $\alpha_{in}\rightarrow\alpha_{in}\left(1-M{\rm cos}(\Omega_m t)\right)$, the subtracted noise power becomes

$$\langle|\delta i_{o1}|^2\rangle-\langle|\delta i_{o2}|^2\rangle=2g_{\rm D}^2\alpha_{\rm in}\alpha_{\rm LO}\left(1-M{\rm cos}(\Omega_{\rm m}t)\right){\rm cos}\theta. \tag{3.34}$$

Similarly, the final phase locking error signal is attainable by demodulating the subtracted detector photocurrents and filtering out the high frequency components,

$$\xi_{\rm ES,AM}=g_{\rm D}^2 M\alpha_{\rm in}\alpha_{\rm LO}{\rm cos}\theta_0. \tag{3.35}$$

Equation 3.35 indicates that the application of amplitude modulation, unlike the phase modulation, would enable one to lock the local oscillator in quadrature (out of phase) to the signal beam.

3.4.2 PDH Locking

Pound-Drever-Hall locking was originally proposed as a powerful technique for stabilizing the frequency of a laser by locking it to a Fabry-Parot cavity [66, 67, 68]. It exploits

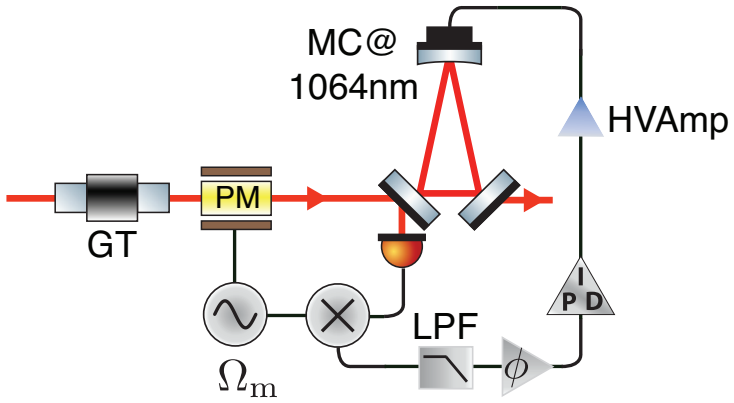

Figure 3.7: Schematic for locking the mode cleaner (MC) on the fundamental beam (1064nm) using PDH technique. ϕ: phase shift to compensate any unequal delay between the signal and the electronic local oscillatior for demodulation and to provide a way to select either the sine or the cosine components of the detector output; GT: glan-thompson polarizer; LPF: low pass filter used to isolate the low frequency component of the output of the mixer; HVAmp: high voltage amplifier, PID: PID controller implemented by a LabVIEW FPGA system.

differences in the cavity's response when the frequency of its incident beam changes about resonance: above resonance, an increase in the laser's frequency increases the reflected power; on the contrary, below resonance, an increase in the laser's frequency reduces the reflected power. Interrogation of the reflected power thus creates an error signal that reveals changes in the laser's frequency and in turn can be fed back to the laser to stabilize its frequency. Although frequency stabilization remains its primary usage, it has a much wider domain of applications. A prominent example is to probe and control the length of a cavity to keep it on resonance to a particular incoming laser, as shown in Fig. 3.7.

Recall a light field that is phase modulated at frequency $\Omega_{\rm m}$ (see Eq. (3.6))

$$\alpha(t) \approx \alpha_0 \left[e^{i\omega_0 t} + i\frac{M}{2}\left(e^{i(\omega_0+\Omega_{\rm m})t} + e^{i(\omega_0-\Omega_{\rm m})t} \right) \right] \tag{3.36}$$

and is injected into a symmetric, lossless cavity. The reflected field of the cavity can then be expressed as

$$\alpha_{\rm ref}(t) = \alpha_0 \left[\mathcal{F}(\omega_0) e^{i\omega_0 t} + i\frac{M}{2}\mathcal{F}(\omega_0+\Omega_m) e^{i(\omega_0+\Omega_{\rm m}t)} + i\frac{M}{2}\mathcal{F}(\omega_0-\Omega_m) e^{i(\omega_0-\Omega_{\rm m}t)} \right], \tag{3.37}$$

where

$$\mathcal{F}(\omega) = \frac{r\left(e^{i\phi}-1\right)}{1-r^2 e^{i\phi}}, \tag{3.38}$$

is the reflection coefficient of the cavity. It depends on r, the reflectivity of the input

coupler and ϕ, the phase the light picks up per cavity round trip:

$$\phi = 2\pi\frac{L}{\lambda} = 2\pi\frac{f}{\nu_{\text{fsr}}}. \tag{3.39}$$

Here, L denotes the cavity round trip length, f is the laser frequency while $\nu_{\text{fsr}} = c/nL$ is the free spectral range of the cavity; n refers to the refractive index of the cavity space. The power in the reflected beam that is given by $\alpha^*_{\text{ref}}(t)\alpha_{\text{ref}}(t)$ can be derived,

$$\begin{aligned} P_{\text{ref}} = \alpha_0^2 \Bigg[& |\mathcal{F}(\omega_0)|^2 + \frac{M^2}{4}\left(|\mathcal{F}(\omega_0+\Omega_{\text{m}})|^2 + |\mathcal{F}(\omega_0-\Omega_{\text{m}})|^2\right) \\ & - M\text{Re}\left[\mathcal{F}(\omega_0)^*\mathcal{F}(\omega_0+\Omega_{\text{m}}) - \mathcal{F}(\omega_0)\mathcal{F}(\omega_0-\Omega_{\text{m}})^*\right]\sin(\Omega_{\text{m}}t) \\ & - M\text{Im}\left[\mathcal{F}(\omega_0)^*\mathcal{F}(\omega_0+\Omega_{\text{m}}) - \mathcal{F}(\omega_0)\mathcal{F}(\omega_0-\Omega_{\text{m}})^*\right]\cos(\Omega_{\text{m}}t)\Bigg]. \end{aligned} \tag{3.40}$$

Here we omitted the terms involving $e^{\pm 2i\Omega_{\text{m}}t}$ that result from the interference between the two sidebands. In situation where the modulation frequency is high, namely $\Omega_{\text{m}} \gg \nu_{\text{fsr}}/f$, the sidebands are far from resonance which are therefore fully reflected. This means $\mathcal{F}(\omega_0 \pm \Omega_{\text{m}}) \approx -1$, so

$$\mathcal{F}(\omega_0)^*\mathcal{F}(\omega_0+\Omega_{\text{m}}) - \mathcal{F}(\omega_0)\mathcal{F}(\omega_0-\Omega_{\text{m}})^* \approx -i2\text{Im}\left[\mathcal{F}(\omega_0)\right], \tag{3.41}$$

thereby only the cosine term dominates and the sine term vanishes. The resulting error signal is attainable by mixing P_{ref} with $\cos(\Omega_{\text{m}}t)$ and extracting only the DC component

$$\xi_{\text{PDH,ES}} = \alpha_0^2 M\text{Im}\left(\mathcal{F}(\omega_0)^*\mathcal{F}(\omega_0+\Omega_{\text{m}}) - \mathcal{F}(\omega_0)\mathcal{F}(\omega_0-\Omega_{\text{m}})^*\right). \tag{3.42}$$

We plot $\xi_{\text{PDH,ES}}$ in Fig. 3.8 (a). It is noteworthy that the zero crossing of error signal occurs when either the carrier or the sidebands is resonant in the cavity. Nevertheless, because the sign of the error signal's slope is opposite for the carrier and the sidebands, one can always lock the cavity only to the carrier by inverting the electronic feedback gain.

Conversely, if a low frequency modulation is applied, i.e. $\Omega_{\text{m}} \ll \nu_{\text{fsr}}/f$, the standing wave built up inside the cavity stays always in equilibrium with the incoming light field, so $\mathcal{F}(\omega_0)^*\mathcal{F}(\omega_0+\Omega_{\text{m}}) - \mathcal{F}(\omega_0)\mathcal{F}(\omega_0-\Omega_{\text{m}})^*$ is purely real [67]. Pulling out the sine term in Eq. (3.40), we obtain the error signal

$$\xi_{\text{PDH,ES}} = \alpha_0^2 M\text{Re}\left[\mathcal{F}(\omega_0)^*\mathcal{F}(\omega_0+\Omega_{\text{m}}) - \mathcal{F}(\omega_0)\mathcal{F}(\omega_0-\Omega_{\text{m}})^*\right], \tag{3.43}$$

which is plotted in Fig. 3.8 (b).

In both circumstances, the error signals arise from the beating between the sidebands and the carrier. Thanks to the contribution of α_0^2, the negligible sideband signal is amplified, rendering the error signal observable.

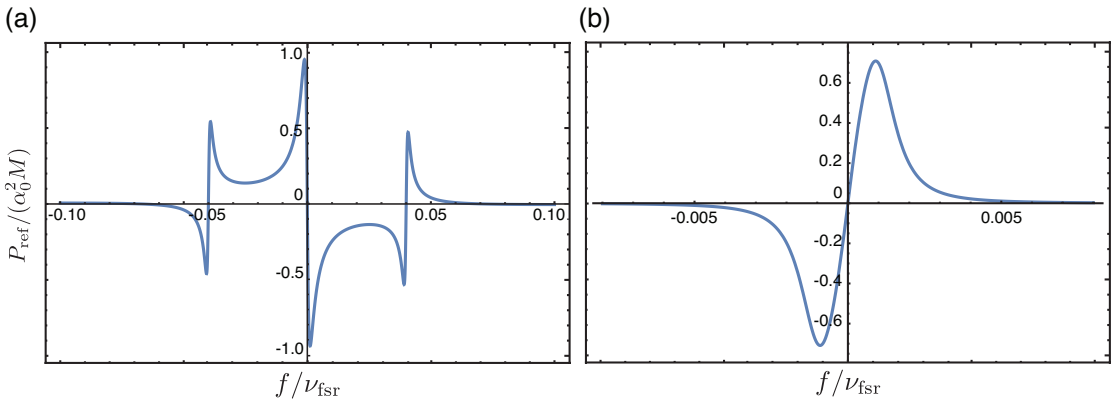

Figure 3.8: The PDH locking error signal for (a) high frequency phase modulation with $\Omega_m = 4\%$ free spectral range, and (b) low frequency phase modulation with $\Omega_{\rm m} = 0.1\%$ free spectral range. The reflectivity of the input coupler is 0.9975.

Chapter 4

Inverse-Gaussian Filter and Measurement-Based Noiseless Linear Amplification

Overview

In this chapter, we introduce an inverse Gaussian filter that serves as an essential component in this thesis. As shall be shown in chapter 6 – 9, it can be adopted in a wide range of CV quantum information tasks that involve a measurement-and-feed-forward stage. In particular, we show that it can be utilized to improve the fidelity of a squeezing gate, to enhance the signal-to-noise ratio of coherent states, to enable quantum cloning with fidelity surpassing the no-cloning limit, and to improve the fidelity of quantum teleportation. We thus believe it provides an effective and versatile tool to refine the conventional Gaussian toolbox for CV quantum information.

The filter function was originally formulated to emulate a noiseless linear amplifier (NLA) [22], due to the fact that present physical implementations of NLA are considerably resource and technique intensive [69, 70, 71, 72, 73, 74, 75]. Moreover, the success rates of these experiments are significantly lower than the theoretical expectation, thereby rendering the implementations quite unreliable in practical quantum information tasks, especially in field deployment settings. J. Fiurášek *et al.* proposed that in circumstances when NLA precedes a dual homodyne directly, its function can be faithfully simulated by an appropriate post-processing on the measurement outcomes. This virtual emulation of NLA is called a "measurement-based NLA (MB-NLA)". In this way, the experimental challenges are mitigated.

In this chapter, we first provide a review of the construction of the filter function in the context of noiseless linear amplification. Parameters that determine the performance of the filter function are discussed. We then present a detailed study on the similarities and differences between the measurement-based and the physical implementations of NLA by investigating their abilities to preserve the input Gaussianity and their probabilities of success. Moreover, by embedding both amplifiers into a feed-forward loop, we

construct two noiseless linear amplifiers that produce free-propagating amplified quantum states. The respective signal-to-noise ratios and fidelities of the two amplitication shemes are examined as well. We conclude that the way how MB-NLA's performance depends upon the effective parameters coincide with that of its physical counterpart; however, subtle differences remain. Only if one takes into account of all the parameters, their equivalence holds valid.

The above study provides quantitative criteria for engineering the filter function so that the trade-off between different figure of merits can be optimized. It is therefore of great instructional significance to the rest of the thesis.

The work presented in this chapter has been published in the journal article:

• J. Zhao J. Y. Haw, S. M. Assad, T. Symul, and P. K. Lam. *Characterization of measurement-based noiseless linear amplifier and its applications.* Physical Review A **96**, 012319, (2017).

4.1 Introduction

It is well known, since the seminal work of Caves [76], that deterministic phase-preserving amplification would inevitably introduce additional noise. Although this serves as the crucial basis for secure quantum communication, it imposes unavoidable limits on signal processing and quantum metrology. The first ingenious idea to evade this noise penalty was proposed by Lund and Ralph [21], and independently by Fiurášek [22]. A device called *noiseless linear amplifier* (NLA) was proposed which can amplify probabilistically the amplitude of an input state and meanwhile preserves its noise characteristics. This proposal opens up many promising applications in quantum computing and communication, such as quantum key distribution [77, 78, 79, 72, 74], quantum cloning [80], entanglement distillation [69, 81, 82], quantum repeater [83], phase estimation [75], and error correction [84].

However, even should one sacrifice some untriggered events, exact implementation of the NLA would still necessitate a vanishing success probability. Nevertheless, practical benefits of the noiseless amplification can be retained, if one further renounces the exactness of the NLA to reach a compromise between fidelity and success probability. A faithful approximation can be made by restricting the distribution of input states to a finite set [85] or alternatively, by truncating the working space of the amplifier. Physical implementations of NLA include methods such as quantum scissor [21, 86, 69, 70, 71, 72], photon addition-subtraction [87, 88, 73, 74], and noise addition [75]. Here, they are designated as *physical NLA* (P-NLA), for they take an input state and transform it into an amplified free-propagating output state. P-NLA has also been studied theoretically in several aspects, in particular, on optimizing the architecture and the success probability for different input distributions [89, 90, 85]. More recently, the

cascading of P-NLA and a deterministic linear amplifier was proposed and investigated as a part of a continuum of linear amplifiers [91]. However, due to various technical difficulties, current experiments on P-NLA are yet restricted to small gains and small input amplitudes.

For the case where the amplifier directly precedes a dual homodyne measurement, for example in quantum key distribution, probabilistic NLA can be emulated by conditioning upon the measurement records via a classical filter function [79, 81, 92]. This post-selection scheme, which we term as *measurement-based* NLA (MB-NLA), was shown to be equivalent to its ideal physical counterpart as long as the measurement that follows the amplification is informationally complete [81]. It is demonstrated experimentally that such post-selection scheme permits distillation of entanglement beyond the accessible with a perfect entangled resource experiencing the same loss [81]. Recently, it was proposed that MB-NLA can be integrated into continuous variable quantum teleportation [93] and quantum cloning protocol [94] to surpass the deterministic bounds.

In spite of this, in practice, it is not apparent how the effective parameters of an MB-NLA affect its performance and how they relate to those of a P-NLA. For instance, analogous to truncating the amplification operator on the photon number basis for a P-NLA, the MB-NLA also requires a virtual cut-off on the post-selection filter to emulate an NLA. Since increasing this cut-off will deteriorate the success probability, one might conclude that it resembles the truncation of a P-NLA. However, as we shall demonstrate in this chapter, the P-NLA truncation and the MB-NLA cut-off indeed act in a different manner. In fact, only when one takes into account of all of the relevant effective parameters (i.e. input amplitude, effective gain, and cut-off) can such equivalence between the measurement-based and the physical implementations be drawn.

In this work, we provide a detailed analysis on the MB-NLA, focussing in particular on coherent-state input. We compare the performance of MB-NLA with a P-NLA scheme based on an optimal positive-valued measure (POVM) [89, 90] which maximizes both the success probability and the fidelity. We show that the requirement for MB-NLA to obtain output statistics closely resembles that of an NLA is to choose appropriately the effective parameters appropriately.

4.2 Construction of the Inverse-Gaussian Filter

The filter function is constructed following the idea to recover the same statistical properties of the output of an ideal NLA, which is the exact implementation of a noiseless linear amplifier. We first recall that such an ideal NLA can be represented by the unbounded amplification operator $g^{\hat{n}}$ with $g > 1$, that realizes the following transformation [21, 22]:

$$g^{\hat{n}} \left|\alpha\right\rangle = e^{\frac{1}{2}(g^2-1)|\alpha|^2} \left|g\alpha\right\rangle \ . \tag{4.1}$$

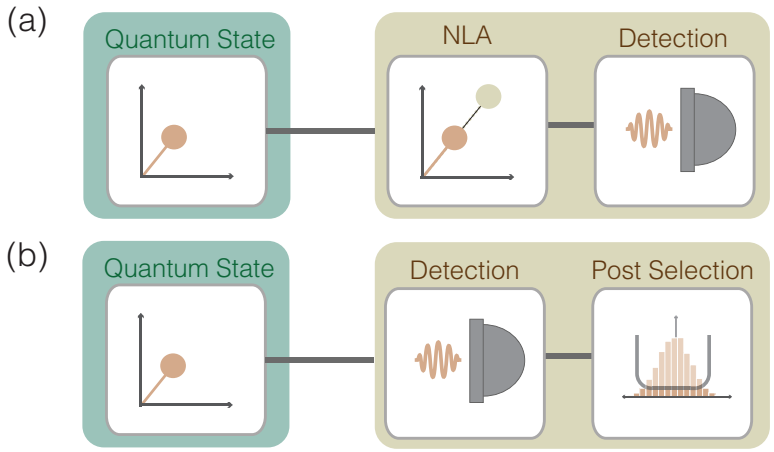

Figure 4.1: Two equivalent noiseless linear amplification schemes. (a) An ideal NLA immediately followed by a dual homodyne measurement. (b) Measurement-based NLA that emulates the NLA by applying Gaussian post-selection on the measurement outcomes.

Here $\hat{n}$ refers to the photon number operator. As discussed in [79, 81], the statistics of a POVM set $\{\pi_k\}$ upon the output of an arbitrary quantum map $\sum_i E_i \rho E_i^\dagger$ can be reconstructed by instead conditioning on measurements ($\{\tilde{\pi}_k\}=\sum_i E_i^\dagger \pi_k E_i$) on the original state. Although this reconstruction is valid in general, for unphysical quantum mapping, for example, NLA, it is permissible only when the POVM set $\{\tilde{\pi}_k\}$ is informationally complete (IC)[81]. A dual homodyne measurement, which is essentially a coherent state projection, is such an IC-POVM.

Based on Eq. (4.1), we can write down the Q function of the amplified state:

$$\begin{aligned} Q(\alpha) &= \frac{1}{\pi}\left\langle \alpha | g^{\hat{n}} \rho_{\text{in}} g^{\hat{n}} | \alpha \right\rangle \\ &= \exp\left[\left(g^2-1\right)|\alpha|^2\right] \frac{1}{\pi}\left\langle g\alpha | \rho_{\text{in}} | g\alpha \right\rangle , \end{aligned} \tag{4.2}$$

where ρ_{in} denotes the input state. Performing a change of variable, $\alpha = \alpha_m/g$, we get

$$Q(\alpha_m) = \exp\left[\left(1-\frac{1}{g^2}\right)|\alpha_m|^2\right] \frac{1}{\pi}\left\langle \alpha_m | \rho_{\text{in}} | \alpha_m \right\rangle \ . \tag{4.3}$$

This equation allows us to determine the appropriate post-selection filter to approximate an ideal NLA prior to a dual homodyne measurement, as illustrated in Fig. (4.1).

In Refs. [79, 92], it was shown how noiseless amplification can be achieved *virtually* through a Gaussian post-selection. Comparison of Eqs. (4.2) and (4.3) provides a three-step recipe for emulating the ideal NLA with gain g via a measurement-based algorithm. We first perform a dual homodyne measurement on an input state ρ_{in}, resulting in a measured value α_m that follows the probability distribution

$$p(\alpha_m) = \frac{1}{\pi}\left\langle \alpha_m | \rho_{\text{in}} | \alpha_m \right\rangle \ . \tag{4.4}$$

We then employ a probabilistic filter on the measurement records to realize the prefactor $\exp\left[\left(1-\frac{1}{g^2}\right)|\alpha_m|^2\right]$ in Eq. (4.3). To make the filter probability convergent, the filter is truncated by a real cut-off parameter α_c, resulting in a piecewise function given by

$$f(\alpha_m) = \begin{cases} \exp\left[\left(|\alpha_m|^2 - \alpha_c^2\right)\left(1-\frac{1}{g^2}\right)\right] & \text{if } |\alpha_m| < \alpha_c, \\ 1 & \text{otherwise.} \end{cases} \tag{4.5}$$

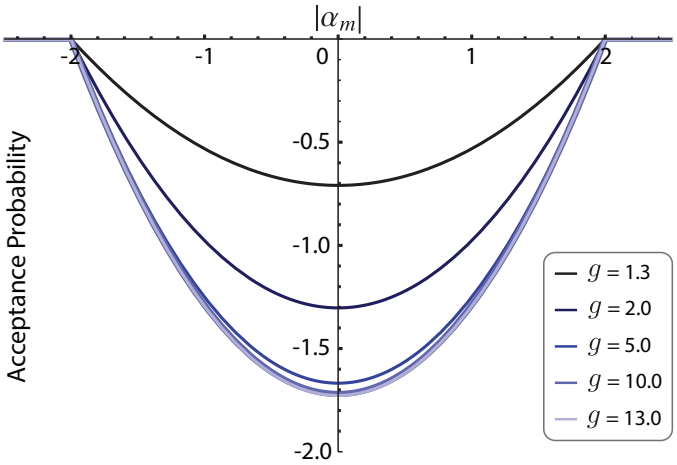

Figure 4.2: MB-NLA filter function as a function of the filter strength g, where $g = 1.3, 2.0, 5.0, 10.0, 13.0$ are shown in darker to lighter blue. The cut-off is chosen to be $\alpha_c = 2.0$ and the acceptance probability here is plotted in the logarithmic scale.

In Fig. 4.2, we plot the filter function to obtain a clear visualization of its profile, where we see a inverse Gaussian shape that denotes the acceptance probability of data points based on their amplitude. In practice, all measurement outcomes with magnitude less than α_c are selected with probability specified by Eq. (4.5); a lower acceptance rate is enforced on data points with small amplitudes, *i.e.* close to the center of origin. On the contrary, data samples lying beyond the cut-off α_c are kept with unity probability. The overall effect leads to a displaced distribution given by

$$\tilde{p}(\alpha_m) = \frac{1}{p_S^{(\mathrm{mb})}} p(\alpha_m) f(\alpha_m), \tag{4.6}$$

where $p_S^{(\mathrm{mb})}$ denotes the success probability of the MB-NLA:

$$p_S^{(\mathrm{mb})} = \iint \mathrm{d}^2\alpha_m \, p(\alpha_m) f(\alpha_m) \ . \tag{4.7}$$

The final step to emulate an ideal NLA is a linear rescaling that maps α_m to $g\alpha$. The output after this step will be distributed according to $Q^{(\mathrm{mb})}(\alpha)$, where

$$Q^{(\mathrm{mb})}(\alpha) = \tilde{p}(g\alpha)\, g^2, \tag{4.8}$$

by requiring $Q^{(\mathrm{mb})}(\alpha)\mathrm{d}^2\alpha = \tilde{p}\,(\alpha_m)\,\mathrm{d}^2\alpha_m$. It is this last step that ensures the noise characteristic of the input state is preserved during amplification.

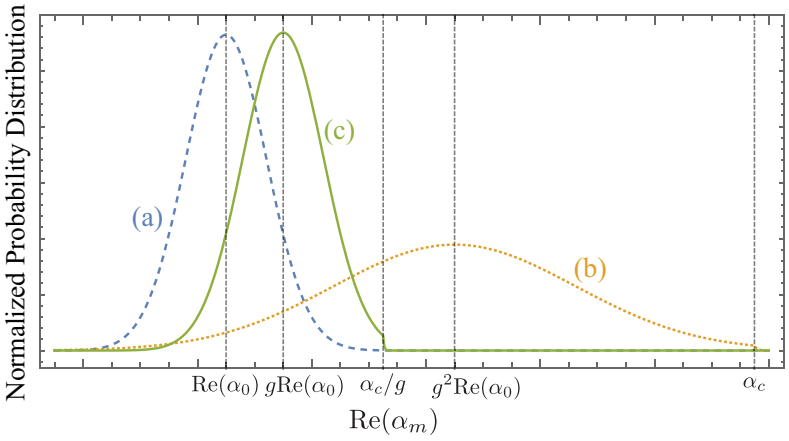

Figure 4.3: Procedures of an MB-NLA. (a) Distribution of the input state, revealed by a direct dual homodyne measurement. (b) Probability distribution after implementing the filter function with cut-off α_c. (c) The final probability distribution after rescaling which leads to the target distribution with the input mean being amplified by a factor of g.

In the following, we shall concern ourselves explicitly with a coherent input state $|\alpha_0|$. Without loss of generality, the analysis can be straightforwardly generalized to other Gaussian states. Figure (4.3) provides a pictorial representation of the aforementioned three steps for constructing the filter function. Note that in accordance with Eq. (4.4), a direct dual homodyne measurement is first performed on the input to reveal its probability distribution:

$$p\,(\alpha_m) = \frac{1}{\pi}\exp\left(-\left|\alpha_m - \alpha_0\right|^2\right)\,. \tag{4.9}$$

The real part of this distribution is centered at $\mathrm{Re}(\alpha_0)$ and has a variance of $\mathrm{Var}[\mathrm{Re}(\alpha_m)]=\mathrm{Var}[\mathrm{Im}(\alpha_m)]=0.5$, as shown as curve (a) in Fig. 4.3. Next, we apply the filter function in Eq. (4.5) which increases both the mean and variance of the distribution by g^2 (see Fig. 4.3 (b)). Lastly, a change in variable is performed to rescale the distribution by $1/g$; by doing this, the mean is reduced to $g\alpha_0$, while the variance goes back to 0.5. The net effect of post-selection together with the post-rescaling on the statistics of a coherent state is hence to approximately increase its mean by g and simultaneously preserves its minimum-uncertainty noise characteristic (Fig. 4.3 (c)). Due to a finite cut-off α_c, there is a discontinuity of the gradient of the resultant distribution appearing around α_c/g, as shown in Fig. 4.3, curves (b) and (c). More specifically, the output distribution

after post-selection ends up being

$$Q^{(\mathrm{mb})}(\alpha) = \frac{1}{p_S^{(\mathrm{mb})}} \begin{cases} \frac{g^2}{\pi} \exp\left(-\left|\alpha - g\alpha_0\right|^2\right) \exp\left[\left(g^2-1\right)\left(\left|\alpha_0\right|^2 - \frac{\alpha_c^2}{g^2}\right)\right] & \text{if } |\alpha| < \frac{\alpha_c}{g}, \\ \frac{g^2}{\pi} \exp\left(-\left|g\alpha - \alpha_0\right|^2\right) & \text{otherwise,} \end{cases} \tag{4.10}$$

which is essentially a concatenation of two Gaussian distributions joined at the circle $|\alpha| = \alpha_c/g$. The success probability $p_S^{(\mathrm{mb})}$ will be discussed in the next section. To exemplify the amplification, we plot $Q_{(\alpha)}^{(\mathrm{mb})}$ in Fig. 4.4 for an input coherent state with amplitude of α_0=0.5, and several different cut-offs. The performance of the MB-NLA is examined with respect to the ideal NLA under varying filter strengths. Among all the plots, only Figs. 4.4 (e), 4.4 (i), and 4.4 (j) resemble the output of an ideal NLA. As the filter strength increases, the output starts to be squeezed along the radial direction, and a larger cut-off is demanded to eliminate this contamination of the output distribution. As we further enhance the filter strength, *i.e.* in the limit of $g \gg 1$, the output distribution eventually asymptotes a Dirac delta function centered at α_c/g, and finally tends to be 0 as $g \to \infty$, irrespective of the amplitude of the input state.

4.2.1 Probability of Success

We characterize in this section the heralding rate of the post-selection acting upon the outcomes of a homodyne detection on a coherent input. It is parametrized by three effective parameters, namely the filter strength g, the cut-off α_c, and the amplitude of the coherent input $|\alpha_0|$, which can be expressed as

$$\begin{aligned} p_S^{(\mathrm{mb})} = & \underbrace{\frac{g^2}{\pi} \exp\left[\left(g^2-1\right)\left(\left|\alpha_0\right|^2 - \frac{\alpha_c^2}{g^2}\right)\right] \iint\limits_{|\alpha|<\frac{\alpha_c}{g}} \exp\left(-\left|\alpha - g\alpha_0\right|^2\right) \mathrm{d}^2\alpha}_{p_{S,\mathrm{in}}^{(\mathrm{mb})}} \\ & + \underbrace{\frac{g^2}{\pi} \iint\limits_{|\alpha|\geq\frac{\alpha_c}{g}} \exp\left(-\left|g\alpha - \alpha_0\right|^2\right) \mathrm{d}^2\alpha}_{p_{S,\mathrm{out}}^{(\mathrm{mb})}} . \end{aligned} \tag{4.11}$$

The first term $p_{S,\mathrm{in}}^{(\mathrm{mb})}$ involves an integration, within a circle with radius of α_c/g, of a two-dimensional Gaussian distribution centered at $g\alpha_0$. The second term $p_{S,\mathrm{out}}^{(\mathrm{mb})}$ can be rewritten as $1/\pi \iint\limits_{|\alpha|\geq\alpha_c} \exp\left(-\left|\alpha - \alpha_0\right|^2\right) \mathrm{d}^2\alpha$, which is independent of g. Although both terms contribute to the total success probability, only the fraction $p_{S,\mathrm{in}}^{(\mathrm{mb})}$ represents the part of the output that is properly amplified. In contrast, the fraction $p_{S,\mathrm{out}}^{(\mathrm{mb})}$ is the remnant from the input distribution that is retained with unity probability due to its lying beyond the cut-off. The total success probability is plotted in Fig. 4.5 (a) as a function of

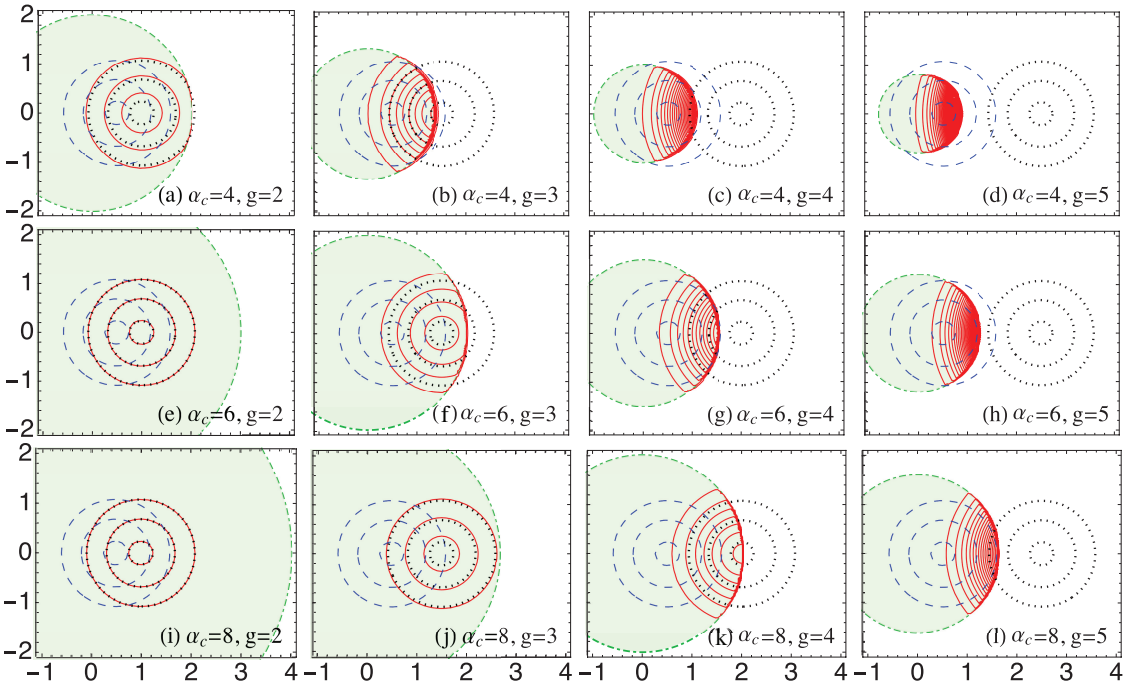

Figure 4.4: Output distribution of a measurement-based NLA. Dashed blue line depicts the Q distribution of an input coherent state with a real amplitude of 0.5, while the red solid line refers to the distribution of the outcomes of an MB-NLA with different cut-offs and filter strengths. As a reference, the output distribution of an ideal NLA is superimposed in dotted black line. Note that the output distribution of an MB-NLA consists of two Gaussian distributions joined at the green circle (dot-dashed) with radius of $|\alpha| = \alpha_c/g$. The contour levels are 0.1, 0.2, 0.3, and so forth. The x and y axes are $\mathrm{Re}(\alpha)$ and $\mathrm{Im}(\alpha)$, respectively. The probability density contours are plotted with incremental steps of 0.1. Some output contours have higher local values due to the more confined distribution in phase space.

the filter strength for different cut-offs, and in Fig. 4.5 (c) as a function of cut-off at different filter strengths. We see that the success probability decreases rapidly as g and α_c increase. For example, at a fixed gain $g = 2$, the success probability drops from 10^{-4} to 10^{-11} when α_c rises from 4 to 6. (Fig. 4.5 (c)).

It is noteworthy that for a fix α_c, the success probability $p_{S,\mathrm{in}}^{(\mathrm{mb})}$ tends to be a constant at the limit of large gain g, as shown in Fig. 4.5 (a). This phenomenon is a direct consequence of the mechanism of the MB-NLA. We notice that, as g becomes relatively large compared to the input amplitude and the cut-off, the filter function asymptotes to $\exp\left(|\alpha_m|^2 - \alpha_c^2\right)$ when $|\alpha_m| < \alpha_c$ (see Eq. (4.5)). In this situation, the filter becomes independent of g, as is illustrated in Fig. 4.2. As a result, the measurement outcomes lying within the cut-off amplitude will always be kept with a constant nonzero probability.

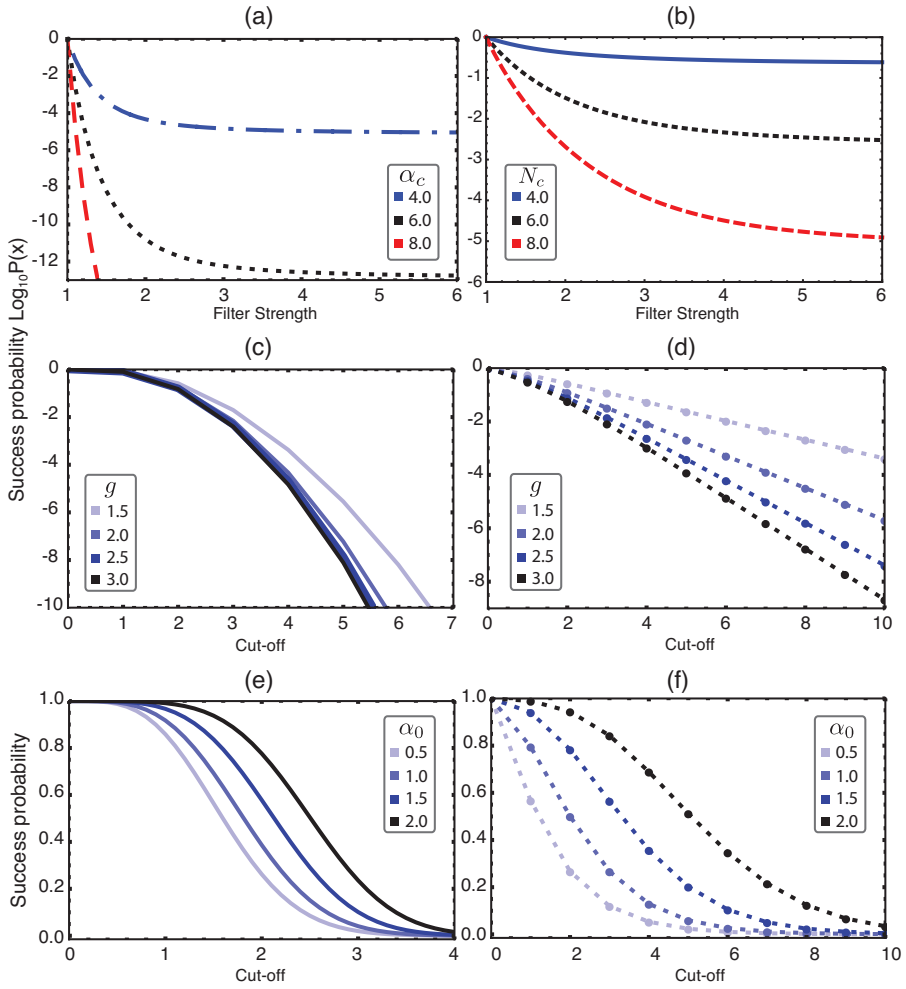

Figure 4.5: Success probabilities of MB-NLA (left column) and P-NLA (right column), respectively, with varying filter strengths and cut-offs. The probabilities of success in (a-d) are plotted in the logarithmic scale.

More specifically, $p_{S,\text{in}}^{(\text{mb})}$ tends to be independent of g which can be expressed as:

$$\begin{aligned} p_{S,\text{in}}^{(\text{mb})}\Big|_{g\to\infty} &= \iint\limits_{|\alpha|<\alpha_c} \frac{1}{\pi} \exp\left[2\,\text{Re}(\alpha\alpha_0^*) - |\alpha_0|^2 - \alpha_c^2\right] \mathrm{d}^2\alpha \\ &= \exp\left[-|\alpha_0|^2 - \alpha_c^2\right] \frac{\alpha_c}{|\alpha_0|} I_1(2|\alpha_0|\alpha_c)\,, \end{aligned} \tag{4.12}$$

where I_1 is the modified Bessel function.

4.3 Comparing the Measurement-based NLA and the Physical NLA

Consider that the filter function originates from the idea to emulate an NLA by a measurement-based scheme, it is thus instructive to compare the performances of the

direct implementation of an NLA, the so called "physical NLA (P-NLA)" and the "measurement-based NLA (MB-NLA)" in different operational regimes. We believe this comparison would be helpful to illuminate the behavior of the filter function.

4.3.1 An Ideal Physical Implementation of NLA

Here we look in particular at a theoretical model that realizes the NLA optimally with both working probability and fidelity saturating the theoretical bound [89]. Amplification with a gain of g in this architecture is carried out by a two-outcome POVM, where the successful outcome is specified by the operator [90]

$$\hat{M}_S = \underbrace{\frac{1}{g^{N_c}} \sum_{n=0}^{\lfloor N_c \rfloor} g^n \left|n\right\rangle \left\langle n\right|}_{\hat{M}_{S,1}} + \underbrace{\sum_{n=\lceil N_c \rceil}^{\infty} \left|n\right\rangle \left\langle n\right|}_{\hat{M}_{S,2}} . \tag{4.13}$$

In analogy to α_c of the filter function in Eq. (4.5), the photon number truncation N_c fulfills the projection of the operator $g^{\hat{n}}$ onto the subspace spanned by the first N_c eigenstates and therefore ensures the amplification is physical. For an input state ρ_{in}, we can calculate the success probability of the P-NLA

$$p_S^{(\text{phy})} = \text{Tr}\left(\hat{M}_S \rho_{\text{in}} \hat{M}_S^\dagger\right) . \tag{4.14}$$

Here, $p^{(\text{phy})}$ denotes also the optimal success probability achievable for any physical implementation of an NLA. More specifically, it can be expressed as the sum of two terms,

$$p_S^{(\text{phy})} = \underbrace{\text{Tr}\left(\hat{M}_{S,1} \rho_{\text{in}} \hat{M}_{S,1}\right)}_{p_{S,1}^{(\text{phy})}} + \underbrace{\text{Tr}\left(\hat{M}_{S,2} \rho_{\text{in}} \hat{M}_{S,2}\right)}_{p_{S,2}^{(\text{phy})}} , \tag{4.15}$$

where $p_{S,2}^{(\text{phy})}$ is independent of g. Similar to the success probability of an MB-NLA in Eq. (4.11), the first term results from a proper amplification while the events in the second term arise due to the truncation on the operating space of operator $g^{\hat{n}}$ when a finite cut-off N_c is enforced (c.f. Eq. (4.13)). For an input coherent state, $p_S^{(\text{phy})}$ can be written analytically as [89, 90]

$$p_S^{(\text{phy})} = 1 - Q\left(N_c + 1, |\alpha_0|^2\right) + \tag{4.16}$$

$$g^{-2N_c} \exp\left[\left(g^2 - 1\right)|\alpha_0|^2\right] Q\left(N_c + 1, |g\alpha_0|^2\right) . \tag{4.17}$$

Here, $Q(N,\lambda)$ is the regularized incomplete gamma function defined as the ratio of the incomplete gamma function $\Gamma(N,\lambda)$ over the complete gamma function $\Gamma(N)$

$$Q(N,\lambda) = \Gamma(N,\lambda)/\Gamma(N) \ . \tag{4.18}$$

The resultant output state of the P-NLA can be expressed as

$$\rho_S = \frac{\hat{M}_S \rho_{\text{in}} \hat{M}_S^\dagger}{p_S^{(\text{phy})}} \ . \tag{4.19}$$

4.3.2 Output Husimi Q Fuction

We first compare the two distinct NLA schemes by examining their respective output Husimi Q distributions. For comparison, in Fig. 4.6, we plot $Q^{(\text{phy})}(\alpha)$ with the same input amplitude $\alpha_0 = 0.5$ and filter strengths $g = 2, 3, 4, 5$ as those in Fig. 4.4. Similar to the MB-NLA, the physical NLA emulates an ideal NLA faithfully only when the truncation point N_c properly accommodates $|\alpha_0|$ and g (Fig. 4.6 (e) and 4.6 (i)).

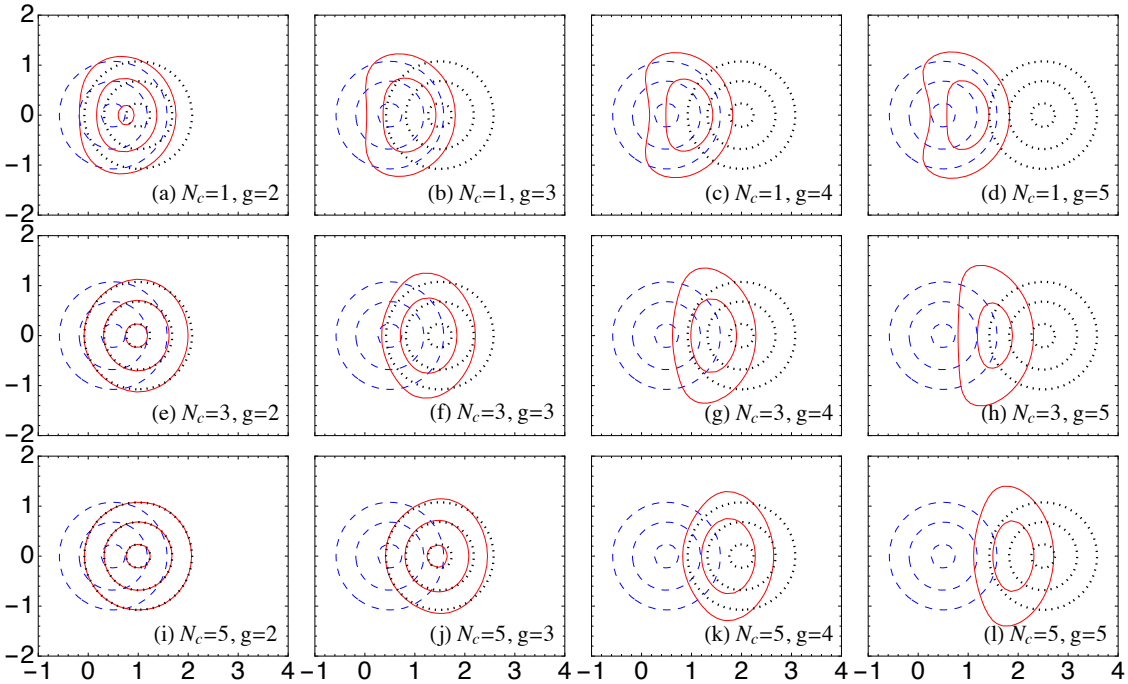

Figure 4.6: Output distribution of a physical NLA. Dashed blue line gives the distribution of the input coherent state with amplitude of $\alpha_0 = 0.5$. Dotted black line gives the output distribution of an ideal NLA with infinite photon number cut-off. Red solid line is the distribution of the outcome of a physical NLA with photon number cut-offs of $N_c = 1, 3$, and 5, and different filter strengths. For a fixed amplification gain, a larger cut-off would lead to a better approximation of an ideal NLA. The contour levels are 0.1, 0.2 and 0.3. The x and y axes are $\text{Re}(\alpha)$ and $\text{Im}(\alpha)$, respectively.

By comparing Fig. 4.4 and 4.6, we note that while the output of a P-NLA is always a physical state, the output distribution of MB-NLA does not necessarily represent a

valid Husimi Q-distribution and thus can result in an unphysical state. We emphasize that the MB-NLA is not an emulation of the P-NLA, but rather the device to reconstruct the measurement statistics of an ideal NLA (see Eq. (4.3)). For example, when the input to a P-NLA is a Fock state, the probabilistic output is the same Fock state regardless of the cut-off N_c. However, for MB-NLA, as long as the cut-off is finite, the output will not be an exact Fock state.

4.3.3 Probability of Success

We then compare MB-NLA and P-NLA with respect to their success probabilities. Both $p_S^{(\mathrm{mb})}$ (c.f. Eq. (4.11)) and $p_S^{(\mathrm{phy})}$ (c.f. Eq (4.16)) are plotted as functions of filter strengths for different cut-offs (Fig. 4.5 (a,b)), and alternatively as functions of cut-offs at varying filter strengths (Fig. 4.5 (c,d)).

We note that the trend of how the success probability of a P-NLA descends resembles that of an MB-NLA, that is the higher the cut-off N_c, the lower the success probability, but the better the P-NLA approximates an ideal NLA. While the relation between the MB-NLA cut-off α_c and the P-NLA photon-number cut-off N_c is not straightforward due to different implementation mechanisms, comparison of the plots suggests that the success probability of the former is much lower. For example, at g=2 the output Q functions of the two amplifiers exhibit similar features at $\alpha_c = 6$ (Fig. 4.4 (e)) and $N_c = 5$ (Fig. 4.6 (i)). However, their corresponding success probabilities under these settings differ by 8 orders of magnitude (see Figs. 4.5 (a) and 4.5 (b)). Nevertheless, it is worth emphasizing that, in contrary to $p_S^{(\mathrm{mb})}$, which is attainable using current techniques [81, 94], $p_S^{(\mathrm{phy})}$ stands for the upper bound of the success probability of a P-NLA.

For completeness, in Fig. 4.5 (e) and Fig. 4.5 (f), we depict $p_S^{(\mathrm{mb})}$ and $p_S^{(\mathrm{phy})}$ with varying cut-offs for different input amplitudes α_0. We see that as $|\alpha_0|$ gets larger, the success probability for both amplifiers actually increases. In fact, under a fixed cut-off, a higher input amplitude will result in a larger fraction of the amplified output lying beyond cut-off which are always kept with unit probability. The undesirable part $p_{S,\mathrm{out}}^{(\mathrm{mb})}$ ($p_{S,2}^{(\mathrm{phy})}$) therefore accounts for a larger fraction of the overall success probability. The output distribution, as a result, departs increasingly from that of the ideal NLA. This observation implies that success probability on its own is not a complete figure of merit to characterize the performance of an amplifier; it has to be combined with other measures able to quantify the closeness of the amplifier to an ideal NLA operation.

Another implication of these plots is that in situations where the amplifiers are acting on a distribution of input states with different amplitudes, the net success probability will be a weighted sum of the success probability for each individual input. Because the success probability varies between input coherent states with different amplitude, the output will be distributed in a different manner than the input.

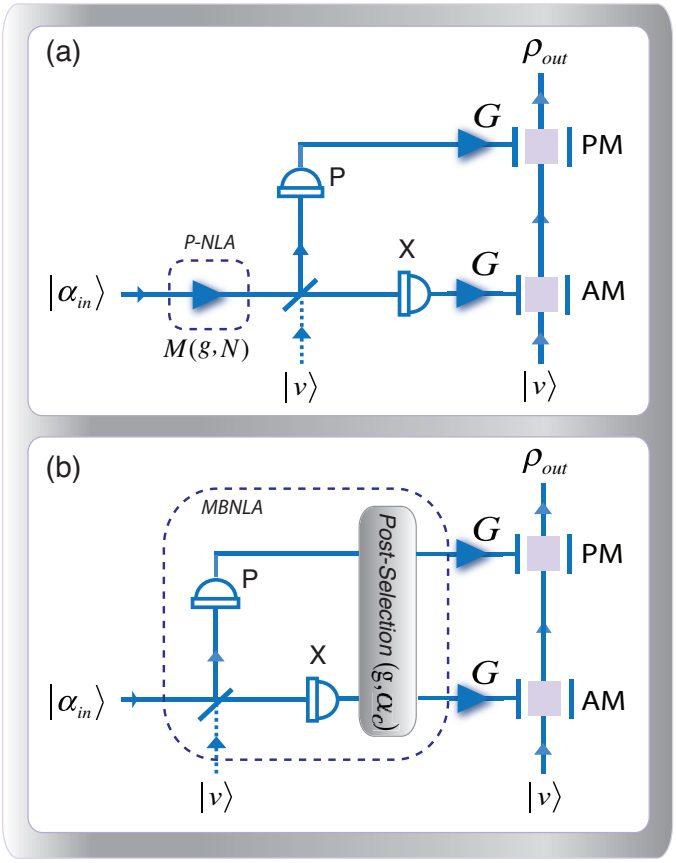

Figure 4.7: Schematic of embedding (a) P-NLA and (b) MB-NLA into a measure-and-prepare setup. AM: amplitude modulator; PM: phase modulator.

4.3.4 Applications: Measure-and-Prepare Amplifiers

In this section, we present two applications for the MB-NLA as a building block of, respectively, a measure-and-prepare (M-P) amplifier and a 1-to-infinity cloner. Moreover, the amplifier and cloner are also constructed based on the P-NLA for comparison. The output signal-to-noise ratio (SNR) and the cloning fidelity of both the MB-NLA-based and P-NLA-based schemes are subject to scrutiny to explore their similarity and difference.

In Fig. 4.7 (a), we integrate an MB-NLA into a measure-and-prepare diagram, which consists of a dual homodyne measurement followed by a displacement on a vacuum state by gain G. By doing this, we are able to generate a free-propagating amplified copy of the input, mitigating the drawback of the measurement-based NLA. To compare the performance of the MB-NLA with respect to its physical counterpart, we simply replace the MB-NLA with P-NLA followed by a dual homodyne, as depicted in Fig. 4.7 (b).

In both setups, when the measured distribution is used to displace a vacuum state,

the resultant output will be a statistical mixture of coherent states given by

$$\rho_{\text{out}} = \iint \mathrm{d}^2\alpha \; Q\left(\alpha\right) \left| \frac{G}{\sqrt{2}}\alpha \right\rangle \left\langle \frac{G}{\sqrt{2}}\alpha \right| \;, \tag{4.20}$$

where G is an electronic gain applied before the displacement.

To quantify the performance of the M-P amplifiers, we calculate the output SNR as our figure of merit, which is defined as the ratio of the signal of interest over its accompanied noise. More specifically, recall the quadrature operators defined in Eq. (2.9)

$$X_+ = a + a^\dagger, \quad X_- = i(a^\dagger - a), \tag{4.21}$$

where X_+ and X_- refer to the amplitude and phase quadratures of the electric field. Without loss of generality, throughout the rest of this chapter, we focus on the amplitude quadrature measurement and the conclusion holds valid for the phase quadrature. The mean and variance of X_+ are given by

$$\langle X_+ \rangle = \text{Tr}\left[X_+ \rho_{\text{out}}\right] = \iint \mathrm{d}^2 \; Q\left(\alpha\right) 2\text{Re}(\alpha) \;, \tag{4.22}$$

$$\begin{aligned} \langle \delta(X_+)^2 \rangle &= \text{Tr}\left[X_+^2 \rho_{\text{out}}\right] - \text{Tr}\left[X_+ \rho_{\text{out}}\right]^2 \\ &= \iint \mathrm{d}^2\alpha \; Q\left(\alpha\right) \left(4\text{Re}(\alpha)^2 + 1\right) \;, \end{aligned} \tag{4.23}$$

where the electronic gain G has been set to $\sqrt{2}$. The SNR for X_+ quadrature is hence given by $\langle X_+ \rangle^2 / \langle \delta(X_+)^2 \rangle$. In the following three subsections, we examine and compare the mean, variance, and SNR of the two distinct setups with varying filter strengths, cut-offs, and input amplitudes.

M-P Amplifiers with Varying Filter Strengths

We plot the output mean, variance, and SNR for the MB-NLA-based M-P amplifier in Figs. 4.8 (c), 4.8 (e), 4.8 (g) as a function of the filter strength with three different cut-off values. Similar plots for P-NLA-based M-P amplifier are presented in Figs. 4.8 (d), 4.8 (f), 4.8 (h). For an ideal NLA implementing $g^{\hat{n}}$ over the entire Hilbert space, the output mean is $2g\text{Re}(\alpha_0)$, which increases linearly with g. However, in practise, due to a finite cut-off, both P-NLA and MB-NLA will inevitably deviate from the ideal mean as the filter strength increases. This drop off occurs earlier for a smaller cut-off. Note that for both amplifiers, there is a saturation point of the output mean after which the mean stops growing, drops instead as the filter strength increases, and finally degrades to zero as the filter strength goes to infinity. Even though the expectation values for MB-NLA and P-NLA exhibit similar behavior, the two amplifiers indeed produce essentially different output distributions. For P-NLA, an increasing filter strength yields eventually a Fock state with photon number of N_c and henceforth, the mean of the X quadrature is zero. In contrast, the output distribution of the MB-NLA tends to squash along the

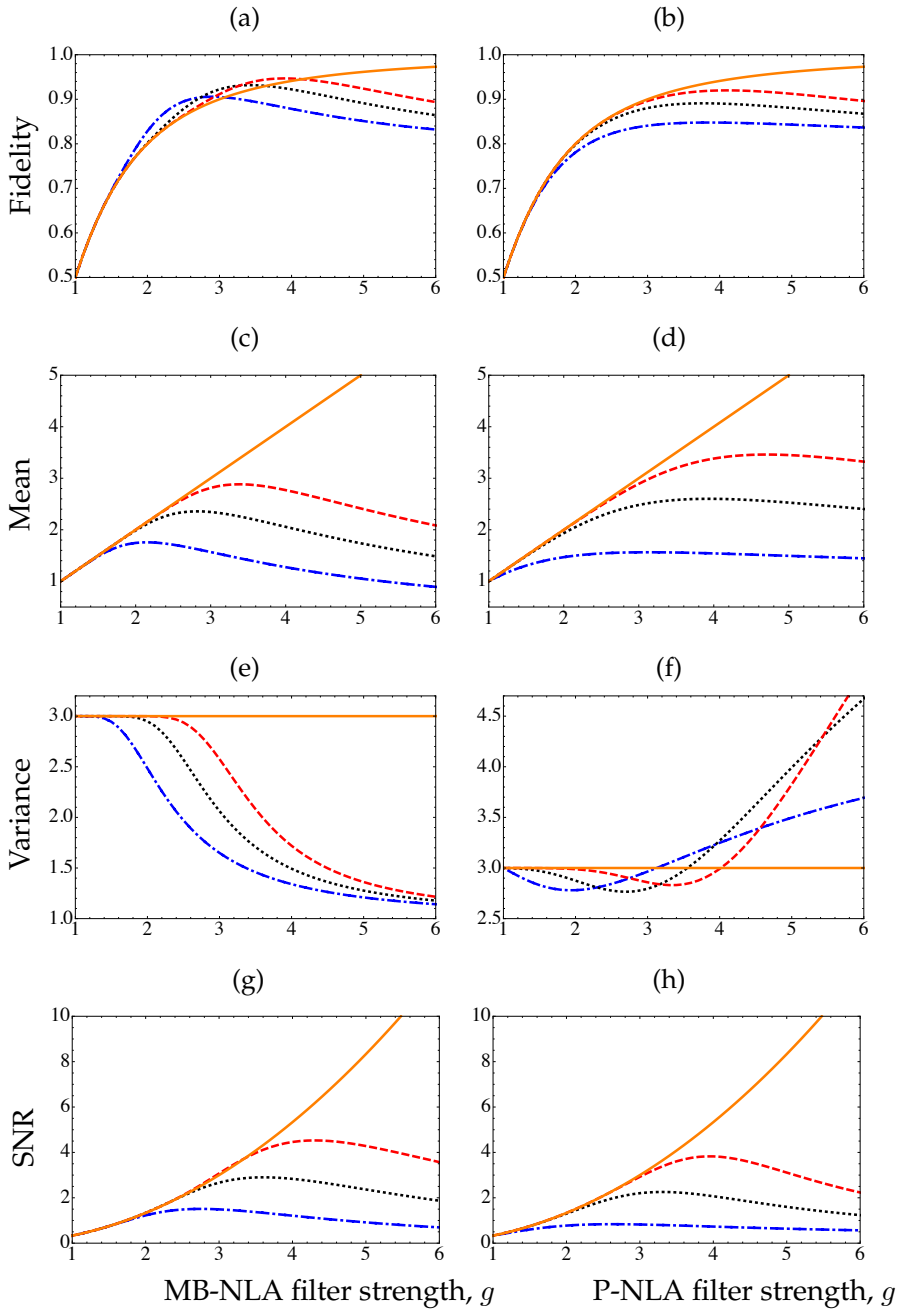

Figure 4.8: (left column) MB-NLA with varying filter strengths and cut-offs α_c=4, 6, and 8 represented, respectively, by dotdashed blue, dotted black, and dashed red curves. (right column) P-NLA with varying filter strengths and photon number cut-offs N_c=1, 3, and 5 (dotdashed blue, dotted black, and dashed red). For all plots, the input state has an amplitude of $\alpha_0 = 0.5$. For comparison, the orange-thick line is shown to illustrate the results based on an ideal amplifier with an inifinite cut-off.

radial direction, which gradually becomes a delta function peaked at α_c/g. In other words, in the high gain regime,

$$\langle X\rangle_{\rm phy} \to 0 \quad \text{and} \quad \langle X\rangle_{\rm mb} \to \frac{\alpha_c}{g} \,. \tag{4.24}$$

Ideally, the minimum variance of the output state would be $G^2 + 1 = 3$. This can be seen as a gain of $\sqrt{2}$ is needed to compensate for the 50:50 beamsplitter in the dual homodyne setup. For both P-NLA-based and MB-NLA-based amplifiers, the variance remains close to 3 for relatively small g, denoting that the input state is properly amplified. However, as g continues to increase, the output variance of the two amplifiers start to behave in completely different manner. For the P-NLA-based amplifier, the output variance becomes slightly less than 3, and decreases gradually as the filter strength goes up. This reveals the fact that the cut-off no longer suffices, with respect to the filter strength, to preserve the Gaussianity of the input state, such that the output standard deviation is squeezed along the X quadrature whilst being anti-squeezed along the P quadrature in compliance with the Heisenberg uncertainty principle (Fig. 4.6). As the filter strength keeps increasing, the variance rises rapidly, surpasses 3, and eventually approaches $2N_c + 2$, i.e.

$$\lim_{g\to\infty} \mathrm{Var}\,[X]_{\mathrm{phy}} = 2N_c + 2\ . \tag{4.25}$$

This implies that in the limit of high filter strength, the P-NLA generates a Fock state with photon number of N_c. In contrast, for the MB-NLA, the output variance decreases monotonically with the filter strength, and asymptotes 1, i.e.

$$\lim_{g\to\infty} \mathrm{Var}\,[X]_{\mathrm{mb}} = 1\ . \tag{4.26}$$

In this extreme situation, output distribution after the MB-NLA operation becomes a delta function centered at α_c/g, and therefore, is no longer a Q-representation of any *bona fide* quantum state. In order to circumvent such problem, we propose that a sufficiently large cut-off should meet the following condition

$$\alpha_c \geq g^2|\alpha_0^{\max}| + \beta g/\sqrt{2}, \quad \beta \geq 1\ . \tag{4.27}$$

As discussed in Sec. 4.2, the resultant distribution of an MB-NLA is a concatenation of two Gaussians joint at the circle which centered at the origin, and has a radius of α_c/g. Setting the cut-off to be β ($\beta \geq 1$) standard deviations away from the amplified mean ensures that the cut-off region is sufficient in embracing the desired part of the output distribution, which is denoted by the first part of the piecewise function $Q^{\mathrm{mb}}(\alpha)$ in Eq. (4.10). Since a larger β leads to a smaller success probability, a compromise should be made between the success probability and the fidelity with respect to an ideal NLA. Here, in order to preclude any distortion of the output distribution while optimizing the success probability, we suggest β to be 3, so that 99.9% of the amplified distribution lies within the cut-off circle.

We now look at the SNR of the output state. Analytically it is $4g^2\mathrm{Re}(\alpha_0)^2/3$ in the ideal case, which increases quadratically with the filter strength. But realistically, although the SNRs of both amplifiers increase at first as a function of the amplification

gain, eventually the SNRs diverge from the ideal curve due to the cut-offs being too small to embrace most of the amplified output (Fig. 4.8 (g) and (h)). From Eq. (4.24), we conclude that SNRs of both amplifiers asymptote to zero in the large-filter-strength limit.

M-P Amplifiers with Varying Cut-offs

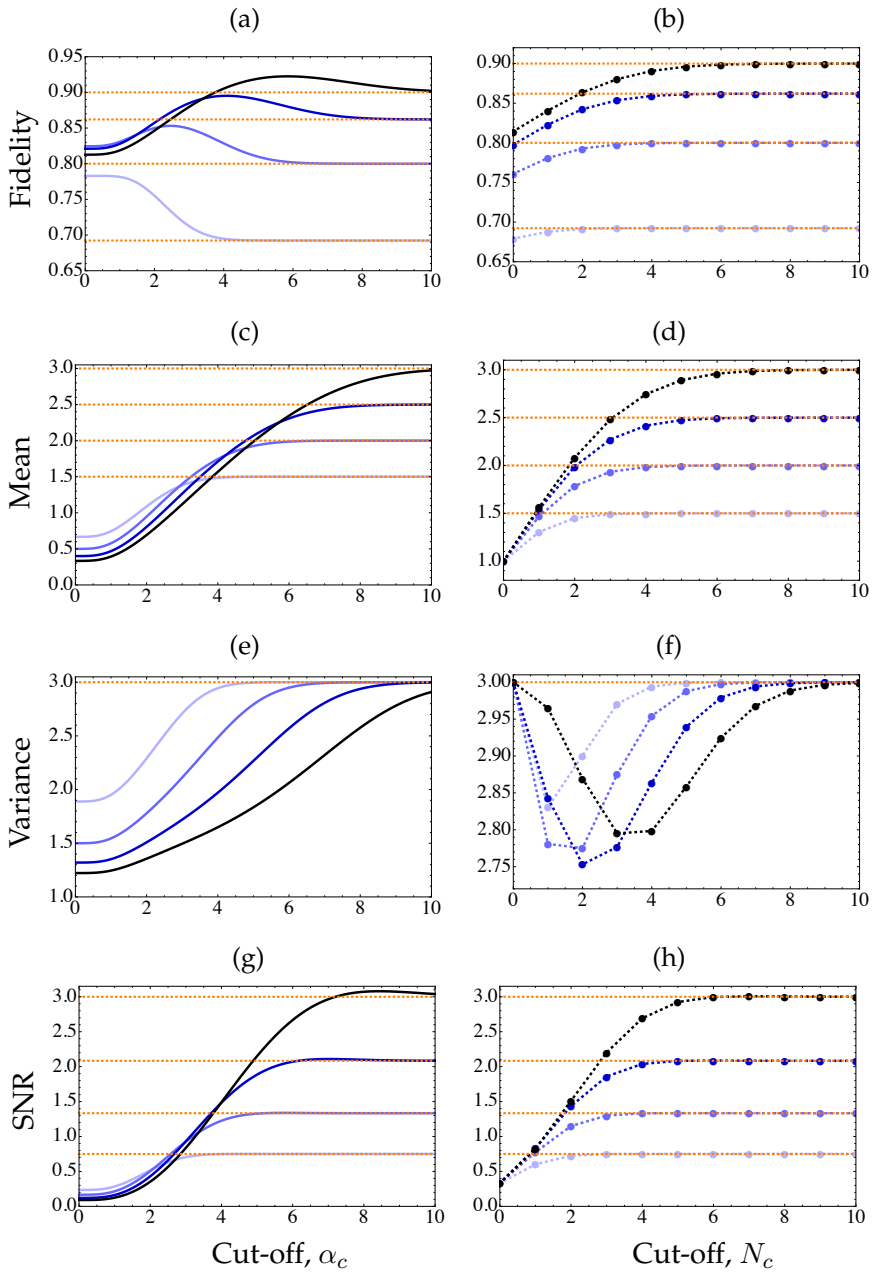

Figure 4.9: (left column) MB-NLA (left column) and P-NLA (right column) with varying cut-offs. For all plots, we have an input amplitude of $\alpha_0 = 0.5$ and varying filter strengths (g=1.5, 2, 2.5, and 3, shown in brighter to darker blue). Note that while the cut-off α_c for the MB-NLA is continuous, the photon number truncation N_c for the P-NLA only takes discrete values.

Next, we study alternatively the output mean, variance, and SNR as a function of cut-offs by fixing the filter strength to be $g = 1.5$, 2, 2.5, and 3. Figs. 4.9 (c), 4.9 (e), 4.9 (g) plot, respectively, the output mean, variance, and SNR for an MB-NLA-based amplifier, while Figs. 4.9 (d), 4.9 (f), 4.9 (h) illustrate those for a P-NLA-based amplifier.

In Figs. 4.9 (c) and 4.9 (d), we see the quadrature mean of the output grows monotonically with the cut-off until a turning point occurs after which, no further change in the mean is noted. This indicates that for a particular filter strength, there exists a cut-off where the output mean (and SNR) and the success probability can be optimized. The larger the filter strength is, the larger this optimal cut-off is to achieve a better approximation of the ideal NLA. For the P-NLA-based M-P amplifier, when the cut-off is zero, no amplification is applied, and every data point is accepted. However, in contrary, the M-P amplifier based on the MB-NLA still gives a g-dependent output mean $2\mathrm{Re}(\alpha_0)/g$ as a result of the rescaling operation.

Due to the same reason, we notice in Fig. 4.9 (e) that the output variance of an MB-NLA-based amplifier is also g-dependent ($2/g^2$) at zero cut-off, whereas the variance of a P-NLA-based amplifier always starts at 3 regardless of the filter strength. Interestingly, we notice that the output variance for the two schemes exhibit completely different characteristics: on one hand, the output variance of the MB-NLA-based scheme remains unchanged for small cut-offs, demonstrating that the unamplified portion $p_{S,\mathrm{out}}^{(\mathrm{mb})}$ in Eq. (4.11) dominates; on the other hand, the output variance of a P-NLA-based amplifier under a small cut-off decreases at first until a minimum point is reached where the output distribution is no longer Gaussian. Apart from this discrepancy, the output variances for both amplifiers increase when the applied cut-off is beyond a certain threshold, and finally coinciding with that of an ideal NLA.

Both the MB-NLA-based and P-NLA-based amplifiers share the same trend as far as SNR is concerned, as can be seen in Figs. 4.9 (g) and 4.9 (h). They both reach the expected value after increasing sublinearly with the cut-off. Hence, we conclude that if the figure of merit is SNR, the MB-NLA turns out to work equivalently to P-NLA when cut-off is tunable, and the filter strength is fixed.

M-P Amplifiers for Different Input Amplitudes

Now we consider the action of the two M-P amplifiers on coherent states with different amplitudes (α_0=0.5, 1.0, 1.5, and 2.0). We vary the cut-off while keeping the filter strength constant: g=1.5. Notice that the output mean of the P-NLA-based scheme starts from $2\mathrm{Re}(\alpha_0)$, whilst that of the MB-NLA-based scheme starts from $2\mathrm{Re}(\alpha_0)/g$. As discussed before, this results from the rescaling operation in MB-NLA.

As we increase the input amplitude, the output variance of both amplifiers descend to a minimum as the cut-off increases, after which the variances go up gradually, and finally match the results of an ideal NLA. The higher the input amplitude is, the smaller the minimum variance is, and the larger the cut-off required to approximate the ideal

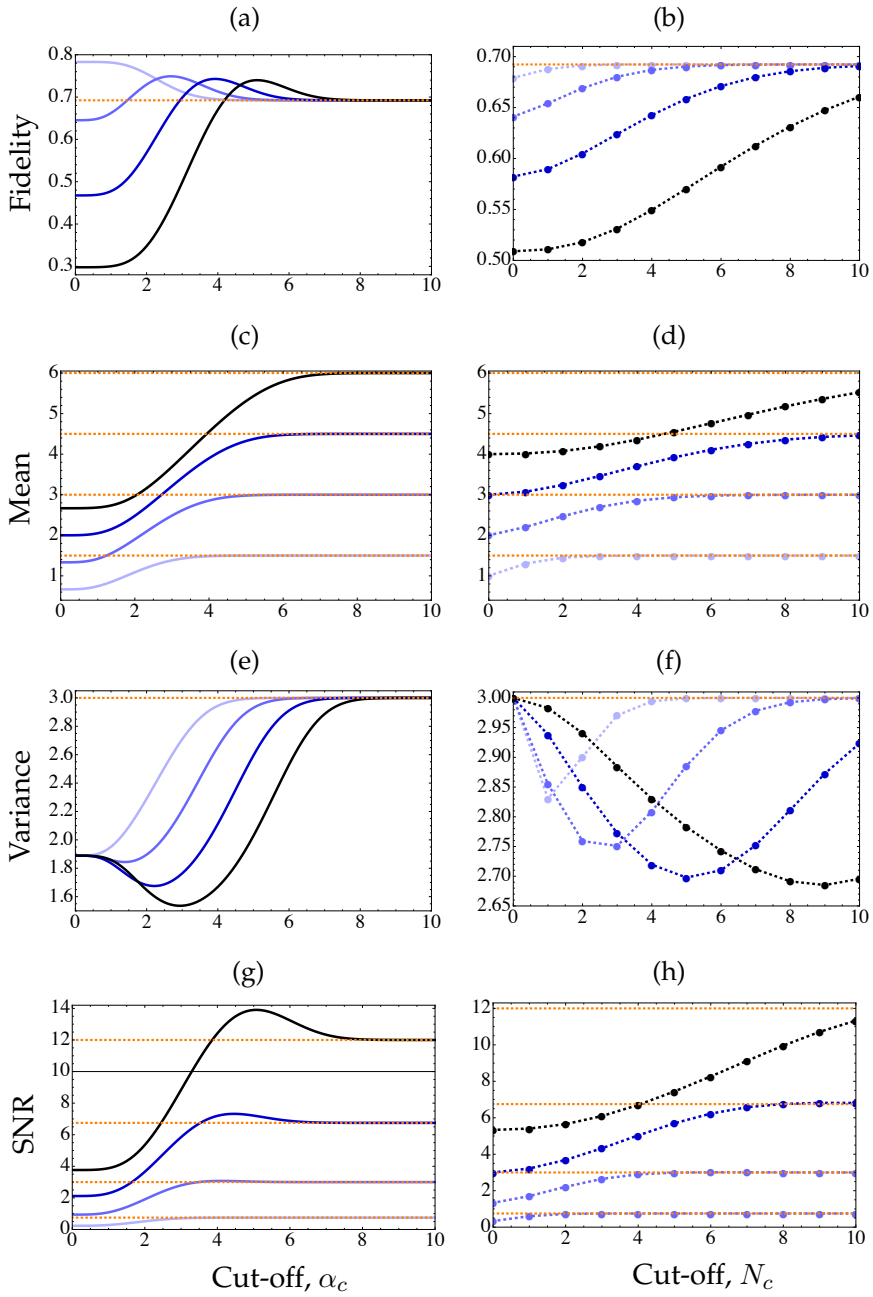

Figure 4.10: (left column) Performance of the MB-NLA (left column) and P-NLA(right column) with different input amplitudes as a function of cut-offs. For all plots, the filter strength is fixed at $g = 1.5$ and the results of an ideal NLA with infinite cut-off are shown in orange-dotted lines for comparison. Plotted curves (brighter to darker blue) are for $\alpha_0 = 0.5$, 1, 1.5, and 2.0.

NLA is, though at the expense of a lower success probability.

By comparing the SNRs in Figs. 4.10 (g) and 4.10 (h), we note that unlike P-NLA, the maximum SNR of an MB-NLA can even surpass that is attainable with an ideal NLA. This phenomenon becomes more dramatic when the input amplitude is higher. Nevertheless, this bump in SNR appears when the output mean is smaller than the ideal case, and it is the deamplification of the variance that pushes up the SNR. This suggests

that while the SNR is a good measure of the performance of a P-NLA, as is suggested in [91], precautions should be taken when it is used to quantify the action of an MB-NLA.

4.3.5 Applications: 1→ ∞ Cloner

In this section, we look at a potential application of MB-NLA by constructing an NLA-based $1\to\infty$ cloner, for which we use cloning fidelity as our figure of merit. As shown in [95], the optimal N-to-M cloning transformation of coherent states that yields copies identical to the input will necessarily induce a minimum amount of additional noise

$$\sigma^2_{N,M} = \frac{M-N}{MN} \ , \tag{4.28}$$

Therefore, the maximum achievable N-to-M cloning fidelity is upper bounded by

$$F_{N,M} = \frac{MN}{(MN+M-N)} \ . \tag{4.29}$$

Here, we show that by integrating a noiseless linear amplifier into a M-P setup, it is possible to build a $1\to\infty$ cloner with fidelity surpassing its fidelity bound ($F_{1,\infty}$=1/2).

The schemes of the P-NLA-based and the MB-NLA-based $1\to\infty$ cloners are pictured in Fig. 4.7, with gain G being set to $G=\sqrt{2}/g$. We compare the two schemes by investigating their fidelity with respect to the target state $|\alpha_0\rangle$:

$$\begin{aligned} F_c &= \langle\alpha_0|\rho_{\text{out}}|\alpha_0\rangle \\ &= \iint \mathrm{d}^2\alpha \; Q(\alpha) \exp\left[-\left|\frac{\alpha}{g}-\alpha_0\right|^2\right] \ . \end{aligned} \tag{4.30}$$

It can be derived that the cloning fidelity using an ideal NLA is

$$F_i = \frac{1}{1+\frac{1}{g^2}} \ . \tag{4.31}$$

This equation implies that the ideal fidelity grows monotonically as a function of the filter strength, and eventually would approach 1.

Similar to Sec. 4.3.4, we analyze in the following the effects of the filter strength, the cut-off, and the input amplitude on the fidelity of the cloners. We see that a high fidelity is obtainable as long as an appropriate combination of filter strength and cut-off is applied. However, due to the finite cut-off, the increasing filter strength eventually results in a fidelity approaching $\exp\left(-|\alpha_0|^2\right)$. Remarkably, in Fig. 4.10 (a), we note that the fidelity of the MB-NLA-based cloner can even surpass that of the cloner using an ideal NLA, which is never the case for its physical counterpart. This is because when the cut-off becomes not sufficiently large, the output state after a P-NLA preserves its physical nature. Although the variance of one quadrature is squeezed, the variance of the conjugate quadrature is correspondingly enlarged. The MB-NLA, however, can

produce a distorted output distribution as discussed in Sec. 4.2, which may no longer represents any real physical state.

We now change to another perspective to examine the behavior of the cloners under varying cut-offs. As depicted in Fig. 4.9 (b), the common feature of both amplifiers is that a higher peak fidelity can be achieved provided a larger filter strength is allowed. In particular, as we increase the cut-off, the fidelity of a P-NLA-based cloner gradually approaches the ideal fidelity. The fidelity of an MB-NLA-based cloner (see Fig. 4.9 (a)), on the contrary, goes beyond the ideal fidelity. As the cut-off keeps growing, it degrades back to the ideal result. This degradation is more pronounced when a smaller filter strength is applied.

We plot the cloning fidelity versus cut-off when higher input amplitude is considered for MB-NLA in Fig. 4.10 (a), and for P-NLA in Fig. 4.10 (b). We notice that for both schemes, when a small cut-off is applied, a high fidelity is only obtainable with a small input amplitude. This imposes a limit to the input amplitude when one implements an NLA-based cloner with small cut-off due to experimental constraints. In order to reach the optimal fidelity for higher input amplitude, a larger cut-off is required with subsequent reduction in the success probability, and also increase in the experimental difficulty.

4.4 Conclusions and Summary

In summary, we provide the recipe for constructing the inverse-Gaussian filter that is utilized throughout this thesis. Considering that such a filter was originally proposed to emulate a noiseless linear amplifier, which is referred to as the "measurement-based NLA", we investigate its functionality by studying the behavior of the MB-NLA and comparing its performance with the direct implementation of NLA, the so-called "physical NLA". On the one hand, we have examined their subtle differences in terms of the output Q distribution, the signal-to-noise ratio, and the fidelity when embedding both amplifiers into a measure-and-prepare setup to generate free-propagating amplified states. On the other hand, we have demonstrated the scenarios within which their equivalence holds. We note that the performance of both amplifiers depends on three effective parameters: the input amplitude, the filter strength, and the cut-off. These parameters dominate the trade-off between the amplification success probability and other figure of merits. In comparison with the optimal P-NLA, the major disadvantage of MB-NLA is its exceedingly low success probability. This discrepancy rises exponentially as the cut-off increases. Another drawback of MB-NLA is its inability to produce a free-propagating amplified state, as illustrated in [81]. This is a direct consequence of its inherent post-selective feature; nevertheless, there has emerged a novel hybrid approach by combining the deterministic linear amplifier and MB-NLA to alleviate this constraint [94, 91].

In addition, we observe that MB-NLA indeed concatenates two Gaussian distribu-

tions and hence, a sufficient cut-off should satisfy the criterion that the part of amplified states lying beyond the circular cut-off area is negligible. We provide the explicit expression of such criterion which offers a quantitative instruction for choosing cut-off in the work presented in this thesis. We show theoretically that once an insufficient cut-off is adopted, the output becomes distorted towards the edge of the circle, and in the large-filter-strength limit, eventually tends to a delta function independent of the input amplitude. It is this property that allows MB-NLA to attain the noise figure and fidelity that exceed the maximum achievable using an ideal NLA. Thus, we assert that fidelity alone cannot quantify conclusively the properties of the amplifier; success probability as well as the output distribution are more valuable characteristics. In applications that require extraction of signals masked under noise, SNR would be a particularly useful figure of merit.

We believe the results shown in this section, from the operational viewpoint, should provide helpful instructions in reconciling the effective parameters, and hence optimizing the utility of the filter function under different circumstances.

Chapter 5

Construction and Characterization of Doubly-Resonant Bow-tie Squeezers

The construction of two optical parametric amplification (OPA) squeezers and the investigation of their performance form the theme of this chapter. We first give a brief review on the breakthroughs in squeezing generation on various experimental platforms. The classical behaviour of the squeezer is theoretically modelled by solving the classical cavity equations of motion. In addition, the noise properties of the cavity modes are obtained by solving the quantum Langevin equation of the squeezer. We lay particular emphasis on the considerations that have been made for configuring the squeezer cavity from both the optical and mechanical perspectives. Finally, we present the experimental characterization of the squeezer parameters, namely its pump threshold, the intra-cavity loss, and the escape efficiency. We report a direct observation of 9.7 dB squeezing, corresponding to 11.5 dB squeezing after correction for the detection loss. A squeezed beam of purity 1.17 was measured. We emphasize that our system is capable of producing higher degree of squeezing by optimizing all relevant squeezer parameters.

5.1 Overview of Squeezing Generation on Different Platforms

The prediction of sub-shot-noise light fields dates back to 1927 when Kennard considered a particular time evolution of the Gaussian wave packet, where the quadrature variances may be arbitrary as long as they comply with the Heisenberg uncertainty principle [194]. Such nonclassical light fields had attracted a number of theoretical invesigations thereafter and the terminology "squeezing" and "squeezing operator" were first introduced by Hollenhorst [195] and Caves [196].

Extensive experimental research had been devoted to this promising area, but it was not until 1985 that the first squeezing was witnessed in a four wave mixing system by Slusher and colleagues [96]. They reported a modest squeezing level of 0.3 dB, arising from the third-order nonlinear interaction between a bright light field and a sodium atomic vapor. Soon after in 1986, another landmarking experiment was successfully conducted by Wu et al. [98] where a dramatically higher noise suppression (4 dB)

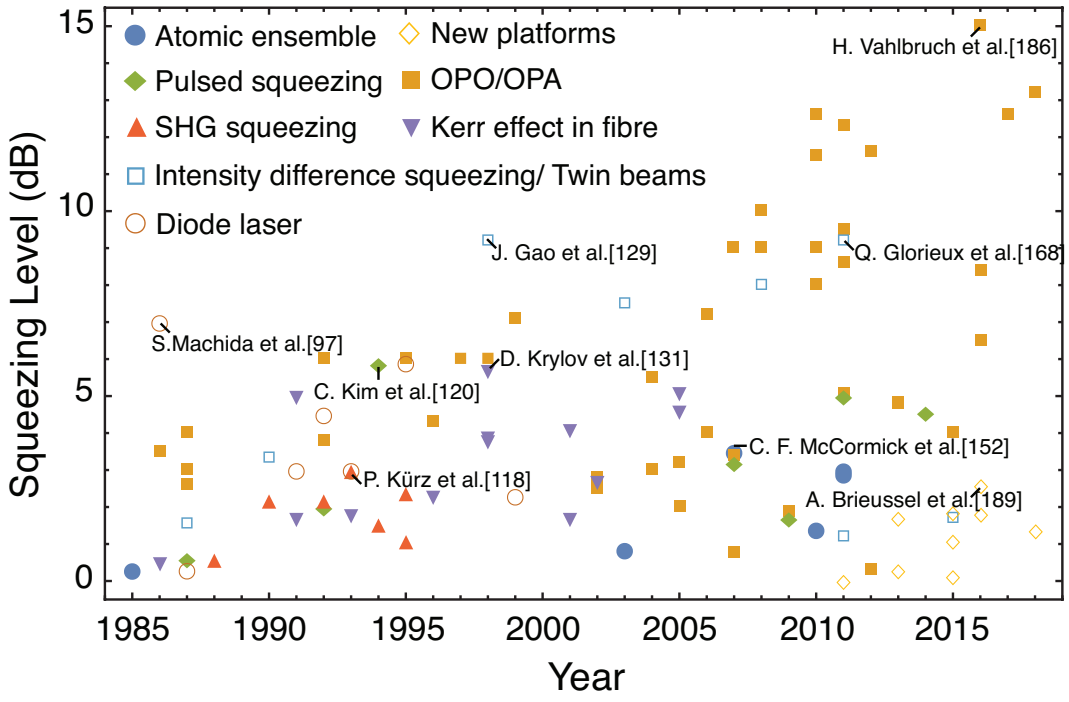

Figure 5.1: Progress in squeezing generation on different platforms, starting from the pioneering work with four wave mixing till now [96] – [193] (cited from left to right, top to bottom in sequence).

was achieved via a sub-threshold triply resonant optical parametric oscillator (OPO). Also impressive was their demonstration of squeezed state as a minimum-uncertainty state for the first time. The team employed instead the second-order nonlinearity of a $MgO:LiNbO_3$ crystal. This circumvents the requirement of a large third-order nonlinear coefficient, which was encountered in the initial atomic experiment. In addition, the cavity configuration offers an appealing way to enhance the nonlinear interaction, so a bright pump beam is not necessary.

The OPO, when seeded by a weak beam at the fundamental frequency, can operate as a phase-sensitive amplifier. It can be utilized to produce the so-called bright squeezing as opposed to the squeezed vacuum. The presence of the seed beam offers more operational flexibility: one can apply a phase modulation on the beam and use it to lock the final homodyne station as well as the relative phase between the pump and fundamental fields. Such a configuration is conventionally termed OPA which can be regarded as a sub-category of the OPO/OPA squeezing as their underlying physics is the same. Substantial progress has been made following this route (cavity OPO/OPA), thanks to the advances in the relevant techniques including coating, polishing, locking, and detection. One particular contribution is from the manufacturing of the periodically-poled potatssium titanyl phosphate (PPKTP) crystal. The periodic poling technque enables the *quasi-phase matching*, where the phase matching condition is satisfied by simply adjusting the crystal temperature. Compared to other nonlinear materials, the PPKTP

crystal also exhibits lower absorption at the squeezing wavelength, and a smaller green-light-induced infrared absorption (GLIIRA) [192]. In fact, among all different platforms shown in Fig. 5.1, OPO/OPA remains the most appealing and reliable approach for squeezing generation. It produced not only the first squeezing of magnitude surpassing 10 dB [156], but also the state-of-the-art squeezing level of 15 dB [192].

Apart from the cavity configuration, pulsed lasers with high peak intensity can also be used to provide highly concentrated field in the χ^2 crystal and hence a reasonable parametric gain. Squeezing over a bandwidth comparable with the phase-matching bandwidth of the crystal is therefore obtainable. The first squeezing generation adopting this approach (0.6 dB) was demonstrated by Slusher's group in 1987 [104]. This result had been improved to 5.8 dB in 1994 [120]; however, due to the limited squeezing bandwidth and the technical difficulties in matching the temporal modes of LO to the squeezed beam, the squeezing of 5.8 dB remains the highest record in this regime.

The inverse process to OPO/OPA, based on parametric upconversion or second harmonic generation (SHG), offers an alternative strategy for generating amplitude squeezed beams. Theoretical predictions of SHG squeezing evolved from using single pass configuration [197] to a doubly-resonant cavity [121]. The development was prompted by the realization that none of the available nonlinear mediums could provide sufficient nonlinearity in the former configuration. As a demonstration of principle, the first SHG squeezing experiment was carried out by Pereira et al. in 1988 [106] by means of a Fabry-Parot cavity containing a nonlinear $LiNbO_3$ crystal. A noise suppression of 0.6 dB at the fundamental field, corresponding to 2.0 dB SHG squeezing, was attained around 4 MHz. This result was further improved by Sizmann et al. (2.2 dB) using a $LiNbO_3$ crystal that had been polished as a monolithic resonator [108]. Such monolithic geometry allows different cavity transfer functions for the fundamental and the second-harmonic beams, and hence an enhancement in the nonlinear interaction. A later experiment using the same monolithic geometry reported a noise suppression of 3 dB, notwithstanding that the squeezing lifetime was only around miliseconds [118].

Doubly-resonant cavities were, for a long time, believed to be indispensable for SHG squeezing until people realized singly-resonant cavities were also applicable in 1994. As such, the operational difficulties of a doubly-resonant setup were mitigated, but the ease of implementation came at the price of an intrinsic limit on the achievable squeezing: under ideal conditions, the best possible noise suppression is nearly 90%, corresponding to a squeezing of 10 dB. The best up-to-date SHG squeezing was achieved in 1995 by Tsuchida where 2.4 dB (5.2 dB after correcting detection loss) SHG squeezing was directly measured at 7.5 MHz [123]. In this experiment, the commonly used $LiNbO_3$ crystal was replaced by a $KNbO_3$ crystal, resulting in a larger nonlinearity and hence a higher magnitude of squeezing. One technical issue associated with any SHG squeezing is that the best squeezing is obtainable at low frequency which, however, would be disguised in the high intensity noise of the laser itself. This detrimental effect can be alleviated by inserting a mode cleaner cavity on path of the fundamental beam. The

cavity serves as a low pass filter, so high-frequency noise are eliminated. As a result, the squeezing generation becomes significantly more stable, as evidenced by [124], where 1.6 dB (3 dB inferred) of noise suppression was observed consistently for hours.

Amplitude squeezing has also been achieved by driving a semiconductor laser with a noiseless pump current. The noise suppression stems from the dipole interaction between the internal field and the electron-hole pairs. Original experiment demonstrated a noise suppression of 7 dB. This squeezing record has never been surpassed; however it only exists in the negative-feedback loop of the semiconductor laser [97]. Later experiments observed the first open-loop squeezing of 3 dB [110], and later improved to 5.9 dB in 1996 [125].

Apart from the conventional approach of OPO/OPA squeezing (below-threshold), operating OPO above threshold provides an alternative method for amplitude squeezing. Because the two output modes of the parametric downconversion are correlated, their intensity difference exhibits noise level below shot noise. The experimental demonstration was first accomplished (1.55 dB) in 1987 [103] and improved more recently to 9.2 dB in 1998 [129].

The observation of squeezed light, an authentic quantum light field, opens the avenue for a wide range of new applications such as entanglement generation, quantum metrology, secure quantum communication, and quantum computation. Inspired by all these new possibilities, great endeavours have been made to increase the magnitude of squeezing over the past 30 years, which culminated with a very recent demonstration of 15 dB squeezing via a hemilithic OPA by Schnabel's group [186]. Such achievement would not have been possible without the numerous development of requisite technologies for squeezing experiments: the improvements in optical coating and polishing, the refinement of phase locking techniques, the manufacturing of periodically poled nonlinear crystal having less loss and defects, the availability of low noise and frequency stabilized lasers, and the invention of high-efficiency photodiodes. The advances in squeezing generation of recent years have, in turn, spurred new technical investigations. For instance, the 15 dB squeezing opens a way to resolve the long-standing technical issue of calibrating the quantum efficiency of InGaAs photodiodes [186].

Other than refinement of the existing techniques, there has been a recent trend towards the production of squeezing on various new platforms. Squeezing on miniaturized devices such as integrated photonic chips were reported independently by Furusawa et al. (4.0 dB) [181] and Lobino (1.38 dB) [193]. Moreover, miniaturization was made possible by abandoning the typical bow-tie or hemilithic cavity configuration, and instead adopting a novel monolithic design. In the work of Brieussel et al. [189], a bulk of $LiNbO_3$ crystal was specially machined by precision diamond turning to form a stable cavity geometry, whereby 2.6 ± 0.5 dB squeezing was measured. These miniaturized devices hold great promise of better scalability, have the potential to be embedded into other quantum processors, and to serve as interfaces between different quantum information platforms. Furthermore, it was shown that the interaction between optical fields

and a mechanical oscillator is capable of reducing noise below shot noise [178, 184], which could be of great usage in quantum metrology. Leveraging the advanced fabrication of integrated chips, Painter et al. reported noise reduction of 0.2 dB (4.5%) from a micromechanical resonator coupled to an on-chip nanophotonic cavity [179]. Different from previous experiments that rely on atomic ensembles, squeezing generated by a single quantum emitter (single atom) was successfully implemented by coupling the atom into a high-finesse optical resonator [174], and a semiconductor quantum dot [185].

In summary, all approaches use one kind of nonlinear effect or another. We plotted the different sources of squeezed light in Fig. 5.1. A thorough review on the production of squeezing can be found in [25, 53, 194, 198].

5.2 Theoretical Modelling of the Squeezers

Theoretical modelling of the two home-built squeezers is provided in this section. We begin with the general formalism of OPA/OPO, where the parametric interaction is significantly enhanced by incorporating the nonlinear crystal into a bow-tie cavity, called here the *squeezers*. By solving the cavity equations of motion, we analytically derive the output noise spectra as well as some important squeezer parameters, namely the pump threshold and the escape efficiency. Instead of aiming for a comprehensive theoretical description for OPA which can be found in [199, 200, 201, 24, 202], we lay particular emphasis on the characterization of the two squeezers in our laboratory.

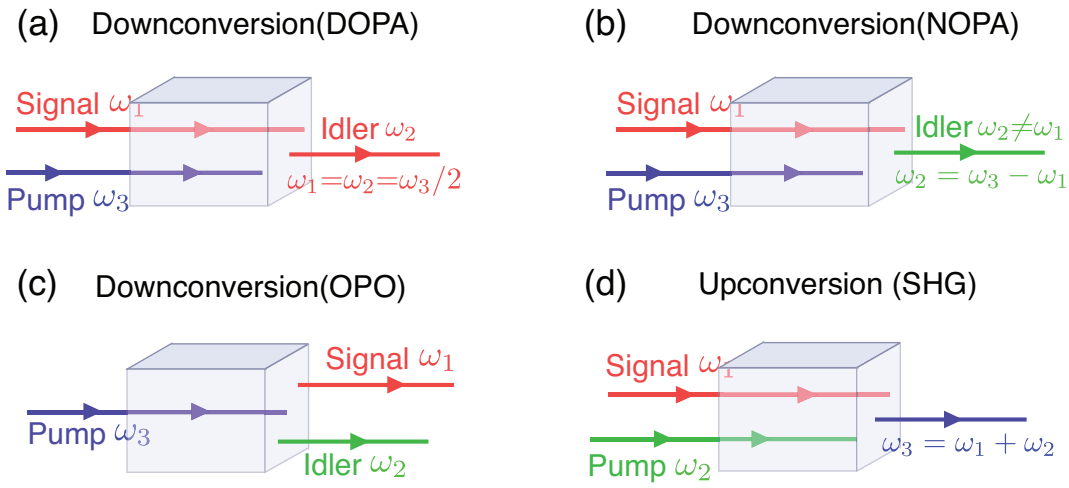

Figure 5.2: Three wave mixing is usually known as a parametric interaction process. It takes place when there are three waves interacting with each other through a second-order nonlinear medium. Depending on which of the three waves serves as input, and which is emitted as output, it takes the form of (a) degenerate optical parametric amplifier, (b) nondegenerate optical parametric amplifier, (c) optical parametric oscillator and (d) parametric upconversion, also known as the second harmonic generation (SHG) when $\omega_1 = \omega_2$.

When an optical beam traverses through a dielectric medium, the induced dipole

polarization $\mathcal{P}$ can be expanded in terms of the optical electric field ε as [201]

$$\mathcal{P} = \epsilon_0 \left(\chi\varepsilon + \chi^{(2)}\varepsilon^2 + \chi^{(3)}\varepsilon^3 + \cdots \right), \tag{5.1}$$

where ϵ_0 is the permittivity of free space and $\chi^{(n)}$ is the nth order nonlinear susceptibility of the medium. Discovery of the nonlinear relationship between $\mathcal{P}$ and ε enabled a host of intriguing phenomena: as shown in the preceding section, the Kerr effect originating from the third-order nonlinearity gives rise to the first observation of squeezed light and remains a compelling candidate for squeezing generation. Here we consider implicitly the second-order nonlinear effect. It has been utilized to produce the amplitude and phase modulations based on the Pockel effect (see Sec. 3.1.4). It also forms the basis of the three wave mixing process, where the mixing of two harmonic components at frequencies ω_1 and ω_2

$$\varepsilon(t) = \mathrm{Re}\left\{ E_0(\omega_1)e^{i\omega_1 t} + E_0(\omega_2)e^{i\omega_2 t} \right\} \tag{5.2}$$

produces a polarization $\mathcal{P}$ containing components at frequencies, 0, $2\omega_1$, $2\omega_2$, $\omega_\pm = \omega_1 \pm \omega_2$. This can be seen by taking $\mathcal{P} = \epsilon_0\chi^{(2)}\varepsilon(t)^2$. Although all five frequency components can be possibly created, in practice only certain frequency components are generated and sustained by the medium depending on the phase matching condition. In particular, the parametric downconversion and upconversion, as shown in Fig. 5.2, can take place once the following conditions are satisfied. First,

$$\omega_1 = \omega_2 + \omega_3, \tag{5.3}$$

ensures the conservation of energy, and second,

$$\mathbf{k}_1 + \mathbf{k}_2 = \mathbf{k}_3, \tag{5.4}$$

also known as the phase matching condition, ensures the conservation of momentum. The subscripts 1, 2, 3 denote the three interacting beams. There exists three conventional approaches to satisfy this phase matching condition. *Type-I phase matching* relies on birefringence of the nonlinear crystal. Because the polarization of the signal and idler modes are the same but orthogonal to that of the pump mode, that is $\uparrow \omega_1 + \uparrow \omega_2 = \rightarrow \omega_3$, they undergo different phase shift passing through the birefringent crystal. By aligning the angle and adjusting the temperature of the crystal, phase matching between the three waves can be achieved. *Type-II phase matching* follows the same mechanism except that the polarizations of the three beams are arranged in a different way: $\uparrow \omega_1 + \rightarrow \omega_2 = \uparrow \omega_3$. The nonlinear coupling strength in terms of phase mismatch takes the shape of a sinc function. The advantage of the birefringent phase matching is that the bandwidth of the optimal temperature or beam wavelength is fairly broad (i.e. the top of the sinc function is relatively flat over a wide range of phase mismatch) [203, 204]. However,

their usage are confined in certain circumstances. For instance, it may require a crystal with high birefringence to compensate the difference in dispersion of the three beams. Besides, the phase matching temperature could be extremely high; for example the typical phase-matching temperature is around 107°C for the MgO:$LiNbO_3$ crystal at 1064 nm [53] . It also excludes the possibility of using d_{33} nonlinear coefficient that is typically larger than the d_{31} coefficient, but is only accessible if the three beams have the same polarization [201]. An alternative technique that complements the first two types of phase matching is known as *quasi-phase matching*. The nonlinear crystal is specially manufactured such that the sign of the nonlinear coupling coefficient is inverted periodically as a function of position.

$$\Lambda = \frac{2\pi}{\mathbf{k}_1 + \mathbf{k}_2 - \mathbf{k}_3} = \frac{2\pi}{\Delta\mathbf{k}}, \tag{5.5}$$

known as the *poling period*, indicates the inversion period: every $\Lambda/2$, the nonlinear coupling sign is alternated. The net effect of the alternation is depicted in Fig. 5.3 where the field amplitude of the generated beam grows monotonically as the beam propagates [56]. The experimental challenge now resides in the fabrication of the periodic grating structure. We adopt this method in our squeezing generation; more specifically, we use a periodically-poled potatssium titanyl phosphate (PPKTP) crystal that has a poling period of 9μm.

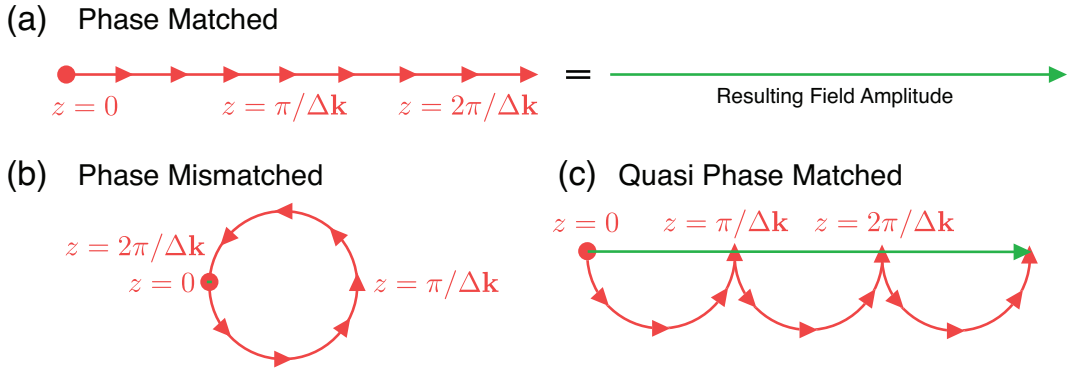

Figure 5.3: Phasors representing the field amplitude of the beam generated from nonlinear interaction under (a) phase matched condition where the field amplitude grows linearly with distance, (b) phase mismatched condition where the field amplitude, instead of growing, oscillates periodically, (c) quasi-phased matched situation where the sign of the nonlinear coefficient is reversed at $\Lambda/2$ intervals.

5.2.1 Degenerate Optical Parametric Amplifier

The theory describing a degenerate optical parametric amplifier (DOPA) was first conceived by Takahashi in 1965 [205], who considered implicitly a dynamical evolution

governed by the Hamiltonian

$$\hat{\mathcal{H}} = \hbar\omega\hat{a}^\dagger\hat{a} + \kappa\hat{a}^{\dagger^2}e^{-2i\omega t - i\phi} + \text{h.c.}, \tag{5.6}$$

in which κ is a coupling constant and ϕ is the phase of the externally imposed oscillator. This was further developed by Mollow and Glauber, who proposed the quantum theory of nondengerate parametric amplifier, described by the interaction Hamiltonian between the two modes $\hat{\mathcal{H}} = \hat{a}^\dagger\hat{b}^\dagger e^{-2i\omega t} + \text{h.c.}$ [40, 206].

By choosing ϕ to be zero at $t = 0$, Eq. (5.6) leads us exactly to the Hamiltonian of a DOPA subject to a classical pump with a complex amplitude of β

$$\hat{\mathcal{H}}_{\text{DOPA}} = \hbar\omega\hat{a}^\dagger\hat{a} - i\hbar\frac{\chi\beta}{2}\left(\hat{a}^2e^{2i\omega t} - \hat{a}^{\dagger^2}e^{-2i\omega t}\right), \tag{5.7}$$

where the coupling constant κ in (5.6) equals to $i\hbar\chi/2$; χ is the second-order susceptibility of the crystal. Note that no leakage and dissipation are embodied in the Hamiltonian in Eq. (5.7), due to the fact that the OPA only operates as an amplifier for a short interval after the seed field is injected [40, 206]. By switching to the interaction picture, which is equivalent to transforming to the rotating frame described in Sec. 3.1.2, we obtain the time-independent Hamiltonian

$$\hat{\mathcal{H}}_{I\text{DOPA}} = -i\hbar\frac{\chi\beta}{2}\left(\hat{a}^2 - \hat{a}^{\dagger^2}\right). \tag{5.8}$$

The subscript I dictates the interaction picture. So the unitary operator describing the time evolution of the system can be derived

$$\hat{U}_{\text{DOPA}}(t) = e^{-i\hat{\mathcal{H}}t/\hbar} = \exp\left[\frac{\chi\beta t}{2}\left(\hat{a}^2 - \hat{a}^{\dagger^2}\right)\right]. \tag{5.9}$$

Note the apparent similarity here with the squeezing operator $\hat{S}(\varepsilon)$ in Eq. (2.19), the only difference being that ε is replaced by $\chi\beta t$. It is perhaps this close resemblance that illuminated originally the role of OPA as a suitable candidate for squeezing generation. The observation $\varepsilon = \chi\beta t$ also explains why a crystal with higher nonlinearity is preferable for the purpose of squeezing production.

We move on to deduce the noise property of the output of a DOPA. Take the Heisenberg equations of motion that follow from the Hamiltonian $\hat{\mathcal{H}}_{I\text{NOPA}}$

$$\frac{\mathrm{d}\hat{a}}{\mathrm{d}t} = \frac{1}{i\hbar}\left[\hat{a}, \hat{\mathcal{H}}_{I\text{NOPA}}\right] = \chi\beta\hat{a}^\dagger, \quad \frac{\mathrm{d}\hat{a}^\dagger}{\mathrm{d}t} = \frac{1}{i\hbar}\left[\hat{a}^\dagger, \hat{\mathcal{H}}_{I\text{NOPA}}\right] = \chi\beta\hat{a}. \tag{5.10}$$

And recall the quadrature operators $\hat{X}_{\pm}$ defined in Eq. (2.9), we obtain

$$\begin{aligned}\frac{\mathrm{d}\hat{X}_{+s}}{\mathrm{d}t} &= \frac{\mathrm{d}\hat{a}}{\mathrm{d}t} + \frac{\mathrm{d}\hat{a}^{\dagger}}{\mathrm{d}t} = \chi\beta\hat{a}^{\dagger} + \chi\beta\hat{a} = \chi\beta\hat{X}_{+s}, \\ \frac{\mathrm{d}\hat{X}_{-s}}{\mathrm{d}t} &= \frac{1}{i}\left(\frac{\mathrm{d}\hat{a}}{\mathrm{d}t} - \frac{\mathrm{d}\hat{a}^{\dagger}}{\mathrm{d}t}\right) = \frac{1}{i}\left(\chi\beta\hat{a}^{\dagger} - \chi\beta\hat{a}\right) = -\chi\beta\hat{X}_{-s}.\end{aligned} \tag{5.11}$$

Solutions of Eq. (5.11) demonstrate the time evolutions of the quadrature operators

$$\hat{X}_{+s}(t) = e^{\chi\beta t}\hat{X}_{+s}(0), \quad \hat{X}_{-s}(t) = e^{-\chi\beta t}\hat{X}_{-s}(0). \tag{5.12}$$

As evidenced by these equations, the amplification imparted on the signal beam is phase sensitive: only one quadrature is amplified, whilst the conjugate quadrature is attenuated. This phase-sensitive amplification occurs on both the quadrature variances and the expectation values of the quadrature amplitudes. The noise of the amplified quadrature grows exponentially with time, while the noise of the attenuated quadrature continuously reduces below the quantum noise limit. This can be immediately seen by calculating the variances of the two quadratures:

$$\langle(\delta\hat{X}_{+s}(t))^2\rangle = e^{2\chi\beta t}\langle(\delta\hat{X}_{+s}(0))^2\rangle = e^{2\chi\beta t}, \quad \langle(\delta\hat{X}_{-s}(t))^2\rangle = e^{-2\chi\beta t}\langle(\delta\hat{X}_{-s}(0))^2\rangle = e^{-2\chi\beta t}. \tag{5.13}$$

Here we assume the signal beam is initially shot noise limited, that is $\langle(\delta\hat{X}_{\pm s}(0))^2\rangle = 1$. Recall that the complex amplitude of the pump field is $\beta = |\beta|e^{\mathrm{i}\phi}$ where ϕ denotes the relative phase between the pump and the signal. Phase-squeezed state is therefore obtained when $\phi = 2m\pi, m \in \mathbb{Z}$, whilst amplitude-squeezed state is attained when $\phi = (2m+1)\pi$.

5.2.2 Classical Modelling of the Squeezer Cavity

Equation (5.7) manifests the three requisites for producing a high-degree of squeezing via parametric downconversion: a crystal with large nonlinear susceptibility, a pump beam with high amplitude, and a long interaction time between the three waves. There are two typical ways to accommodate these requirements: firstly, a pulsed laser may serve as the pump beam to provide a high peak intensity, and secondly, a cavity containing a nonlinear crystal may be used to increase the interaction time. Here we focus particularly on the second approach. Interestingly, the cavity configuration was originally considered to be useless in the early 1980's, due to the prediction that the intracavity field can be squeezed by no more than 3 dB under steady-state conditions [207]. Fortunately, this argument was found to be incorrect as it disregards the interference between the reflected input and the exiting mode of the cavity, which turns out to be of great importance in noise suppression. The cavity parametric process, in principle, permits an arbitrarily large squeezing level around threshold [50].

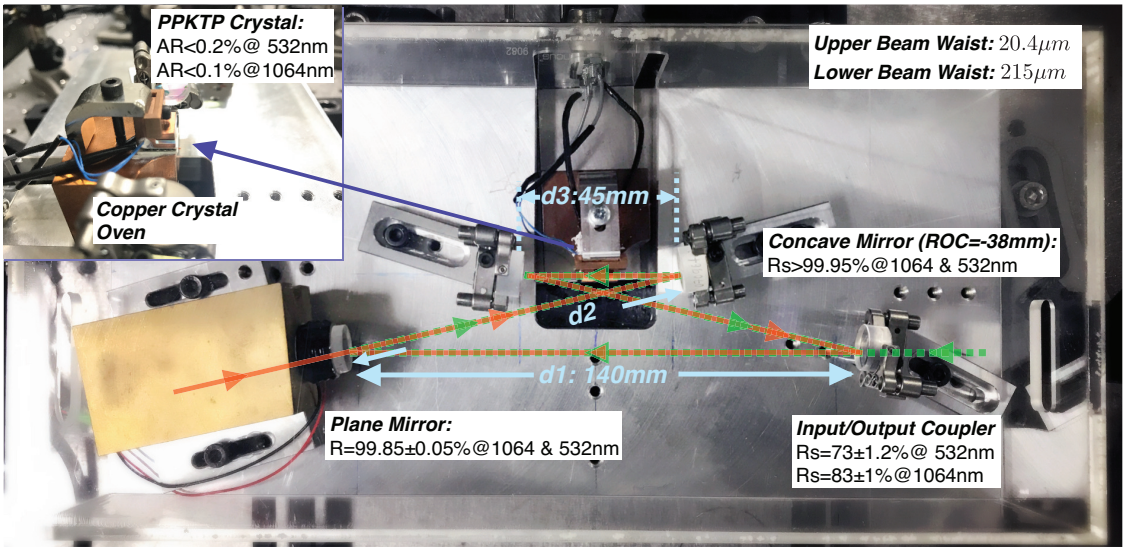

Figure 5.4: Squeezer layout: a doubly-resonant OPA. The cavity is a *travelling-wave* or *ring* resonator, which means the seed beam that is directly reflected off the input/output coupler and the field that – after resonating inside the cavity – is re-emitted propagate along different directions. Conversely, a *standing-wave* resonator has the two beams propagating along with each other. A wedged PPKTP crystal with dimension of $1 \times 5 \times 10.7$mm is placed in the cavity serving as the nonlinear source. The magnified inset displays the copper mount customized for the crystal which is connected to a temperature controller via a thermometer. The idea behind its design is presented in Sec. 5.3.2.

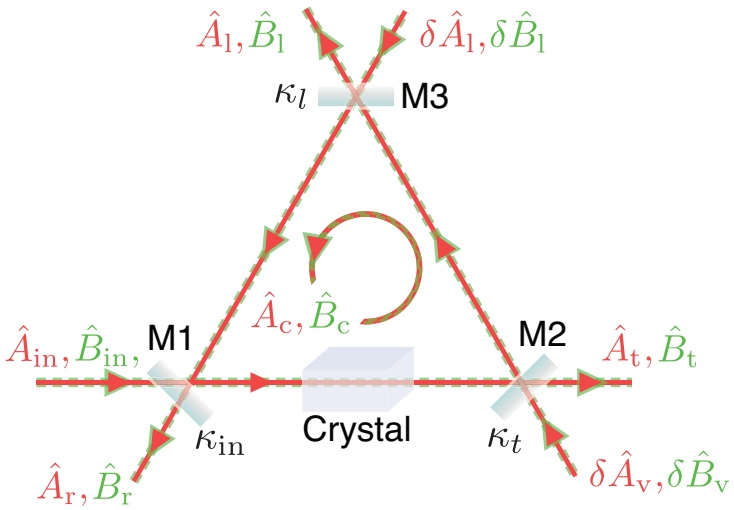

Figure 5.5: Conceptual model of the OPA squeezer. The subscripts in, t, r, l, c refer to the input, the reflected, the transmitted, the loss, and the cavity standing modes, respectively. The quantum description of the squeezer also include the vacuum noise $\delta\hat{A}_v$ that is coupled into the cavity through unused ports.

The configuration of our doubly-resonant squeezer is illustrated in Fig. 5.4. A symmetrical cavity, regardless of its geometry complexity, can be viewed equivalently as a conceptual model comprised of three mirrors, as sketched in Fig. 5.5. The behavior of

the squeezer cavity can then be rigorously characterized in the Heisenberg picture by solving the quantum Langevin equation. We first examine the classical behavior of the cavity by ignoring the nonlinear crystal in Fig. 5.5 [25]

$$\dot{\alpha} = (i\Delta - \kappa_{\text{in}} - \kappa_l - \kappa_t)\alpha + \sqrt{2\kappa_{\text{in}}}\alpha_{\text{in}}. \tag{5.14}$$

Here, α is the amplitude of the cavity standing mode that equals α_c/τ, where α_c is the cavity circulating mode. Δ dictates the cavity detuning, and κ is the cavity decay rate defined by [208]

$$\kappa_i = \frac{1-\sqrt{R_i}}{\tau}, \quad \tau = \frac{nL}{c}. \tag{5.15}$$

Here, τ refers to the cavity round trip time, L the cavity round trip length, and n the refractive index of cavity space. For cavities sitting in free-space, $n = 1$. κ quantifies the total energy loss that the intra-cavity mode undergoes in one round trip. By calculating the mode reflected off the first mirror and the mode transmitted through, we obtain the classical cavity boundary conditions

$$\alpha_r = \sqrt{T_{\text{in}}}\alpha_c - \sqrt{1-T_{\text{in}}}\alpha_{\text{in}} \approx \sqrt{2\kappa_{\text{in}}}\alpha - \alpha_{\text{in}}, \quad \alpha_t = \sqrt{T_t}\alpha_c \approx \sqrt{2\kappa_t}\alpha. \tag{5.16}$$

These boundary conditions, together with the cavity equation of motion, enable the evaluations of the outgoing modes of a cavity, which are often of more interest than the intra-cavity mode.

Before proceeding to the quantum description of the cavity evolution, it is worthwhile to briefly review some basic cavity parameters. Note that $n = 1$ is taken for granted in the following analysis.

We start with the *free spectral range* (FSR) that is inversely proportional to the cavity round trip time τ (see Eq. (5.15))

$$\nu_{\text{FSR}} = \frac{1}{\tau} = \frac{c}{L}. \tag{5.17}$$

It reveals the spacing c/L of cavity modes in frequency domain, resulting from the cavity resonance condition. Explicitly, for a standing wave, $U(z) = |U|\sin(\mathbf{k}\cdot z)$, to be able to resonate, the phase accumulated in half round trip $\mathbf{k}\cdot z$ is restricted to be an integer multiple of π. This resonance condition can be formulated as

$$\frac{\pi L}{\lambda} = m\pi \quad \rightarrow \quad \nu = mc/L, (m \in \mathbb{Z}), \tag{5.18}$$

where ν dictates the resonant frequencies that only take values of integer multiples of c/L.

Another important parameter, the cavity *finesse*, is defined as

$$\mathscr{F} = \frac{\pi\sqrt{\mathrm{R}}}{1-\mathrm{R}}, \quad R = \sqrt{\mathrm{R_{in}} \times \mathrm{R}_t \times \mathrm{R}_l}. \tag{5.19}$$

It quantifies the average number of times that the internal field bounces around the resonator before exiting the cavity. In order to achieve high finesse to build up the intracavity power, one would need to minimize the total loss of the system. A lossless cavity would possess a finesse approaching ∞, thereby only light exactly at the resonant frequency is sustained and the mode shape of the resonator would tend to a delta function. The cavity loss falls into two categories: loss attributable to the imperfect reflection of mirrors and the loss originating from absorption or scattering occurred in any medium contained in the cavity.

The cavity buildup time can then be approximated by multiplication of $\mathscr{F}$ and the single round trip time τ, in accordance with the intuition that the resonating mode cannot grow instantaneously. Taking its inverse, one obtains the cavity *linewidth*, defined as the full width half maximum of the field intensity spectrum,

$$\nu_{\mathrm{FWHM}} = \frac{\nu_{\mathrm{FSR}}}{\mathscr{F}}. \tag{5.20}$$

Equation (5.20) can be readily verified by considering the cavity decay time,

$$\tau_d = \frac{\mathscr{F}L}{2\pi c} = \frac{\mathscr{F}}{2\pi\nu_{\mathrm{FSR}}}. \tag{5.21}$$

that equals the time at which the stored energy is reduced by a factor of e after blocking the input [209]. With the help of Eq. (5.21) we obtain therefore the same resonance spectral width,

$$\nu_{\mathrm{FWHM}} = \frac{1}{2\pi\tau_d} = \frac{\nu_{\mathrm{FSR}}}{\mathscr{F}}, \tag{5.22}$$

as was set forth in Eq. (5.20).

5.2.3 Quantum Langevin Equation of the Squeezer Cavity

Applying the canonical quantization of classical equations of motion leads us explicitly to the quantum Langevin equation of the cavity field operator $\hat{a}$

$$\dot{\hat{a}} = -(\kappa - i\Delta)\hat{a} + \sqrt{2\kappa_{\mathrm{in}}}\hat{A}_{\mathrm{in}} + \sqrt{2\kappa_l}\hat{A}_l + \sqrt{2\kappa_t}\hat{A}_v. \tag{5.23}$$

The cavity decay rate κ now takes into account the leakages from all three mirrors,

$$\kappa = \kappa_{\mathrm{in}} + \kappa_l + \kappa_t. \tag{5.24}$$

Comparison between Eq. (5.14) and (5.23) gives more insights into the difference between classical and quantum optics: vacuum fluctuation that rarely plays a role in characterizing a classical system becomes indispensable in the quantum picture. In the quantum treatment of the OPA cavity, the quantum shot noise is coupled into the cavity via each unused input port, and thus has a perceptible impact on the noise properties of the cavity modes. The classical boundary conditions in Eq. (5.16) can be transformed to account for quantum fluctuations following the same canonical quantization approach:

$$\hat{A}_r = \sqrt{2\kappa_{\text{in}}}\hat{a} - \hat{A}_{\text{in}}, \quad \hat{A}_t = \sqrt{2\kappa_t}\hat{a} - \delta\hat{A}_v. \tag{5.25}$$

We write each mode operator in its linearized form to decompose it into a time-invariant complex amplitude and a time-dependent fluctuation term. The complex amplitudes adhere to the steady-state solution of Eq. (5.14), whilst the fluctuation terms obey Eq. (5.23) as follows

$$\begin{aligned}
\dot{\delta\hat{a}} &= -(\kappa - i\Delta)\delta\hat{a} + \sqrt{2\kappa_{\text{in}}}\delta\hat{A}_{\text{in}} + \sqrt{2\kappa_l}\delta\hat{A}_l + \sqrt{2\kappa_t}\delta\hat{A}_v, \\
\dot{\delta\hat{a}^\dagger} &= -(\kappa + i\Delta)\delta\hat{a}^\dagger + \sqrt{2\kappa_{\text{in}}}\delta\hat{A}^\dagger_{\text{in}} + \sqrt{2\kappa_l}\delta\hat{A}^\dagger_l + \sqrt{2\kappa_t}\delta\hat{A}^\dagger_v.
\end{aligned} \tag{5.26}$$

We can then evaluate fluctuations in the amplitude and phase quadratures of the cavity outgoing modes. Take the amplitude quadrature as an example, we obtain the time evolution of its fluctuation,

$$\delta\dot{\hat{X}}_+ = \frac{\dot{\delta\hat{a}} + \dot{\delta\hat{a}^\dagger}}{2} = -\kappa\delta\hat{X}_+ + \sqrt{2\kappa_{\text{in}}}\delta\hat{X}_{+\text{in}} + \sqrt{2\kappa_l}\delta\hat{X}_{+l} + \sqrt{2\kappa_t}\delta\hat{X}_{+v}. \tag{5.27}$$

In order to probe the amplitude noise spectrum for the reflected and transmitted modes, we solve the above quadrature equation of motion in frequency domain. Using the property of Fourier transform $\mathcal{F}(\mathrm{d}f(t)/\mathrm{d}t) = -i2\pi\omega\mathcal{F}(f(t))$, we first deduce from Eq. (5.27) that

$$\delta\tilde{X}_+ = \frac{\sqrt{2\kappa_{\text{in}}}\delta\tilde{X}_{+\text{in}} + \sqrt{2\kappa_l}\delta\tilde{X}_{+l} + \sqrt{2\kappa_t}\delta\tilde{X}_{+v}}{\kappa - i2\pi\omega}. \tag{5.28}$$

Combing this with the boundary conditions in Eq. (5.25), the frequency-dependent amplitude fluctuation of the two modes are derived as follows

$$\begin{aligned}
\delta\tilde{X}_{+r} &= \frac{(2\kappa_{\text{in}} - \kappa + i2\pi\omega)\,\delta\tilde{X}_{+\text{in}} + 2\sqrt{\kappa_{\text{in}}\kappa_t}\delta\tilde{X}_{+v} + 2\sqrt{\kappa_{\text{in}}\kappa_l}\delta\tilde{X}_{+l}}{\kappa - i2\pi\omega}, \\
\delta\tilde{X}_{+t} &= \frac{2\sqrt{\kappa_{\text{in}}\kappa_t}\delta\tilde{X}_{+\text{in}} + (2\kappa_t - \kappa + 2i\pi\omega)\,\delta\tilde{X}_{+v} + 2\sqrt{\kappa_l\kappa_t}\delta\tilde{X}_{+l}}{\kappa - i2\pi\omega},
\end{aligned} \tag{5.29}$$

where $\tilde{a}$ dictates that the operator a is interrogated in frequency domain. Noise spectra

of light reflected off and transmitted through the cavity can then be determined as

$$\begin{aligned} V_{+r}(\omega) &= \langle|\delta\tilde{X}_{+r}|^2\rangle = \frac{\left[(2\kappa_{\text{in}}-\kappa)^2+(2\pi\omega)^2\right]V_{+\text{in}}+4\kappa_{\text{in}}\kappa_t V_{+v}+4\kappa_{\text{in}}\kappa_l V_{+l}}{\kappa^2+(2\pi\omega)^2}, \\ V_{+t}(\omega) &= \langle|\delta\tilde{X}_{+t}|^2\rangle = \frac{4\kappa_{\text{in}}\kappa_t V_{+\text{in}}+\left[(2\kappa_{\text{t}}-\kappa)^2+(2\pi\omega)^2\right]V_{+v}+4\kappa_l\kappa_t V_{+l}}{\kappa^2+(2\pi\omega)^2}. \end{aligned} \tag{5.30}$$

For convenience, the variance notation $\langle(\delta\hat{X}_{\pm})^2\rangle$ used before is replaced here by $V_{\pm}$. The importance of Eq. (5.30) lies in illuminating the propagation of noise: noise from the input beam V_{in}, that attributed to the intra-cavity loss V_l, and the quantum noise V_v coupled into the cavity through mirror 2 (M2 in Fig. 5.5), all contribute to the variance of the outgoing modes of the cavity. In the special case where all incident modes are shot noise limited, i.e. $V_{\text{in}} = V_l = V_v = 1$, the output modes retain the noise property and stay as coherent states. An output state that exhibits sub-shot-noise feature is only obtainable by injecting an input that has suppressed noise in one quadrature. This conclusion is applicable to linear cavities; nevertheless, as shall be presented in the next section, by placing a nonlinear crystal into the cavity, squeezed state can be created with coherent/vacuum input.

Intriguingly, the results in Eq. (5.30) also reveal the frequency-dependent phase response of a cavity. Assume the cavity is lossless ($\kappa_l = 0$) and impedance matched so that $\kappa_{\text{in}} = \kappa_t = \kappa/2$, and therefore the output variance in Eq. (5.30) specializes to

$$V_{+r}(\omega) = \frac{\kappa^2 V_{+\text{in}}+(2\pi\omega)^2 V_{+v}}{\kappa^2+(2\pi\omega)^2}, \quad V_{+t}(\omega) = \frac{(2\pi\omega)^2 V_{+\text{in}}+\kappa^2 V_{+v}}{\kappa^2+(2\pi\omega)^2}. \tag{5.31}$$

From Eq. (5.31), we see that for high-frequency fluctuations ($\omega^2 \gg (\kappa^2/4\pi)$), the output noise follows

$$V_{+r}(\omega) \approx V_{+\text{in}}, \quad V_{+t}(\omega) \approx V_{+v}. \tag{5.32}$$

The cavity in this circumstance acts as an opaque "beam block" that immediately reflects the fluctuation in the input mode. In stark contrast, for low frequencies ($\omega \to 0$), fluctuations impinged onto each mirror pass straight through the cavity and stay intact as

$$V_{+r}(\omega) \approx V_{+v}, \quad V_{+t}(\omega) \approx V_{+\text{in}}. \tag{5.33}$$

Together with Eq. (5.32), the above noise transfer function verifies the functionality of a mode cleaner cavity as a low pass filter. It allows access to shot-noise-limited light at frequency above the cavity linewidth, and meanwhile lets the low-frequency laser relaxation noise pass through.

5.2.4 Equations of Motion of the Squeezer

To better understand our squeezer, in the previous sections, we analyzed the classical and quantum behaviors of our cavity in the absence of the PPKTP crystal. To account for the nonlinear element and the injection of an intense but nonclassical pump field $\hat{b}$, the cavity equations of motion in Eq. (5.23) and the Hamiltonian in Eq. (5.7) are modified as follows

$$\begin{aligned}\dot{\hat{a}} &= \frac{1}{i\hbar}\left[\hat{a}, \mathcal{H}_{\text{SQ}}\right] - \kappa_a \hat{a} + \sqrt{2\kappa_{\text{in}}^a}\hat{A}_{\text{in}} + \sqrt{2\kappa_l^a}\delta\hat{A}_l + \sqrt{2\kappa_t^a}\delta\hat{A}_l, \\ \dot{\hat{b}} &= \frac{1}{i\hbar}\left[\hat{b}, \mathcal{H}_{\text{SQ}}\right] - \kappa_b \hat{b} + \sqrt{2\kappa_{\text{in}}^b}\hat{B}_{\text{in}} + \sqrt{2\kappa_l^b}\delta\hat{B}_l + \sqrt{2\kappa_t^b}\delta\hat{B}_l.\end{aligned} \tag{5.34}$$

The input field operators $\hat{A}_{\text{in}}$ and $\hat{B}_{\text{in}}$ are defined in rotating frame of the same frequency as the driving fields, namely ω and 2ω . In analogy to Eq. (5.24), κ_a and κ_b contain the losses suffered by the fundamental and second harmonic fields, respectively, via all interfaces,

$$\kappa_a = \kappa_{\text{in}}^a + \kappa_l^a + \kappa_t^a, \quad \kappa_b = \kappa_{\text{in}}^b + \kappa_l^b + \kappa_t^b. \tag{5.35}$$

Here, $\mathcal{H}_{\text{SQ}}$ represents Hamiltonian of the closed system, ignoring the energy transfer between the cavity and the ambient heatbath [210, 211],

$$\hat{\mathcal{H}}_{\text{SQ}} = \hbar\Omega^a \hat{a}^\dagger \hat{a} + \hbar\Omega^b \hat{b}^\dagger \hat{b} + \frac{i\hbar\chi}{2}\left(\hat{a}^{\dagger 2}\hat{b} - \hat{a}^2\hat{b}^\dagger\right), \tag{5.36}$$

where Ω^a and Ω^b refer to the resonating frequencies of the fundamental and pump fields, respectively. Substitution of Eq. (5.36) into (5.34) gives the full expression of the operator Langevin equations

$$\begin{aligned}\dot{\hat{a}} &= -(\kappa_a + i\Delta)\hat{a} + \chi\hat{a}^\dagger\hat{b} + \sqrt{2\kappa_{\text{in}}^a}\hat{A}_{\text{in}} + \sqrt{2\kappa_l^a}\delta\hat{A}_l + \sqrt{2\kappa_t^a}\delta\hat{A}_v, \\ \dot{\hat{b}} &= -(\kappa_b + i\Delta)\hat{b} - \frac{\chi}{2}\hat{a}^2 + \sqrt{2\kappa_{\text{in}}^b}\hat{B}_{\text{in}} + \sqrt{2\kappa_l^b}\delta\hat{B}_l + \sqrt{2\kappa_t^b}\delta\hat{B}_v.\end{aligned} \tag{5.37}$$

Note that $\Delta = \Omega^{a(b)} - \omega(2\omega)$ is the cavity detuning with respect to the fundamental (pump) field. In the non-ideal situation a differential phase shift maybe imparted on the fields during circulation, resulting in $\Delta \neq 0$. Here we concern ourselves with the situation where the two fields stay always on resonance, which means $\Delta = 0$. We make the assumption that the squeezer operates below-threshold and the pump is bright, which are normally satisfied in squeezing experiments. This means the pump field is undepleted by the nonlinear interaction, and thus can be essentially treated as constant, so $\dot{\hat{b}} = 0$ and $\hat{b} \to \beta$ where β is a complex number denoting the pump amplitude. As a

result of the above assumptions, the squeezer equations of motion simplify to

$$\begin{aligned}\dot{\hat{a}} &= -\kappa_a \hat{a} + \chi \hat{a}^\dagger \beta + \sqrt{2\kappa_{\text{in}}^a}\hat{A}_{\text{in}} + \sqrt{2\kappa_l^a}\delta\hat{A}_l + \sqrt{2\kappa_t^a}\delta\hat{A}_v, \\ 0 &= -\kappa^b \beta - \frac{\chi}{2}\hat{a}^2 + \sqrt{2\kappa_{\text{in}}^b}\beta_{\text{in}} + \sqrt{2\kappa_l^b}\delta\hat{B}_l + \sqrt{2\kappa_t^b}\delta\hat{B}_v.\end{aligned} \tag{5.38}$$

We adopt the same linearization methodology as before to decompose each field operator into a steady-state expectation value and an alternating fluctuation by making the following substitutions $\hat{a} \rightarrow \alpha + \delta\hat{a}$ and $\hat{A}_{\text{in}} \rightarrow \alpha_{\text{in}} + \delta\hat{A}_{\text{in}}$. We shall analyze the two parts separately in the following sections. The investigation of the first term constitutes the classical behavior of the squeezer similar to the analysis in Sec. 5.2.2, while the examination of the second term encapsulates the quantum behavior of the squeezer analogous to that described in Sec. 5.2.3. For a squeezer operating above threshold, a full quantum analysis would require a nonclassical treatment of the pump field.

Classical Behavior of the Squeezer

The classical behaviour of the squeezer can be extrapolated by examining the steady-state solution of Eq. (5.37). In other words, the quantum fluctuation terms in the equations of motion are ignored, namely $\delta\hat{A}_l = \delta\hat{A}_v = 0$. Hence, we obtain

$$\begin{aligned}0 &= -\kappa_a \alpha + \chi\beta\alpha^* + \sqrt{2\kappa_{\text{in}}^a}\alpha_{\text{in}}, \\ 0 &= -\kappa_a \alpha^* + \chi\beta^*\alpha + \sqrt{2\kappa_{\text{in}}^a}\alpha_{\text{in}}, \\ 0 &= -\kappa_b \beta - \frac{\chi}{2}\alpha^2 + \sqrt{2\kappa_{\text{in}}^b}\beta_{\text{in}}.\end{aligned} \tag{5.39}$$

α_{in} and β_{in} are real since all the modes are interrogated under the rotating frame. Based on the above simplifications, one may derive the solution of Eq. (5.39) as

$$\alpha = \frac{\sqrt{2\kappa_{\text{in}}^a}\alpha_{\text{in}}\left(1 + (\chi\beta)/\kappa_a\right)}{\kappa_a\left(1 - (\chi|\beta|)^2/\kappa_a^2\right)}. \tag{5.40}$$

Using the classical cavity boundary conditions in Eq. (5.16), the amplitude of the output of the squeezer can be obtained

$$\alpha_t = \frac{2\sqrt{\kappa_{\text{in}}^a\kappa_t^a}\alpha_{\text{in}}\left(1 + (\chi\beta)/\kappa_a\right)}{\kappa_a\left(1 - (\chi|\beta|)^2/\kappa_a^2\right)}, \tag{5.41}$$

which gives an output power of

$$P_{\text{out}} = \alpha_t^*\alpha_t = \frac{4\kappa_{\text{in}}^a\kappa_t^a\alpha_{\text{in}}^2\left[1 + (\chi|\beta|)^2/\kappa_a^2 + (2\chi|\beta|\cos\phi)/\kappa_a\right]}{\kappa_a^2\left[1 - (\chi|\beta|)^2/\kappa_a^2\right]^2}. \tag{5.42}$$

$\beta = |\beta|e^{i\phi}$ is used in the above equation where ϕ dictates the relative phase between the signal and pump fields. Equation (5.41) demonstrates analytically the phase-sensitive

amplification arising from the three waving mixing process: maximum amplification happens when the signal and the pump beams are in phase, giving rise to the amplified noise in the anti-squeezed quadrature, whilst maximum de-amplification occurs when the two beams are out-of-phase, whereby squeezing ensues. As the relative phase changes, the output alternates between squeezing and anti-squeezing accordingly, as illustrated in Fig. 5.6.

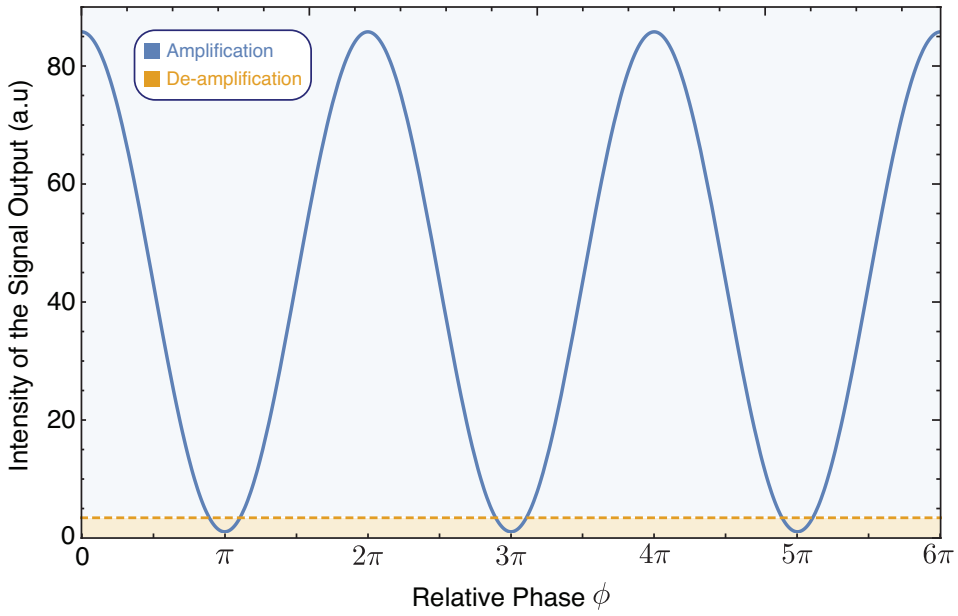

Figure 5.6: The OPA amplification (blue shading) and de-amplification (yellow shading) curves. The yellow dashed line plots the signal power when no pump is inserted.

Parametric gain can then be defined as the ratio of the signal power in the presence of a pump beam to the signal power in the absence of the pump beam:

$$\begin{aligned} \text{Amplification}: \quad \mathscr{G}_{+} &= \frac{P_{\text{out}}(\phi = 2m\pi)}{P_{\text{out}}(\beta = 0)} = \frac{[1 + (\chi|\beta|)/\kappa_a]^2}{\kappa_a^2\,[1 - (\chi|\beta|)^2/\kappa_a^2]^2}, \\ \text{De-amplification}: \quad \mathscr{G}_{-} &= \frac{P_{\text{out}}(\phi = (2m+1)\pi)}{P_{\text{out}}(\beta = 0)} = \frac{[1 - (\chi|\beta|)/\kappa_a]^2}{\kappa_a^2\,[1 - (\chi|\beta|)^2/\kappa_a^2]^2}. \end{aligned} \tag{5.43}$$

Being a particularly crucial experimental parameter, $\mathscr{G}_{\pm}$ directly determines the optimal OPA amplification, which in turn implies the best achievable output squeezing. We plot $\mathscr{G}_{\pm}$ in Fig. 5.7 as a function of $\chi|\beta|/\kappa_a$. As to be expected, a higher parametric gain is obtainable provided a larger nonlinear coefficient χ, a more intense pump $|\beta|$, and less loss κ_a suffered by the signal. One may ask: how much incident pump power is required to approach the infinite parametric gain? In response to this question, we introduce another important squeezer parameter, the *pump threshold* P_{thr}^{b}. The relationship between the incoming pump field and the intra-cavity pump mode can be deduced by solving

Eq. (5.39)

$$\beta_{\text{in}} = \frac{\kappa_b \beta}{\sqrt{2\kappa_{\text{in}}^b}}. \tag{5.44}$$

Owing to the fact that the signal beam is dramatically weaker than the pump beam, the term α^2 is negligible and hence is neglected. Because P_{thr}^b is defined in the extreme case when $\chi|\beta| \to \kappa_a$, we may derive from Eq. (5.44) that

$$P_{\text{thr}}^b = \frac{hc}{\lambda_b}\beta_{\text{in}}^*\beta_{\text{in}}|_{(|\beta|=\kappa_a/\chi)} = \left(\frac{\kappa_a\kappa_b}{\chi\sqrt{2\kappa_{\text{in}}^b}}\right)^2 \frac{hc}{\lambda_b}. \tag{5.45}$$

It can be immediately seen from Eq. (5.44) and (5.45) that $|\beta_{\text{in}}/\beta_{\text{thr}}| = \chi|\beta|/\kappa_a$. With the aid of this observation, Eq. (5.43) can be cast in a simpler form

$$\mathscr{G}_{\pm} = \frac{\left(1 \pm |\beta_{\text{in}}/\beta_{\text{thr}}|\right)^2}{\kappa_a^2\left(1 - |\beta_{\text{in}}/\beta_{\text{thr}}|^2\right)^2}. \tag{5.46}$$

It is also worth noting the different behaviors of the OPA in the amplification and de-amplification regimes as shown in Fig. 5.7. Whilst the parametric gain has a vertical asymptote when the pump power approaches the OPA threshold, the de-amplification gain increases comparatively slow and eventually reaches its optimal. The unphysical infinite parametric gain is indeed a virtual effect resulting from the assumption of no pump depletion.

Quantum Behavior of the Squeezer Operating Below-threshold

To probe the quadrature noise spectra of the squeezed output, we first recall the quantum leftover fluctuation terms in Eq. (5.37)

$$\delta\dot{\hat{a}} = -\kappa_a\delta\hat{a} + \chi\beta\delta\hat{a}^\dagger + \sqrt{2\kappa_{\text{in}}^a}\delta\hat{A}_{\text{in}} + \sqrt{2\kappa_l^a}\delta\hat{A}_l + \sqrt{2\kappa_t^a}\delta\hat{A}_v. \tag{5.47}$$

Following the same methodology as Sec. 5.2.3, fluctuations associated with amplitude and phase quadratures can be deduced by adding Eq. (5.47) with the conjugate operator $\delta\dot{\hat{a}}^\dagger$

$$\delta\dot{\hat{X}}_{\pm a} = \left(-\kappa_a \pm \chi\beta\right)\delta\hat{X}_{\pm a} + \sqrt{2\kappa_{\text{in}}^2}\delta\hat{X}_{\pm\text{in}} + \sqrt{2\kappa_l^a}\delta\hat{X}_{\pm l} + \sqrt{2\kappa_t^a}\delta\hat{X}_{\pm v}. \tag{5.48}$$

We employ the property of Fourier transform $\mathcal{F}\left(\mathrm{d}f(t)/\mathrm{d}t\right) = -i2\pi\omega\mathcal{F}\left(f(t)\right)$ to transform Eq. (5.48) from time domain to frequency domain:

$$\delta\tilde{X}_{\pm a} = \frac{\sqrt{2\kappa_{\text{in}}^2}\delta\tilde{X}_{\pm\text{in}} + \sqrt{2\kappa_l^a}\delta\tilde{X}_{\pm l} + \sqrt{2\kappa_t^a}\delta\hat{X}_{\pm v}}{\kappa_a \mp \chi\beta - 2i\pi\omega}. \tag{5.49}$$

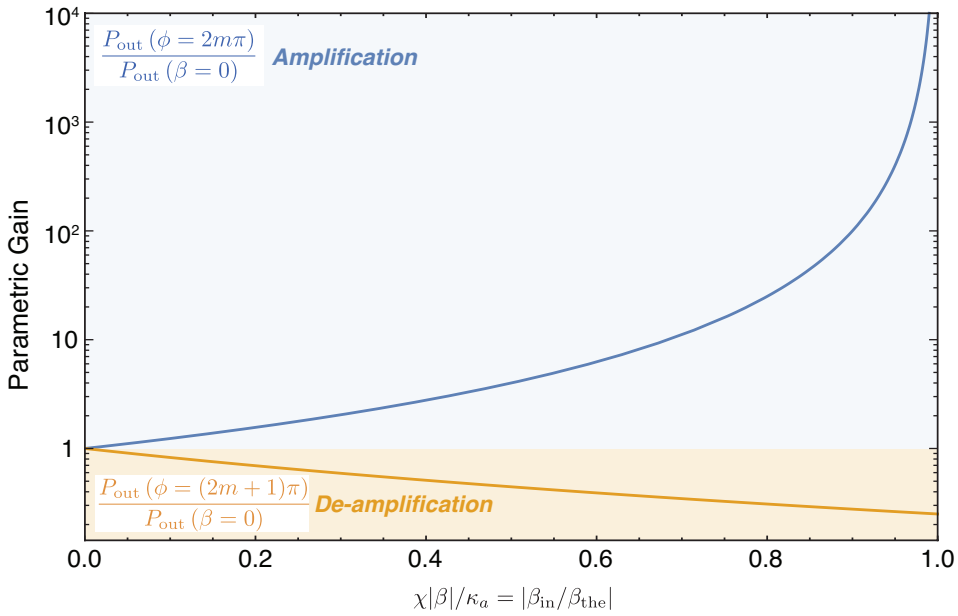

Figure 5.7: Parametric gain against $|\beta_{\rm in}/\beta_{\rm thr}|$. The blue shaded area plots the OPA amplification obtained when the relative phase between pump and signal is an even multiple of π. On the contrary, the yellow shading illustrates the OPA de-amplification with ϕ being an odd multiple of π.

Applying the cavity boundary conditions in Eq. (5.25), the fluctuations in amplitude and phase of the squeezed output can be formed

$$\delta\tilde{X}_{\pm t} = \frac{2\sqrt{\kappa_{\rm in}^a \kappa_t^a}\delta\tilde{X}_{\pm \rm in} + 2\sqrt{\kappa_l^a \kappa_t^a}\delta\tilde{X}_{\pm l} + \left(2\kappa_t^a - \kappa_a \pm \chi\beta + i2\pi\omega\right)\delta\tilde{X}_{\pm v}}{\kappa_a \mp \chi\beta - 2i\pi\omega}. \tag{5.50}$$

We can then determine the noise spectra of the squeezer output

$$V_{\pm}(\omega) = \frac{4\kappa_{\rm in}^a \kappa_t^a V_{\pm \rm in} + 4\kappa_l^a \kappa_t^a V_{\pm l} + \left[\left(2\kappa_t^a - \kappa_a + \chi\beta\right)^2 + (2\pi\omega)^2\right] V_{\pm v}}{\left(\kappa_a \mp \chi\beta\right)^2 + (2\pi\omega)^2}. \tag{5.51}$$

It is useful to consider shot noise limited incoming fields, so the noise terms in Eq. (5.51) all equal to 1, namely $V_{\pm \rm in} = V_{\pm l} = V_{\pm v} = 1$. This gives the simplified variances of the squeezed and anti-squeezed quadratures

$$\begin{aligned} V_{+\rm SQ}(\omega) &= 1 + \frac{\kappa_t^a}{\kappa_a}\frac{4(\chi\beta/\kappa_a)}{\left(1 - \chi\beta/\kappa_a\right)^2 + \left(2\pi\omega/\kappa_a\right)^2}, \\ V_{-\rm SQ}(\omega) &= 1 + \frac{\kappa_t^a}{\kappa_a}\frac{4(\chi\beta/\kappa_a)}{\left(1 + \chi\beta/\kappa_a\right)^2 + \left(2\pi\omega/\kappa_a\right)^2}. \end{aligned} \tag{5.52}$$

We have made use of the definition of κ_a in Eq. (5.35). Based on Eq. (5.52), we put forward another critical parameter, namely the OPA *escape efficiency*

$$\eta_{\text{esc}} = \frac{\kappa_t^a}{\kappa_a}, \tag{5.53}$$

which, as its name suggested, quantifies the efficiency with which the squeezed light may exit the cavity. Replace $\chi\beta/\kappa_a$ by the more intuitive equivalent $\beta_{\text{in}}/\beta_{\text{thr}}$ and account for detection imperfection η_D (see Eq. (3.24)), the output variances can be formulated into

$$\begin{aligned} V_{+\text{SQ}}(\omega) &= 1 + \eta_{\text{esc}}\eta_D \frac{4\beta_{\text{in}}/\beta_{\text{thr}}}{(1-\beta_{\text{in}}/\beta_{\text{thr}})^2 + (2\pi\omega/\kappa_a)^2}, \\ V_{-\text{SQ}}(\omega) &= 1 + \eta_{\text{esc}}\eta_D \frac{4\beta_{\text{in}}/\beta_{\text{thr}}}{(1+\beta_{\text{in}}/\beta_{\text{thr}})^2 + (2\pi\omega/\kappa_a)^2}. \end{aligned} \tag{5.54}$$

Figure 5.8 plots the $V_{\pm\text{SQ}}$ as a function of frequency. Here we assume the relative phase $\phi = 2m\pi$ so $\beta_{\text{in}}/\beta_{\text{thr}}$ is real and positive. Intuitively, the output squeezing level degrades at frequencies above the cavity linewidth. The disparity between the three curves clearly demonstrates the degradation of observable squeezing due to experimental loss, thus verifying how squeezing is vulnerable to any loss it encounters inside or outside the OPA cavity.

As signified by Eq. (5.54) and depicted in Fig. 5.9, there are two dominant parameters in determining the magnitude of squeezing one is able to observe: the pump threshold and the escape efficiency. A smaller pump threshold is more desirable to avoid problems coming with high-power operations. This can be achieved by increasing either $R_{\text{in/t}}^b$ or $R_{\text{in/t}}^a$ as shown in Fig. 5.10 (a). On the other hand, an important requisite for a large output squeezing is to have higher escape efficiency, which is accessible by either minimizing the intra-cavity loss, equivalent to increasing R_l^a, or reducing $R_{\text{in/t}}^a$ as illustrated in Fig. 5.10 (b). Hence, a compromise needs to be made between the two parameters to ensure a high escape efficiency is guaranteed without significantly increasing the pump threshold. One way to resolve this problem is to decrease the OPA threshold by tuning up $R_{\text{in/t}}^b$ to compensate the decrease in $R_{\text{in/t}}^a$, that is necessary for a high escape efficiency.

5.3 Squeezer Characterization: Cavity Configuration

Figure 5.4 shows the schematic of our doubly-resonant squeezer. The advantage of a doubly-resonant squeezer against its singly-resonant counterpart is threefold: firstly, it significantly reduces the required pump power to reach the same parametric gain as if a singly-resonnat cavity is used instead; secondly, the co-resonance between pump and the signal beam natually ensures that their intra-cavity beamwaist ratio is $\sqrt{2}$, which coincides exactly with the optimal waist size for second-order nonlinear interaction imposed by the Boyd-Kleinman criterion [212, 201], and thirdly, it offers an additional

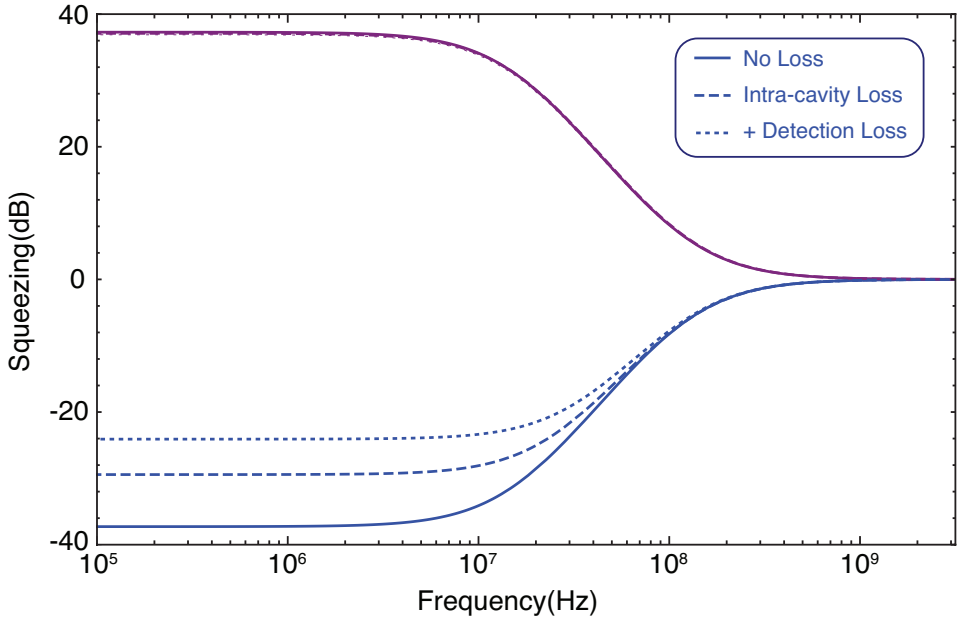

Figure 5.8: Squeezing and anti-squeezing spectra. The solid curves show the ouput variances when no loss is present, whilst the dashed curves represent the variances assuming the setup is only subject to intra-cavity loss. The dotted curves, on the contrary, illustrate the variances when both intra-cavity and detection losses are taken into account. The variance in the anti-squeezed quadrature stays almost intact; in contrast, the squeezing is dramatically contaminated by the additional loss. The relevant parameters are chosen to be consistent with the coresponding specifications of our experimental setup: cavity round trip length $L = 0.374$m, input/output coupler $R^a_{\text{in/t}} = 0.83$, $R^b_{\text{in/t}} = 0.73$, intra-cavity loss at the fundamental frequency $R^a_l = 0.9963$, $\beta_{\text{in}}/\beta_{\text{thr}} = 0.625$, and homodyne efficiency $\eta_D = 0.99 \times 0.99^2$.

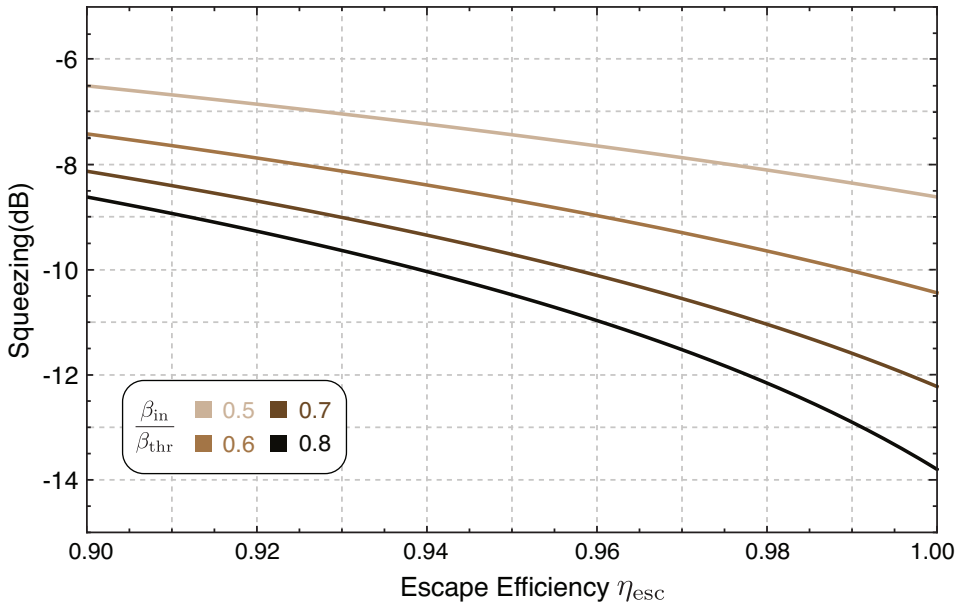

Figure 5.9: Squeezing as a function of escape efficiency for a series of pump powers. Detection efficiency is assumed to be $\eta_D = 0.99 \times 0.99^2$.

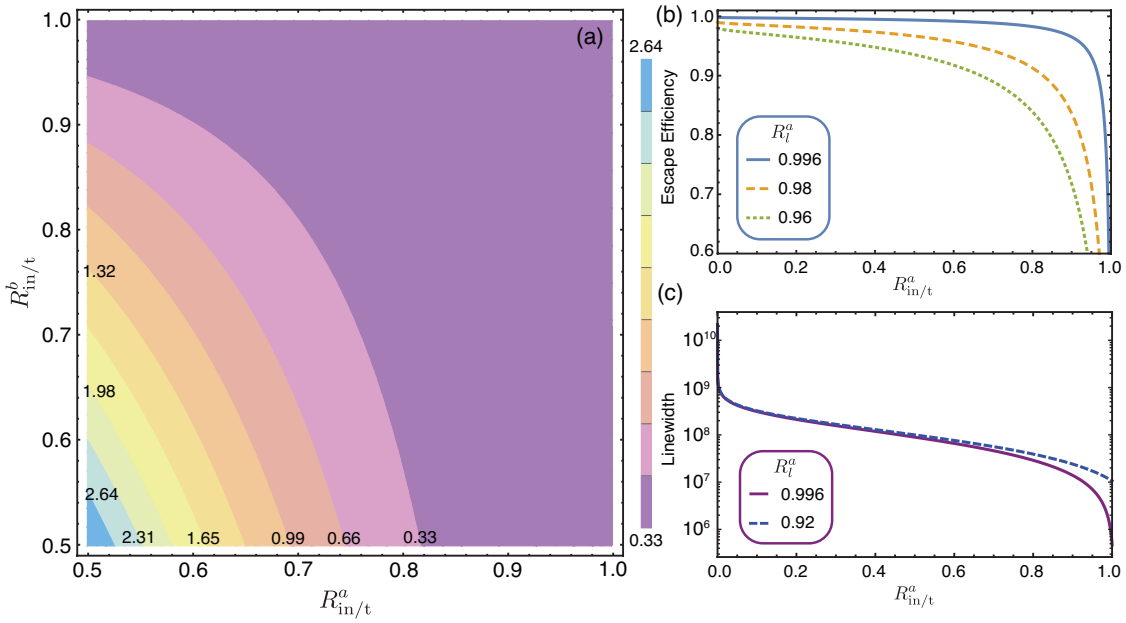

Figure 5.10: (a) Contour plot of OPA threshold in terms of $R^a_{\mathrm{in/t}}$ and $R^b_{\mathrm{in/t}}$. (b) and (c) show, respectively, the OPA escape efficiency and linewidth as functions of $R^a_{\mathrm{in/t}}$ for multiple intra-cavity losses R^a_l.

option for cavity length locking. Instead of applying modulation on the signal beam which is inaccessible for running OPO, phase modulation on the pump beam works just as well. We also point out the practical drawbacks of this method: the intense intra-cavity pump power could exacerbate the green induced infrared absorption, and thus decrease the escape efficiency [213, 214, 215]. It may also aggravate the photothermal effect and, in turn, causes cavity length instability.

We select bow-tie as the geometry of our squeezer cavity. The advantage of such a travelling-wave cavity over its standing-wave counterpart lies mostly in its flexibility: the ability to avoid backscattered light and the accesiblity of multiple input/output ports that are spatially separated. Hence, various locking techniques can be employed that would otherwise be difficult in the standing-wave setup. There are drawbacks with this geometry as well. Because more interfaces are present inside the cavity, the cavity mode suffers higher loss and dispersion compared to that of a monolithic or hemilithic cavity [186, 192]. Apart from the bow-tie geometry, the exact cavity configuration is yet to be decided. Here, we report in detail how we came up with the final cavity design as presented in Fig. 5.4.

We begin the discussion with a brief review of Gaussian beams and Kogelnik's ABCD law [216, 217, 218] that governs the transformation of Gaussian beams through free space as well as some periodic systems such as optical resonators. The treatment of how intra-cavity light propagates will then be handled by this ABCD matrix.

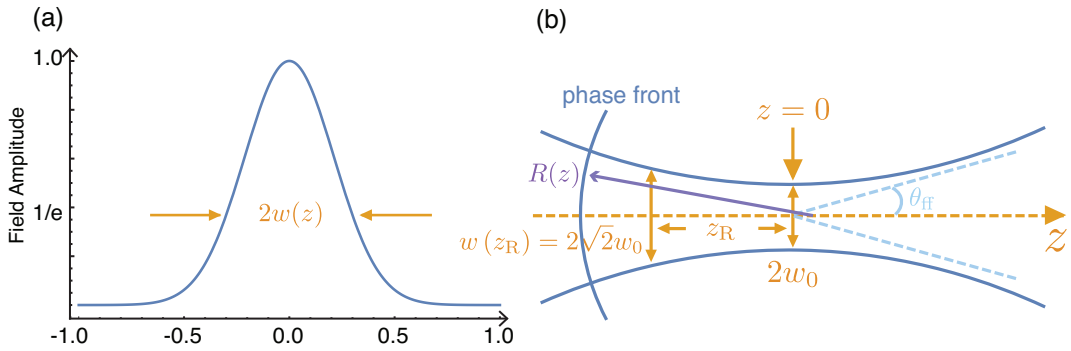

Figure 5.11: (a) Transverse cross section of a Gaussian beam. The field intensity distribution exhibits a Gaussian profile. (b) Variation of beam width and wavefront radius of curvature along z-axis.

5.3.1 Gaussian Beams and Kogelnik's ABCD Law

The properties of a Gaussian beam can be derived either using the Kirchhoff-Huygens diffraction integral or directly by solving the paraxial wave equation [217, 218]. A Gaussian beam is any beam having a Gaussian transverse intensity distribution everywhere along its propagation axis. It can be uniquely characterized by two parameters: its beam width $w(z)$ and the radius of curvature (RoC) of its phase front $R(z)$, that are shown in Fig. 5.11. As both parameters are functions only of the beam waist w_0, the properties of a Gaussian beam at any given point along the axis can be completely inferred based on the prior knowledge of its w_0. The general expression of a Gaussian beam in the paraxial approximation takes the form

$$\psi(x,y,z) = \frac{w_0}{w(z)} A \exp\left\{-i\left[kz - \arctan\left(\frac{\lambda z}{\pi w_0^2}\right) + \frac{\pi r^2}{\lambda R(z)}\right]\right\} e^{-(r/w(z))^2}, \tag{5.55}$$

where $r^2 = x^2 + y^2$ and A is a prefactor proportional to the field amplitude.

$$w(z) = w_0\left[1 + \left(\frac{\lambda z}{\pi w_0^2}\right)^2\right]^{1/2} \tag{5.56}$$

represents the *beam half width* at which the field amplitude decays to $1/e$ of its maximum, indicating that transversely more than 86% beam power is contained in a circle of radius $w(z)$. $w(0) = w_0$ defines the beam waist, also the narrowest spot, of a Gaussian beam.

$$R(z) = z\left[1 + \left(\frac{\pi w_0^2}{\lambda z}\right)^2\right] \tag{5.57}$$

represents the *radius of curvature of the beam phase front*. The last exponential term $\exp\left[-(r/w(z))^2\right]$ in Eq. (5.55) describes the field intensity in the transverse direction. The first term in Eq. (5.55) denotes the phase of a plane wave, while second and third terms show the additional phase shift imparted on the beam as it travels along the z-

axis. In particular, the phase term

$$\Phi(z) = \arctan\left(\lambda z/\pi w_0^2\right) \tag{5.58}$$

refers to the *Gouy phase shift* that can be interpreted as an analogue of the phase anomaly for point focus (spherical wave) originally observed by Gouy in 1890. It describes the phase shift a converging beam undergoes as it passes through its beam waist in propagating from $-\infty$ to ∞, whereupon a phase change of π is incurrred as a result [219, 220]. The total phase shift attributed to both exponential terms accumulates and departs the beam wavefront further away from that of a plane wave. However, as $z \to \infty$, both $1/R(z)$ and the arctangent function vanish, thereby giving a plane wave again in resemblance to the original wave form at $z = 0$.

From an experimental perspective, we introduce another important parameter, namely the beam *Rayleigh range*,

$$z_{\mathrm{R}} = \frac{\pi w_0^2}{\lambda}, \tag{5.59}$$

which describes the distance at which the beam width increases to $\sqrt{2}w_0$. A Gaussian beam can be approximated to be collimated at $z < z_{\mathrm{R}}$, and for $|z| \gg z_{\mathrm{R}}$, its beam width increases linearly with z. Its profile, as depicted in Fig. 5.11, forms a hyperbola with oblique asymptotes inclined to z axis at the far-field *beam half angle*:

$$\theta_{\mathrm{ff}} = \lim_{z\to\infty} \frac{w(z)}{z} = \frac{1}{z_{\mathrm{R}}}. \tag{5.60}$$

It is responsible for the beam divergence and indeed the expression in Eq. (5.55) is only a valid solution of the wave equation $\nabla^2\psi + k^2\psi = 0$ when $\theta_{\mathrm{ff}} \ll 1$, which means the light field is substantially confined to a narrow cone about the z axis and hence the paraxial approximation that underlies the analysis holds [219].

It is desirable to combine the parameters $w(z)$ and $R(z)$ since they are sufficient to characterize a Gaussian beam. This simplification gives rise to a crucial parameter in studying the transformation of Gaussian beams, the *complex beam parameter* q, defined as [216, 217]

$$\frac{1}{q} = \frac{1}{R} - i\frac{\lambda}{\pi w(z)^2} \quad \to \quad q = z + i\frac{\pi w_0^2}{\lambda}. \tag{5.61}$$

Here the origin $z = 0$ corresponds to the position of the beam waist.

ABCD Matrix

A periodic system is a cascade of idential unit systems of which the behavior can be modelled by a beam-transfer matrix, often called the *ABCD matrix* [56, 218, 216, 217]. An optical resonator is one example of such systems where the light coupled into the

cavity repeatedly bounces back and forth on the intra-cavity mirrors. By successively concatenating the individual matrix for each optical element of the cavity, the dynamics of the cavity, and hence the propagation of the incident light beam, can be extrapolated. Note that this ABCD matrix approach covers a wide range of optical systems, but is not applicable to systems where the beam undergoes distortions.

Consider an input beam q_{in} (refer to Eq. (5.61)) that traverses through a periodic optical structure described by a matrix $(A, B; C, D)$, the output is uniquely determined:

$$q_{\mathrm{out}} = \frac{q_{\mathrm{in}}A + B}{q_{\mathrm{in}}C + D}. \tag{5.62}$$

With the help of Fig. 5.4, we first evaluate the ABCD matrix of our squeezer

$$M_{\mathrm{SQ}} = M_{\mathrm{lc}}M_{\mathrm{d1}}M_{\mathrm{rc}}M_{\mathrm{d2}}M_{\mathrm{d3}}M_{\mathrm{d2}}M_{\mathrm{rc}}M_{\mathrm{d1}}M_{\mathrm{lc}}, \tag{5.63}$$

where the origin $z = 0$ is designated by the beam waist position at the center of the crystal. d_1, d_2, and d_3 represent, respectively, the separation between the two curved mirrors, that between the flat and the curved mirrors, and that between the two flat mirrors. l_{c} is the length of the nonlinear crystal. The elementary matrices are given by

$$\begin{gathered} M_{\mathrm{lc}} = \begin{pmatrix} 1 & \frac{l_{\mathrm{c}}}{2n} \\ 0 & 1 \end{pmatrix}, \quad M_{d_1} = \begin{pmatrix} 1 & \frac{d_1 - l_{\mathrm{c}}}{2} \\ 0 & 1 \end{pmatrix}, \quad M_{\mathrm{rc}} = \begin{pmatrix} 1 & 0 \\ -\frac{2}{R_{\mathrm{e}}} & 1 \end{pmatrix}, \\ M_{\mathrm{d2}} = \begin{pmatrix} 1 & \frac{d_1 + d_3}{2\cos\theta} \\ 0 & 1 \end{pmatrix}, \quad M_{\mathrm{d3}} = \begin{pmatrix} 0 & d_3 \\ 0 & 1 \end{pmatrix}, \end{gathered} \tag{5.64}$$

where n is the refractive index of the nonlinear crystal, $R_{\mathrm{e}} = R_{\mathrm{c}}\cos\theta$ for the tangential mode and $R_{\mathrm{e}} = R_{\mathrm{c}}/\cos\theta$ for the sagittal mode. θ here refers to the angle of incidence for the curved mirror, while R_{c} indicates the mirror radius of curvature.

5.3.2 Rules for Squeezer Designing

We have shown that the complex beam parameter encapsulates completely the properties of a Gaussian beam. Together with the ABCD matrix of a given optical system, it describes the transformation of an input Gaussian beam through the system. We can thus calculate the optimal cavity configuration using these handy formalisms. We put forward five considerations in the following that are summarized in Fig. 5.12.

No Clipping Condition

First, we require the beam to pass through and to be fully confined in the nonlinear crystal, thus no clipping at the edge of the crystal is present. As depicted in Fig. 5.12 (b) and the blue lines in the main figure, these two requirements set an upper and a lower

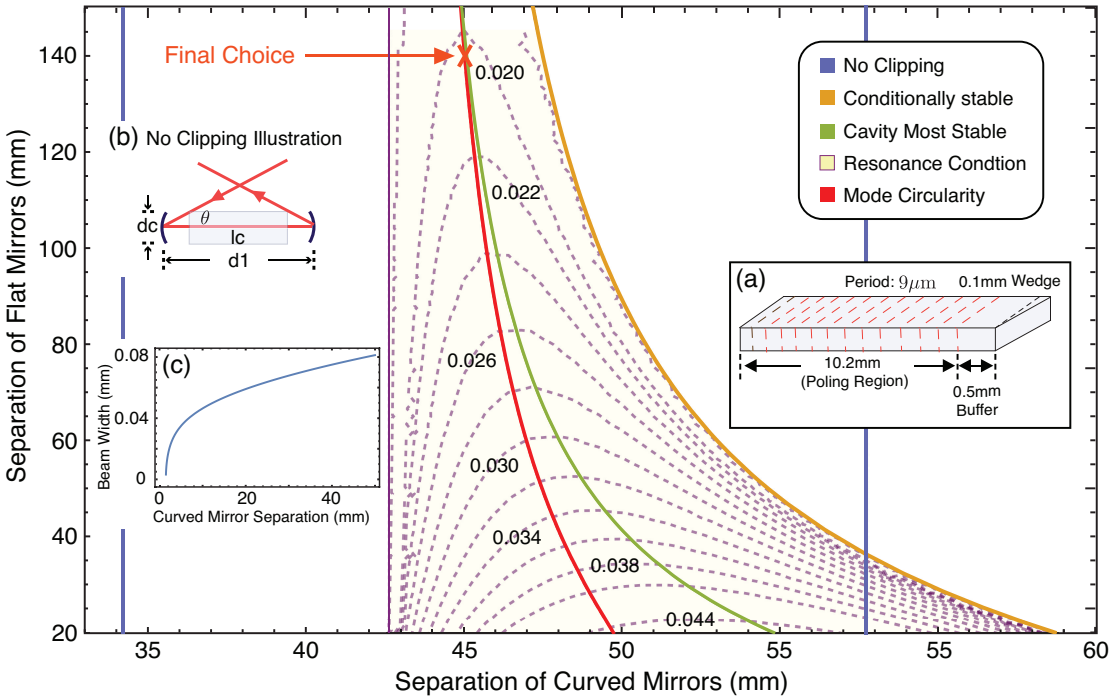

Figure 5.12: Various considerations for the design of the squeezer cavity configuration. Contour plots illustrate the resulting beam waist as a function of mirror separations. Inset (a) shows the crystal dimension: $1 \times 5 \times 10.7$mm; (b) sketches the scheme under which we derive the no clipping condition (Eq. (5.65)), while (c) shows the beam width at the edge of the crystal against the distance between the two curved mirrors.

bound on the distance d_1 at which the two curved mirrors are placed:

$$\frac{2d_c}{\tan\theta} + l_c \geq d_1 \geq \frac{d_c}{\tan\theta} + l_c. \tag{5.65}$$

As an aside, we calculate the beam size at the edge of the crystal to ensure it is smaller than the width of the crystal. Because a well coupled beam would have its beam shape matched to that of the cavity modes, its phase front curvature at where the curved mirror is located should conform to the mirror radius R_c. We obtain therefore the beam waist at $z = 0$ using Eq. (5.56) and (5.57)

$$R(d_1/2) = \frac{d_1}{2} + \frac{8\pi w_0^2}{\lambda^2 d_1} = R_c, \quad \rightarrow \quad w_0^2 = \frac{\lambda}{2\pi}\sqrt{2R_c d_1 - d_1^2}. \tag{5.66}$$

The beam width $w(l_c/2)$ is thus attainable by replacing w_0 in Eq. (5.56) by that in (5.66). We plot $w(l_c/2)$ as a function of the curved-mirror separation in Fig. 5.12 (c), verifying that the beam size is significantly less than the width of the crystal (5mm), so no clipping happens in our system.

Resonance Condition: Self-consistency of Cavity Modes

Second, to be a mode of the squeezer cavity, the beam must be capable of retracing itself after every round trip. In other words, a mode-matched beam must retain its beam width and radius of curvature of its phase front while circulating in the cavity. This recurrence condition can be cast into the expression

$$q_0 = \frac{q_0 A + B}{q_0 C + D}, \tag{5.67}$$

of which the solution is

$$q_0 = \frac{A - D}{2} \pm \frac{\sqrt{A^2 + 4BC - 2AD + D^2}}{2C}. \tag{5.68}$$

Because q_0 is the beam complex parameter at its origin, it equals to $i\pi w_0^2/\lambda$ (see Eq. (5.61)). The importance of this fact is twofold: first, the real part of q_0 vanishes, so $A = D$, and second, the imaginary part of q_0 must be postivie, so $B/C < 0$. These considerations impose a restriction on the mirror separations which is shown as the yellow shaded area in Fig. 5.12.

Confinement Condition: Cavity Stability

A stable cavity is always more desirable, since it provides a better confinement of light, rendering it less sensitive to misalignment. In this regard, the Fabry-Parot cavity comprised of two parallel plane mirrors of finite dimensions is a disadvantageous configuration. Any misalignment of the cavity mirrors or nonzero inclination of the incoming beam would cause the beam to depart further and further away from the optical axis and eventually wander out of the cavity. The confinement condition can be quantitatively expressed in terms of the cavity ABCD matrix

$$-1 \leq \frac{A + D}{2} \leq 1, \tag{5.69}$$

provided that the determinant of the matrix $\det[M_{\mathrm{SQ}}] = 1$. Because $\det[M_{\mathrm{SQ}}] = n_1/n_2$, where n_1 and n_2 dictate the refractive indices of the initial and final segments of the system, $\det[M_{\mathrm{SQ}}] = 1$ is applicable to our analysis.

Before proceeding to examine our squeezer cavity, we first invoke a simple model of the Fabry-Parot cavity as an aid to a better operational understanding of the stability of a cavity. Without loss of generality, we assume the two cavity mirrors have radii of curvature R_1 and R_2 and are separated by d. It can be easily verified that the ABCD matrix describing such a system is given by

$$\begin{pmatrix} 1 + \frac{2d}{R_2} & 1 + \frac{2d^2}{R_2} + d \\ \frac{2}{R_1} + \frac{4d}{R_1 R_2} + \frac{2}{R_2} & \frac{4d^2 + 2R_2 + 2d(R_1 + R_2)}{R_1 R_2} + 1 \end{pmatrix}. \tag{5.70}$$

Condition (5.69) therefore specializes to

$$0 \leq \left(1 + \frac{d}{R_1}\right)\left(1 + \frac{d}{R_2}\right) \leq 1, \tag{5.71}$$

where $g_1 = 1 + d/R_1$ and $g_2 = d/R_2$ are known as the cavity *g parameters*. Equation (5.71) can be alternatively derived by calculating the Rayleigh range of the resonating beam using $R_1 = -d/2 - 2z_{\mathrm{R}}^2/d$, and $-R_2 = d/2 + 2z_{\mathrm{R}}^2/d$. The requirement for z_{R} to be real leads precisely to Eq. (5.71) derived based on the ABCD matrix. Figure 5.13 sketches the confinement condition in terms of the g parameters. The left inequality in (5.71) implies that a stable cavity would access only the first and third quadrants, while the right inequality signifies that stable resonators should lie within the unshaded area enclosed by the hyperbola $g_1 g_2 = 1$. At the boundary, a resonator is considered to be conditionally stable. A planar-mirror resonator is one such example exhibiting only conditional stability.

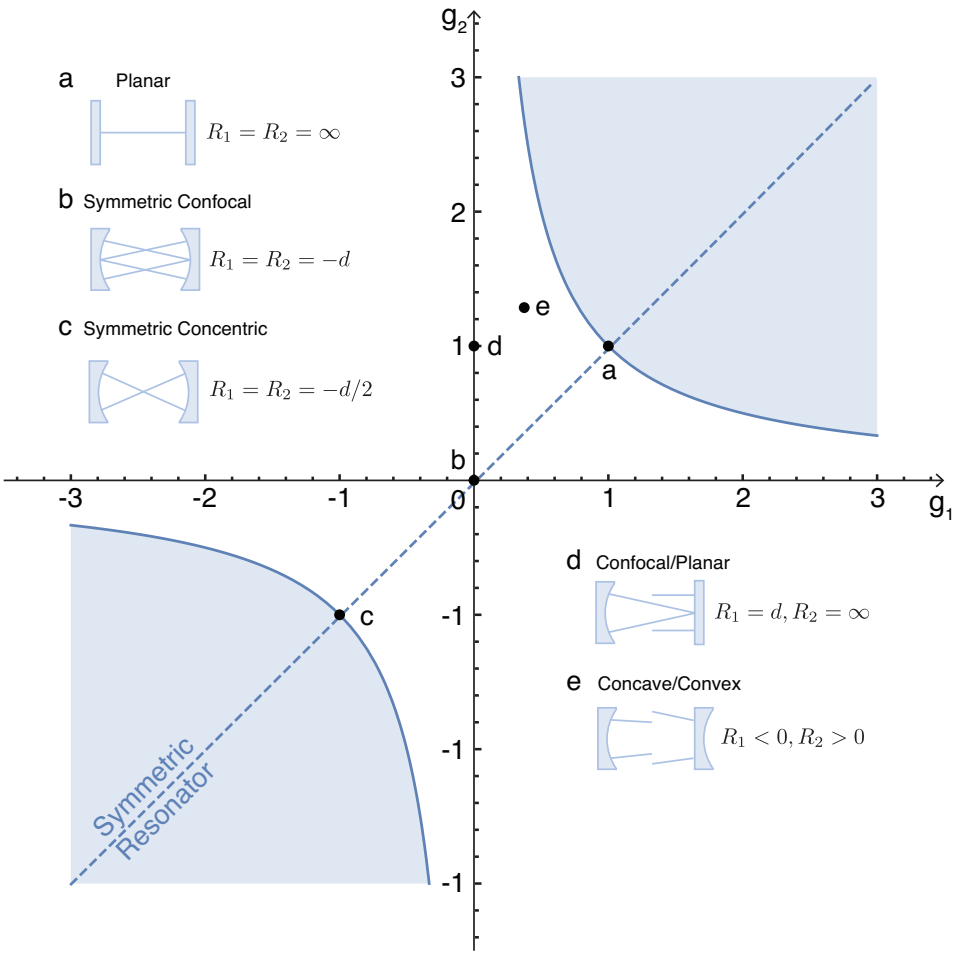

Figure 5.13: Cavity stability diagram. A Fabry-Parot cavity is considered to be stable if the parameters g_1 and g_2 lie between the hyperbolic curves on the first and third quadrants. Resonators that have a symmetric geometry $g_1 = g_2$ lie along the dashed line. The possible cavity geometries are presented aside and indicated by letters correspondingly on the diagram.

For our squeezer, the argument (5.69) is graphically shown in Fig. 5.12 as the yellow shaded area. Interestingly, this coincides exactly with the resonance condition discussed in the previous section, and hence provides an insight into the intrinsic equivalence between how a cavity maintains its stability and how it appropriately forms a mode. The dark yellow curve here identifies the conditionally stable region of the squeezer corresponding to $|(A+D)/2| = 1$, whilst the green line indicates the most stable region of the cavity, where $(A+D) = 0$.

Mode Circularity Condition

Fourthly, we require the beam at its waist to be circular to avoid astigmatism. This means the beam waist on the tangential plane must equal to that on the sagittal plane. The beam waist w_0, in accordance with (5.61) and (5.68), is given by

$$w_{0\mathrm{i}} = \sqrt{\frac{\lambda q_{0\mathrm{i}}}{i\pi}} = \sqrt{\frac{\lambda}{\pi}\sqrt{-\frac{B_\mathrm{i}}{C_\mathrm{i}}}}, \quad i \in (\mathrm{T}, \mathrm{S}), \tag{5.72}$$

where the subscripts T and S denote the tangential and sagittal mode, respectively. The condition $w_{0\mathrm{T}} = w_{0\mathrm{S}}$ is depicted as the red curve in Fig. 5.12. As demonstrated in Fig. 5.14, the circularity condition only holds for one particular separation of the curved mirrors; it therefore imposes the most stringent restriction on the cavity configuration.

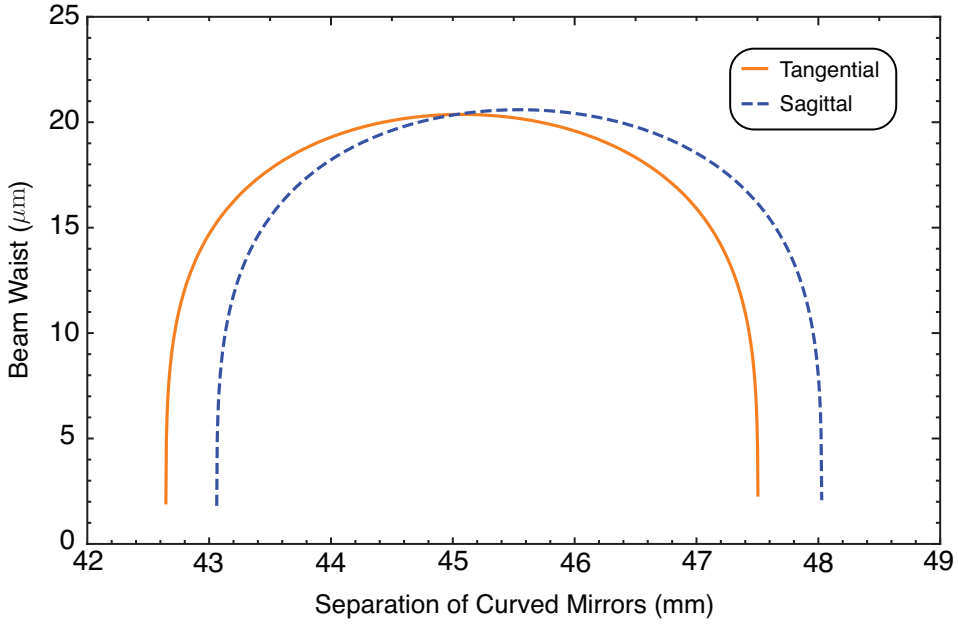

Figure 5.14: Beam waists on the tangential and sagittal planes.

Optimal Nonlinearity Condition: Boyd-Kleimann Criterion

The last consideration relates to optimizing the nonlinear interaction in the presence of a focused Gaussian beam. This optimization problem was elucidated by Boyd and Kleinman in their comprehensive work [212], applicable to second harmonic generation and other parametric generation (PG) such as sum- and difference-frequency generation. It was shown that in the absence of double refraction, the optimum conditions for SHG and PG are essentially the same. The optimum condition emerges when the beam waist is located at the center of the crystal (assuming no absorption loss is present) and the focussing parameter $\xi = L_c/(2z_{\mathrm{R}})$ lies in the range $1.392 \leq \xi \leq 2.84$ dependent on the double refraction value B. In cases where $B = 0$, the single optimum ξ equals to 2.84. This corresponds to an optimum waist for the pump beam, being

$$w_{0\mathrm{opt}_b} = \sqrt{\frac{L_c \lambda_b}{2\pi n_b \xi}} \simeq 13\mu\mathrm{m}, \tag{5.73}$$

where $n_b \simeq 1.88$ is the refractive index of the crystal at 532nm [202]. Worth noting is that the SHG conversion efficiency remains within 10% of its maximum over the range $1.52 < \xi < 5.3$, rendering the dependence of the nonlinear interaction strength on ξ less critical in practice.

5.4 Squeezer Characterization: OPA Parameters

We have shown that the pump threshold and escape efficiency are the two parameters that primarily determine the amount of available squeezing. We experimentally examined these parameters of our squeezer and compared the results with their expected values based on the coating specifications. The experimental setup is sketched in Fig. 5.15. A continuous-wave frequency-doubled Nd:YAG laser (Innolight Diablo) is employed to produce a pump beam at 532 nm and a fundamental beam (seed) at 1064 nm. The pump is injected into the squeezer cavity through the input/output coupler, whilst the fundamental beam is fed in through the mirror attached to a PZT that is used to scan the cavity length. A phase modulation at 11.25 MHz is applied on the pump beam for locking the cavity length, and the fundamental beam is phase modualted at 41.5625 MHz to lock the two beams in phase. The temperature of the PPKTP crystal was optimized with respect to the parametric gain for all measurements. With the help of a commercialized temperature controller, the crystal temperature can be stabilized to its optimum within $\pm 0.01^{\circ}$C.

5.4.1 Pump Threshold

We first characterize the pump threshold. This was done by measuring the transmitted seed power on one of the homodyne detectors both in the absence of and in the presence

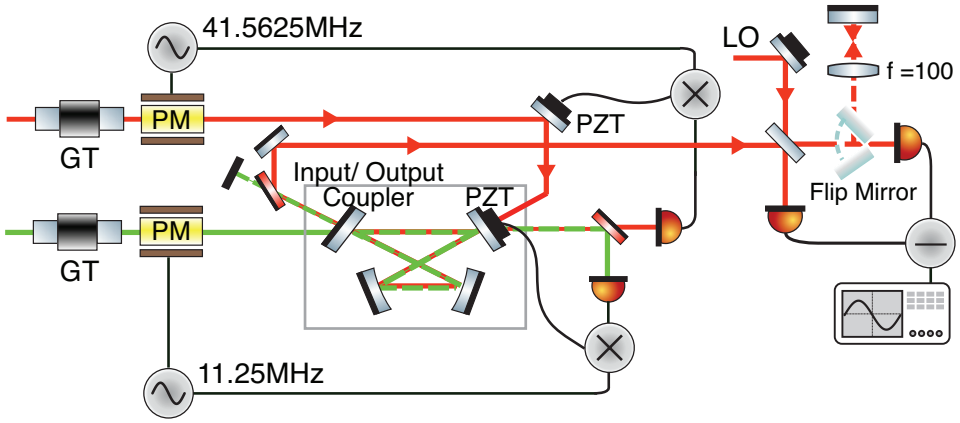

Figure 5.15: Layout for the experimental characterization of the squeezer parameters. Three lockings are involved in this setup. The phase modulations implemented on the pump and fundamental fields are utilized to lock the cavity length and the relative phase between the two fields, respectively. The error signal for the latter lock comes from the amplification/de-amplification trace arising from the nonlinear interaction between the pump and the seed. On the homodyne station, a typical relative phase locking technique (see Sec. 3.4.1) is adopted to probe the noise spectra of the squeezed and anti-squeezed quadratures. A flip mirror is placed before one of the homodyne detectors to reflect the LO back to the squeezer for the purpose of measuring the cavity escape efficiency. Because the LO is mode-matched to the squeezed output, in this configuration, only one lens is required to appropriately couple the LO into the squeezer cavity.

of the pump field. The parametric gain, in accordance with Eq. (5.43), can then be calculated by taking the ratio of the two powers. Figure 5.16 (a) plots the parametric gain as a function of the input pump amplitude. The optimal fitting of experimental data into (5.46) indicates the pump threshold of our squeezer is 163.6mW. As a by-product, using Eq. (5.45)

$$P^b_{\text{thr}} = \frac{hc}{\lambda_b}\beta^*_{\text{in}}\beta_{\text{in}}|_{(|\beta|=\kappa_a/\chi)} = \left(\frac{\kappa_a\kappa_b}{\chi\sqrt{2\kappa^b_{\text{in}}}}\right)^2 \frac{hc}{\lambda_b}, \tag{5.74}$$

we obtain a good estimate of the coupling coefficient χ (857.6) of our crystal.

5.4.2 Escape Efficiency

The investigation of escape efficiency η_{esc} provides a way to show the intra-cavity loss of our squeezer and therefore yields an empirical estimation of the obtainable magnitude of squeezing in our system. This can be seen from Eq. (5.53),

$$\eta_{\text{esc}} = \frac{\kappa^a_{\text{in/out}}}{\kappa^a_{\text{in/out}} + \kappa^a_l}. \tag{5.75}$$

In practice, the intra-cavity loss may be straightforwardly estimated according to the coating specifications (refer to Table. 5.1). The equivalent total loss is given by the

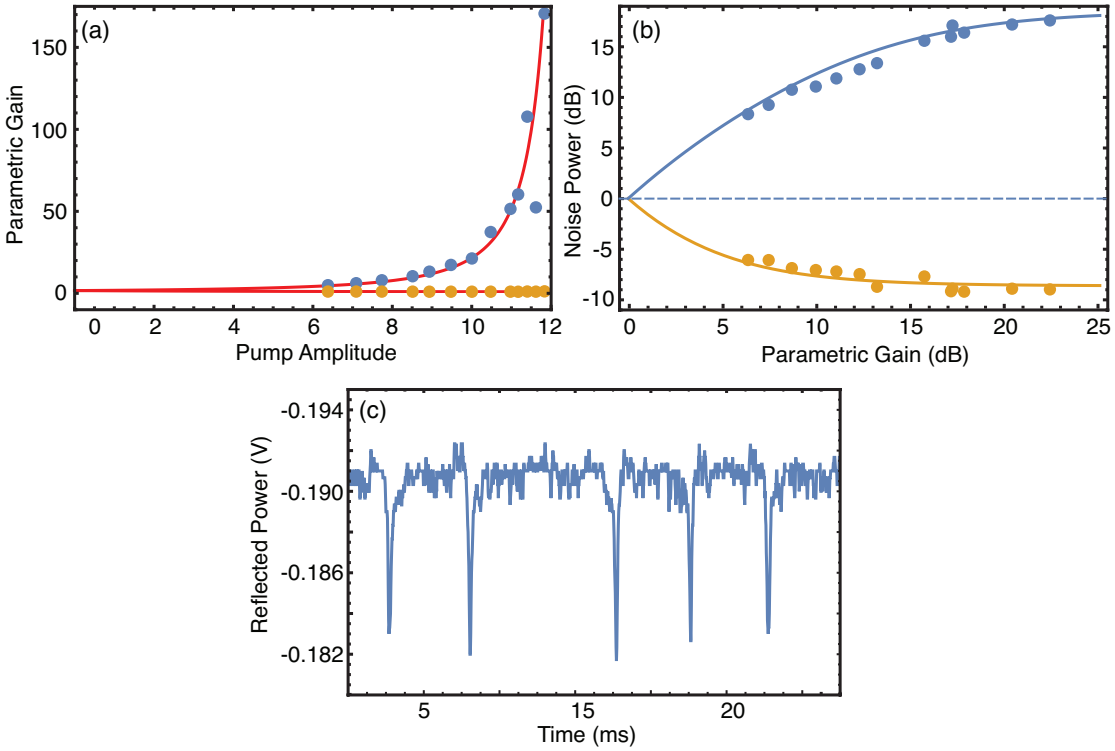

Figure 5.16: (a) Experimental parametric gain against the pump amplitude for amplification (blue dots) and de-amplification (yellow dots), superimposed by the theoretical fitting. (b) Experimental results and the theoretical fitting for squeezing and anti-squeezing levels as functions of parametric gains. (c) Reflected fundamental power on the squeezer input/output coupler.

multiplication of loss associated with each cavity component

$$R_l^a = \underbrace{0.9985 \times 0.9999 \times 0.9999}_{\text{Mirror Losses}} \times \underbrace{0.999 \times 0.999}_{\text{Crystal AR Coating}} \underbrace{\times 0.9979}_{\text{Crystal Absorption}} = 0.9961 \pm 0.0005, \tag{5.76}$$

where the PPKTP absorption is estimated to be $0.02\%/\text{cm}$ [215]. This results in an escape efficiency of 0.987 ± 0.003.

A more accurate way to evaluate the intra-cavity loss is to measure η_{esc} directly by investigating the cavity response with respect to its outgoing modes. To simplify the characterization, the pump beam is blocked so that $\beta = 0$. Using Eq. (5.40) and the boundary conditions (5.16), we obtain the reflected field amplitude

$$\alpha_r = \frac{2\kappa^a_{\text{in/out}} - \kappa_a}{\kappa_a} \alpha_{in}, \tag{5.77}$$

and thus the amount of incident power that is reflected off the cavity

$$\frac{P_r}{P_{\text{in}}} = \left(\frac{\kappa^a_{\text{in/out}} - \kappa^a_l}{\kappa^a_{\text{in/out}} + \kappa^a_l} \right)^2. \tag{5.78}$$

Note that this power ratio is fully determined by the intra-cavity loss. For an impedance matched cavity where $2\kappa_{\text{in}}^{a} = \kappa_a$, no light would be reflected from the resonator. The escape efficiency can then be derived by a simple substitution of Eq. (5.78) into (5.75)

$$\eta_{\text{esc}} = \frac{1}{2}\left(1 + \sqrt{\frac{P_r - P_{r'}}{P_{\text{in}} - P_{r'}}}\right). \tag{5.79}$$

Here $P_{r'}$, the reflected power of the higher order TEM modes, is deducted to avoid an overestimation of the escape efficiency.

As depicted in Fig. 5.15, we measure the reflected power in the laboratory by reflecting back the homodyne local oscillator that has been well mode matched to the squeezer cavity. In this configuration, the mode matching is accomplished quite conveniently with only one lens ($f = 100$ in our case), thus mitigating the need to build a lens telescope that would otherwise be required for coupling light into a resonator [53, 56]. Another advantage of this setup resides in its flexibility: when flipping down the flip mirror in Fig. 5.15, one can conduct a squeezing measurement with the homodyne detection, whilst when the flip mirror is up, one can measure the escape efficiency without reconfiguring the setup. The measurement result is shown in Fig. 5.16 (c), where the base voltage, corresponding to off-resonance reflection, denotes the input power P_{in}. The resultant escape efficiency is 0.984 ± 0.002, thereby showing a reasonable agreement with the expected value derived from coating specifications. It also leads to the inference that the intra-cavity loss of our system is around 1.4%, indicating that a reasonable magnitude of squeezing should be obtainable from our setup.

5.4.3 Noise Response: Squeezing and Anti-Squeezing against OPO Nonlinear Parametric Gains

To further characterize the performance of our system, we measured the output squeezing and anti-squeezing levels for a series of input pump powers. The measurement results along with the theoretical fitting into Eq. (5.54) are shown in Fig. 5.16 (b). There is no clear decrease of the output squeezing as we turning up the parametric gain, therefore implying that the phase noise in our system is reasonably small. Otherwise, in the presence of significant phase noise, the observable squeezing would first increase as the parametric gain grows, stop increasing when the gain reaches a particular turning point dependent upon the phase noise level, and degrade thereafter. In addition, the results presented here help us to infer the propagation and detection loss in our setup, which is around 6.1%, accounting for the photodiode efficiency (0.99), the homodyne visibility (0.985), and losses from two lenses (0.98), one dichroic mirror (0.999), and two HR mirrors (0.9995).

In conclusion, the agreement between the coating specifications and experimental results is evidently quite reasonable, which justifies the faithfulness of the specifications. The parameters of our squeezer are tabulated in Table 5.1.

5.5 Measurement of the Output Squeezing Levels

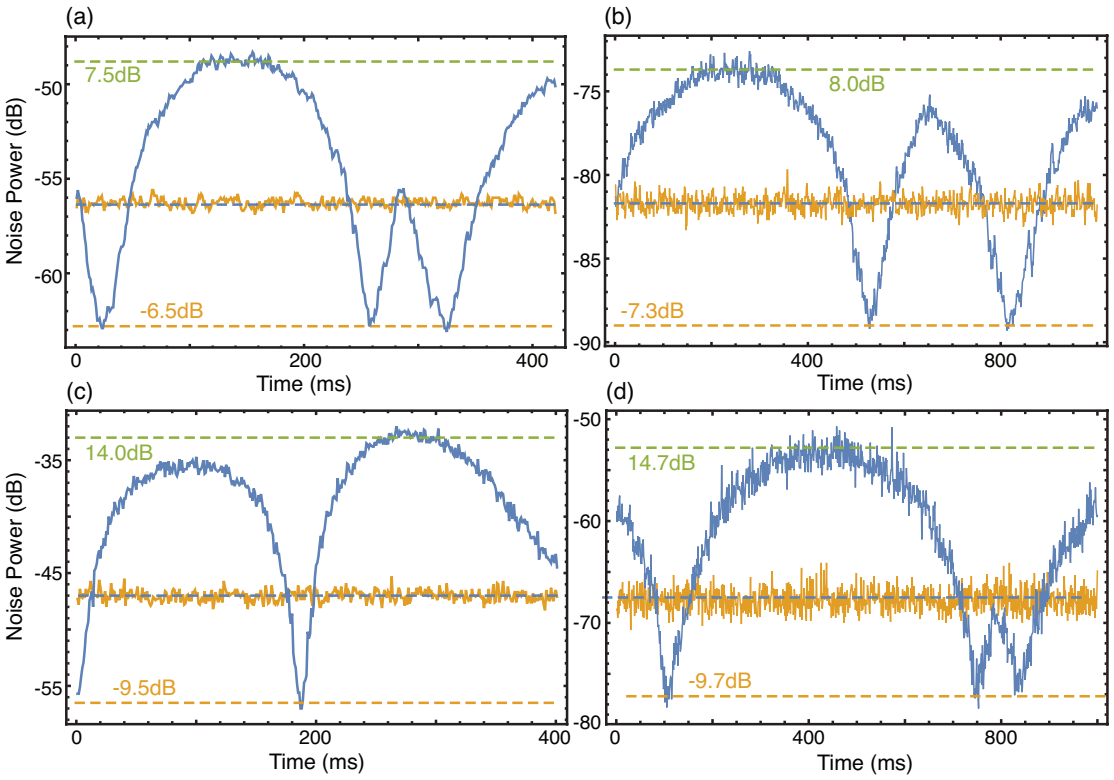

Figure 5.17: Different magnitudes of squeezing are generated by increasing the input pump power in presence of a weak seed beam (1 mW). The measurement was conducted at 4 MHz and 2 MHz, respectively, for (a), (b) and (c), (d). The local oscillator is scanned at 1 Hz to capture the noise spectra in a continuum of quadrature phases. Other measurement settings are: RBW of 300 kHz and VBW of 1 kHz for (a) and (c); RBW of 100 kHz and VBW of 3 kHz for (b); RBW of 100 kHz and VBW of 3 MHz for (d); the sweep time is set to be around 0.1 s for all traces.

Figure 5.17 shows the end results of the output squeezing in our system after optimizing all experimental parameters. The experimental schematic is plotted in Fig. 5.15 where the relative phase between pump and seed is locked to be an even multiple of π, corresponding to the de-amplification condition of the OPA. The phase of the homodyne local oscillator is scanned continuously, so all quadrature variances can be traced out as shown in Fig. 5.17. By increasing the pump power, the parametric gain is consequently increased, and a higher level of squeezing is attained at the expense of a lower squeezing purity. The highest squeezing we observed was around 11 dB; however the measurement trace was lost. A squeezing level of 9.7 dB was reported in Fig. 5.17 (d), implying that 11.5 dB squeezing was produced by the OPA if the detection loss is corrected (0.99×0.985^2). Moreover, we present a purer squeezed output with 7.3 dB squeezing and a purity of 1.17.

The squeezed beams produced by the two squeezers are combined on a 50:50 beamsplitter to generate a pair of CV entangled state. The characterization of the squeezer

Cavity Parameters	Value	Unit
Fundamental Wavelength (Squeezing) λ_a	1064	nm
Second Hamonic Wavelength (Pump) λ_b	532	nm
Cavity Round Trip Length L	374	mm
Flat Mirros: Separation d_f	140	mm
Curved Mirros: Separation d_c	45	mm
Curved Mirrors: Radius of Curvature Roc	-38	mm
Cavity Mode Upper Beamwaist (Fundamental) w^a_{u0}	215	μm
Cavity Mode Upper Beamwaist (Pump) w^b_{u0}	152	μm
Cavity Mode Lower Beamwaist (Fundamental) w^a_{l0}	20.4	μm
Cavity Mode Lower Beamwaist (Pump) w^b_{l0}	14.4	μm
PPKTP Crystal Dimensions	$1 \times 5 \times 10.7$	mm
Input/Output Coupler Reflectivity (Fundamental) $R^a_{\text{in/t}}$	0.83 ± 0.01	-
Input/Output Coupler Reflectivity (Pump) $R^b_{\text{in/t}}$	0.73 ± 0.012	-
Piezo Mirror Reflectivity (1064 & 532)	0.9985 ± 0.0005	-
Curved Mirros Reflectivity (1064 & 532)	0.9999	-
Crystal Anti-Reflectivity 1064 (532)	$< 0.1 (< 0.2)$	-
Total Intra-Cavity Loss 1064 (532) $R^a_l (R^b_l)$	0.996 (0.9943)	-
Finesse 1064 (532) $\mathscr{F}^a (\mathscr{F}^b)$	29 (17)	-
Linewidth 1064 (532) $\nu^a_{\text{FWHM}} (\nu^b_{\text{FWHM}})$	36 (60)	MHz
Pump Threshold P^b_{thr}	163.6	mW
Escape Efficiency η_{esc}	0.984 ± 0.002	-
Coupling Coefficient χ	858	-
Focusing Parameter ξ_{SQ}	2.84	-
Crystal Refractive Index n	1.83	-

Table 5.1: Optical and mechanical specifications of the OPA squeezers.

parameters, together with the measurement of the output squeezing levels, are of great operational importance. It is used to predict the performance of the squeezing-powered quantum information protocols that shall be presented in chapters 7, 8, and 9.

Part II

Post-selective Continuous Variable Quantum Information Protocols

Chapter 6

Hybrid Linear Amplifier and Its Applications

Overview

Due to the pervasive nature of decoherence, protection of quantum information during transmission is of critical importance for any quantum network. A linear amplifier that can enhance quantum signals stronger than their associated noise while preserving quantum coherence is therefore of great use. This seemingly unphysical amplifier property is achievable for a class of probabilistic amplifiers that does not work deterministically. Here we present a linear amplification scheme that realizes this property for coherent states by combining a heralded measurement-based noiseless linear amplifier and a deterministic linear amplifier. The amplifier is phase-insensitive and can enhance the signal-to-noise ratio of the incoming optical signal. Besides, the concatenation of two amplifiers introduces the flexibility that allows one to tune between the regimes of high-gain or high noise-reduction, and control the trade-off of these performances against a finite heralding probability. We demonstrate an amplification signal transfer coefficient of $\mathcal{T}_s > 1$ with no statistical distortion of the output state. By partially relaxing the demand of output Gaussianity, we can obtain further improvement to achieve a $\mathcal{T}_s = 2.55 \pm 0.08$ with an amplification gain of $g_{\text{eff}} = 10.54$.

We provide one application of this hybrid linear amplifier: a quantum cloning machine that is constructed by adopting the *amplify-and-split* approach [221]. We demonstrate the production of up to five clones with fidelity for each clone significantly surpassing their corresponding no-cloning limit. Considering that our amplification scheme only relies on linear optics and a post-selection algorithm, we anticipate it to have the potential to be used as a versatile tool in a broad class of noise-sensitive quantum information protocols.

Publications relevant to the work in this chapter include:

• J. Zhao, J. Dias, J. Y. Haw, T. Symul, M. Bradshaw, R. Blandino, T. Ralph, P. K. Lam, and S. Assad. *Quantum enhancement of signal-to-noise ratio with a heralded linear amplifier*,

Optica **4**, 1421, (2017).

• J. Zhao, J. Dias, J. Y. Haw, T. Symul, M. Bradshaw, R. Blandino, T. Ralph, P. K. Lam, and S. Assad. *Quantum enhancement of signal-to-noise ratio for arbitrary coherent states using heralded linear amplifier*, 2017 Conference On Lasers and Electro-Optics Pacific Rim (CLEO-Pr), IEEE, (2017).

• J. Y. Haw, J. Zhao, J. Dias, S. M. Assad, M. Bradshaw, R. Blandino, T. Symul, T. C. Ralph, and P. K. Lam. *Surpassing the no-cloning limit with a heralded hybrid linear amplifier*, Nature Communications **7**, 13222, (2016).

6.1 Introduction

The question of quantum noise in linear amplifiers has stirred considerable interest not only because of its technical significance, but also owing to its intimate connection with the most fundamental features of quantum theory. A *perfect linear amplifier* (PLA) increases the power of an incoming signal without introducing a degradation to its signal-to-noise ratio (SNR). This is achievable easily for classical signals. However, in the quantum world, a PLA cannot function deterministically. Due to the bosonic nature of photons, an optical amplifier unavoidably introduces noise to any signal it processes. The noise penalty arises from the interaction between the initially independent input mode and the internal modes of an amplifier. This quantum property of amplifiers was theoretically elucidated by Haus and Mullen [222] and was quantitatively expressed as the *amplifier uncertainty principle* [76]. In particular, for a phase-insensitive amplifier, the minimum amount of additional noise is equivalent to $|G-1|$ units of vacuum noise, where G denotes the power gain for the input signal. This noise penalty prevents the increase of distinguishability of quantum states under amplification. It therefore ensures that by means of the *amplify-and-split* approach [80], two orthogonal quadrature amplitudes of a bosonic mode cannot be measured simultaneously with arbitrary precision, in compliance with the Heisenberg uncertainty principle.

One way to circumvent the excess noise is to instead apply phase-sensitive amplification. One such example is to utilize optical parametric amplifier to squeeze either the input mode, or the internal mode, such that the amplified output has reduced noise in one quadrature at the expense of degrading the conjugate quadrature [223, 224, 225, 226]. Besides, phase-insensitive amplification can also be realized using a series of light emitter detectors in conjunction with high-quantum-efficiency photodetectors [227]. This device can achieve, in principle, a signal transfer limited only by the photodetector efficiency ($\mathrm{SNR}_{\mathrm{out}}/\mathrm{SNR}_{\mathrm{in}} \approx \eta_d$, where η_d is the quantum efficiency of the photodetector) for a sufficiently large number of emitters. However, while the intensity of light is amplified, all phase information is destroyed. Another method of low-noise amplification is to use an electro-optic feed-forward loop [228]. The setup

avoids the requirement of nonlinear optical process, and due to the fact that not all of the input light is destroyed, some of the phase information can be retained.

If one demands an amplification of both quadratures equally, an alternative way to evade the noise penalty is to allow a probabilistic operation. Fiurášek proposed a probabilistic amplification method that could be applied to coherent states of fixed amplitude but unknown phase [22]. Ralph and Lund extended this idea and proposed independently the noiseless linear amplifier (NLA) [21] that could in principle be applied to arbitrary ensembles. This amplifier outperforms the perfect linear amplifier by preserving the noise characteristics of the input state and is hence, from a classical point of view, a noise-reduced amplifier, as illustrated in Fig. 6.1. The price to pay is that the process has to be probabilistic and approximate in terms of the output states produced. A better approximation is attainable at the expense of a lower success probability [229, 21]. This compromise guarantees that, on average, the Heisenberg uncertainty relation remains satisfied. Nevertheless, the successfully amplified quantum states can be heralded and thus is valuable in extending the range of loss-sensitive protocols. We note that given the access to correlated inputs, it is possible to achieve phase-insensitive noise reduction deterministically via the cancellation of the internal noise, albeit the total SNR is at best conserved [230]. This entanglement-based quantum amplifier was demonstrated in [231] and applied in [232] as an enhanced interferometer for phase estimation.

Various physical implementations of NLA have been proposed and experimentally demonstrated, including the quantum scissor setup [69, 70, 71, 72], the photon-addition and -subtraction [73, 74], and noise addition [75] schemes. In all these approaches, a large truncation is often imposed on the unbounded amplification operator in the photon-number basis. The high-fidelity operating region of the amplification is consequently restricted to small input amplitude and small gains [89, 91]. The current realisations require non-classical light sources and non-Gaussian operations like photon counting, thereby rendering their application to many systems and protocols very challenging. Intriguingly, as recently proposed [79, 92] and experimentally demonstrated [81], the benefits of noise-reduced amplification can be retained via classical post-processing, provided that the NLA precedes a dual homodyne measurement directly. Although the simplicity of this measurement-based noiseless linear amplifier (MB-NLA) is appealing, its post-selective nature confines it to point-to-point applications such as quantum key distribution. To overcome this drawback, the concatenation of an NLA and a deterministic linear amplifier (DLA) that uses MB-NLA and yet outputs a quantum state was proposed recently and studied in the context of quantum cloning [94], where the production of clones with fidelity surpassing the deterministic no-cloning bound was demonstrated.

In the current paper, for the first time, we realize a quantum enhancement of signal-to-noise-ratio for arbitrary coherent states and amplification gains using a heralded noise-reduced linear amplifier. This amplifier combines the advantages of a DLA and an MB-NLA. Owing to the fully tunable cut-offs and independent control of the NLA and

DLA gains, great versatility in the effective gain and the input amplitude is attained, mitigating therefore the undesirable constraints in previous physical implementations. We show a signal transfer of 110% from input to output with an amplification gain of 6.18 when Gaussian statistics is maintained. Furthermore, by marginally compromising the Gaussianity of the output state, we demonstrate an SNR enhancement of more than 4dB for a coherent state amplitude of $|\alpha|$=0.5 with an amplification gain of 10.54.

Unlike the previous measurement-based NLA scheme [81], a heralded and free-propagating amplified state is produced with our amplifier. It is worth stressing that the setup uses Gaussian elements and a post-selection algorithm only, and hence has a better compatibility with other CV protocols.

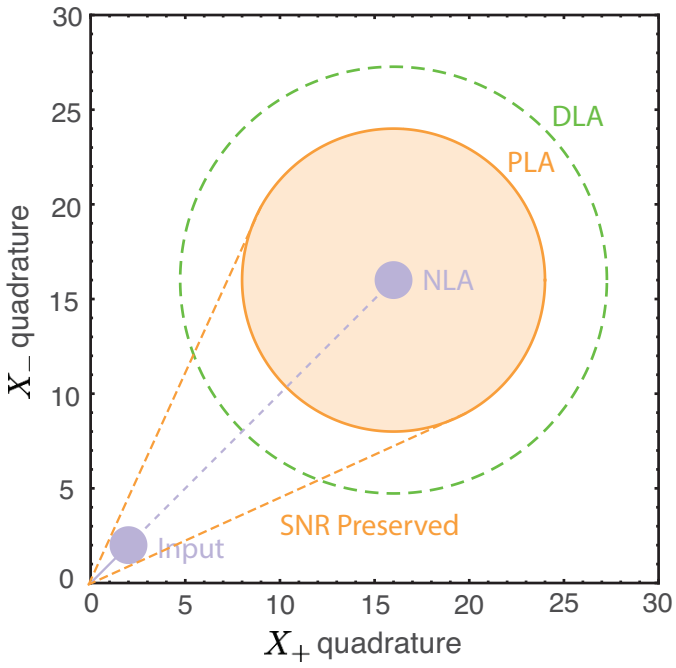

Figure 6.1: Wigner function contours of input and output coherent states for a continuum of linear amplifiers. The green dashed circle here refers to the best possible deterministic linear amplifier, which adds the minimum amount of noise imposed by quantum mechanics; any amplifier that introduces less noise is necessarily probabilistic. One example of the probabilistic amplifiers is the PLA that preserves the SNR of an incoming signal while amplifying its power (refer to PLA in the graph). Amplifiers capable of enhancing SNR are called noise-reduced amplifiers (shaded area in orange, including the NLA) and the extreme case of the noise-reduced amplifier is NLA that not only amplifies the amplitude of an input state, but also preserves its noise characteristics.

6.2 Construction of the Hybrid Linear Amplifier

6.2.1 Theoretical Modelling

First we study the behavior of our amplifier in a general operating scenario by considering an ensemble of coherent states as its input. We then concern ourselves with

a particular instance where the input state is a single coherent state selected randomly from phase space.

As is depicted in Fig. 6.2 (a), the behavior of our amplifier is dominated by the interfacing between the two intrinsically different amplifiers. A larger DLA gain would contribute to a higher success probability, but also introduce a larger noise penalty, while a larger NLA gain is the requisite to attain an increase of SNR, however, at the expense of reducing the success probability.

The effect of our linear amplifier on an unknown input state $\hat{\rho}_{\rm in}$ is to transform the state as follows:

$$\hat{\rho}_{\rm out} = \mathcal{N}\mathrm{Tr}_v\{\hat{U}_{g_{\rm DLA}} g_{\rm NLA}^{\hat{n}} \hat{\rho}_{\rm in} \otimes |0\rangle\langle 0|_v g_{\rm NLA}^{\hat{n}} \hat{U}_{g_{\rm DLA}}^{\dagger}\} \,, \tag{6.1}$$

where the constant $\mathcal{N}$ is a normalisation factor. The operator $g_{\rm NLA}^{\hat{n}}$ here models the action of the NLA on the input density operator, whilst $\hat{U}_{g_{\rm DLA}} = e^{-\theta\left(\hat{a}\hat{a}_v - \hat{a}^{\dagger}\hat{a}_v^{\dagger}\right)}$ is a unitary transformation acting on the input mode and an ancillary vacuum mode which models the action of the DLA. The parameter θ relates to the gain of the DLA via $g_{\rm DLA} = \cosh(\theta)$. The ancilla mode is traced out to give the final output. We can characterize the outcome of this interaction by considering the expectation value of an observable $\hat{M}(\hat{a}, \hat{a}^{\dagger})$,

$$\begin{aligned}\langle \hat{M} \rangle &= \mathrm{Tr}\{\hat{M}\hat{\rho}_{\rm out}\} \\ &= \mathrm{Tr}\{\hat{M}\hat{U}_{g_{\rm DLA}} g_{\rm NLA}^{\hat{n}} \hat{\rho}_{\rm in} \otimes |0\rangle\langle 0|_v g_{\rm NLA}^{\hat{n}} \hat{U}_{g_{\rm DLA}}^{\dagger}\} \\ &= \mathrm{Tr}\{\hat{M}_{\rm DLA}\hat{\rho}_{\rm NLA}\} \,,\end{aligned} \tag{6.2}$$

where we use the cyclic permutation of the trace and $\hat{M}_{\rm DLA} = \hat{U}_{g_{\rm DLA}}^{\dagger}\hat{M}\hat{U}_{g_{\rm DLA}}$, $\hat{\rho}_{\rm NLA} = g_{\rm NLA}^{\hat{n}}\hat{\rho}_{\rm in}g_{\rm NLA}^{\hat{n}}$.

We first consider the input $\hat{\rho}_{\rm in}$ to be an ensemble comprised of a Gaussian distribution of coherent states:

$$\hat{\rho}_{\rm in}(\lambda) = \frac{1}{\pi}\frac{1-\lambda^2}{\lambda^2}\int \mathrm{d}^2\alpha e^{-\frac{1-\lambda^2}{\lambda^2}|\alpha|^2}|\alpha\rangle\langle\alpha| \tag{6.3}$$

where λ ($0 \leq \lambda < 1$) relates to the variance of the distribution by $V = \frac{1+\lambda^2}{1-\lambda^2}$. Due to the linearity of the NLA operator, the distribution $\hat{\rho}_{\rm in}(\lambda)$ changes as $g_{\rm NLA}^{\hat{n}}\hat{\rho}_{\rm in}(\lambda)\, g_{\rm NLA}^{\hat{n}} \propto \hat{\rho}(g_{\rm NLA}\lambda)$ under noiseless linear amplification [77]. That is, if Alice sends a distribution of coherent states of width λ, the conditional state after the successful operation of NLA is proportional to a distribution of width $g_{\rm NLA}\lambda$. Correspondingly, the variance of the ensemble of coherent states becomes $V = \frac{1+g_{\rm NLA}^2\lambda^2}{1-g_{\rm NLA}^2\lambda^2}$. We note that for the amplified distribution to be physical, $g_{\rm NLA}^2\lambda^2$ must be less than one. The state $\hat{\rho}_{\rm NLA}(g_{\rm NLA}\lambda)$ is then amplified by the DLA to give the final output state. The expectation value of an

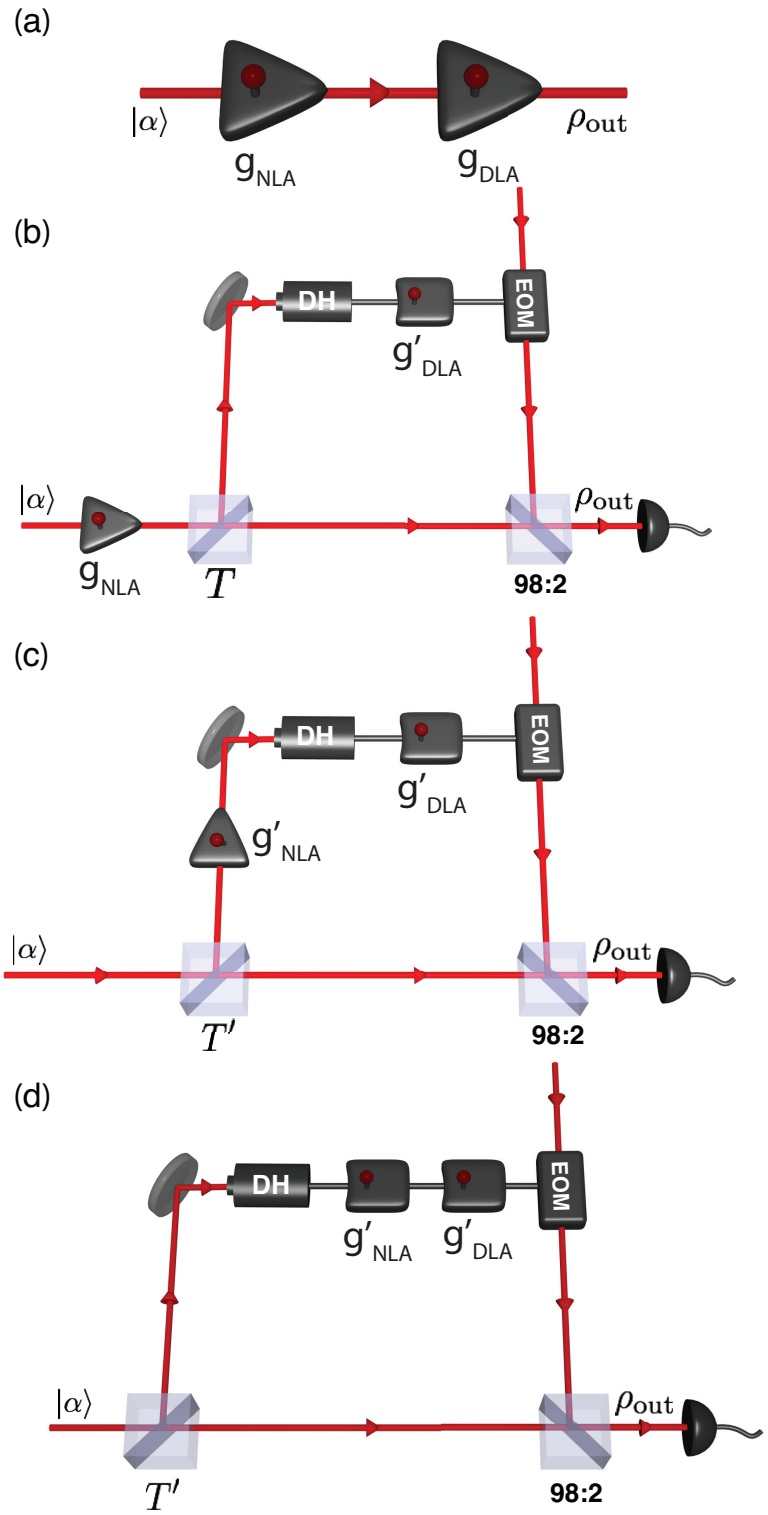

Figure 6.2: Construction of our amplifier. The transformation from (a) to (d) involves two intermediate steps: first, we implement the DLA using a feed-forward circuit; second, we move the NLA from the input to the reflected port of the BS so it can be emulated by the measurement-based NLA scheme.

arbitrary observable $M(\hat{a}_{\rm out}, \hat{a}^\dagger_{\rm out})$ can then be constructed using [76, 233]

$$\begin{aligned}\hat{a}_{\rm out} &= \hat{U}^\dagger_{g_{\rm DLA}} \hat{a}_{\rm in} \hat{U}_{g_{\rm DLA}} \\ &= \hat{a}_{\rm in}\, g_{\rm DLA} + \hat{a}^\dagger_v \sqrt{g^2_{\rm DLA} - 1}\,,\end{aligned} \tag{6.4}$$

So far, we have described how an ensemble of coherent states evolves by our amplifier. We now examine the action of our amplifier on each individual coherent state $|\alpha\rangle$.

The NLA probabilistically amplifies the complex amplitude of an input coherent state $|\alpha\rangle$ to $|g_{\rm NLA}\alpha\rangle$ with a gain $g_{\rm NLA}{>}1$. The DLA then performs the deterministic transformation as shown in Eq. (6.4). The mean of the amplitude $\hat{X}_+ = \hat{a} + \hat{a}^\dagger$ and phase $\hat{X}_- = -i(\hat{a} - \hat{a}^\dagger)$ quadratures of the electric field is therefore amplified by

$$\langle \hat{X}_\pm \rangle_{\rm out} = g_{\rm NLA} g_{\rm DLA} \langle \hat{X}_\pm \rangle_{\rm in}\,. \tag{6.5}$$

To quantify the amplification of the signal, we define $g_{\rm eff} = g_{\rm NLA} g_{\rm DLA}$ as the effective gain. Since the NLA incurs no additional noise, the overall output noise is only a function of the DLA gain (where the quantum noise level is 1)

$$\langle (\delta \hat{X}_\pm)^2 \rangle_{\rm out} = 2 g^2_{\rm DLA} - 1\,. \tag{6.6}$$

6.2.2 Equivalent Experimental Scheme

Here we present in details the recipe for constructing the amplifier setup, shown in Fig. 6.2 (d), from the conceptual picture, 6.2 (a). The recipe involves two intermediate stages. Starting from the simple diagram of the amplifier, first we adopt the proposal in Ref. [233] to implement the DLA based on the a measurement and feed-forward circuit. More specifically, in order to realize the deterministic linear amplification, the input coherent state, after being amplified by an NLA, is first fed through a beam splitter (BS) with transmission of

$$T = \frac{1}{g^2_{\rm DLA}}\,. \tag{6.7}$$

The reflected mode is then subject to a dual homodyne setup locked to simultaneously measure the amplitude and phase quadratures. The measurement outcome is then electronically amplified with gain $g'_{\rm DLA}$ which is related to $g_{\rm DLA}$ as

$$g'_{\rm DLA} = \sqrt{2\left(g^2_{\rm DLA} - 1\right)}\,. \tag{6.8}$$

The rescaled outcome is finally feed-forwarded as input to a pair of amplitude and phase modulators on a bright auxiliary beam. The beam is then coupled to the transmitted input through a 98:2 BS to fulfil the displacement operation, thereby realizing the transformation in Eq. (6.4).

The remaining task is to embed the NLA into this DLA configuration. Although

this may be hard for the physical implementations of NLA, it is tractable for the measurement-based scheme, since it also relies upon a dual homodyne detection. Consider that to emulate an NLA in such post-selection manner, the measurement-based NLA is required to precede the dual homodyne station directly [79], and thus in step Fig. 6.2 (c), we move the NLA from before the BS to the in-line output port of the BS. To make this translation valid, we ensure that the output of the BS remains enact, which is given by $|\sqrt{T}g_{\rm NLA}\alpha\rangle_t|\sqrt{1-T}g_{\rm NLA}\alpha\rangle_r$ where the subscripts t and r represent the transmitted and reflected modes, respectively. Note that the same output can be attained by modifying the NLA gain to $g'_{\rm NLA}$

$$g'_{\rm NLA} = \sqrt{\frac{1-T}{1-Tg^2_{\rm NLA}}}g_{\rm NLA} \tag{6.9}$$

and meanwhile, replacing the BS by a beam splitter with transmission of

$$T' = g^2_{\rm NLA}/g^2_{\rm DLA}\ . \tag{6.10}$$

The NLA now appears to be followed immediately by the in-line dual homodyne detection, and can therefore be virtually implemented via the measurement-based scheme. The MB-NLA, in a nutshell, comprises of a filter function that is applied on the measurement outcome, $\alpha_{\rm m}{=}(x_{\rm m}+ip_{\rm m})/\sqrt{2}$, of the in-line dual homodyne and a rescaling factor $1/g'_{\rm NLA}$ that eliminates the additional noise arising from the filtering. The functionality of the filter function has been elucidated in chapter 4; therefore, we provide only a brief summary of its key feature here. The probabilistic Gaussian filter can be written in the following form

$$P(\alpha_m) = \begin{cases} \exp\left(|\alpha_{\rm m}|^2{-}|\alpha_{\rm c}|^2\right)\left(1-\frac{1}{(g'_{\rm NLA})^2}\right) & \text{if } |\alpha_{\rm m}|{\leq}\alpha_{\rm c}, \\ 1 & \text{otherwise,} \end{cases} \tag{6.11}$$

where the cut-off parameter $\alpha_{\rm c} > 0$ acts as the truncation on the working phase space of the unbounded amplification operator. More specifically, all measurement outcomes α_m with magnitude less than α_c are selected or rejected with probability specified in Eq. (6.11), while those α_m falling beyond the cut-off amplitude are kept with unit probability [234]. The cut-off, α_c, therefore determines how closely the filter approximates an ideal NLA and also the success probability of the protocol. This filter function heralds the successful amplification and over-amplifies both the mean and the variance of the measured statistics by ${g'_{\rm NLA}}^2$. Thus, to retrieve the target mean and dispose of the additional noise, a rescaling factor of $1/g'_{\rm NLA}$ is applied to the filtered statistics.

The construction presented so far provides an experimental realization for the cascaded NLA and DLA. We can therefore derive the output mean and variance of the

quadrature amplitudes:

$$\langle \hat{X}_{\pm} \rangle_{\rm out} = \left(\sqrt{\frac{1-T'}{2}}\, g'_{\rm DLA}\, g'_{\rm NLA} + \sqrt{T'} \right) \langle \hat{X}_{\pm} \rangle_{\rm in}, \tag{6.12}$$

$$\langle (\delta \hat{X}_{\pm})^2 \rangle_{\rm out} = 1 + (g'_{\rm DLA})^2 \ . \tag{6.13}$$

We quantify the performance of our amplifier by introducing the signal transfer coefficient,

$$\mathcal{T}_s = {\rm SNR}_{\rm out}/{\rm SNR}_{\rm in} \ , \tag{6.14}$$

which is equal to

$$g_{\rm eff}^2/(2g_{\rm DLA}^2 - 1) \tag{6.15}$$

for a quantum-limited amplification [233] and is larger than 1 for a noise-reduced operation. From Eq. (6.12) and (6.14), we obtain the theoretical $\mathcal{T}_s$ for both quadratures for our setup,

$$\mathcal{T}_s = \frac{(\sqrt{\frac{1-T'}{2}}\, g'_{\rm DLA}\, g'_{\rm NLA} + \sqrt{T'})^2}{1 + (g'_{\rm DLA})^2} \ . \tag{6.16}$$

Besides, to identify the operating region where the amplification is experimentally feasible, one can also calculate the success probability $P_{\rm S}$ of our amplification scheme in a similar way to that has been addressed in chapter 4:

$$\begin{aligned} P_{\rm S} = {} & \frac{g^2}{\pi} \exp\left[(g^2 - 1) \left(|\alpha_0|^2 - \frac{\alpha_c^2}{g^2} \right) \right] \\ & \iint\limits_{|\alpha| < \frac{\alpha_c}{g}} \exp\left(- |\alpha - g\alpha_0|^2 \right) {\rm d}^2\alpha \\ & + \frac{g^2}{\pi} \iint\limits_{|\alpha| \geq \frac{\alpha_c}{g}} \exp\left(- |g\alpha - \alpha_0|^2 \right) {\rm d}^2\alpha \ . \end{aligned} \tag{6.17}$$

The key features of our hybrid linear amplifier are threefold: first, the output is a free-propagating amplified physical state; second, the setup only depends on linear optics; third, the two cascading gains can be tuned independently and our cut-off is fully adjustable. This introduces more flexibility in optimizing the success rate while preserving high fidelity with an ideal implementation of NLA. It also largely extends the operating region of the amplifier by alleviating the constraints of previous physical implementations where amplification is confined to small input amplitudes and low amplification gains.

Figure 6.3 illustrates the operational degrees of freedom of our noise-reduced linear amplifier. The amount of noise reduction depends on both the product and the ratio of $g_{\rm NLA}$ and $g_{\rm DLA}$, which correspond to, respectively, the values of the effective gain $g_{\rm eff}$

and the transmittivity T' in Fig. 6.2 (d). Intuitively, for a fixed effective gain g_{eff}, a higher signal transfer coefficient $\mathcal{T}_s$ becomes more pronounced with a larger g_{NLA}, since the associated noise determined by g_{DLA} decreases while the input amplitude undergoes the same amount of amplification. Hence, under the same effective gain, a higher T' would always lead to a larger signal transfer coefficient.

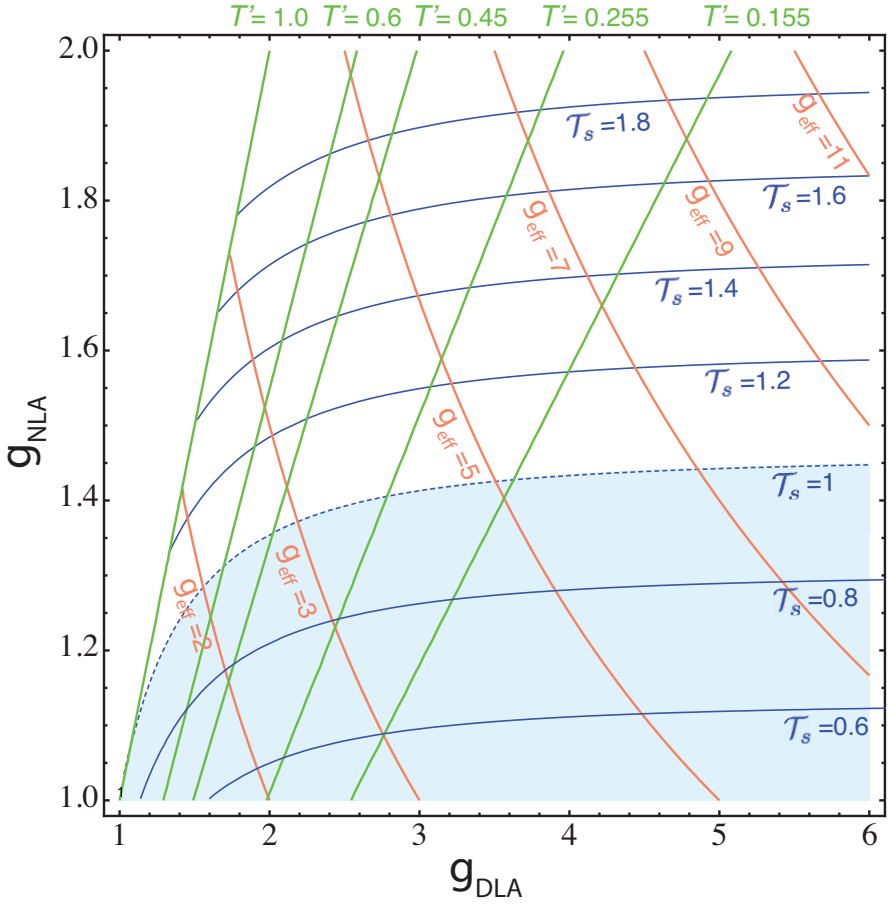

Figure 6.3: Tunability of the amplifier. Signal transfer coefficient (blue contours), various effective gains (red contours), and T' (green lines) as the function of g_{NLA} and g_{DLA}. The blue-dotted line denotes the amplification process where the input SNR is preserved, while the enclosed shaded area refers to the region where additional noise is introduced. We note that, without a sufficiently high NLA gain, increasing g_{DLA} alone would not suffice to approach the noise-reduced amplification.

We note that there is an ultimate limit of our current setup embodied in Eq. (6.10). Because $T' < 1$, g_{NLA} must be smaller than g_{DLA}. Recall that the signal transfer coefficient takes the form

$$\begin{aligned}\mathcal{T}_s &= \frac{g_{\text{eff}}^2}{2g_{\text{DLA}}^2 - 1} \\ &= \frac{g_{\text{eff}}^2}{\frac{2g_{\text{DLA}}}{g_{\text{NLA}}} g_{\text{DLA}} g_{\text{NLA}} - 1}\end{aligned} \tag{6.18}$$

Together with the condition that $g_{\mathrm{DLA}} > 1$, Eq. (6.10) poses a limit on the signal transfer as

$$\mathcal{T}_s < \frac{g_{\mathrm{eff}}^2}{2g_{\mathrm{eff}} - 1}. \tag{6.19}$$

Nonetheless, as shown in Fig. 6.3, an arbitrarily high $\mathcal{T}_s > 1$ is attainable using the current setup by applying well-tailored T' and g_{eff}.

6.3 Quantum Enhancement of Signal-to-Noise Ratios

In this section, the hybrid linear amplifier is employed to resolve the signal-to-noise ratio degradation problem that is unavoidable in any deterministic phase-insensitive linear amplification. We report, for the first time, a quantum enhancement of signal-to-noise ratio of an arbitrary incoming coherent state using only linear optics.

6.3.1 Experimental Setup

The light source for this experiment is an Nd:YAG laser producing continuous wave single mode light at 1064 nm. The coherent state at a sideband frequency is generated by sending modulation signals at 4MHz to a pair of electro-optical modulators (EOMs) on the signal beam. The laser was found to be shot-noise-limited at this frequency and the amplitudes of the modulation signals determine the complex amplitude of the coherent state. To amplify the coherent state, we first inject the input state into a beamsplitter with transmissivity of T' where it is split to the transmitted and reflected modes. A dual homodyne measurement is then performed on the reflected mode and the measurement outcomes are divided into two parts. The fist part is used to extract the 4 MHz modulation and to reveal the term $|\alpha_m|$ in Eq. (6.11) which is used to provide the heralding signal. To this end, the outcome is demodulated by mixing it with an electronic local oscillator, before being low pass filtered at 100 kHz and oversampled on a 12 bit analog-to-digital converter at 625 kSa per second. Once the quadrature amplitude of the input subject to the in-line dual homodyne is obtained, denoted by $|\alpha_m|$, it is utilized to compute $p(\alpha_m)$ in Eq. (6.11) which is then compared with a random number picked up from a uniform distribution between 0 and 1. Because the data acquisition for the in-line dual homodyne and the final verifying homodyne are paired up shot-by-shot, whenever one obtains an $|\alpha_m|$ that results in a $p(\alpha_m)$ smaller than the corresponding random number, the corresponding final homodyne data point is discarded; otherwise, the final homodyne measurement outcome is kept.

Second, the outcomes of the dual homodyne measurement are employed to accomplish the feed-forwarding. They are amplified electronically with a gain $g_{\mathrm{ele}}{=}g'_{\mathrm{DLA}}/g'_{\mathrm{NLA}}$ and fed into a pair of EOMs modulating a bright auxiliary beam. This intense beam is then coupled in phase with the transmitted signal beam by an asymmetric beam splitter of transmissivity 98% to realize the displacement operation.

The combined beam is then characterized by a homodyne measurement, locked successively to amplitude and phase quadratures. The homodyne measurement goes through the same signal processing and at least 5×10^7 data points are acquired. To ensure optical fields are combined either in phase or in quadrature, the relative phase locking technique discussed in Sec. 3.4.1 is employed. More specifically, an amplitude modulation at 30 MHz is used to for locking the Heterodyne phase station and the homodyne to phase quadrature, while a phase modulation at 21.4 MHz is utilized for locking the Heterodyne amplitude station and the homodyne to amplitude quadrature.

6.3.2 Theoretical Model Involving Error Analysis

Before we move on to present the experimental results, we explain first how we correct $\mathcal{T}_s$ in Eq. (6.16) by taking into account of experimental imperfections, and how we write $\mathcal{T}_s$ as a function of the effective gain g_{eff} to obtain the theoretical results depicted in the following sections. This helps us to correctly examine the performance of our amplifier.

First we express the output mean and variance of the quadrature amplitudes in terms of effective parameters that take experimental imperfections into account:

$$\bar{x}_{\text{out}} = \left(\sqrt{\frac{1-T'}{2}} g_{\text{fil}}^2 \eta_{\text{ff}} g_{\text{ele}} + \sqrt{T'} \right) \bar{x}_{\text{in}} \tag{6.20}$$

$$\sigma^2_{x_{\text{out}}} = 1 + (g_{\text{fil}} g_{\text{ele}})^2 \, . \tag{6.21}$$

For brevity, we express here the quadrature mean $\langle \hat{X}_\pm \rangle$ and variance $\langle \delta(\hat{X}_\pm)^2 \rangle$, respectively, as $\bar{x}$ and σ_x^2, and the subscript in/out denotes the input/output mode. In contrast to Eq. (6.12), the effective parameter g_{fil} indicates the amplification realized by applying the filter function (Eq. (6.11)) alone, which amplifies both the mean and variance of the output of the dual homodyne by $(g'_{\text{NLA}})^2$. The rescaling factor $1/g'_{\text{NLA}}$ associated with noise renormalization is combined with g'_{DLA}, composing the electronic gain g_{ele}, i.e. $g_{\text{ele}}{=}g'_{\text{DLA}}/g'_{\text{NLA}}$. And η_{ff} here summarizes the net effect of losses induced in the dual homodyne detection (including mode matching and photodiode efficiency) and the imperfect tuning of g_{ele}. Therefore, the signal transfer coefficient that assumes infinite cut-off and takes into account of all experimental imperfections can be re-written as

$$\begin{aligned} \mathcal{T}_s &= \frac{\bar{x}^2_{\text{out}} \sigma^2_{x_{\text{in}}}}{\sigma^2_{x_{\text{out}}} \bar{x}^2_{\text{in}}} \\ &= \frac{(\sqrt{\frac{(1-T')}{2}} g_{\text{fil}}^2 \eta_{\text{ff}} g_{\text{ele}} + \sqrt{T'})^2}{1 + (g_{\text{fil}} g_{\text{ele}})^2} \, . \end{aligned} \tag{6.22}$$

In order to express $\mathcal{T}_s$ as a function of g_{eff}, we need to determine the values for the effective parameters g_{ele} and η_{ff}. For each experimental run, we first infer the in-loop electronic gain g_{ele} from the experimental values of $\mathcal{T}_s$, $\bar{x}_{\text{in}}$, $\bar{x}_{\text{out}}$, and $\sigma^2_{x_{\text{out}}}$ when no post-

selection is implemented (i.e $g_{\text{fil}=1}$), which gives

$$\mathcal{T}_s|_{g_{\text{fil}}=1} = \frac{\bar{x}^2_{\text{out}}\sigma^2_{x_{\text{out}}}}{\bar{x}^2_{\text{in}}(1+g^2_{\text{ele}})} \ . \tag{6.23}$$

From Eq. (6.23), we can thus solve for g_{ele}.

We then estimate the overall inefficiency η_{ff} based on the prediction of the output mean. By setting $g_{\text{fil}}=1$ in Eq. (6.20), we obtain

$$(\sqrt{\frac{(1-T')}{2}}\eta_{\text{ff}}g_{\text{ele}} + \sqrt{T'})\bar{x}_{\text{in}}=\bar{x}_{\text{out}} \ . \tag{6.24}$$

Substituting g_{ele} for the value obtained from Eq.(6.23) and T' which is fixed when undertaking the experiment, the effective parameter η_{ff} is hence determined.

Since $\bar{x}_{\text{out}}/\bar{x}_{\text{in}}=g_{\text{eff}}$, from Eq. (6.20), g_{fil} can be written as the function of g_{eff}

$$(g_{\text{fil}})^2 = \frac{\sqrt{2}(g_{\text{eff}} - \sqrt{T'})}{g_{\text{ele}}\sqrt{\eta_{\text{ff}}(1-T')}} \ . \tag{6.25}$$

Substituting Eq. (6.25) into Eq. (6.22), the signal transfer coefficient therefore can be derived purely as a function of g_{eff}.

In practice, to avoid an overestimation of $\mathcal{T}_s$, for all experimental runs, the mean and variance of the input and output states are corrected for the homodyne efficiency, which is typically around 85%, including the photodiode quantum efficiency and the mode-matching visibility.

Error bars for signal transfer coefficients are calculated based on the statistics of the first and second moments of $X_{\pm}$. Writing $\mathcal{T}_s$ as

$$\mathcal{T}_s = \frac{\bar{x}^2_{\text{out}}}{\sigma^2_{x_{\text{out}}}} \times \frac{\sigma^2_{x_{\text{in}}}}{\bar{x}^2_{\text{in}}} \ , \tag{6.26}$$

its uncertainty can be estimated as

$$\begin{aligned}\text{Var}(\mathcal{T}_s) = &\left(\frac{\partial \mathcal{T}_s}{\partial \bar{x}_{\text{out}}}\right)^2 \text{Var}(\bar{x}_{\text{out}}) + \left(\frac{\partial \mathcal{T}_s}{\partial \sigma^2_{x_{\text{out}}}}\right)^2 \text{Var}(\sigma^2_{x_{\text{out}}}) \\ &+ \left(\frac{\partial \mathcal{T}_s}{\partial \bar{x}_{\text{in}}}\right)^2 \text{Var}(\bar{x}_{\text{in}}) + \left(\frac{\partial \mathcal{T}_s}{\partial \sigma^2_{x_{\text{in}}}}\right)^2 \text{Var}(\sigma^2_{x_{\text{in}}}) \ ,\end{aligned} \tag{6.27}$$

where $\text{Var}(x)$ refers to the variance of x. The partial derivatives included can be expressed straightforwardly as functions of the measured means and variances.

6.3.3 Linearity of the Amplifier

Figure 6.4 shows the performance of our linear amplifier for input coherent states with different complex amplitudes $|(x+ip)/2\rangle$. As illustrated in Fig. 6.4 (a), we demonstrate the phase-preserving property of the amplifier, and observe symmetric noise spectrum

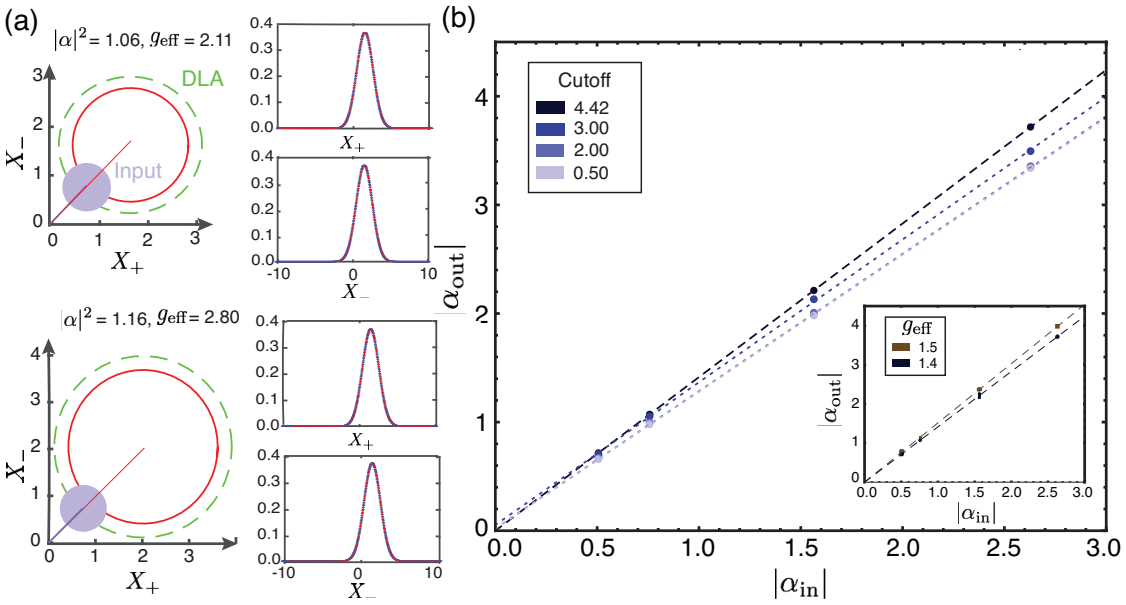

Figure 6.4: Linearity of the amplifier. (a) Amplification for coherent states with different amplitudes. Left panels: noise contours (one standard deviation width) of the amplified states, depicted in red. Right panels: normalized probability distribution for amplitude and phase quadratures of the output states. (b) Output magnitudes vs input magnitudes as we reduce the cut-off whilst maintaining the values of $g_{\text{NLA}'}$ and $g_{\text{DLA}'}$. Inset: Output magnitudes vs input magnitudes with cut-off being $\alpha_c = 4.42$ at different effective gains.

of amplitude and phase quadratures. These results emerge from the linearity and phase invariance of the present setup, as is also clearly demonstrated in Fig. 6.4 (b). In particular, under the same T' (0.6), by selecting input states with different complex amplitudes $(x, p) = (-0.71, 0.72), (-0.01, -1.51), (2.23, 2.19), (5.26, -0.02)$, we plot the output magnitudes against the input magnitudes as we vary the cut-off values, or alternatively as we vary the effective gains. The amplifier behaves linearly in either circumstance, thus verifying the independence of the amplification on the input states.

Apart from the relationship between $|\alpha_{\text{out}}|$ and $|\alpha_{\text{in}}|$ shown in Fig. 6.4, we also notice that as we reduce the cut-off, the output states start to exhibit non-uniform noise between the in-phase and out-of-phase fluctuations. More specifically, as the cut-off is decreased from 4.42 to 0.50, we observe the output noise $[\langle(\delta\hat{X}_+)^2\rangle_{\text{out}}, \langle(\delta\hat{X}_-)^2\rangle_{\text{out}}]$ reduces, respectively, from $[1.83, 1.83]$ to $[1.59, 1.70]$ for input $(x, p) = (-0.01, -1.51)$, and from $[1.87, 1.86]$ to $[1.70, 1.58]$ for input $(x, p) = (5.26, -0.02)$. In these cases, the cut-off with respect to the effective gain no longer suffices to preserve the Gaussianity, i.e. a Gaussian probability distribution, of the output state and the amplified states start to squash along the radial direction [89]. This produces mixed, non-Gaussian states. Nevertheless, the amplification remains phase-insensitive due to the fact that it is always the variance of the quadrature along the radial direction that becomes classically "squeezed", whilst that of the orthogonal quadrature inclines to be anti-squeezed. In-

terestingly, it is worth emphasizing that, even in this operating region, the amplifier still works linearly regardless of the insufficient cut-off (refer to the light blue line in Fig. 6.4 (b)). This special property would be of great benefit for coherent states discrimination. For example, we consider multiple weak coherent states, in a quadrature phase-shift-keyed format [35], as inputs of our linear amplifier. Regardless of the phases of the input states, the amplifier increases their complex amplitudes consistently and, meanwhile, suppresses the added noise along the radial direction. The amplification works conditionally, whereas as long as a heralding signal reveals that the amplifications succeed for all input states, the distinguishability of these states would be enhanced.

6.3.4 Quadrature Independence and the Success Probability

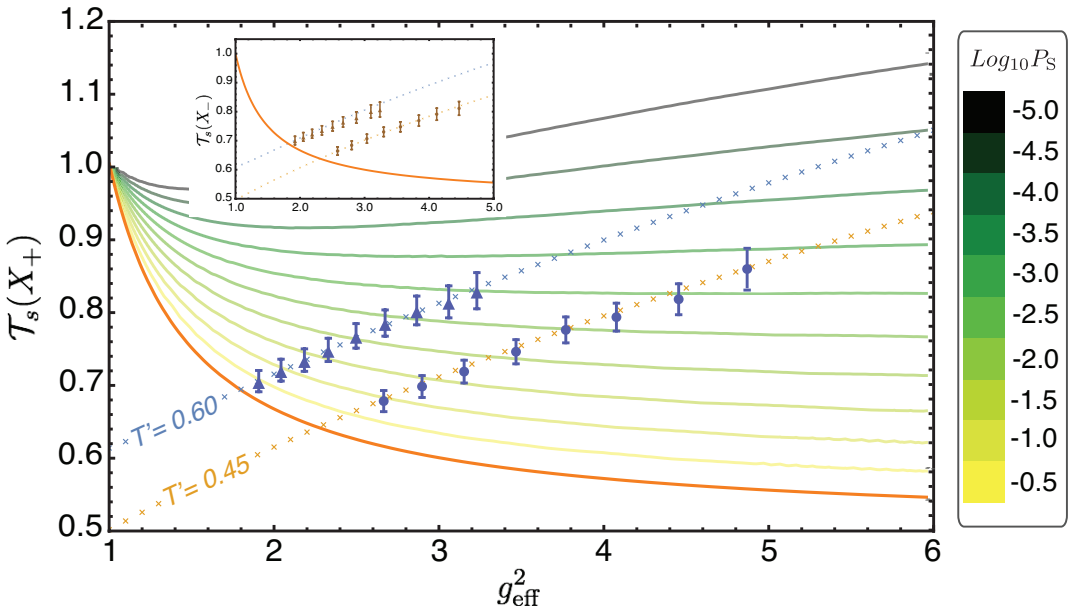

Figure 6.5: Amplifier performance: noise properties and contour plot of the success probability P_{S} in logarithmic scale as a function of $\mathcal{T}_s$ and g_{eff}. The success probability decreases as we increase the effective gain. The signal transfer coefficient for amplitude quadrature (blue symbols) is also superimposed as a function of g^2_{eff} for varying T': 0.6, 0.45. The theoretical prediction, assuming infinite cut-off, is depicted in crosses. It is clearly shown that the experimental $\mathcal{T}_s$ increases in compliance with the prediction, demonstrating that the cut-off ($\alpha_c = 4.3$) selected is sufficient and no over- or under-estimation of $\mathcal{T}_s$ appears. For the sake of comparison, the best achievable $\mathcal{T}_s$ of an optimal deterministic linear amplifier (also termed as the quantum noise limit) is shown in orange solid line. This illustrates that our amplifier surpasses the quantum limit for a phase-insensitive amplifier, and this superiority becomes more distinguished as we increase the g_{eff}. Inset: the experimental data superimposed with its theoretical prediction for phase quadrature.

Figure 6.5 demonstrates the tunability and versatility of our amplifier. The signal transfer coefficients of the amplitude and phase quadratures, superimposed by the success probability, are plotted as a function of increasing effective gains. We examine an input coherent state with complex amplitude of $(x, p) = (1.51, 1.54)$ for all plots. Two

different transmissions, $T' = 0.60$, and 0.45, are picked to test the amplifier in different settings.

In accordance with Fig. 6.3, data points with the same T' illustrate evidently the improvement in $\mathcal{T}_s$ as g_{eff} increases, corresponding to moving along the green lines in Fig. 6.3. Alternatively, when keeping $\mathcal{T}_s$ constant, lowering T' results in a smaller success probability, which also coincides with Fig. 6.3, because this decrease of the success probability results from the increase of g_{NLA}.

We note that all $\mathcal{T}_s$, for both amplitude and phase quadratures, exceed the quantum limit regardless of the values of T', among which the maximum achieved $\mathcal{T}_s$ are 0.830 ± 0.025 and 0.860 ± 0.024 for $T' = 0.6$, and $T' = 0.45$, respectively. These results significantly surpass the maximum allowable signal transfer in the deterministic regime (c.f. Eq. (6.15)) by around 10 and 12 standard deviations, respectively. All the observed values of $\mathcal{T}_s$ show good agreement with the theoretical model assuming infinite cut-off and taking into account the experimental imperfections (see Supplementary material 3). The corresponding success probability ranges between 10^{-3} and 0.3, rendering the amplifier still relatively practicable. Slight discrepancies are observed between X_+ and X_- owing to the different losses experienced by the two quadratures during feed-forwarding, as illustrated in Fig 6.6. Small deviations of the experimental data from the prediction are attributed to other in-line electronic noise.

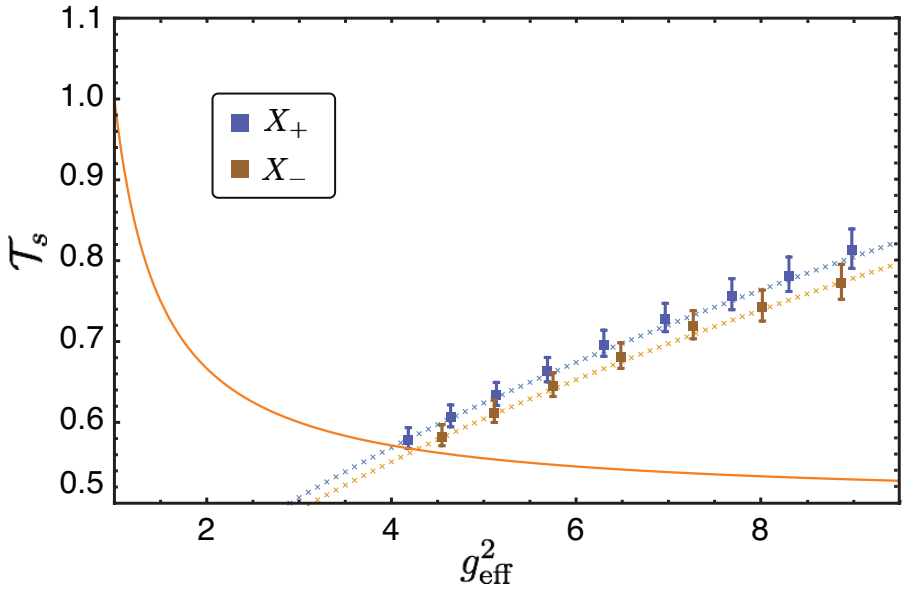

Figure 6.6: Gain dependence of the signal transfer coefficient for coherent input state with $|\alpha|^2 = 2.16$ and $T' = 0.3$.

6.3.5 High Signal Transfer Coefficient

In Fig. 6.7, we summarize our experimental results when our amplifier is operating in the large gain domain for an input state (x, p)=$(0, 1.01)$($|\alpha|$=0.5) and $T' = 0.155$. As is

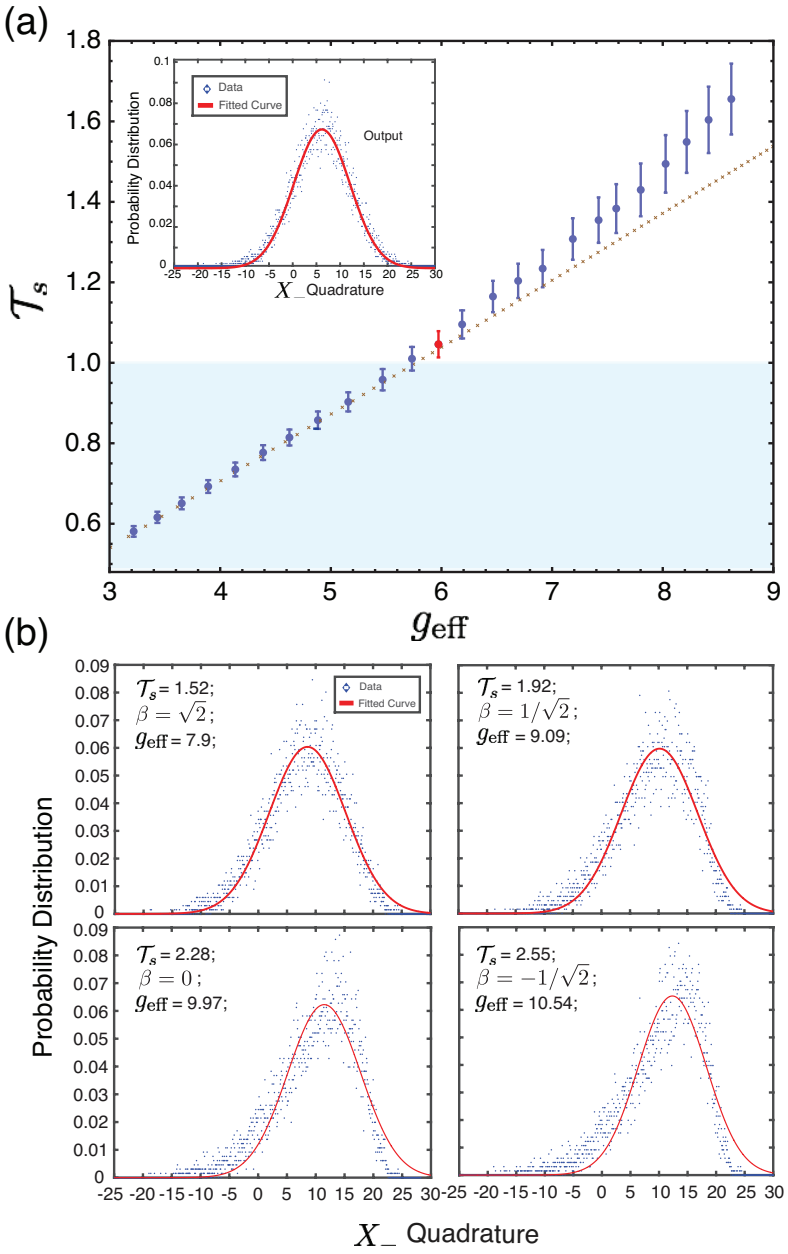

Figure 6.7: Signal transfer coefficients in the large gain regime. (a) $\mathcal{T}_s$ exceeding 1 with increasing g_{eff} for $\alpha_c = 4.5$ and a coherent state amplitude of $|\alpha| = 0.5$. The experimental $\mathcal{T}_s$ shows good agreement with the theory plot (in crosses) until around $g_{\text{eff}} = 6.5$ where the data points start to depart, thereby indicating that the cut-off no long suffices to maintain the output Gaussianity. Inset: probability distribution of the amplified state labeled in red. (b) Probability distributions of the phase quadrature of the amplified state with cut-offs given by (6.28). Data points are the post-selected ensemble out from 2.7×10^9 homodyne measurements while the red curves indicate the corresponding best-fitted Gaussian distributions.

shown in Fig. 6.7 (a), a higher $\mathcal{T}_s$ is obtained at the expense of a lower success probability. We see that the increasing of $\mathcal{T}_s$ as a function of g_{eff} coincides with the theoretical model based on an infinite cut-off (see 6.3.2), indicating that the cut-off employed is suf-

ficient to encompass the amplified distribution and thus exclude any distortion of the output. In this high-fidelity operating region, a $\mathcal{T}_s$ larger than 1 (specifically, 1.10 ± 0.04) is observed, thus verifying a clear fulfillment of the noise-reduced amplification. As g_{eff} keeps increasing, a wider discrepancy appears between the experimental value of $\mathcal{T}_s$ and its theoretical prediction, as the result of an insufficient cut-off. In [234], it was shown that the Gaussian profile of the output state of a measurement-based NLA depends on the amplitude of the input state, the NLA gain, and the cut-off in the filter function Eq. (6.11). If Gaussian-output statistics are desired, the cut-off value can be adjusted according to g'_{NLA}, the target T_s, and the maximum input size of the ensemble. To be more explicit, it was proposed in [234] that,

$$\alpha_c = (g'_{\text{NLA}})^2 |\alpha_{\text{m}}| + \beta\sqrt{0.5} g'_{\text{NLA}}. \tag{6.28}$$

The parameter β quantifies how well the cut-off circle embraces the distribution of the amplified state. We note that a sufficient amount of data points should be retained to characterize the output properly.

To complete the investigation of our setup, we also explore the relationship between $\mathcal{T}_s$ and the output Gaussianity while keeping the success probability unchanged (around 10^{-6}), as shown in Fig. 6.7 (b). In this case, as we relax the requirement for the output Gaussianity, it is possible to enjoy a higher effective gain and therefore achieve a considerably larger $\mathcal{T}_s$ without decreasing the success probability. We experimentally obtained an signal transfer of $\mathcal{T}_s$=2.55 ± 0.076 from input to output with an amplification gain of 10.54.

6.4 Quantum Cloning

6.4.1 Conceptural Picture

We extend the noise-reduced linear amplifier to construct a quantum cloning machine that is able to surmount the no-cloning limit imposed by the Heisenberg uncertainty principle and the linearity of quantum mechanics. The underlying concept here is similar: although it is impossible to perfectly duplicate an unknown quantum state deterministically, as is stated in the "no-cloning theorem", this predicament can be alleviated by renouncing determinism. It was proved that probabilistic exact cloning is possible if the quantum states to be cloned are chosen from a discrete, linearly independent set [235, 236, 85, 237]. On the other hand, if the input states are linearly dependent, non-deterministic cloning is also conceivable with fidelity arbitrarily close to unity [22]. In the current work, we propose a new scheme that allows high-fidelity probabilistic quantum cloning for an arbitrary coherent input state. Adopting the *amplify-and-split* approach in Ref. [221], one can first amplify the input state using our noise-reduced linear amplifier presented in Sec. 6.3 and then split the amplified signal equally into multiple copies, as illustrated in Fig. 6.8. Due to the fact that less noise is incurred in the

amplification stage, high fidelity is achievable after splitting.

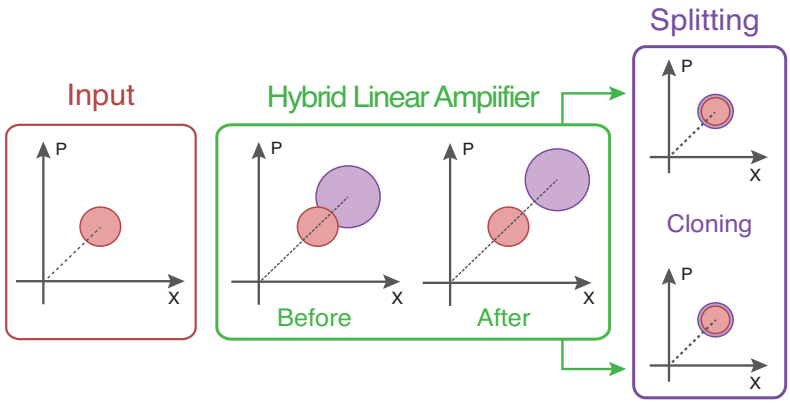

Figure 6.8: Schematic of the heralded quantum cloner in phase space. The input state, after being amplified through the hybrid linear amplifier, is subsequently split into multiple copies, which constitute the output of the quantum cloning machine.

In order to characterize the performance of our heralded cloning machine (HCM) with respect to the no-cloning limit, we calculate the output fidelity $F = \langle\alpha|\rho_i|\alpha\rangle$ which quantifies the overlap between the input state $|\alpha\rangle$ and the i-th clone ρ_i. It can be derived that fidelity of our HCM is given by [238]:

$$F(N) = \frac{1}{1+(g_{\mathrm{DLA}}^2-1)/N}\exp\left[-\frac{(g-1)^2|\alpha_{\mathrm{i}}|^2}{1+(g_{\mathrm{DLA}}^2-1)/N}\right], \tag{6.29}$$

where the number of clones, N, determines the overall effective gain in the following way: $g_{\mathrm{eff}} = g_{\mathrm{DLA}}g_{\mathrm{NLA}} = \sqrt{N}$. This is enforced by the unity-gain condition that requires the quadrature amplitude of each clone to be identical to that of the input. The unity-gain condition avoids the overestimation arose when the amplitude of the input state is small [238]. Once the unity-gain condition is satisfied, the fidelity shown in Eq. (6.29) takes a more succinct form:

$$F(N) = \frac{1}{1+(g_{\mathrm{DLA}}^2-1)/N}, \tag{6.30}$$

Notice that although the multiplication of the two distinct control knobs, *i.e.* g_{NLA} and g_{DLA} is fixed, the flexibility of our HCM resides in the tunability of T' in Fig. 6.2 (d), which stands for the the ratio between the two gains (see Eq. (6.10)). Provided a target cloning number N *a priori*, higher cloning fidelity is always achievable by increasing T', at the expense of a lower success probability.

6.4.2 Experimental Results

The experimental results are summarized in Fig. 6.9 (a), where the input coherent state under interrogation has an amplitude of $|\alpha| \simeq 0.5$, and the average fidelities of the clones

for $N = 2, 3, 4$ and 5 are 0.695 ± 0.002, 0.634 ± 0.012, 0.600 ± 0.009 and 0.618 ± 0.008, respectively. All exprimental results not only significantly exceed the achievable fidelity of a classical cloner $(1/2)$, but also apparently surpass the corresponding quantum no-cloning limit given by [239]

$$F_{M,N} = \frac{MN}{MN + N - M}. \tag{6.31}$$

Here M indicates how many copies of the input state is injected into the cloner, while N refers to the number of final clones. Consider a single copy of coherent input, this no-cloning limit reduces to $F_M = M/(2M - 1)$. In particular, we show in Fig. 6.9 (a) that by further increasing the NLA gain, three clones can be produced with fidelity of each clone (on average, $F = 0.684 \pm 0.009$) even surpassing F_2. This implies that given only fidelity, unlike the deterministic unity-gain cloner, it is impossible for a receiver with only two clones to determine whether the clones originate from a two-clone or three-clone probabilistic protocol. We emphasize that, for all experimental runs, the cloner always operates under the unity-gain condition such that any overestimation of the resultant fidelity is avoided.

Figure 6.9 (b) plots the theoretical prediction of fidelity as a function of success probability superimposed with experimental data. We find that all our results lie well within the expected fidelities, with the probability of success ranging between 5% and 15%. Remarkably, by keeping 5% of the data points, the average cloning fidelity for $N = 5$ can be enhanced by more than 15%, and hence exceeding the no-cloning limit F_5 by 11.2%.

6.5 Conclusions and Summary

In summary, we demonstrate an enhancement of signal-to-noise ratio for arbitrary coherent states with a noise-reduced linear amplifier that profitably combines a measurement-based noiseless linear amplifier and a determnistic linear amplifier. We also investigate the possibility of applying our amplifier to an ensemble of coherent states. Furthermore, we propose a heralded quantum cloning machine based on the hybrid noise-reduced linear amplifier to circumvent the cloning fidelity limit imposed by the Heisenberg uncertainty principle. Up to five clones are generated for an arbitrarily chosen input coherent state with fidelity of each clone clearly exceeding the corresponding no-cloning limit.

The hybrid nature of the amplifier retains the flexible and operational characteristics of the measurement-based NLA, which, as opposed to the physical implementations, evades the demand of nonclassical light sources and the restriction to small input states and low amplification gains. It also preserves the free-propagating amplified states and thus circumvents the drawback of a pure measurement-based setup whose output can only be classical statistics. Even though the amplifier works conditionally, a heralding signal is generated for successful events. We circumvent the additional noise associated

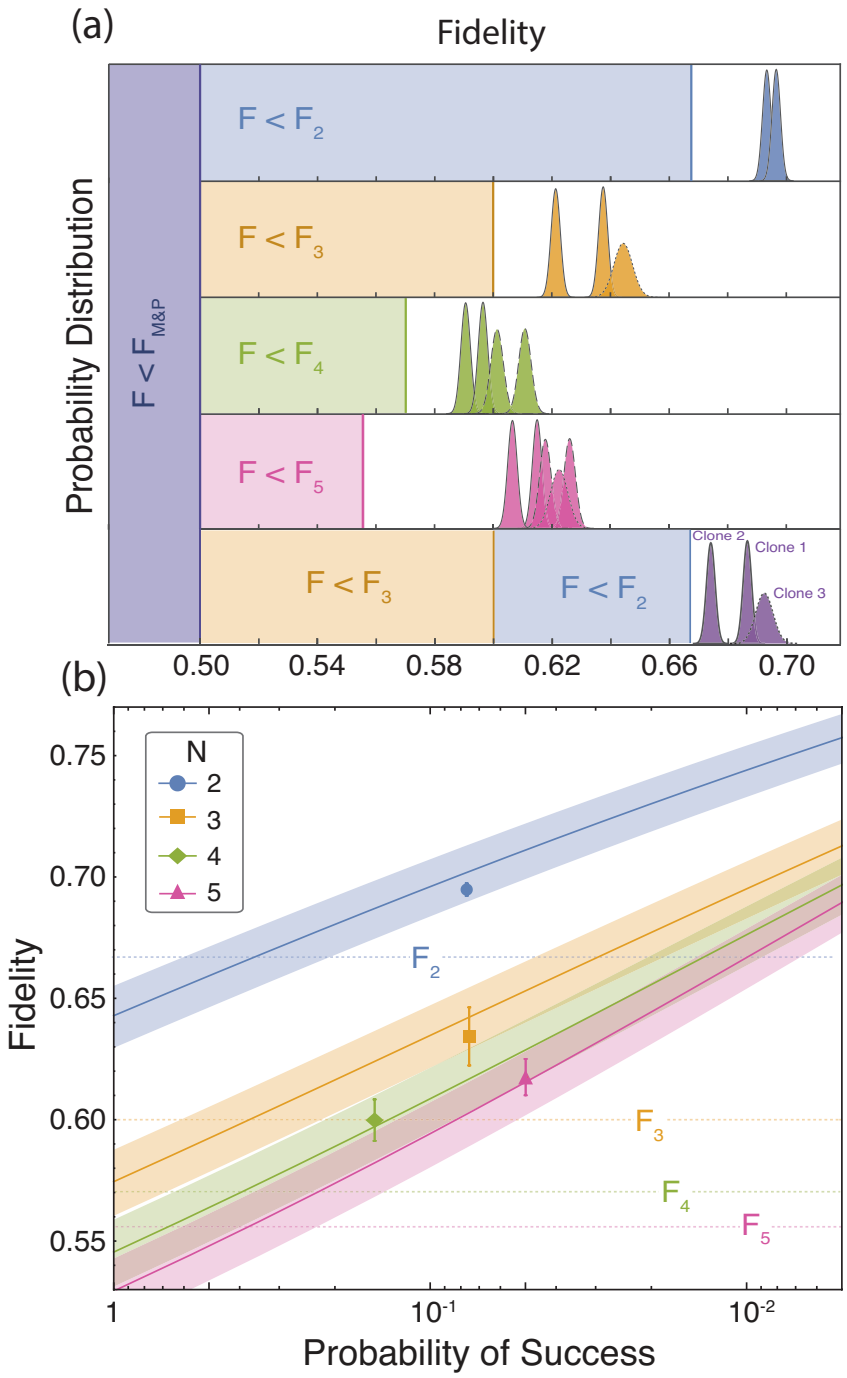

Figure 6.9: Experimental results. (a) Fidelity of N clones beyond the no-cloning limit. For $N > 2$, only two of the output clones are directly measured (solid lines). The remaining $N - 2$ clones' fidelity distributions are obtained either from rescaled data of different runs (dashed) or estimation of the remaining intensities (dotted). A sample size of 5×10^7 data points is used for all N. The spreads in fidelity distributions are predominately due to imperfect splitting.(b) Fidelity as a function of heralding success probability for different N. Theoretical simulations (solid lines) are superimposed with the experimental points (symbols) and the no-cloning limits F_N (dotted lines). Error bars and the shaded regions represent the experimental and theoretical 1 s.d..

with any phase-insensitive deterministic optical amplifier with success probability ranging from 0.1% to 30%. We further demonstrate the superiority of our amplifier over an ideal phase-sensitive amplifier in the amplified quadrature by observing a signal transfer coefficient $\mathcal{T}_s$ larger than 1, clearly showing that the amplification is noise-reduced. We show that higher $\mathcal{T}_s$ – more specifically, $\mathcal{T}_s = 2.56$ with $g_{\text{eff}} = 10.54$ – is attainable if one is willing to accept a lower success probability (around 10^{-6}) or instead to compromise slightly the output Gaussianity. Interestingly, we also notice that there exists an operating region where the amplifier works linearly, regardless of the relatively small distortion of the output. This would provide a useful coherent state discrimination machine.

Owing to the composability, tunability, and ease of implementation of our amplifier, it provides several interesting avenues for future research in loss-sensitive quantum information protocols. First, the access to the two variable knobs - deterministic and probabilistic - provides a spectrum of effective gain and success probability. For protocols with high SNR demands, such as long distance quantum communication [240], the signal transfer coefficient can be enhanced by intensifying the probabilistic gain. When signal transfer speed is the critical requirement, the deterministic amplification can play the leading role while maintaining the same effective gain. An interesting extension of this work would be to study the optimality of these gains for a given channel loss and excess noise in various quantum communication protocols, including other quantum cloning schemes [241, 242, 243, 244, 245, 246], quantum key distribution [77], entanglement distillation [69, 74, 81] and quantum repeaters [84, 83]. Secondly, by having a priori information about the input alphabet, the amplification cut-off value can be easily tailored to achieve maximum SNR gain for a given success probability. Such is the case for a phase covariant input with fixed amplitude [75] or an input distribution with finite energy [247]. Furthermore, the preservation of the quantum state over the heralded channel opens up the possibility of overcoming deterministic bounds of various feed-forward-based protocols such as quantum teleportation [248, 249] upon suitable modification of our scheme. Lastly, since our scheme only relies upon linear optics and feed-forwarding, it is wavelength agnostic. Hence, it has the potential to improve the transmission distance of optical communication at telecom wavelengths, in particular to enhance the signal transfer coefficient per distance when applied in conjunction with an ultra-low-loss fiber [250].

Chapter 7

High-fidelity Squeezing Gate for CV Quantum Light Fields: Theory

7.1 Overview

Squeezing has been shown to be a crucial element in the Gaussian toolbox of quantum information processing. Achieving pure and high-level of squeezing, however, still remains a resource intensive task. In particular, an universal squeezing gate, one that can process arbitrary input states, presents an added level of complexity and hence a formidable experimental challenge. The conventional way to resolve this problem is to build a squeezing gate based on measurement and feed-forward, akin to the principle of the measurement-based quantum computation. An ancillary squeezed vacuum is used to drive the universal squeezing gate. However, the fidelity of this conventional approach is ultimately limited by the magnitude of the squeezed ancilla, and unit fidelity is in principle unattainable for any target squeezing levels. Here we circumvent this limit by constructing a heralded squeezing gate that employs the post-selection filter elucidated in chapter 4. A significantly higher fidelity is obtainable compared to a conventional squeezing gate–when benchmarked on the same ancillary squeezing. More intriguingly, with a modest level of ancillary squeezing, our squeezing gate allows one to obtain unit fidelity for target up to the same squeezing level as the original ancilla.

The work presented in this chapter can be found in the following article:

• J. Zhao, K. Liu, J. Hao, M. Gu, J. Thompson, S. Assad, and P. K. Lam. *High-fidelity squeezing gate for continuous-variable quantum light fields.* (2018).

7.2 Introduction

Among all Gaussian operations, the squeezing operation constitutes the most resource intensive task. Whilst many effort has been devoted to the generation of squeezed vacuum with the recent benchmarking experiment reporting 15 dB of squeezing [96, 98, 186], the development of a universal squeezing gate that can act on arbitrary

input states has been lagging behind. Directly seeding a nonlinear crystal with an arbitrary light field presents a significant experimental complexity [251, 252, 253, 254], rendering the conventional approach for squeezed vacuum generation not applicable to engineer a universal squeezer. Nevertheless, the universality of such squeezer opens up new possibilities in quantum information [255, 256, 196, 257, 258, 259]. It serves as an essential building block for constructing a universal continuous-variable (CV) quantum computer [260]. It can also be utilized to realize a controlled-Z gate [261, 262, 263], a quantum non-demolition sum gate [264] and a resonator-induced phase gate [265]. Moreover, the application of a universal squeezing gate upon non-Gaussian states holds great promise across a variety of quantum information tasks, such as slowing down decoherence of non-classical states [266], interconversion between single photon and Shrödinger cat state [251], and quantum state discrimination of coherent-state qubits [267].

To alleviate the experimental challenge, one can exploit an ancillary squeezed vacuum as a resource to drive a squeezing gate by means of measurement and feed-forward [268, 269, 270, 271, 272], akin to the underlying principle of measurement-based quantum computation. In this conventional diagram, the input state is first combined with a single-mode ancillary squeezed vacuum, where one of the outgoing modes is subject to a single-quadrature measurement of which the measurement outcome is fed-forward to the remaining mode to perform local displacement operations. Although the need to directly seed a nonlinear medium with arbitrary light fields is mitigated, the difficulty of this approach resides in the requirement of a highly squeezed ancilla in order to achieve a reasonable fidelity. The same problem is also confronted by the general CV measurement-based quantum computation, where the gate fidelity is intrinsically limited by the accessible squeezing in the pre-established cluster states [273, 274]. Unity fidelity is unachievable due to the in-principle finite squeezed sources irrespective of the target squeezing. As a result, this limitation impairs the concatenation of fundamental operations towards truly universal quantum computation.

In this work, we overcome this limit by constructing a heralded squeezing gate that relies on an inverse-Gaussian filter in the feed-forward loop. The ability to perform unconditioned operations is sacrificed in favour of a significant improvement in fidelity. We verify its operation by injecting several coherent states with different quadrature amplitudes. Compared to its deterministic counterpart having access to the same amount of squeezed source but no experimental imperfections, a significant improvement in fidelity is observed independent of the input amplitudes. This enhancement in fidelity is achievable by simply increasing the filter strength without reconfiguring the gate setup that would otherwise be required in the deterministic scheme. Moreover, the filter strength can be tailored to optimize the trade-off between fidelity and success probability. It is worthwhile to note that unity fidelity, although is impossible deterministically, can be approached via our scheme with sufficiently high filter strength. We report in particular a fidelity up to 0.985 ± 0.006 for a target squeezing of 2.3 dB, achieved with

success probability of 2.9×10^{-3} and a 6.0 dB squeezed ancilla. This result would be impossible for a deterministic gate subject to the same experimental imperfections, even if pure and infinitely squeezed resource was used. From experimental perspective, our scheme retains the advantages of CV quantum information approach, such as its ease of implementation, high detection efficiency, and its great compatibility with conventional information technology. Our squeezing gate in this regards offers a particularly attractive avenue towards fault-tolerant quantum computation and other squeezing-powered quantum information protocols, such as Gaussian quantum adaptation [275, 276] and protection of quantum states against decoherence [266].

7.3 Squeezing Gate and Fidelity

The universal squeezing gate performs a unitary operation $S(r_{\rm t}) = \exp\left[\frac{1}{2}(r_{\rm t}^* a^2 - r_{\rm t} a^{\dagger 2})\right]$, where a denotes the annihilation operator of the incident mode and $r_{\rm t}$ refers to the squeezing parameter that determines both the target squeezing strength and quadrature. When $r_{\rm t} > 0$, the amplitude quadrature $X = a + a^\dagger$ is attenuated such that $X_{\rm out} = X_{\rm in} e^{-r}$, while the phase quadrature $Y = i(a - a^\dagger)$ is amplified with $Y_{\rm out} = Y_{\rm in} e^{r}$. The operation thus suppresses the amplitude noise at the expense of amplifying the phase noise in compliance with the Heisenberg uncertainty principle.

To quantify the faithfulness of a squeezing gate, we calculate fidelity as our figure of merit that measures the overlap between the output state $\rho_{\rm out}$ and the ideal target state $\rho_{\rm t}{=}S(r_{\rm t})\rho_{in}S(r_{\rm t})^\dagger$, and is defined as $\mathcal{F}(\rho_{\rm out}, \rho_{\rm t}){=}\left[{\rm Tr}\left(\sqrt{\sqrt{\rho_{\rm t}}\rho_{\rm out}\sqrt{\rho_{\rm t}}}\right)\right]^2$ [277, 278]. Consider situations where the output squeezed state $\rho_{\rm out}(\bar{d}_{\rm out}, \mathbf{V}_{\rm out})$ and the target state $\rho_{\rm t}(\bar{d}_{\rm t}, \mathbf{V}_{\rm t})$ are single-mode Gaussian states, the fidelity between them can be simplified as a function of their corresponding covariance matrix $\mathbf{V}$ and the mean of the quadrature amplitudes $\bar{d} = (\bar{X}, \bar{Y})$ [35]:

$$\mathcal{F}(\rho_{\rm out}, \rho_{\rm t}) = \frac{2}{\sqrt{\Delta + \delta} - \sqrt{\delta}} \exp\left[-\frac{1}{2}\mathbf{d}^T(\mathbf{V}_{\rm out} + \mathbf{V}_{\rm t})^{-1}\mathbf{d}\right], \tag{7.1}$$

where $\Delta := \det(\mathbf{V}_{\rm out} + \mathbf{V}_{\rm t})$, $\delta := (\det\mathbf{V}_{\rm out} - 1)(\det\mathbf{V}_{\rm t} - 1)$, and $\mathbf{d} := \bar{d}_{\rm out} - \bar{d}_{\rm t}$. Expressing Eq. 7.1 in terms of mean and standard deviation of the quadrature amplitudes of the output and target states, we obtain

$$\begin{aligned} \mathcal{F} = & \frac{2}{\sqrt{\left(\sigma_{X_{\rm out}}^2 + e^{-2r_{\rm t}}\right)\left(\sigma_{Y_{\rm out}}^2 + e^{2r_{\rm t}}\right)}} \\ & \exp\left[-\frac{1}{2}\left(\frac{(\bar{X}_{\rm out} - e^{-r_{\rm t}}\bar{X}_{\rm in})^2}{\sigma_{X_{\rm out}}^2 + e^{-2r_{\rm t}}} + \frac{(\bar{Y}_{\rm out} - e^{r_{\rm t}}\bar{Y}_{\rm in})^2}{\sigma_{Y_{\rm out}}^2 + e^{2r_{\rm t}}}\right)\right]. \end{aligned} \tag{7.2}$$

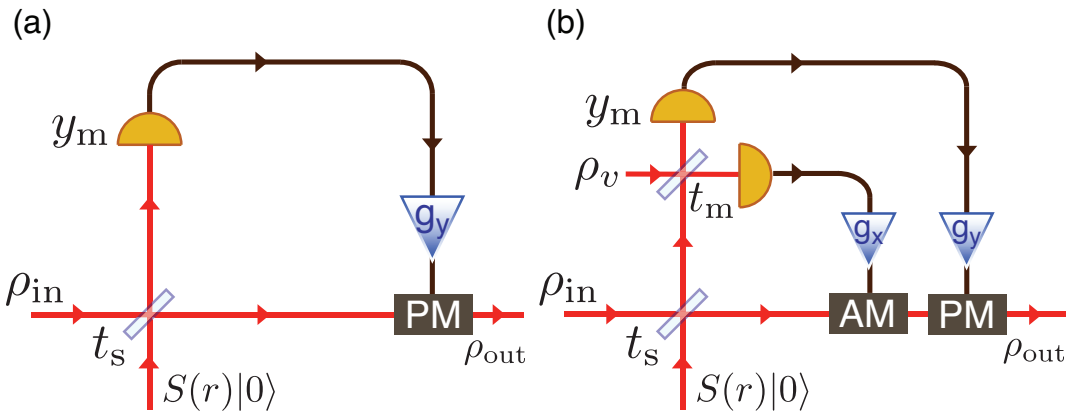

Figure 7.1: (a) Conceptual scheme of the conventional squeezing gate. (b) Conventional squeezing gate with dual-quadrature homodyne performed in the feed-forward loop. PM: electro-optic phase modulator. g_y: rescaling factor of the electronic signal.

Note that $\mathcal{F}$ becomes independent of the input state by fulfilling

$$\bar{X}_{\text{out}} = e^{-r_t} \bar{X}_{\text{in}}, \tag{7.3}$$

$$\bar{Y}_{\text{out}} = e^{r_t} \bar{Y}_{\text{in}}, \tag{7.4}$$

which is known as the *unity-gain condition*. The fidelity in Eq. 7.2 under the unity-gain condition specializes to

$$\mathcal{F} = \frac{2}{\sqrt{(\sigma^2_{X_{\text{out}}} + e^{-2r_t})(\sigma^2_{Y_{\text{out}}} + e^{2r_t})}}. \tag{7.5}$$

To guarantee the squeezing gate is input-independent and hence universal, it is crucial to operate the squeezing gate under this condition. Equations (7.2) and (7.5) will be used for characterizing the performance of both the deterministic squeezing gate and our heralded squeezing gate in the following sections.

7.4 Deterministic Squeezing Gate Scheme

Figure 7.1 (a) sketches the conventional implementation of a squeezing gate (SG) based on measurement and feed-forward [279, 269]. This SG scheme represents a CV analogue of the measurement-induced nonlinearity that was previously utilized to realize a controlled-NOT gate in DV quantum computation. Consider an input mode, denoted by its quadrature amplitudes $(X_{\text{in}}, Y_{\text{in}})$, that is combined with an amplitude-squeezed ancillary mode $(X_{\text{sq}}, Y_{\text{sq}})$ on a beam splitter with transmission of t_s, the outputs of the

beam splitter are given by:

$$\begin{aligned} X_{\rm m} &= \sqrt{t_{\rm s}}X_{\rm in} + \sqrt{1-t_{\rm s}}X_{\rm sq}, \quad Y_{\rm m} = \sqrt{t_{\rm s}}Y_{\rm in} + \sqrt{1-t_{\rm s}}Y_{\rm sq}, \\ X_{\rm trans} &= \sqrt{ts}X_{\rm sq} - \sqrt{1-t_{\rm s}}X_{\rm in}, \quad Y_{\rm trans} = \sqrt{t_{\rm s}}Y_{\rm sq} - \sqrt{1-t_{\rm s}}Y_{\rm in}. \end{aligned} \tag{7.6}$$

A homodyne measurement is subsequently performed on the phase quadrature (anti-squeezed quadrature) of the reflected mode and its measurement outcome is then rescaled by a gain factor $g_{\rm y}$. The resultant input-output relation is given by:

$$X_{\rm out} = \sqrt{t_{\rm s}}X_{\rm in} + \sqrt{1-t_{\rm s}}X_{\rm sq}, \quad Y_{\rm out} = (\sqrt{t_{\rm s}} - g_{\rm y}\sqrt{1-t_{\rm s}})Y_{\rm in} + (\sqrt{1-t_{\rm s}} + g_{\rm y}\sqrt{t_{\rm s}})Y_{\rm sq}. \tag{7.7}$$

The rescaling factor $g_{\rm y}$ is then adjusted appropriately, i.e. $g_{\rm y} = -\sqrt{(1-t_{\rm s})/t_{\rm s}}$, to ensure the mean of the output is consistent with the unity-gain condition, that is $\langle X_{\rm out}\rangle = e^{-r_{\rm t}}\langle X_{\rm in}\rangle$. We therefore obtain the final output of the deterministic squeezing gate:

$$X_{\rm out} = \sqrt{t_{\rm s}}X_{\rm in} + \sqrt{1-t_{\rm s}}X_{\rm sq}, \quad Y_{\rm out} = \frac{1}{\sqrt{t_{\rm s}}}Y_{\rm in}. \tag{7.8}$$

Equation 7.8 stands for a squeezing operation with target squeezing $r_{\rm t}$ that is fully determined by the transmittance of the beam splitter: $r_{\rm t} = -\ln\sqrt{t_{\rm s}}$. Thanks to the correlation between the reflected and transmitted modes of the first beam splitter, the second term in $Y_{\rm out}$ (see Eq. (7.7)) vanishes after feed-forward, and therefore, the major noise attributed from the anti-squeezed quadrature is eliminated. Assuming an ancillary squeezing with squeezing parameter $r_{\rm a}$ is at our disposal, the deterministic squeezing gate yields a fidelity:

$$\mathcal{F} = \sqrt{\frac{2}{2 + (e^{2r_{\rm t}} - 1)\, e^{-2r_{\rm a}}}}, \tag{7.9}$$

which depends only on the target squeezing and the initially available squeezed ancilla.

In the limit of an infinitely squeezed ancilla, namely $\langle\delta(X_{\rm sq})^2\rangle \to 0$, the quadrature amplitudes of the output state in Eq. (7.8) becomes

$$X_{\rm out} = \sqrt{t_{\rm s}}X_{\rm in}, \quad Y_{\rm out} = \frac{1}{\sqrt{t_{\rm s}}}Y_{\rm in}. \tag{7.10}$$

This represents a perfect squeezing operation that saturates the Heisenberg Uncertainty principle: $\langle\delta(X_{\rm out})^2\rangle\langle\delta(Y_{\rm out})^2\rangle = 1$ and unity fidelity is achieved in this ideal situation. The advantage of the deterministic squeezing gate is apparent: it mitigates the experimental difficulty for directly squeezing an quantum light field other than vacuum. The drawback, however, is that the achievable fidelity is completely determined by the squeezing level of the original squeezed ancilla, thereby implying that a higher fidelity would call for a more squeezed ancilla. Besides, it is also impossible to attain

an output squeezing that is of the same squeezing level as the original ancilla, which means there is non-classicality lost inevitably during the squeezing operation.

As illustrated in Fig. 7.1 (b), we further explore the obtainable fidelity if an unbalanced dual homodyne measurement is exploited in-loop. One can derive that the input-output relation now becomes:

$$\begin{aligned} X_{\rm out} &= (\sqrt{t_{\rm s}} - g_{\rm x}\sqrt{t_{\rm m}(1-t_{\rm s})})X_{\rm in} + (\sqrt{1-t_{\rm s}} + g_{\rm x}\sqrt{t_{\rm s}t_{\rm m}})X_{\rm sq} - g_{\rm x}\sqrt{1-t_{\rm m}}X_{\rm v}, \\ Y_{\rm out} &= (\sqrt{t_{\rm s}} - g_{\rm y}\sqrt{(1-t_{\rm s})(1-t_{\rm m})})Y_{\rm in} + (\sqrt{1-t_{\rm s}} + g_{\rm y}\sqrt{t_{\rm s}(1-t_{\rm m})})Y_{\rm sq} + g_{\rm y}\sqrt{t_{\rm m}}Y_{\rm v}. \end{aligned} \tag{7.11}$$

Similarly, to operate the gate faithfully as a squeezing gate, we require

$$\sqrt{t_{\rm s}} - g_{\rm x}\sqrt{t_{\rm m}(1-t_{\rm s})} = e^{-r_{\rm t}}, \quad \sqrt{t_{\rm s}} - g_{\rm y}\sqrt{(1-t_{\rm m})(1-t_{\rm s})} = e^{-r_{\rm t}}. \tag{7.12}$$

This determines the values of the rescaling factors $g_{\rm x}$ and $g_{\rm y}$ in the feed-forward loop:

$$g_{\rm x} = \frac{\sqrt{t_{\rm s}} - e^{-r_{\rm t}}}{\sqrt{t_{\rm m}(1-t_{\rm s})}}, \quad g_{\rm y} = \frac{\sqrt{t_{\rm s}} - e^{-r_{\rm t}}}{\sqrt{(1-t_{\rm m})(1-t_{\rm s})}}. \tag{7.13}$$

Substituting Eq. (7.13) into Eq. (7.11) and Eq. (7.5), and optimizing $\mathcal{F}$ with respect to $t_{\rm s}$ and $t_{\rm m}$, we obtain the optimal fidelity for a deterministic squeezing gate. It turns out to be that the optimal fidelity is achieved when $t_{\rm m} = 1$, which reduces to the squeezing gate scheme presented in Fig. 7.1 (a). The additional information for the squeezed quadrature obtained from the dual-quadrature homodyne is redundant, which indeed decreases the correlation between the transmitted and the reflected modes.

7.5 Theoretical Modelling of the Squeezing Gate: Heisenberg Picture

In the following, we propose a novel squeezing gate diagram that overcomes the fidelity limit on deterministic squeezing gate. A heralding filter is implemented in the feed-forward loop, whereby an enhancement in fidelity can be achieved by increasing the filter strength alone without requiring more squeezed resource. More intriguingly, we show that our squeezing gate is even capable of yielding unity fidelity for $r_{\rm a} \leq r_{\rm t}$ which is otherwise impossible deterministically.

The schematic of our squeezing gate is depicted in Fig. 7.2. We start with a single mode signal, $(X_{\rm in}, Y_{\rm in})$, as our input and an ancillary squeezed vacuum that is utilized as our nonlinear resource. The ancilla is denoted by its quadrature amplitudes $(X_{\rm sq}, Y_{\rm sq}) = (X_{\rm v}e^{-r_{\rm ax}}, Y_{\rm v}e^{-r_{\rm ay}})$, where $X_{\rm v}(Y_{\rm v})$ indicates the vacuum fluctuation in amplitude (phase) and $r_{\rm ax}$ ($r_{\rm ay}$) refers to the squeezing (anti-squeezing) parameter of the ancilla.

After combining the input state and the ancilla on a beam splitter with transmission of $t_{\rm s}$, the amplitude and phase quadratures of the reflected mode are measured simulta-

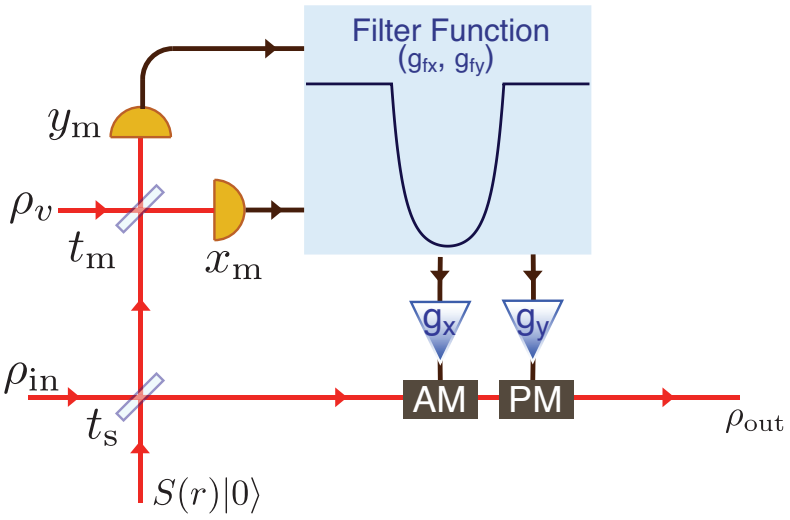

Figure 7.2: Schematic of our heralded squeezing gate. An unbalanced dual-quadrature homodyne is performed in-loop, measuring the squeezed and anti-squeezed quadratures simultaneously. An inverse-Gaussian filter is incorporated into the feed-forward loop to refine the correlation between the reflected and the transmitted modes of the first beam splitter. In this scheme, t_{s} together with t_{m} determines the target squeezing. AM/PM: electro-optic amplitude/phase modulators.

neously by an unbalanced dual homodyne detection, as illustrated in Fig. 7.2. And the outcome is distributed according to:

$$\begin{aligned} X_{\mathrm{m}} &= \sqrt{t_{\mathrm{m}}}X_{\mathrm{v}} + \sqrt{(1-t_{\mathrm{s}})(1-t_{\mathrm{m}})}X_{\mathrm{in}} - \sqrt{t_{\mathrm{s}}(1-t_{\mathrm{m}})}X_{\mathrm{sq}}, \\ Y_{\mathrm{m}} &= -\sqrt{1-t_{\mathrm{m}}}Y_{\mathrm{v}} + \sqrt{t_{\mathrm{m}}(1-t_{\mathrm{s}})}Y_{\mathrm{in}} - \sqrt{t_{\mathrm{s}}t_{\mathrm{m}}}Y_{\mathrm{sq}}. \end{aligned} \tag{7.14}$$

We also obtain the transmitted mode which is given by

$$\begin{aligned} X_{\mathrm{trans}} &= \sqrt{t_{\mathrm{s}}}X_{\mathrm{in}} + \sqrt{1-t_{\mathrm{s}}}X_{\mathrm{sq}}, \\ Y_{\mathrm{trans}} &= \sqrt{t_{\mathrm{s}}}Y_{\mathrm{in}} + \sqrt{1-t_{\mathrm{s}}}Y_{\mathrm{sq}}. \end{aligned} \tag{7.15}$$

Expressing this transmitted mode as a function of the measured values $(X_{\mathrm{m}}, Y_{\mathrm{m}})$ accordingly gives

$$\begin{aligned} X_{\mathrm{trans}} &= c_{\mathrm{x}}X_{\mathrm{m}} + x_0 + X_n, \\ Y_{\mathrm{trans}} &= c_{\mathrm{y}}Y_{\mathrm{m}} + y_0 + Y_n. \end{aligned} \tag{7.16}$$

To ensure this equality holds true, we can derive the coefficients c_{x} and c_{y} that must

satisfy the following relations:

$$
\begin{aligned}
c_{\mathrm{x}} &= \frac{\mathrm{cov}(X_{\mathrm{trans}}, X_{\mathrm{m}})}{\sigma^2_{X_{\mathrm{m}}}} = \frac{\sqrt{t_{\mathrm{s}}(1-t_{\mathrm{m}})(1-t_{\mathrm{s}})}(1-e^{-2r_{\mathrm{ax}}})}{t_{\mathrm{m}} + (1-t_{\mathrm{m}})(1-t_{\mathrm{s}}+t_{\mathrm{s}}e^{-2r_{\mathrm{ax}}})}, \\
c_{\mathrm{y}} &= \frac{\mathrm{cov}(Y_{\mathrm{trans}}, Y_{\mathrm{m}})}{\sigma^2_{Y_{\mathrm{m}}}} = \frac{\sqrt{t_{\mathrm{s}}t_{\mathrm{m}}(1-t_{\mathrm{s}})}(1-e^{2r_{\mathrm{ay}}})}{(1-t_{\mathrm{m}}) + t_{\mathrm{m}}(1-t_{\mathrm{s}}) + t_{\mathrm{s}}t_{\mathrm{m}}e^{2r_{\mathrm{ay}}}}.
\end{aligned}
\tag{7.17}
$$

Here, $\mathrm{cov}(X_{\mathrm{trans}}, X_{\mathrm{m}})$ denotes the covariance between the two modes X_{trans} and X_{m}. $x_0(y_0)$ is a constant and $X_{\mathrm{n}}(Y_{\mathrm{n}})$ represents an additional noise term with mean of zero, i.e $\bar{X}_{\mathrm{n}} = \bar{Y}_{\mathrm{n}} = 0$. Substituting Eq. (7.14), (7.15), and (7.17) into Eq. (7.16), we obtain

$$
\begin{aligned}
x_0 &= \left(\sqrt{t_{\mathrm{s}}} - c_{\mathrm{x}}\sqrt{(1-t_{\mathrm{s}})(1-t_{\mathrm{m}})}\right)\bar{X}_{\mathrm{in}}, \\
y_0 &= \left(\sqrt{t_{\mathrm{s}}} - c_{\mathrm{y}}\sqrt{t_{\mathrm{m}}(1-t_{\mathrm{s}})}\right)\bar{Y}_{\mathrm{in}},
\end{aligned}
\tag{7.18}
$$

and

$$
\begin{aligned}
\sigma^2_{X_{\mathrm{n}}} &= \frac{1 + (e^{2r_{\mathrm{ax}}}-1)t_{\mathrm{s}}t_{\mathrm{m}}}{t_{\mathrm{s}} - t_{\mathrm{s}}t_{\mathrm{m}} + e^{2r_{\mathrm{ax}}}(1-t_{\mathrm{s}}+t_{\mathrm{s}}t_{\mathrm{m}})}, \\
\sigma^2_{Y_{\mathrm{n}}} &= \frac{t_{\mathrm{s}} - t_{\mathrm{s}}t_{\mathrm{m}} + e^{2r_{\mathrm{ay}}}(1-t_{\mathrm{s}}+t_{\mathrm{s}}t_{\mathrm{m}})}{1 + (e^{2r_{\mathrm{ay}}}-1)t_{\mathrm{s}}t_{\mathrm{m}}},
\end{aligned}
\tag{7.19}
$$

where $\bar{X}_{\mathrm{mod}}$ and $\sigma_{X_{\mathrm{mod}}}$ represent the mean and standard deviation of the amplitude quadrature of the corresponding mode.

The filter function that has been elucidated in Sec. 4.2

$$
p(\alpha_{\mathrm{m}}) = \begin{cases} \exp\left[\left(|\alpha_{\mathrm{m}}|^2 - \alpha_{\mathrm{c}}^2\right)\left(1 - \frac{1}{g_{\mathrm{f}}}\right)\right] & \text{for } |\alpha_{\mathrm{m}}| < \alpha_{\mathrm{c}}\,, \\ 1 & \text{for } |\alpha_{\mathrm{m}}| \geq \alpha_{\mathrm{c}}\,. \end{cases}
\tag{7.20}
$$

is then adopted to enact an amplification on both the mean and variance of the measurement outcome of the in-loop dual homodyne by g_{f} (c.f. also Ref. [234]). Its functionality can be emulated by the following transformation

$$
X_{\mathrm{m}} \to \tilde{X}_{\mathrm{m}}, \quad Y_{\mathrm{m}} \to \tilde{Y}_{\mathrm{m}},
\tag{7.21}
$$

where

$$
\bar{\tilde{X}}_{\mathrm{m}} = g_{\mathrm{f}}\bar{X}_{\mathrm{m}}, \quad \sigma^2_{\tilde{X}_{\mathrm{m}}} = g_{\mathrm{f}}\sigma^2_{X_{\mathrm{m}}}.
\tag{7.22}
$$

We stress that Eq. (7.21) manifests only the manipulation of the filtering on the classical ensemble α_{m}, but does not stand for a physical unitary transformation of the mode quadrature operators X_{m} and Y_{m}. The functionality of this filtering operation is dominated by two parameters: a higher filter strength g_{f} promotes the enhancement of fidelity, while a larger cut-off α_{c} designates a wider operational regime of the filter function, guaranteeing therefore the squeezing operation is carried out faithfully. Both ben-

efits come at the price of a reduced success probability, constituting a trade-off between fidelity, faithfulness, and the success probability of the new squeezing gate scheme.

Upon a successful heralding, the filtered statistics $\tilde{X}_{\mathrm{m}}$ and $\tilde{Y}_m$ are rescaled, respectively, by g_{x} and g_{y}, and fed through a pair of amplitude and phase modulators to displace the transmitted mode accordingly. The displacement accomplishes the squeezing operation, yielding an output that is given by

$$\begin{aligned} X_{\text{out}} &= c_{\mathrm{x}}\tilde{X}_{\mathrm{m}} + x_0 + X_{\mathrm{n}} + g_{\mathrm{x}}\tilde{X}_{\mathrm{m}}, \\ Y_{\text{out}} &= c_{\mathrm{Y}}\tilde{Y}_{\mathrm{m}} + y_0 + Y_{\mathrm{n}} + g_{\mathrm{y}}\tilde{Y}_{\mathrm{m}}. \end{aligned} \tag{7.23}$$

The mean and variance of the amplitude quadrature of the final output state can be obtained as:

$$\begin{aligned} \bar{X}_{\text{out}} &= (c_{\mathrm{x}} + g_{\mathrm{x}})g_{\mathrm{f}}\sqrt{(1-t_{\mathrm{s}})(1-t_{\mathrm{m}})}\bar{X}_{\mathrm{in}} + x_0, \\ \sigma^2_{X_{\text{out}}} &= (c_{\mathrm{x}} + g_{\mathrm{x}})^2 g_{\mathrm{f}}\left(t_{\mathrm{m}} + (1-t_{\mathrm{m}})(1-t_{\mathrm{s}} + t_{\mathrm{s}}e^{-2r_{\mathrm{ax}}})\right) + \sigma^2_{X_{\mathrm{n}}}. \end{aligned} \tag{7.24}$$

One can also derive the mean and variance of the phase quadrature similarly

$$\begin{aligned} \bar{Y}_{\text{out}} &= (c_{\mathrm{y}} + g_{\mathrm{y}})g_{\mathrm{f}}\sqrt{t_{\mathrm{m}}(1-t_{\mathrm{s}})}\bar{Y}_{\mathrm{in}} + y_0, \\ \sigma^2_{Y_{\text{out}}} &= (c_{\mathrm{y}} + g_{\mathrm{y}})^2 g_{\mathrm{f}}\left(1 - t_{\mathrm{s}} + t_{\mathrm{s}}e^{2r_{\mathrm{ay}}}\right) + \sigma^2_{Y_{\mathrm{n}}}. \end{aligned} \tag{7.25}$$

In accordance with the deterministic squeezing gate, we ensure our squeezing gate operates in the unity-gain regime, which means $\bar{x}_{\text{out}} = e^{-r_{\mathrm{t}}}\bar{x}_{\mathrm{in}}$ and $\bar{y}_{\text{out}} = e^{r_{\mathrm{t}}}\bar{y}_{\mathrm{in}}$. This condition determines the relationship between the filter strength g_{f} and the rescaling factor g_{x}, g_{y}

$$\begin{aligned} g_{\mathrm{x}} &= \frac{e^{-2r_{\mathrm{t}}} - \sqrt{t_{\mathrm{s}}} + (1-g_{\mathrm{fx}})c_{\mathrm{x}}\sqrt{(1-t_{\mathrm{s}})(1-t_{\mathrm{m}})}}{g_{\mathrm{fx}}\sqrt{(1-t_{\mathrm{s}})(1-t_{\mathrm{m}})}}, \\ g_{\mathrm{y}} &= \frac{e^{2r_{\mathrm{t}}} - \sqrt{t_{\mathrm{s}}} + (1-g_{\mathrm{fy}})c_{\mathrm{y}}\sqrt{t_{\mathrm{m}}(1-t_{\mathrm{s}})}}{g_{\mathrm{fy}}\sqrt{t_{\mathrm{m}}(1-t_{\mathrm{s}})}}. \end{aligned} \tag{7.26}$$

Once such rescaling factors are employed, the output variances become

$$\begin{aligned} \sigma^2_{X_{\text{out}}} &= \left(\frac{e^{-r_{\mathrm{t}}} - \sqrt{t_{\mathrm{s}}} + c_{\mathrm{x}}\bar{X}_{\mathrm{m}}}{\bar{X}_{\mathrm{m}}}\right)^2 \frac{\sigma^2_{X_{\mathrm{m}}}}{g_{\mathrm{fx}}} + \sigma^2_{X_{\mathrm{n}}}, \\ \sigma^2_{Y_{\text{out}}} &= \left(\frac{e^{r_{\mathrm{t}}} - \sqrt{t_{\mathrm{s}}} + c_{\mathrm{y}}\bar{Y}_{\mathrm{m}}}{\bar{Y}_{\mathrm{m}}}\right)^2 \frac{\sigma^2_{Y_{\mathrm{m}}}}{g_{\mathrm{fy}}} + \sigma^2_{Y_{\mathrm{n}}}. \end{aligned} \tag{7.27}$$

Substituting Eq. (7.27) into the fidelity formula in Eq. (7.5), we notice that $\mathcal{F}$ can always be optimized by tailoring t_{s} and t_{m} jointly. Given an initial squeezed resource r_{a} and a target squeezing r_{t}, fidelity can always be improved by increasing the filter strength g_{x} and g_{y} alone at the expense of a lower success probability.

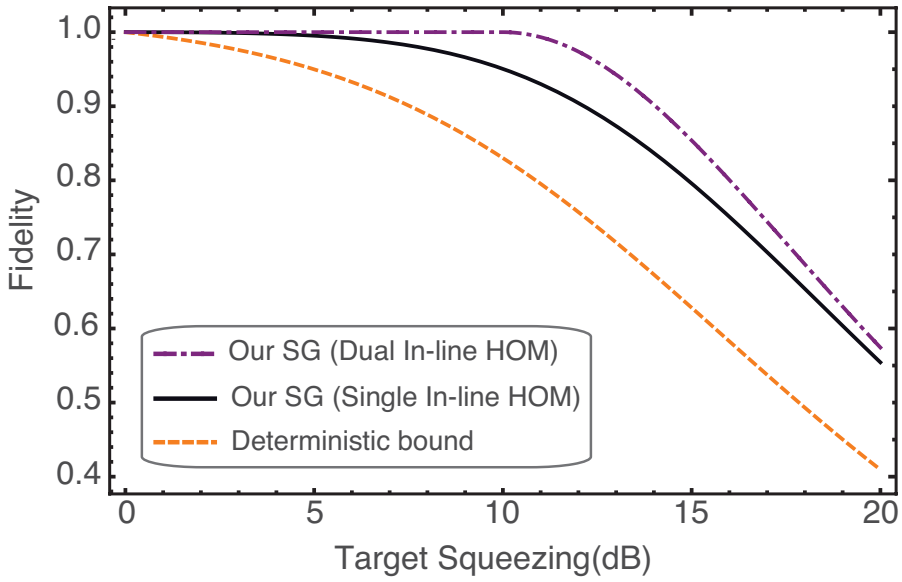

Figure 7.3: Fidelity as a function of target squeezing. Assuming we have a 10 dB pure ancillary squeezed resource at our disposal, our squeezing gate offers a distinct advantage over the deterministic scheme with respect to the achievable fidelity. And ultimately it is shown to be capable of achieving unit fidelity for target squeezing up to the same level as the initial squeezed ancilla, which is otherwise impossible deterministically.

7.5.1 High Gain Regime

In the extreme case where the filter strength g_{f} is sufficiently large, the output variance can be made arbitrarily close to $e^{-2r_{\mathrm{t}}}$ for the amplitude quadrature and $e^{2r_{\mathrm{t}}}$ for the phase quadrature, given that the following relationship is fulfilled

$$t_{\mathrm{s}} = \frac{e^{2r_{\mathrm{a}}} - e^{2r_{\mathrm{t}}}}{(e^{2r_{\mathrm{a}}} - 1)(1 - t_{\mathrm{m}} + t_{\mathrm{m}} e^{2r_{\mathrm{t}}})}. \tag{7.28}$$

Here we assume that the initial squeezed ancilla is pure, which means $r_{\mathrm{a}} = r_{\mathrm{ax}} = r_{\mathrm{ay}}$. The achievable fidelity of our squeezing gate in this scenario is plotted as a function of target squeezing in Fig. 7.3. As is shown as the purple curve in Fig. 7.3, unity fidelity for any target squeezing $r_{\mathrm{t}} < r_{\mathrm{a}}$ is in principle approachable. This showcases the theoretical bound of the performance of our squeezing gate, which is only accessible with vanishing success probability.

On the contrary for $r_{\mathrm{t}} \geq r_{\mathrm{a}}$ which means the desired state is more squeezed than the initial squeezed ancilla, linear optics alone no longer suffice and the optimal squeezing operation is given by setting $t_{\mathrm{s}} = 0$ such that the output has at most r_{a} level of squeezing.

The observations here draw an apparent distinction between the deterministic SG [269] and our SG: unity fidelity, that is unattainable for any target squeezing deterministically, is conceivable once probabilistic operation is allowed. More remarkably, even the same amount of noise suppression as the initial ancilla is obtainable by tailoring t_{s} provided a dual homodyne measurement is performed in-loop. The mechanism

behind this improvement is that post-selection enhances the precision of the in-line homodyne measurement, refines the correlation between the reflected and the transmitted modes and as a result, leads to a more efficient noise cancellation during feed-forward.

7.5.2 Low Gain Regime

We now turn to the alternative regime identified by a favourable success probability. As shown in Fig. 7.4, one can anticipate more than 68% of the possible fidelity enhancement (up to unity) with a success probability higher than 0.01 by adopting a relatively small g_{f}. We note that in this case a single-quadrature homodyne, i.e. $t_{\mathrm{m}} = 1$, tends to achieve near-optimal fidelity as if a dual homodyne is implemented, and likewise offers a distinct advantage against the conventional SG scheme. The amplitude quadrature which is here the squeezed quadrature, stays intact after feed-forwarding, so

$$\begin{aligned} \bar{X}_{\mathrm{out}} &= \sqrt{ts}\bar{X}_{\mathrm{in}}, \\ \sigma^2_{X_{\mathrm{out}}} &= t_{\mathrm{s}} + (1-t_{\mathrm{s}})e^{-2r_{\mathrm{ax}}}. \end{aligned} \tag{7.29}$$

Because $\bar{X}_{\mathrm{out}} = e^{-r_{\mathrm{t}}}\bar{X}_{\mathrm{in}}$ for a squeezing operation with target squeezing of r_{t}, we obtain $e^{-2r_{\mathrm{t}}} = t_{\mathrm{s}}$. The transmission t_{s} therefore determines exclusively the amount of target squeezing $t_{\mathrm{s}} = e^{-2r_{\mathrm{t}}}$, which in turn indicates $\bar{Y}_{\mathrm{out}} = e^{r_{\mathrm{t}}}\bar{y}_{\mathrm{in}} = 1/\sqrt{t_{\mathrm{s}}}\bar{Y}_{\mathrm{in}}$. Such relation poses a requirement on the rescaling factor, g_{y}, acted upon the phase quadrature in the feed-forward loop:

$$g_{\mathrm{y}} = \frac{\sqrt{1-t_{\mathrm{s}}}\left(1+(e^{2r_{\mathrm{ay}}}-1)g_{\mathrm{f}}t_{\mathrm{s}}\right)}{\sqrt{t_{\mathrm{s}}}\left(g_{\mathrm{f}}+(e^{2r_{\mathrm{ay}}}-1)g_{\mathrm{f}}t_{\mathrm{s}}\right)}. \tag{7.30}$$

The variance of the phase quadrature of the output state can then be derived which takes the form

$$\sigma^2_{Y_{\mathrm{out}}} = \frac{1+(e^{2r_{\mathrm{a}}}g_{\mathrm{f}}-1)t_{\mathrm{s}}}{g_{\mathrm{f}}t_{\mathrm{s}}\left(1+(e^{r_{\mathrm{a}}}-1)t_{\mathrm{s}}\right)}. \tag{7.31}$$

Substituting Eq. (7.29) and Eq. (7.31) into Eq. (7.5), we obtain the resultant fidelity:

$$\mathcal{F} = 2\sqrt{\frac{t_{\mathrm{s}}}{(2t_{\mathrm{s}}+(1-t_{\mathrm{s}})e^{-2r_{\mathrm{a}}})\left(1+\frac{1+(e^{2r_{\mathrm{a}}}g_{\mathrm{f}}-1)t_{\mathrm{s}}}{g_{\mathrm{f}}+(e^{r_{\mathrm{a}}}-1)g_{\mathrm{f}}t_{\mathrm{s}}}\right)}}. \tag{7.32}$$

We notice that there are three effective parameters for determining the output fidelity: the available squeezed resource, the target squeezing level one aims for, and the filter strength. Given a target r_{t} and an ancillary squeezed resource r_{a}, higher fidelity is always attainable by increasing the filter strength g_{f} alone without reconfiguring the experimental setup. This enhancement in fidelity would require a more squeezed an-

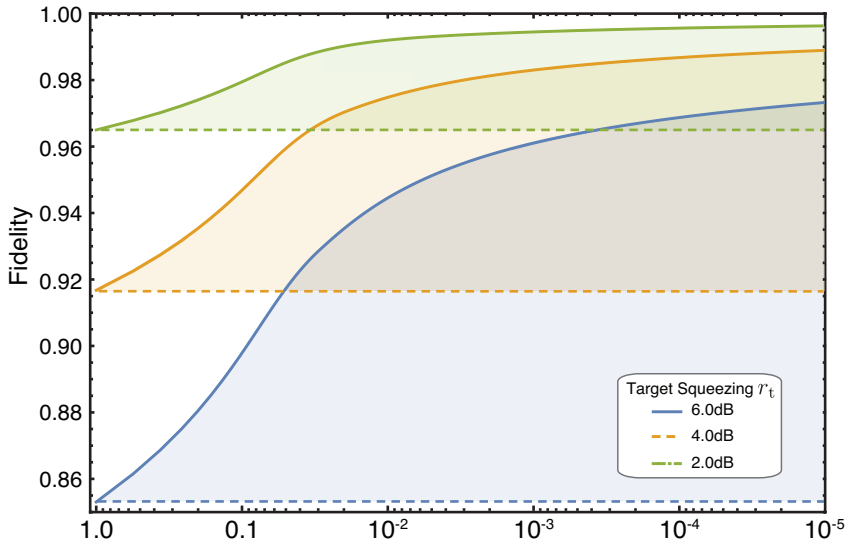

Figure 7.4: Fidelity against success probability for various target squeezings. Assuming we start with a pure squeezed ancilla of 6 dB, the fidelity is plotted as a function of probability of success for three values of the target squeezing, being 2 dB, 4 dB, and 6 dB. For comparison, the fidelity of a conventional deterministic squeezing gate is superimposed (dashed lines). In all cases, a substantial enhancement in fidelity is achieved with our scheme, although at the expense of a lower success probability. The cut-off α_c is chosen such that more than 98% of the filtered statistics lie within it to preserve the output Gaussianity.

cilla if a conventional deterministic SG is used instead. If determinism is more desirable than high fidelity, by setting $g_{\mathrm{f}} = 1$ our SG reduces straightly to a conventional SG, so additional flexibility is offered by our SG in this regard.

7.5.3 Dependence of Gate Fidelity on Source Purity

We point out that as opposed to the conventional deterministic SG, our SG is no longer immune to the purity of the ancillary squeezed resource. As illustrated in Fig. 7.5, regardless of whether a dual-quadrature homodyne or a single-quadrature homodyne is implemented in-loop, the output fidelity always degrades if an impure squeezed ancilla is utilized. A single-quadrature homodyne in conjunction with a pure initial squeezed ancilla outperforms a dual-quadrature homodyne plus an impure squeezed resource. This degradation arises because with impure squeezed resource, the variance of the transmitted mode conditioned upon the measurement outcome of the in-line homodyne increases. This additional noise cannot be compensated by the filtering process, and as a consequence, the final fidelity decreases.

7.5.4 Alternative Theoretical Modelling: Covariance Matrix

We provide an alternative approach to model our squeezing gate by considering the full symplectic map of the modes quadrature operators [35]. This analysis is shown to be consistent with the results detailed in the preceding sections that directly examine

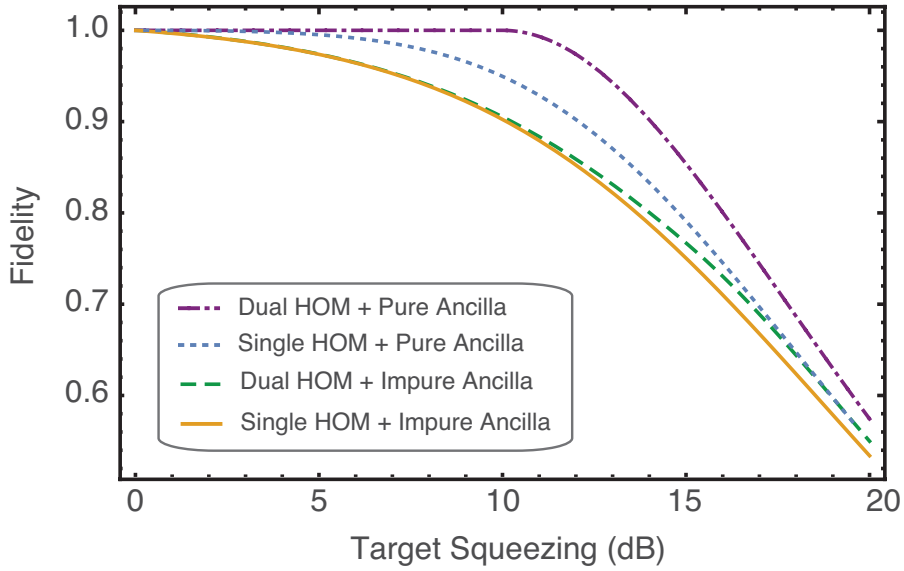

Figure 7.5: Fidelity against target squeezing when an impure squeezed ancilla is employed. The purple (dashed-dotted) and the green (dashed) line shows the gate fidelity for a pure (10 dB squeezing) and impure initial squeezed ancilla (10 dB squeezing and 13 dB anti-squeezing), respectively, with a dual-quadrature homdoyne being performed in-loop. In contrast, the blue dotted and the orange line show the corresponding fidelity when a single-quadrature homodyne measurement is performed instead. A degradation in fidelity is observed when the initial squeezed ancilla is impure.

the evolutions of quadrature amplitudes. Without loss of generality, we consider here an in-loop single quadrature homodyne, which can be extended to account for a dual-quadrature homodyne following the same methodology described in Sec. 9.3.4.

We begin by coupling an input mode with an ancillary squeezed beam on a beam splitter with transmission of t_{s}. The linear unitary Bogoliubov transformation denoting the two-mode beam splitter can be written as:

$$\begin{pmatrix} \sqrt{t_{\mathrm{s}}} & 0 & \sqrt{1-t_{\mathrm{s}}} & 0 \\ 0 & \sqrt{t_{\mathrm{s}}} & 0 & \sqrt{1-t_{\mathrm{s}}} \\ -\sqrt{1-t_{\mathrm{s}}} & 0 & \sqrt{t_{\mathrm{s}}} & 0 \\ 0 & -\sqrt{1-t_{\mathrm{s}}} & 0 & \sqrt{t_{\mathrm{s}}} \end{pmatrix}. \tag{7.33}$$

The quadrature operators of the combined output state becomes $\left(\sqrt{1-t_{\mathrm{s}}}X_{\mathrm{in}} + \sqrt{t_{\mathrm{s}}}X_{\mathrm{sq}}, \sqrt{1-t_{\mathrm{s}}}Y_{\mathrm{in}} + \sqrt{t_{\mathrm{s}}}Y_{\mathrm{sq}}, \sqrt{t_{\mathrm{s}}}X_{\mathrm{in}} - \sqrt{1-t_{\mathrm{s}}}X_{\mathrm{sq}}, \sqrt{t_{\mathrm{s}}}Y_{\mathrm{in}} - \sqrt{1-t_{\mathrm{s}}}Y_{\mathrm{sq}}\right)^T$,

and its covariance matrix CV_{SG} is given by:

$$CV_{\mathrm{SG}} = \begin{pmatrix} 1+t_{\mathrm{s}}(e^{-2r_{\mathrm{a}}}-1) & 0 & \sqrt{t_{\mathrm{s}}(1-t_{\mathrm{s}})}(1-e^{-2r_{\mathrm{a}}}) & 0 \\ 0 & 1+t_{\mathrm{s}}(e^{2r_{\mathrm{a}}}-1) & 0 & \sqrt{t_{\mathrm{s}}(1-t_{\mathrm{s}})}(1-e^{2r_{\mathrm{a}}}) \\ \sqrt{t_{\mathrm{s}}(1-t_{\mathrm{s}})}(1-e^{-2r_{\mathrm{a}}}) & 0 & t_{\mathrm{s}}+(1-t_{\mathrm{s}})e^{-2r_{\mathrm{a}}} & 0 \\ 0 & \sqrt{t_{\mathrm{s}}(1-t_{\mathrm{s}})}(1-e^{2r_{\mathrm{a}}}) & 0 & t_{\mathrm{s}}+(1-t_{\mathrm{s}})e^{2r_{\mathrm{a}}} \end{pmatrix}. \tag{7.34}$$

We set $t_{\mathrm{m}} = 1$ (see Fig. 7.2), and perform a single-quadrature homodyne on the anti-squeezed quadrature of the reflected mode. The mean of the transmitted mode conditioned upon the single-shot measurement outcome y_{m} can be expressed as:

$$\begin{aligned} \mu_{X_{\mathrm{t}}|y_{\mathrm{m}}} &= \bar{X}_{\mathrm{trans}} + \frac{CV_{\mathrm{SG}}(3,2)}{CV_{\mathrm{SG}}(2,2)}(y_{\mathrm{m}} - \bar{Y}_{\mathrm{m}}) = \sqrt{t_{\mathrm{s}}}\bar{X}_{\mathrm{in}}, \\ \mu_{Y_{\mathrm{t}}|y_{\mathrm{m}}} &= \bar{Y}_{\mathrm{trans}} + \frac{CV_{\mathrm{SG}}(4,2)}{CV_{\mathrm{SG}}(2,2)}(y_{\mathrm{m}} - \bar{Y}_{\mathrm{m}}), \\ &= \sqrt{t_{\mathrm{s}}}\bar{Y}_{\mathrm{in}} + \frac{2\mathrm{Sinh}(r_{\mathrm{a}})\sqrt{t_{\mathrm{s}}(1-t_{\mathrm{s}})}}{\mathrm{Cosh}(r_{\mathrm{a}}) + \mathrm{Sinh}(r_{\mathrm{a}})(2t_{\mathrm{s}}-1)}(\sqrt{1-t_{\mathrm{s}}}\bar{Y}_{\mathrm{in}} - y_{\mathrm{m}}), \end{aligned} \tag{7.35}$$

where $CV_{\mathrm{SG}}(m,n)$ indicates the element of the covariance matrix at position mth row and nth column. After averaging over all possible results for y_{m}, the second term of $\mu_{\mathrm{Yt}|y_{\mathrm{m}}}$ vanishes, and therefore, $\mu_{\mathrm{Yt}|y_{\mathrm{m}}} = \sqrt{t_{\mathrm{s}}}\bar{Y}_{\mathrm{in}}$. Additionally, we can derive the conditional variance of the transmitted mode:

$$\begin{aligned} \Sigma_{X_{\mathrm{t}}|y_{\mathrm{m}}} &= \sigma^2_{X_{\mathrm{trans}}} - \frac{CV_{\mathrm{SG}}(3,2)CV_{\mathrm{SG}}(2,3)}{CV_{\mathrm{SG}}(2,2)} = t_{\mathrm{s}} + (1-t_{\mathrm{s}})e^{-2r_{\mathrm{a}}}, \\ \Sigma_{Y_{\mathrm{t}}|y_{\mathrm{m}}} &= \sigma^2_{Y_{\mathrm{trans}}} - \frac{CV_{\mathrm{SG}}(4,2)CV_{\mathrm{SG}}(2,4)}{CV_{\mathrm{SG}}(2,2)} = \frac{1}{t_{\mathrm{s}} + (1-t_{\mathrm{s}})e^{-2r_{\mathrm{a}}}}. \end{aligned} \tag{7.36}$$

Note that the conditional variance of the amplitude quadrature remains unchanged after the in-loop homodyne due to the fact that there is no correlation between the phase quadrature of the reflected mode and amplitude quadrature of the transmitted mode. On the contrary, the conditional variance of the phase quadrature equals to the inverse of the conditional amplitude noise. The conditional transmitted mode therefore becomes a minimum Heisenberg Uncertainty state with its amplitude noise being suppressed below shot noise whilst its phase noise being amplified accordingly.

The measurement outcome of the in-line homodyne is subsequently kept or rejected according to the acceptance probability specified by the inverse-Gaussian filter in Eq. (7.20) (c.f. Sec. 4.2). This, from the statistical viewpoint, leads to an amplification of both the mean and variance of the measurement ensemble, as shown in Eq. (7.21) and (7.22). Assume the covariance matrix of the combined state now becomes

CV_{SGPS}. The amplification effect resulting from the post-selection leads to the relationship: $CV_{SGPS}(2,2) = g_{\rm f} CV_{SG}(2,2)$. Moreover, owing to the fact that filtering should not affect the probability distribution of the transmitted mode conditioned upon the measurement outcomes of the in-line homodyne, the following relations must hold valid.

$$\begin{aligned}
\frac{CV_{\rm SG}(4,2)}{CV_{\rm SG}(2,2)} &= \frac{CV_{\rm SGPS}(4,2)}{CV_{\rm SGPS}(2,2)}, \\
CV_{\rm SG}(4,4) - \frac{CV_{\rm SG}(4,2)CV_{\rm SG}(2,4)}{CV_{\rm SG}(2,2)} &= CV_{\rm SGPS}(4,4) - \frac{CV_{\rm SGPS}(4,2)CV_{\rm SGPS}(2,4)}{CV_{\rm SGPS}(2,2)}.
\end{aligned} \tag{7.37}$$

One shall be able to derive the full entries of the covariance matrix $CV_{\rm SGPS}$ based on the above equalities and Eq. (7.22):

$$CV_{\rm SGPS} = \begin{pmatrix}
1+t_{\rm s}(e^{-2r_{\rm a}}-1) & 0 & \sqrt{t_{\rm s}(1-t_{\rm s})}(1-e^{-2r_{\rm a}}) & 0 \\
0 & CV_{\rm SGPS}(2,2) & 0 & CV_{\rm SGPS}(2,4) \\
\sqrt{t_{\rm s}(1-t_{\rm s})}(1-e^{-2r_{\rm a}}) & 0 & t_{\rm s}+(1-t_{\rm s})e^{-2r_{\rm a}} & 0 \\
0 & CV_{\rm SGPS}(4,2) & 0 & CV_{\rm SGPS}(4,4)
\end{pmatrix}, \tag{7.38}$$

where

$$\begin{aligned}
CV_{\rm SGPS}(2,2) &= g_{\rm f} + g_{\rm f} t_{\rm s}(e^{2r_{\rm a}} - 1), \\
CV_{\rm SGPS}(2,4) &= CV_{\rm SGPS}(4,2) = -g_{\rm f}\sqrt{t_{\rm s}(1-t_{\rm s})}(e^{2r_{\rm a}} - 1), \\
CV_{\rm SGPS}(4,4) &= \frac{g_{\rm f} t_{\rm s}(1-t_{\rm s})(e^{2r_{\rm a}}+1)^2 + e^{2r_{\rm a}}}{1 + t_{\rm s}(e^{2r_{\rm a}} - 1)}.
\end{aligned} \tag{7.39}$$

A rescaling operation, denoted by the rescaling factors $g_{\rm x}$ and $g_{\rm y}$, is applied on $\tilde{Y}_{\rm m}$ which is then fed-forward to the transmitted mode to realize a displacement operation. The mean and variance of the quadrature amplitudes of the final output state are obtained:

$$\begin{aligned}
\bar{X}_{\rm out} &= \sqrt{t_{\rm s}}\bar{X}_{\rm in}, \quad \sigma^2_{X_{\rm out}} = CV_{\rm SGPS}(3,3), \\
\bar{Y}_{\rm out} &= \mu_{Y_{\rm t}|y_{\rm m}} + \frac{CV_{\rm SGPS}(4,2)}{CV_{\rm SGPS}(2,2)}(g_{\rm f}-1)\sqrt{1-t_{\rm s}}\bar{Y}_{\rm in} + g_{\rm y} g_{\rm f}\sqrt{1-t_{\rm s}}\bar{Y}_{\rm in}, \\
\sigma^2_{Y_{\rm out}} &= CV_{\rm SGPS}(4,4) + g_{\rm y}^2 CV_{\rm SGPS}(2,2) + 2 g_{\rm y} CV_{\rm SGPS}(2,4).
\end{aligned} \tag{7.40}$$

These results are consistent with those shown in Eq. (7.24) and Eq. (7.25). By requiring $\bar{Y}_{\rm out} = 1/\sqrt{t_{\rm s}}\bar{Y}_{\rm in}$, we attain the appropriate value of $g_{\rm y}$ (see Eq. (7.30)), which in turn determines the output variance of the phase quadrature and the output fidelity based on Eq. (7.5).

7.6 Discussions and Conclusions

In summary, we propose and experimentally demonstrate a post-selection-based squeezing gate scheme that allows us to achieve near-unity fidelity with a modest level of ancillary squeezing. The heralded operation circumvents the requirement of a highly squeezed ancilla in the conventional approach, thereby fidelity can be equivalently enhanced by increasing the filter strength of the post-selection. The vast majority of this enhancement is obtainable with a success probability $> 10^{-2}$. Furthermore, the present scheme permits fidelity inaccessible in the conventional way: unity fidelity, that is otherwise impossible, becomes approachable for any target squeezing less than the initial ancillary squeezing.

Looking forward, the squeezing gate can improve the performance of other squeezing-powered protocols such as decoherence mitigation [266, 275, 276], and fault-tolerant quantum computation where high-fidelity gate operations are necessary [273, 274]. Additionally, the filter function can also be adapted to improve the fidelity of non-Gaussian operations such as the photon subtraction and addition [280, 281, 282].

Chapter 8

High Fidelity Squeezing Gate for CV Quantum Light Fields: Experiment

8.1 Overview

In this chapter we experimentally demonstrate the high-fidelity squeezing gate presented in the previous chapter. Provided the same squeezed resource, a substantial improvement in fidelity is experimentally demonstrated compared to the conventional deterministic squeezing gate. In particular, a gate fidelity of 0.98 was measured with a success probability of 2.9×10^{-3} for a 2.3 dB squeezing operation on a coherent state with amplitude of 1.92. This cannot be achieved even with an ideally pure and infinitely squeezed ancilla experiencing the same loss in presence of our experimental setup. Our squeezing gate scheme circumvents the conventional necessity of highly squeezed resource to obtain high-fidelity gate operation. Considering that it can be naturally incorporated into a measurement-based quantum computation framework, we anticipate it to provide a useful tool in continuous variable quantum information.

Our theoretical modelling in chapter 7 has considered general input states; in the following experimental demonstration, we shall concern ourselves with coherent inputs without loss of generality.

The work presented in this chapter can be found in the following article:

• J. Zhao, K. Liu, J. Hao, M. Gu, J. Thompson, S. Assad, and P. K. Lam. *High-fidelity squeezing gate for continuous-variable quantum light fields.* (2018).

8.2 Experimental Details

8.2.1 Experimental Setup

FF? represents the filtering process where measurement outcomes of the unbalanced homodyne are either selected or discarded with probability specified in Eq. (7.20). As depicted in Fig. 8.1, the experiment consists of four parts: a squeezed vacuum source, input preparation, squeezing gate consisting of homodyning and feed-forward, and a homo-

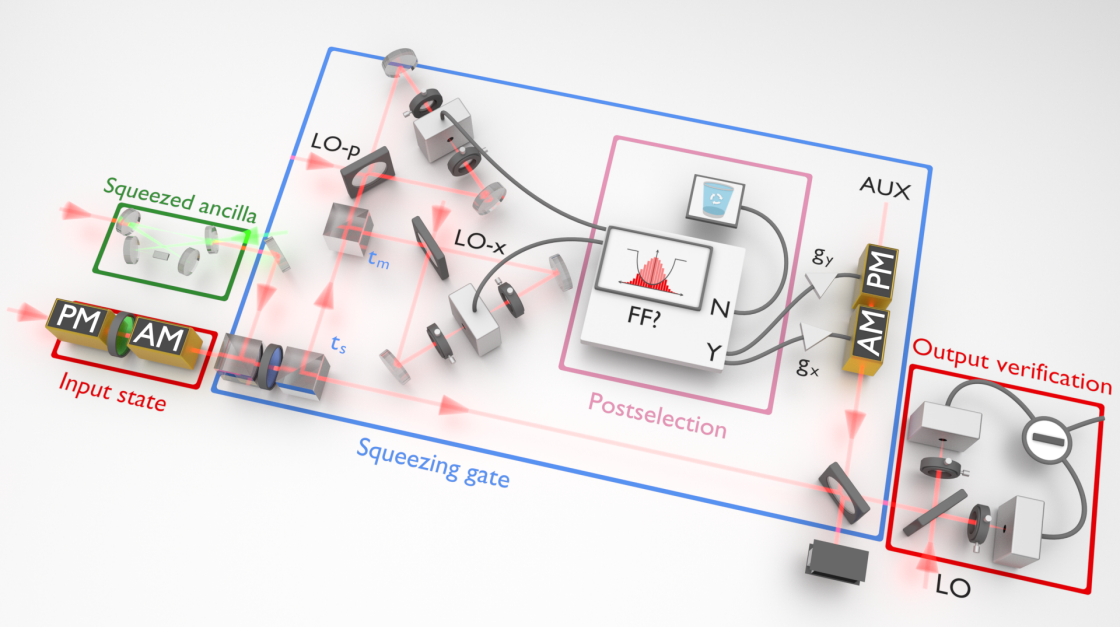

Figure 8.1: Experimental layout of our squeezing gate. The gate scheme is comprised of three parts: first, the input state and an ancillary squeezed vacuum are prepared; second, an unbalanced dual homodyne is performed in-loop. This measurement, in conjunction with postselection, feed-Forwarding, and a displacement operation, constitute the core of our squeezing gate. A verification homodyne station is employed lastly to characterize the squeezed output. In this scheme, t_{s} together with t_{m} determines the target squeezing. Here more operational flexibility is present in our squeezing gate: the unity-gain condition that can only be fulfilled by adjusting the rescaling factors g_{x}, g_{y} in the conventional squeezing gate setup, is now achievable by tailoring three independent parameters, the filter strength g_{f}, g_{x}, and g_{y}, jointly to complement each other. AM/PM: electro-optic amplitude/phase modulators. FF? represents the filtering process where measurement outcomes of the unbalanced homodyne are either selected or discarded with probability specified in Eq. (7.20).

dyne station for characterizing the output state. The main light source is a continuous-wave frequency-doubled Nd:YAG laser (Innolight Diablo), producing approximately 300 mW fundamental wave at 1064 nm and 400 mW second harmonic wave at 532 nm. The fundamental beam passes through a mode cleaner cavity with finesse of 760 to further purify its spatial mode and attenuate the high-frequency noise of the laser output. The squeezed vacuum is prepared in a doubly-resonant bow-tie cavity where below-threshold optical parametric amplification (OPA) takes place using a 10.7 mm potassium titanyl phosphate (KTP) crystal periodically poled with 9 μm period. The front and rear surfaces of the crystal are superpolished and anti-reflection coated with R<0.1% at 1064 nm and R<0.2% at 532 nm. Three intracavity mirrors are coated to be highly reflective at both 1064 nm and 532 nm (R>99.99% for the two concave mirrors and R=99.85±0.05% for the flat mirror), and the input/output coupler has a customized reflection of 83±1% at 1064 nm and 73±1.2% at 532 nm. Up to 11 dB squeezed vacuum can be generated with a bandwidth of around 36 MHz.

An inverse-Gaussian filter is incorporated into the feed-forward loop, which is used to determine if the squeezing gate operation is successful or not. This is accomplished by picking a random number from a uniform distribution between 0 and 1 and comparing that to $p(\alpha_{\rm m})$ in Eq. (7.20), where $\alpha_{\rm m}$ denotes the measurement outcome of the in-loop dual homodyne detection. The operation is heralded as successful when the random number is less than $p(\alpha_{\rm m})$ and as failed otherwise. In the experimental demonstration, the in-loop homodyne measurement heralds successful operation shot-by-shot. We implement the filtering off-line by pairing up the in-line homodyne outcome with the corresponding verifying homodyne outcome during data acquisition, and either keeping or rejecting the latter based on the former. Special precautions were taken for choosing the cut-off parameter α_c in $p(\alpha_{\rm m})$: a larger cut-off enables a wider operational regime of the filter function, however, at the expense of a decreased probability of success. Consider an input ensemble with a large amplitude, then a large $\alpha_{\rm c}$ is required; otherwise, the part of the output distribution beyond $\alpha_{\rm c}$ is subject to distortion (c.f. Sec. 4.2). Hence, $\alpha_{\rm c}$ needs to be carefully tailored according to the input ensemble to ensure a faithful squeezing operation while still maintaining a reasonable probability of success. The accepted data points form the probability distribution of the squeezed output state. For each data set, around 10^7 data points are collected before post-selection with a data sampling rate of 5 MHz and low passed at 100 kHz. This ensures enough data points (10^4) are left to form a complete statistics of the output for an average success probability of 10^{-3} in our experiments. To shorten the data saving time, the raw data have been grouped into histograms on LabView before being written into the PXI hard disk.

8.2.2 Scheme of Servo Control Lockings

Special care was taken in the implementation of all phase locks throughout the experiment. The OPA cavity was locked on co-resonance of both the fundamental beam (1064 nm) and the pump beam (532 nm) by means of the Pound-Drever-Hall technique with a 11.25 MHz phase modulation on the pump. The same modulation signal was also utilized to lock the relative phase between the signal beam and the squeezed ancilla, i.e. output of the OPA. The relative phase between the seed and the pump was carefully controlled using a phase modulation at 41.5625 MHz on the seed beam. We use this modulation to ensure that the OPA always operates at the parametric de-amplification, which yields an amplitude-squeezed vacuum. The interference between the seed and the local oscillators/auxiliary beam on each homodyne station is controlled similarly with an amplitude modulation (24.25 MHz) and a phase modulation (30 MHz) on the signal beam, giving access to the measurement of an arbitrary quadrature angle. A detailed illustration of the locking scheme can be found in Appendix A.

	Input		**Target**			**Measured**			
	x_{in}	y_{in}	x_{out}	y_{out}	r_{t}(dB)	x_{out}	y_{out}	r_{ax}	r_{ay}
A	-2.91	-2.50	-2.23	-3.26	2.30	-2.23	-3.26	1.54	1.76
B	0.00	-1.24	0.00	-2.17	4.81	-0.08	-2.17	2.43	4.46
C	1.46	-1.43	0.74	-0.91	5.84	0.74	-0.91	3.35	4.90
D	1.58	0.86	0.57	2.38	8.85	0.57	2.38	5.16	7.66
E	-0.67	0.68	-0.21	2.20	10.16	-0.21	2.20	4.30	7.77

Table 8.1: Mean values of the five input states, the corresponding targets, and the measured outputs where $\alpha_{\text{m}} = (x_{\text{m}} + iy_{\text{m}})/\sqrt{2}$. In contrast to the deterministic squeezing gate where unity gain is achieved by adjusting the rescaling factor alone, two independent knobs can be tuned jointly here, namely, the filter strength g_{f} and the rescaling factors, g_{x} and g_{y}. This flexibility results in the measured output mean values being in very good agreement with the target values.

8.3 Experimental Results

We now report the experimental results for the heralded squeezing gate. An auxiliary squeezed vacuum with 6.0 dB of squeezing and 6.5 dB anti-squeezing is prepared and used as a resource to drive the squeezing gate. In the experiments, we perform a single-quadrature measurement by setting $t_{\text{m}} = 1$. This allows for a higher success probability compared to a dual-quadrature measurement while maintaining comparable fidelity enhancement as seen in Fig. 8.3. To demonstrate the operation of the squeezing gate, we prepared several coherent input states with different amplitudes and phases and characterized their output by performing homodyne measurements on the amplitude and phase quadratures. To generate enough statistics, the experiment was repeated at least 10^6 times for every input. The detailed experimental results are tabulated in Table. 8.1 and 8.2.

8.3.1 Phase Invariance of the Squeezing Operation

First, we present the results for five input states having different phases and with magnitude $|\alpha_{\text{in}}|$ ranging from 0.70 to 1.92 in Fig. 8.2. The states are labelled from (A) to (E) and the target squeezing varies between 2.3 dB to 10.16 dB. A true squeezing gate should operate on an arbitrary input regardless of its amplitude and phase. This is verified by the measured outputs which demonstrates the phase invariance of our squeezing gate.

8.3.2 Fidelity vs Target Squeezing

Second, we characterize the fidelity as a function of target squeezing and the filter strength for each of the input states in Fig. 8.3. The best conventional output fidelity attainable in an idealized experiment using the same ancillary resource but assuming no loss is plotted as a benchmark. By having a sufficiently large filter strength, we can surpass this benchmark. The trade-off between fidelity and success probability is illus-

State Set	g_f	$\mathcal{F}$	p
A	1	0.881	1.0
	1.52	0.961	2.9e-2
	3.23	0.970	1.4e-3
	12.63	0.985	2.8e-3
B	1	0.840	1.0
	1.87	0.887	2.3e-2
C	1	0.825	1.0
	1.10	0.833	5.9e-1
	1.78	0.861	2.9e-2
	3.51	0.894	2.8e-3

State Set	g_f	$\mathcal{F}$	p
D	1	0.650	1.0
	1.44	0.733	2.1e-1
	2.00	0.791	7.1e-3
	3.41	0.825	2.1e-3
E	1	0.610	1.0
	1.59	0.6778	4.6e-1
	1.74	0.6781	4.0e-1
	2.11	0.714	9.3e-4
	2.78	0.723	2.2e-4

Table 8.2: Success probability, filter strength, and the resultant gate fidelity for various target squeezings.

trated in Fig. 8.3 inset, it shows that for all runs, the success probabilities are greater than 10^{-4}.

8.3.3 Fidelity as a Function of Filter Strength

Next, we plot the relationship between fidelity and filter strength for each target squeezing in Fig. 8.4. The continuous increase in fidelity as a function of filter strength shows good agreement with the theoretical model (see Table. 8.1 and 8.2 for more details). The deterministic limit is plotted to identify the minimum filter strength required to exceed this benchmark. As mentioned before, we clearly surpass this benchmark for all the data sets. Furthermore, by increasing the filter strength, we obtain higher fidelities that would have otherwise required significantly more squeezed ancilla in the conventional setup.

Finally, in contrast to data sets (B)–(E) where the maximum filter strength was limited to 3.5, we increased the filter strength for data set (A) to 12.5 to operate in the high-fidelity regime. In this demonstration, where the input magnitude was $|\alpha_\mathrm{in}| = 1.92$ and target squeezing was 2.3 dB, we measured a fidelity of 0.985 ± 0.001. This exceeds the highest possible fidelity using a deterministic squeezing gate even when a pure and infinitely squeezed ancilla is available after going through the same experimental loss as in our setup. For this dataset, we characterized the experiment with 1.8×10^8 runs and observed a success probability of 2.9×10^{-3}.

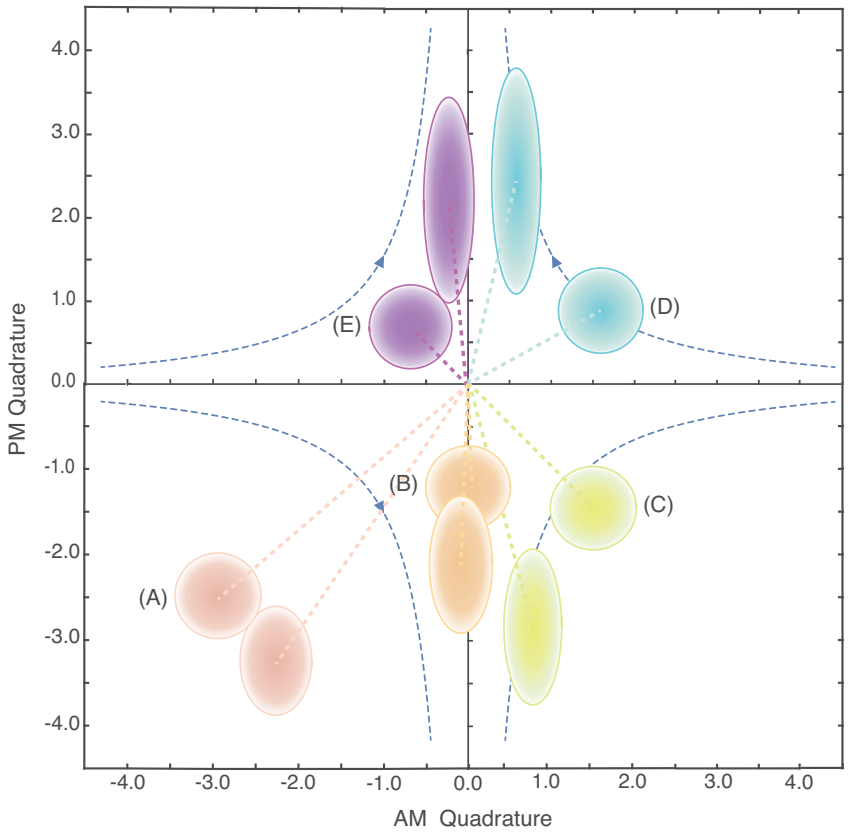

Figure 8.2: Phase space diagram for the squeezing gate. To verify faithfully the phase invariance of the squeezing operation, five coherent states, labelled as (A) to (E) and denoted by the noise contours (1 standard deviation width) of their Wigner functions, are created and inserted into our squeezing gate. The quadrature amplitudes of the input states are $(x_{\rm in}, y_{\rm in})$ =(-2.91,-2.50), (0.00,-1.40), (1.46,-1.43), (1.58,0.86), and (-0.67,0.68). The ellipse having the same colour as the input illustrates the corresponding squeezed output, obtained with highest fidelity.

8.3.4 Theoretical Model with Loss Considerations

In order to faithfully explain the behavior of our squeezing gate, we extend the theoretical model presented in Sec. 7.5 to account for our experimental imperfections. Two main losses are taken into account: first, the loss arising from the feed-forward process $\eta_{\rm d}$ and second, the loss attributed to the dark noise of our in-loop homodyne detectors $\eta_{\rm DN}$.

The loss is modelled as an ideal setup preceded by a virtual beamsplitter with partial transmittance that is determined by the efficiency of the setup. Accounting for the dark noise and the feed-foward noise yields an equivalent reflected mode on the first beam splitter

$$Y'_{\rm m} = \sqrt{\eta_{\rm d} t_{\rm s}} Y_{\rm sq} + \sqrt{\eta_{\rm d}(1-t_{\rm s})} Y_{\rm in} + \sqrt{1-\eta_{\rm d}} Y_{\rm v} + Y_{\rm DN}, \tag{8.1}$$

where the additional dark noise term, $Y_{\rm DN}$, has mean of zero and variance of 0.0625, corresponding to 12 dB dark noise clearance.

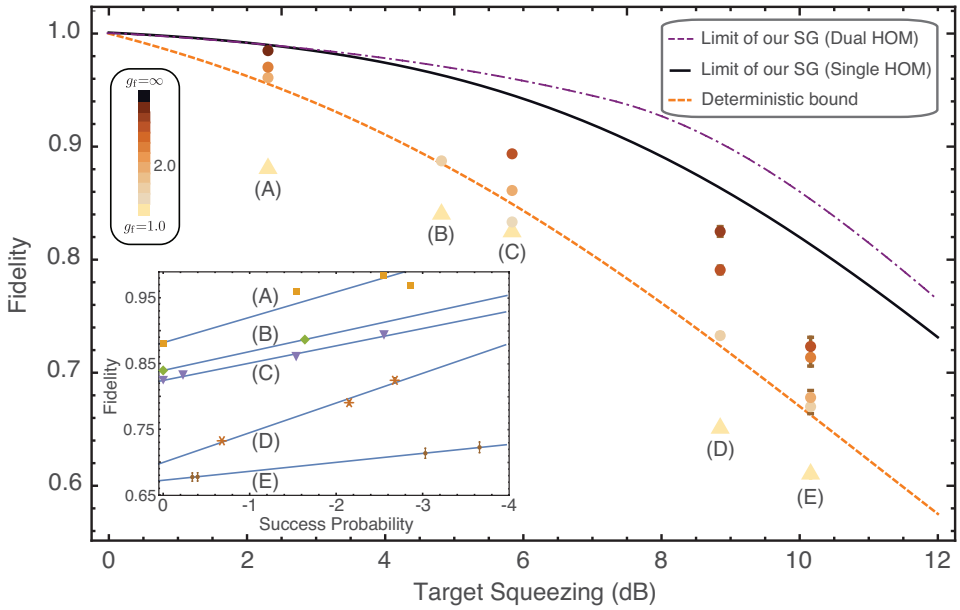

Figure 8.3: Improvement in fidelity over the conventional scheme for a series of target squeezing (A - E). The five target squeezing levels are chosen to be 2.30 dB, 4.81 dB, 5.84 dB, 8.85 dB, and 10.16 dB with t_s in Fig. 8.1 being set to 0.59, 0.33, 0.26, 0.23, and 0.10 accordingly. Performance of the present squeezing gate is examined in two scenarios: whilst the top purple (dash-dotted) line illustrates the best possible fidelity when a dual-quadrature homodyne is performed in-loop, the middle black line benchmarks the achievable fidelity if only the anti-squeezed quadrature is measured in-loop, that is $t_\mathrm{m} = 1$. In contrast, the bottom orange curve shows the obtainable fidelity with a conventional squeezing gate. All three lines assume the same initial squeezing resource as the experimental data sets (6.0 dB squeezing and purity of 1.12), but an ideal setup subject to no experimental imperfections instead. They showcase therefore the theoretical bounds for achievable fidelities in each situation. Experimental results, shown as round markers, are superimposed among which the triangle markers represent the resultant fidelity with filter strength $g_\mathrm{f} = 1$. A progressive enhancement in fidelity is demonstrated with an increase in g_f (darker gradient colour). Inset: success probability in logarithmic scale against fidelity for each target squeezing, where the success probability decays exponentially as the fidelity grows owing to a larger filter strength is applied. HOM: homodyne detection.

Hence the transmitted mode can be expressed correspondingly as

$$Y'_\mathrm{trans} = c'_\mathrm{y} Y'_\mathrm{m} + y'_0 + Y'_n, \tag{8.2}$$

where the correlation term now becomes

$$c'_\mathrm{y} = \frac{\mathrm{cov}(Y'_\mathrm{trans}, Y'_\mathrm{m})}{\sigma^2_{Y'_\mathrm{m}}} = \frac{\sqrt{\eta_\mathrm{d} t_\mathrm{s}(1-t_\mathrm{s})}(1-e^{2r_\mathrm{ay}})}{\eta_\mathrm{d} t_\mathrm{s} e^{2r_\mathrm{ay}} + \eta_\mathrm{d}(1-t_\mathrm{s}) + (1-\eta_\mathrm{d}) + Y_\mathrm{DN}}. \tag{8.3}$$

The mean factor y'_0 and noise factor Y'_n can be obtained in the same way as Eq. (7.18)

and (7.19)

$$\begin{aligned} y_0' &= \left(\sqrt{t_{\rm s}} - c_{\rm y}'\sqrt{\eta_{\rm d}(1-t_{\rm s})}\right)\bar{Y}_{\rm in}, \\ Y_{\rm n}' &= t_{\rm s} - (1-t_{\rm s})e^{2r_{\rm ay}} - c_{\rm y}'^2\left(\eta_{\rm d}t_{\rm s}e^{2r_{\rm ay}} + 1 - \eta_{\rm d}t_{\rm s} + Y_{\rm DN}\right). \end{aligned} \tag{8.4}$$

Applying the filter function in Eq. (7.20), rescaling the statistics $Y_{\rm m}$ to satisfy the unity-gain condition, and feed-forwarding the rescaled statistics onto the transmitted mode, we obtain the output mean and variance

$$\begin{aligned} \bar{Y}_{\rm out}' &= (c_{\rm y}' + g_{\rm y}')\sqrt{\eta_{\rm d}(1-t_{\rm s})}\bar{Y}_{\rm in} + y_0', \\ \sigma^2_{Y_{\rm out}'} &= (c_{\rm y}' + g_{\rm y}')^2 g_{\rm f}(\eta_{\rm d}t_{\rm s}e^{2r_{\rm ay}} + 1 - \eta_{\rm d}t_{\rm s} + Y_{\rm DN}) + Y_{\rm n}', \end{aligned} \tag{8.5}$$

where the rescaling factor $g_{\rm y}'$ can be derived by setting $\bar{y}_{\rm out}' = e^{r_{\rm t}}\bar{y}_{\rm in}$. The resultant fidelity can therefore be expressed as a function of the filter strength $g_{\rm f}$, the target squeezing $r_{\rm t}$, and the initial squeezed ancilla $r_{\rm a}$.

To obtain the theoretical plot in Fig. 8.4, for each target squeezing, we first evaluate the experimental loss η_d by terminating post-selection and implementing the squeezing gate in the conventional deterministic way. The heralded squeezing gate with filtering turned on is then carried out and sufficient data sets are collected to draw a fair comparison between the experiment and theory.

8.3.5 Evaluation of fidelity and its associated uncertainty

To avoid an overestimation of the final fidelity, for all data sets, the mean and variance of both the input and output states are corrected for the homodyne efficiency $\eta_{\rm h}$ (around 96%) which includes the interference visibility (98.5%) and the photodiode quantum efficiency (99%). The input and output mean after loss correction is obtained by rescaling the overall data by $1/\sqrt{\eta_{\rm h}}$ and the corresponding variance is obtained by subtracting $(1-\eta_{\rm h})/\eta_{\rm h}$ from the variance of the rescaled data.

Error bar of the experimental fidelity is ascribed to uncertainties in the output variances, the setting of $t_{\rm t}$ in the lab that determines the target squeezing level $r_{\rm s}$ and the finite sample size (N_x, N_y for amplitude, phase quadrature, respectively). It can be estimated according to the following equation:

$$\sigma^2_{\mathcal{F}} = \left(\frac{\partial\mathcal{F}}{\partial\sigma^2_{X_{\rm out}}}\right)^2 {\rm Var}(\sigma^2_{X_{\rm out}}) + \left(\frac{\partial\mathcal{F}}{\partial\sigma^2_{Y_{\rm out}}}\right)^2 {\rm Var}(\sigma^2_{Y_{\rm out}}) + \left(\frac{\partial\mathcal{F}}{\partial t_{\rm s}}\right)^2 {\rm Var}(\sigma^2_{t_{\rm s}}). \tag{8.6}$$

Suppose the unity-gain condition is always satisfied, so $\bar{X}_{\rm out} = e^{-r_{\rm t}}\bar{X}_{\rm in}$ and $\bar{Y}_{\rm out} =$

$e^{r_\mathrm{t}}\bar{Y}_\mathrm{in}$, the fidelity uncertainty can be written as:

$$\sigma_{\mathcal{F}}^2 = \frac{1}{\left[(t_\mathrm{s}+\sigma_{X_\mathrm{out}}^2)(1/t_\mathrm{s}+\sigma_{Y_\mathrm{out}}^2)\right]^3}\Big[\frac{(1/t_\mathrm{s}+\sigma_{Y_\mathrm{out}}^2)^2 2\sigma_{X_\mathrm{out}}^4}{N_x}, \\ + \frac{(t_\mathrm{s}+\sigma_{X_\mathrm{out}}^2)^2 2\sigma_{Y_\mathrm{out}}^4}{N_y} + \frac{(t_\mathrm{s}^2\sigma_{Y_\mathrm{out}}^2-\sigma_{X_\mathrm{out}}^2)^2 V_{t_\mathrm{s}}}{t_\mathrm{s}^4}\Big]. \tag{8.7}$$

For brevity, we express the output quadrature variance as V_{x_o}, V_{y_o} for amplitude and phase, respectively.

Here we consider the specific case of fidelity between two single-mode Gaussian states and $\rho_\mathrm{t}(\bar{x}_\mathrm{t}, \mathbf{V}_\mathrm{t})$, where the subscript out and t refers to the output squeezed state and the target state of the squeezing operation, respectively.

8.4 Discussions and Conclusions

In summary, we demonstrate a heralded squeezing gate based on measurement, feed-forward, and post-selection. It overcomes the technical difficulties in directly squeezing a quantum light field other than vacuum. Furthermore, we show that thanks to the post-selection, a significantly higher output fidelity is achievable in comparison to the conventional deterministic squeezing gate benchmarked on the same ancillary squeezing. The increase in fidelity as a function of filter strength shows good agreement with the theoretical prediction. In particular, we report a fidelity up to 98.5% for a target squeezing of 2.3 dB, utilizing 6.0 dB of ancillary squeezing. Such a high fidelity is unattainable deterministically even if we have a pure and infinitely squeezed resource at our disposal. More remarkably, by exploiting an unbalanced dual homodyne measurement in-loop, unity fidelity is approachable for any target squeezing less than the initial squeezed ancilla, which is otherwise impossible deterministically. The trade-off between fidelity and the success probability is demonstrated which can be optimized by tailoring the filter strength.

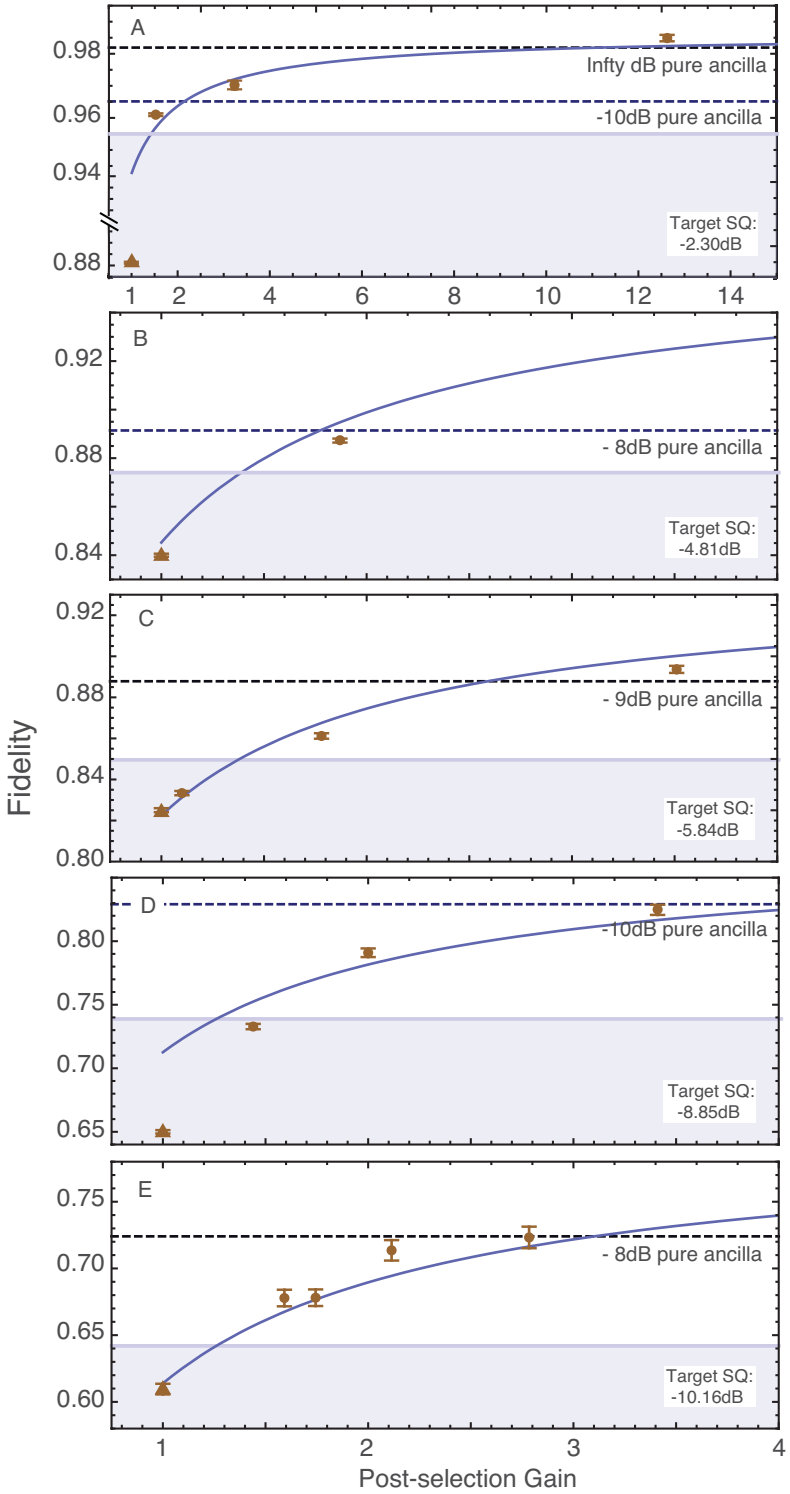

Figure 8.4: Fidelity as a function of the filter strength g_{f}. In all cases where different target squeezings are expected, fidelity consistently increases as a higher g_{f} is adopted, demonstrating a faithful agreement with the theoretical prediction (blue curves) that takes into account of experimental imperfections. The solid blue line denotes the best possible fidelity deterministically assuming no experimental loss is present and hence divides the parameter regime into two sections: the blue shaded area is accessible by a conventional scheme, whilst reaching the fidelity region beyond it would require a larger magnitude of ancillary squeezing. We show evidently this crucial requirement is circumvented with our squeezing gate. For the sake of fair comparison, we present also the obtainable fidelity (dashed darker blue lines) for a conventional squeezing gate operating with a more squeezed ancilla, but confronts the same experimental loss as we do.

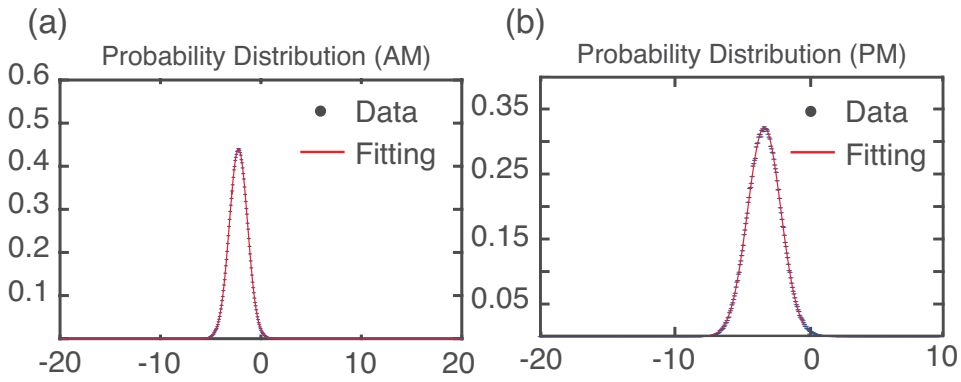

Figure 8.5: Normalized probability distribution for the squeezed (A) and anti-squeezed (B) quadratures of the output state. Blue dots refer to the remaining data points after post-selection that are selected from 1.8×10^8 initial homodyne measurements, while the red curves denote the best-fitted Gaussian distributions.

Chapter 9

Heralded Quantum Teleportation

9.1 Overview

In this chapter, we present a heralded continuous variable quantum teleportation scheme that reconciles the conventional discrete variable and continuous variable quantum teleportation. It allows one to tune between unit-fidelity and unit-success-probability operations by simply adjusting the parameter of a post-selection filter without reconfiguring the actual experimental setup. The remarkable feature of this teleportation scheme lies in its ability to completely correct loss incurred on the receiver's channel. Unit fidelity is attainable irrespective of the loss rate, so the transmission distance can be enhanced to an arbitrary extent. The long-standing technical hurdle - extending the distance of CV quantum teleportation - is surmounted in this way.

We examined the performance of our teleporter in terms of fidelity and an equivalent T-V diagram. We report the highest fidelity, 0.904 ± 0.001, ever achieved for CV quantum teleportation for a coherent state. In contrast to the previous state-of-the-art demonstration using vacuum as input, the unity-gain condition here is faithfully verified by matching the input and output quadrature amplitudes. We also observe the current best signal transfer coefficient and additional noise, $\mathcal{T}_q = 1.63$, $V_q' = 0.05$, for CV quantum teleportation to our knowledge. The simultaneous satisfaction of $\mathcal{T}_q > 1$ and $V_q' < 1$ evidently proclaims the success of a secure quantum teleportation. Our teleporter even enables an enhancement of signal-to-noise ratio of the original unknown input, which is conventionally inaccessible even with perfect EPR correlation. Together with its ability for error correction against a lossy channel, it has the potential to outperform the direct transmission of a coherent state, and hence realize the purification of a quantum information channel. Considering the multiple benefits our teleporter brings about, we envisage it has a wide range of applications in quantum information processing, especially in scale-up quantum networks and distributed quantum computation.

The relevant paper to this chapter is

• J. Zhao, K. Liu, J. Hao, S. Assad, J. Thompson, M. Gu, T. Ralph, and P. K. Lam. *Heralded continuous variable quantum teleportation.* (2018).

9.2 Introduction

Quantum teleportation constitutes one of the most important protocols in the burgeoning field of quantum information. In its own right, it demonstrates the ingenious idea of employing entanglement as a resource to facilitate signal transfer that has no classical analogue. Its discovery greatly spurs the union of quantum mechanics and information science, and therefore gives rise to a variety of novel quantum technologies. Firstly, quantum teleportation serves as an elementary component for constructing quantum networks [283, 284, 285]. Moreover, it has been shown to be an indispensable ingredient in measurement-base quantum computation, a promising framework for universal quantum computing [286].

The first experimental quantum teleportation, since the seminal work of Bennett et al. in 1993 [287], was conducted in photonic systems [288, 289]. Despite the low efficiency, the experiment demonstrated for the first time that this conceptual technique originating from science fiction was indeed feasible. There have been outstanding achievements in this fruitful area, especially among the discrete variable quantum information community. Teleportation has been developed from just a polarization qubit to multiple degree of freedoms of a single photon [290], from photonic to hybrid systems [291, 292, 293, 294, 295, 296, 297, 298, 299, 300, 301], and from laboratory configurations to intercontinental [302, 303, 304], and even ground-to-satellite employment [305]. Unit fidelity of DV teleportation comes with the price of instrinsic non-unit success rate (upper bounded by 50%), because the four Bell states are indistinguishable via only linear optics and photodetections [306, 307, 308].

The complementary continuous variable quantum teleportation [309] is renowned for its unconditional operations, high compatibility with classical communication infrastructure, and ease of implementation for it requires only Gaussian operations. However, the drawback associated with CV teleportation resides in its in-principle non-unit fidelity that is only achievable with infinitely squeezed resource. Besides, in contrast to the DV counterpart where teleportation distance has been remarkably extended to 143 km [304], remote midpoint configuration (up to 30.4 km) [37, 310, 302], and further to 1400 km recently [305], CV teleportation has been confined to a transmission distance of 12 m [311]. In terms of coherent input states which are particularly useful in CV quantum information, especially in CV quantum cryptography, the state-of-the-art quantum teleportation is restricted to table-top demonstrations [312, 313, 314, 315, 316, 317, 318]. This raises a formidable issue for CV quantum information as long-distance quantum teleportation is of crucial importance in large-scale quantum networks [283, 319, 2, 8, 320] and distributed quantum computation [321, 322, 286].

In this work, we propose and experimentally demonstrate a heralded CV quantum teleporter that provides an avenue to surmount the above technical obstacles.

The present scheme empowers one to tune between high-fidelity and high-success-probability teleportation by adjusting a post-selection filter strength, and hence can be regarded as a continuum from the conventional DV teleportation to CV teleportation.

Unity fidelity, previously only possible with infinite energy, can now be obtained by relaxing the requirement of a unit success probability. We report an experimental fidelity of 0.904 ± 0.001 for a coherent input state, which provides a new benchmark for CV quantum telerportation. This result significantly surpasses the classical teleportation limit (50%), and is also beyond the secure quantum teleportation criterion ($\mathcal{F} > 2/3$). More remarkably, we show that the post-selection works equivalently as error-correction that compensates any channel loss at the receiver's station; unit fidelity can be achieved regardless of the channel transmission rate. As such the distance of CV teleportation can be dramatically enhanced. Furthermore, we analyze the equivalent T-V diagram of the heralded quantum teleporter by investigating the signal transfer coefficient and additional noise incurred during the teleportation process. This criterion complements fidelity, making it accessible to evaluate the teleporter in both unity-gain and non-unity-gain regimes. We experimentally demonstrate the best result ever achieved for CV quantum teleporter relative to the T-V criterion: $\mathcal{T}_q = 1.63$ and $V_q' = 0.05$. The simultaneous fulfilment of $\mathcal{T}_q > 1$ and $V_q' < 1$ verifies the success of a quantum teleportation. Intriguingly, we note that in the non-unity gain regime, our heralded quantum teleporter can work analogously to a noiseless linear amplifier. $\mathcal{T}_q > 2$, which is conventionally impossible even with perfect EPR correlation, is within reach of the present scheme. The reconstructed state would possess an improved signal-to-noise ratio compared to the original unknown input, meaning for long distances, our teleporter outperforms the direct transmission of the same state through the same lossy channel.

9.3 Theoretical Modelling of Teleportation

9.3.1 Conventional Deterministic CV Teleportation

Figure 9.1 sketches a conventional CV teleporter that involves four steps. Firstly, a third party, Victor, prepares a quadrature entanglement and shares it between Alice and Bob who are remotely located from each other. Meanwhile, Victor supplies an input state selected from a suitable alphabet to Alice who couples it to her entangled beam and subsequently performs a joint measurement on amplitude and phase quadratures. Thirdly, the measurement outcomes are broadcast to Bob through classical communication. Based on the outcomes, Bob implements a local displacement operation to reconstruct the input state. A characterization of the final output state is independently carried out by Victor as the last step to verify the success of the teleportation. Two communication channels are utilized here. Entanglement serves as the quantum channel that allows for a faithful reconstruction of the input state despite the long distance

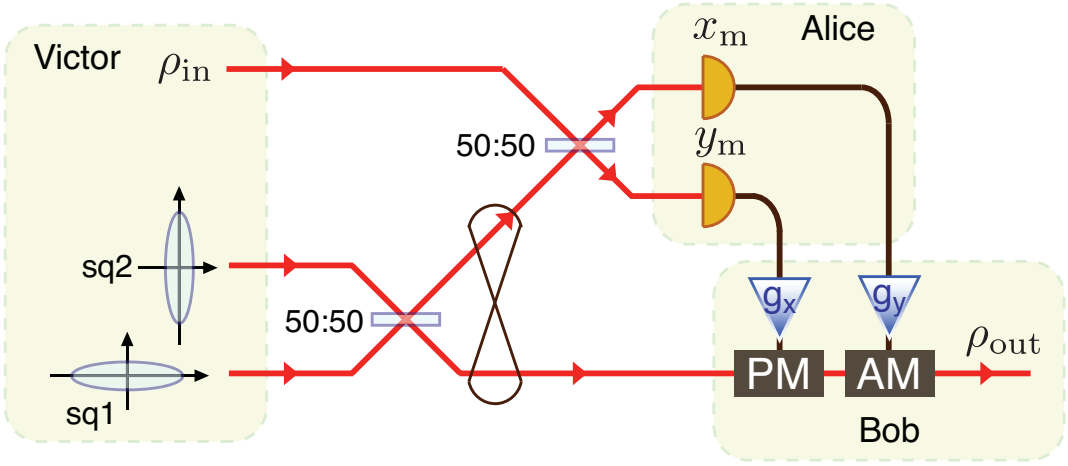

Figure 9.1: Conceptual model of a conventional deterministic continuous variable quantum teleporter. g_x and g_y represent the electronic rescaling factors; AM/PM stands for the amplitude/phase modulation.

between Alice and Bob and the additional noise incurred on Alice's two-quadrature measurement. The classical channel ensures that no information is transmitted faster than the speed of light. The input-output relation for the teleporter in the Heisenberg picture can be derived:

$$\begin{aligned} X_{\rm out} &= \frac{g_{\rm x}}{\sqrt{2}} X_{\rm in} + \left(\frac{g_{\rm x}}{2} + \frac{1}{\sqrt{2}}\right) X_{\rm sq1} + \left(\frac{g_{\rm x}}{2} - \frac{1}{\sqrt{2}}\right) X_{\rm sq2}, \\ Y_{\rm out} &= \frac{g_{\rm y}}{\sqrt{2}} Y_{\rm in} + \left(\frac{g_{\rm x}}{2} - \frac{1}{\sqrt{2}}\right) Y_{\rm sq1} - \left(\frac{g_{\rm x}}{2} + \frac{1}{\sqrt{2}}\right) Y_{\rm sq2}, \end{aligned} \tag{9.1}$$

resulting in an output variance of

$$\begin{aligned} \langle(\delta X_{\rm out})^2\rangle &= \frac{g_{\rm x}^2}{2}\langle(\delta X_{\rm in})^2\rangle + \left(\frac{g_{\rm x}}{2} + \frac{1}{\sqrt{2}}\right)^2 \langle(\delta X_{\rm sq1})^2\rangle + \left(\frac{g_{\rm x}}{2} - \frac{1}{\sqrt{2}}\right)^2 \langle(\delta X_{\rm sq2})^2\rangle, \\ \langle(\delta Y_{\rm out})^2\rangle &= \frac{g_{\rm y}^2}{2}\langle(\delta Y_{\rm in})^2\rangle + \left(\frac{g_{\rm y}}{2} - \frac{1}{\sqrt{2}}\right)^2 \langle(\delta Y_{\rm sq1})^2\rangle + \left(\frac{g_{\rm y}}{2} + \frac{1}{\sqrt{2}}\right)^2 \langle(\delta Y_{\rm sq2})^2\rangle. \end{aligned} \tag{9.2}$$

We see that the mean of the output quadrature amplitudes can be matched to that of the input by setting the electronic rescaling factors to $g_{\rm x} = g_{\rm y} = \sqrt{2}$. This yields an output state of

$$X_{\rm out} = X_{\rm in} + \sqrt{2} X_{\rm sq1}, \quad Y_{\rm out} = Y_{\rm in} - \sqrt{2} Y_{\rm sq2}. \tag{9.3}$$

Thus, the quadrature fluctuations in Eq. (9.2) reduces to (assuming shot-noise limited input, which means $\langle(\delta X_{\rm in})^2\rangle = \langle(\delta Y_{\rm in})^2\rangle = 1$)

$$\langle(\delta X_{\rm out})^2\rangle = 1 + 2e^{-2r_{1x}}, \quad \langle(\delta Y_{\rm out})^2\rangle = 1 + 2e^{-2r_{2y}}. \tag{9.4}$$

In the extreme case where infinite squeezing is accessible, $X_{\text{out}} = X_{\text{in}}$ and $Y_{\text{out}} = Y_{\text{in}}$, so that perfect reconstruction of the input state is achieved. This ideal case would lead to a unit fidelity, a signal transfer coefficient of 2, and zero additional noise incurred during the teleportation.

9.3.2 CV Quantum Teleportation Criteria

While an ideal CV quantum teleporter should be able to reconstruct the input state perfectly, practical teleportation is in principle constrained to non-unit efficiency. A perfect reconstruction is only possible with perfect EPR correlation, which, in continuous variable systems, requires infinitely squeezed resource. One would ask if perfect teleportation is impossible, how could we know if laboratory teleportation succeeds or not? Several empirical criteria have been proposed in this regard to quantify the efficiency of an experimental CV teleporter.

Fidelity and Unity Gain Condition

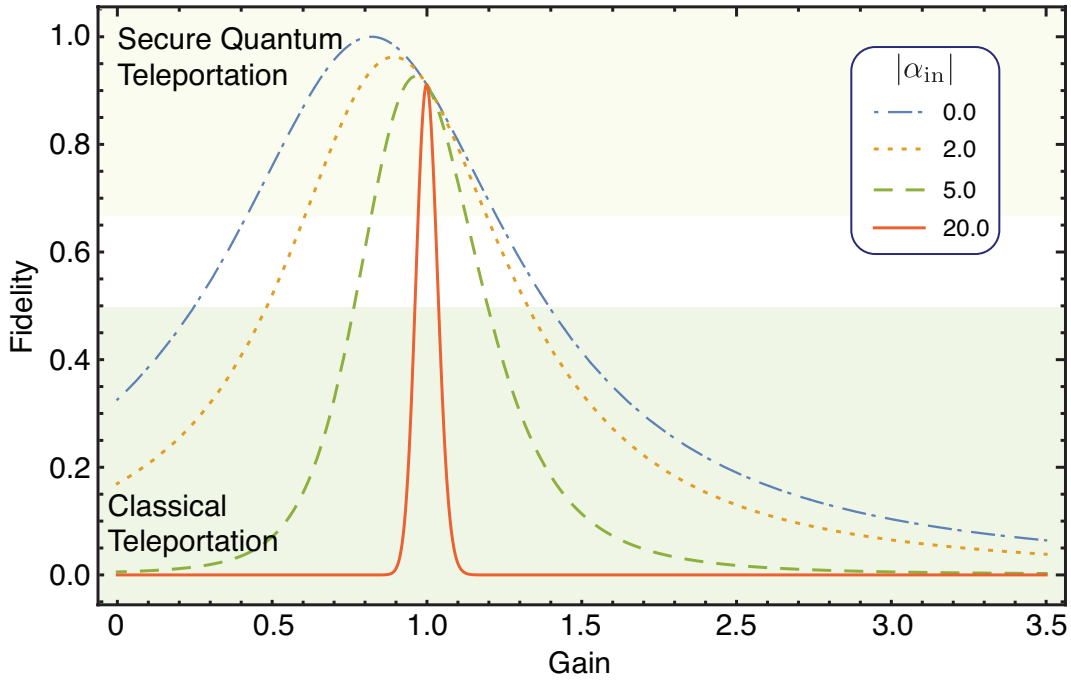

Figure 9.2: Fidelity as a function of the teleportation gain for various input amplitudes. The green shaded area denotes the operational region for a classical teleporter where $\mathcal{F} \leq 0.5$, while the yellow shaded area denotes a secure quantum teleportation with $\mathcal{F} > 2/3$, which could be useful for quantum cryptography. We assume here the magnitude of squeezing is 10 dB.

The most widely used criterion is fidelity that measures the overlap between the input state and the output state [323], as defined in Eq (7.1). Consider an alphabet comprised of coherent states with amplitudes following a Gaussian distribution. Selecting

one randomly as our input, the resultant fidelity is given by

$$\mathcal{F} = \frac{2}{\sqrt{(1+V_{X_{\rm out}})(1+V_{Y_{\rm out}})}} \exp\left[-\frac{1}{2}\left(\frac{(1-g'_x)^2\,\bar{X}^2_{\rm in}}{V_{X_{\rm out}}+1} + \frac{(1-g'_y)^2\,\bar{Y}^2_{\rm in}}{V_{Y_{\rm out}}+1}\right)\right], \tag{9.5}$$

where g'_x and g'_y are the teleportation gains that can be expressed in terms of the electronic rescaling factors in Eq. (9.2)

$$g'_x = g_x/\sqrt{2}, \quad g'_y = g_y/\sqrt{2}. \tag{9.6}$$

$\bar{X}(\bar{Y})$ and $V_X(V_Y)$ in Eq. (9.5) dictate, respectively, the mean and variance of the amplitude (phase) quadrature. The *unity-gain condition* refers to $g'_x = g'_y = 1$, so that $\bar{X}_{\rm out} = \bar{X}_{\rm in}$, $\bar{Y}_{\rm out} = \bar{Y}_{\rm in}$ and therefore, the exponential term in (9.5) vanishes, meaning $\mathcal{F}$ is independent of the input amplitudes. Otherwise, as is evidenced in Figure 9.2, there is an apparent dependence of fidelity on the input amplitudes. For a bright coherent input, the optimum fidelity is attained under the unity-gain condition and the gain bandwidth becomes increasingly narrower as the input amplitude increases. In contrast for a weak coherent state, higher fidelity is obtainable by adopting a smaller teleportation gain. This untrustworthy improvement in fidelity culminates at vacuum input, where unit fidelity can be achieved by simply turning off the teleporter. However, for unknown input picked up from a sufficiently broad alphabet, i.e. $\Delta|\alpha_{in}| \gg 1$, the optimum fidelity averaging over all possible inputs still appears at $g'_x = g'_y \approx 1$ where the equality holds for $\Delta|\alpha_{in}| \to \infty$. This means for the sake of a universal quantum teleporter capable of processing an arbitrary unknown input state, it is critical to fulfil the unity-gain condition to avoid any overestimation of the teleportation fidelity. From the experimental perspective, for vacuum input, it is thus essential to calibrate the system to ensure the unity-gain condition is actually satisfied, while for other input states, the unity-gain condition is satisfied by matching the output mean to that of the input.

There are two crucial bounds for measuring the success of a teleportation process relative to fidelity: first, $\mathcal{F} > 1/2$ identifies teleportation only achievable with the assistance of nonclassical light source, i.e. entangled states, and second, $\mathcal{F} > 2/3$ signifies a secure quantum teleportation where no eavesdropper can intercept more information than the receiver without being noticed by Alice and Bob.

9.3.3 T-V Diagram

Although fidelity provides a useful measure for the efficiency of teleportation with respect to the resemblance between the input and output, it does not reveal the exact information transfer coefficient during the teleportation process. For instances where the input states are non-classical [288, 289, 324, 325, 326, 327, 311], the ability to preserve the quantum feature of the state would constitute a more effective figure of merit. Besides, there might be situations where the input and output can be interconverted by

reversible transformations independent of the input. The output indeed contains all necessary information for an accurate reconstruction. So teleportation in such occasions can be regarded as successful although fidelity may indicate the process is inefficient. To this end, other criteria have been proposed to complement fidelity to offer a more complete assessment of the experimental teleportation systems.

One such example is the T-V diagram proposed by Ralph and Lam [328, 329], which probes the signal transfer coefficient of the system and the quantum correlation between the input and the reconstructed output. It is an analogue of the criterion for quantifying the performance of a quantum non-demolition measurement [330]. $\mathcal{T}_q$ indicates the *joint signal transfer coefficient*

$$\mathcal{T}_q = \mathcal{T}_{\mathrm{x}} + \mathcal{T}_{\mathrm{y}} = \frac{\mathrm{SNR}_{\mathrm{xout}}}{\mathrm{SNR}_{\mathrm{xin}}} + \frac{\mathrm{SNR}_{\mathrm{yout}}}{\mathrm{SNR}_{\mathrm{yin}}} = \frac{\langle X_{\mathrm{out}}\rangle^2}{\langle (\delta X_{\mathrm{out}})^2\rangle} + \frac{\langle Y_{\mathrm{out}}\rangle^2}{\langle (\delta Y_{\mathrm{out}})^2\rangle}, \tag{9.7}$$

while V_q signifies the input-output conditional variance

$$Vq = \frac{V_{X_{\mathrm{out}}|X_{\mathrm{in}}} + V_{Y_{\mathrm{out}}|Y_{\mathrm{in}}}}{2} = \frac{\langle (\delta X_{\mathrm{out}})^2\rangle - \frac{|\langle \delta X_{\mathrm{out}}\delta X_{\mathrm{in}}|^2}{\langle (\delta X_{\mathrm{in}})^2\rangle} + \langle (\delta Y_{\mathrm{out}})^2\rangle - \frac{|\langle \delta Y_{\mathrm{out}}\delta Y_{\mathrm{in}}|^2}{\langle (\delta Y_{\mathrm{in}})^2\rangle}}{2}. \tag{9.8}$$

$\mathcal{T}_q$ identifies how much information is successfully recovered, while V_q dictates how closely the output is correlated to the input. For a perfect reconstruction on the receiving station, $\mathcal{T}_q = 2$, implying that full knowledge of the unknown input is obtained by Bob, and $V_q = 0$, indicating that the output is maximally correlated to the original input. However, this limit is only achievable with perfect EPR correlation that requires infinitely squeezed sources. In stark contrast, the T-V of a classical teleportation subject to no entanglement (the measure-and-prepare scheme) is bounded by

$$V_q \geq 1, \mathcal{T}_q \leq 1. \tag{9.9}$$

The constraints are ascribed to the noise penalty imposed onto simultaneous measurement on conjugate quadratures by Heisenberg uncertainty principle. This additional noise inevitably degrades the signal transfer coefficient and input-output correlation, rendering perfect reconstruction impossible with only classical sources. On the other hand, the criteria for a successful quantum teleportation is $\mathcal{T}_q > 1$ and $V_q < 1$, dictating that both the signal transfer coefficient and input-output correlation have exceeded their corresponding classical limit. In the unity-gain regime, the satisfaction of these criteria is equivalent to the saturation of the no-cloning limit in terms of fidelity $\mathcal{F} > 2/3$ [323]. To achieve this more stringent criterion, both Alice's and Bob's channels are required to have transmission $> 50\%$ for any entanglement, and more than 3 dB of initial squeezing (50% noise suppression) is demanded *a priori* for EPR generation.

One drawback of the T-V diagram is that the conditional variance is not directly measurable, since the original input state is necessarily disembodied during teleportation in compliance with the quantum no-cloning theorem. Grangier and Grosshans

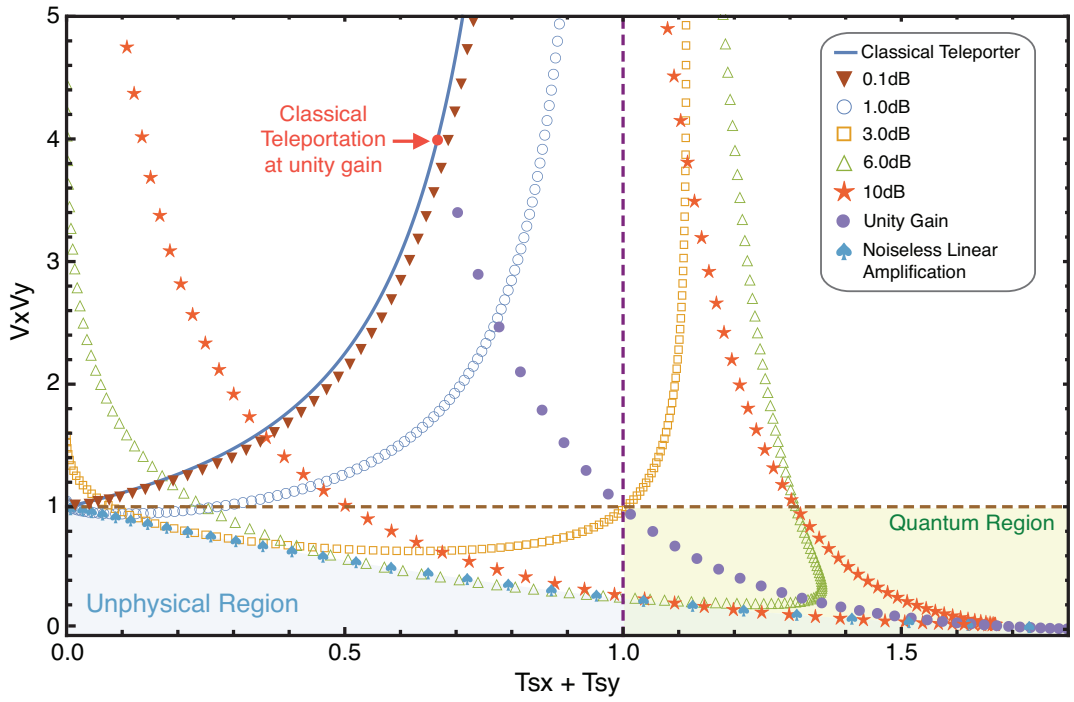

Figure 9.3: Equivalent T-V diagram for the conventional deterministic CV teleporter. The blue curve shows the T-V for a classical teleporter, while different markers illustrate the T-V for teleporter with various levels of squeezed sources. The purple dots refer to teleportation that operates in the unity-gain regime. The blue spades represent the T-V for a noiseless linear amplifier which benchmarks the unphysical region shaded as light blue.

thus suggested to drop V_q and utilize $\mathcal{T}_q$ alone [331]. Another reason for this argument lies in the observation that there is a contradiction between the T-V diagram and the conventionally-used fidelity criterion, where the unity-gain condition that leads to a peaked maximum of fidelity would result in an inferior teleportation performance with respect to signal transfer coefficient and input-output conditional variance. Grangier et al. proposed an alternative criterion for successful teleportation relative to the *equivalent input noise* N_x^{out} and N_y^{out}

$$\delta N_x^{\text{out}} \delta N_y^{\text{out}} < 1, \tag{9.10}$$

where

$$\langle (\delta N_x^{\text{out}})^2 \rangle = \frac{\langle (\delta X_{\text{out}})^2 \rangle}{g_x'^2} - \langle (\delta X_{\text{in}})^2 \rangle, \quad \langle (\delta N_y^{\text{out}})^2 \rangle = \frac{\langle (\delta Y_{\text{out}})^2 \rangle}{g_y'^2} - \langle (\delta Y_{\text{in}})^2 \rangle. \tag{9.11}$$

Here, g_x' and g_y' are the teleportation gains defined in Eq. (9.6). They show that when $g_x' = g_y' = 1$, Eq. (9.10) is equivalent to the criterion $\mathcal{T}_q > 1$ and $\mathcal{F} > 2/3$. The aforementioned disparity between fidelity and the T-V diagram, therefore, disappears if one adheres to the unity-gain condition. In fact in this regime all criteria agree with each other,

so Grangier et al. concluded that teleporation is only valid to operate in the unity-gain regime.

The proof of Eq. (9.10) was accomplished by decomposing $N_x^{\rm out}$ into the noise incurred during Alice's dual-quadrature measurement, X_m, and the noise introduced by Bob's reconstruction, X_r, which means $N_x^{\rm out} = X_m + X_r$. The input-output relation under unity-gain condition then becomes

$$X_{\rm out} = X_{\rm in} + X_m + X_r, \quad Y_{\rm out} = Y_{\rm in} + Y_m + Y_r. \tag{9.12}$$

The success of teleportation is heralded by a violation of the Heisenberg inequality [332], or in other words the presence of non-separability: measurements on conjugate quadratures of mode a would lead to inference on the measurement results of two conjugate quadratures of another remote mode b, in such a way that product of conditional variances apparently violates the Heisenberg inequality [333]

$$V_{X_r|X_m} V_{Y_r|Y_m} \geq 1, \quad V_{X_{\rm m}|X_{\rm r}} V_{Y_{\rm m}|Y_{\rm r}} \geq 1. \tag{9.13}$$

It was proven that this condition is equivalent to Eq. (9.10) and is consistent with $\mathcal{T}_q > 1$ and $\mathcal{F} > 2/3$. We note that in the unity-gain regime, the equivalent input noise in Eq. (9.11) is mathematically and physically equal to the input-output conditional variance in Ralph and Lam's TV diagram, namely $\langle (\delta N_x^{\rm out})^2 \rangle = V_{X_{\rm out}|X_{\rm in}}$. The equivalence between the criteria Eq. (9.10) and $\mathcal{T}_q > 1$, therefore, reasonably verifies the statement that $\mathcal{T}_q$ and V_q give partly redundant information and either one would be sufficient to characterize the performance of the teleporter. But we emphasize that the validity of this statement is restricted to the unity-gain regime.

Warwick Bowen et al. extended the criterion in Eq. (9.10) to the non-unity-gain regime following the same methodology by dividing the total additional noise $N_{\rm xout}$ and $N_{\rm yout}$ into the noise attributed from Alice's measurement, $N_x^{\rm Alice}$, and that results from Bob's reconstruction, $N_x^{\rm Bob}$,

$$N_{\rm xout} = \Pi_x N_x^{\rm Alice} + N_x^{\rm Bob}, \quad N_{\rm yout} = \Pi_y N_y^{\rm Alice} + N_y^{\rm Bob}. \tag{9.14}$$

where Π_x and Π_y denote the gains implemented on amplitude and phase quadratures by Bob for reconstruction. The input-output relation can be expressed as

$$X_{\rm out} = g_x' X_{\rm in} + \Pi_x N_x^{\rm Alice} + N_x^{\rm Bob}, \quad Y_{\rm out} = g_y' Y_{\rm in} + \Pi_y N_y^{\rm Alice} + N_y^{\rm Bob}, \tag{9.15}$$

The requirement that the noise introduced by Alice and Bob are separable leads to the criterion that

$$V_q' = \langle (\delta N_{\rm xout})^2 \rangle \langle (\delta N_{\rm yout})^2 \rangle \geq \left(|g_x' g_y'| + 1 \right)^2. \tag{9.16}$$

Based on Eq. (9.16), Bowen et al. proposed the *gain normalized conditional variance product*

$\mathcal{M}$ as a new measure for the efficiency of teleportation

$$\mathcal{M} = \frac{V_q'}{\left(|g_x' g_y'| + 1\right)^2}. \tag{9.17}$$

Classical teleportation is thus bounded by $\mathcal{M} \geq 1$ where the best result $\mathcal{M} = 1$ is obtained for $g_x' = g_y' = \Pi_x = \Pi_y = 0$.

As showed before, all criteria mentioned above, including fidelity discussed in the previous section, coincide with each other under the unity-gain condition. The ideas behind the input-output conditional variance, the equivalent input noise, and the gain normalized conditional variance product are consistent although disparity exists between these criteria and fidelity in the gain tuning regime. For the quantification of conventional teleporters which are supposed to be an identity channel by default, it is reasonable to adhere to the unity-gain condition. Nevertheless, for more general characterization of teleportation as a combination of a classical and a quantum channel, T-V diagrams would be a more illuminating figure of merit for investigating the channel properties.

In Fig. 9.3, we plot an equivalent T-V diagram for a conventional deterministic teleporter. $\mathcal{T}_q$ here refers to the signal transfer coefficient defined in Eq. (9.7) and V_q' dictates the additional noise during teleportation defined in Eq. (9.16). For the classical teleporter, an increased gain increases the signal transfer coefficient, makes it approach 1, at the expense of introducing more additional noise. The least amount of additional noise occurs when $g_x' = g_y' = 0$; however, information about the input state is completely discarded, giving a signal transfer coefficient of 0. The unity-gain curve (purple dots) intersects with the classical teleportation curve at the red point corresponding to a fidelity of $1/2$. The intersection between the unity-gain curve and the 3 dB squeezing curve gives $\mathcal{T}_q = V_q' = 1$, and a fidelity of $2/3$. In accordance with Ralph and Lam's conclusion, this dictates at least 3 dB of squeezed sources are required to successfully teleport a quantum state with fidelity beyond the no-cloning limit. Any teleportation surpassing this limit enters the quantum teleportation region shown as the yellow shaded area. Note that although a smaller magnitude of squeezing (< 3 dB) allows us to obtain either $V_q' < 1$ or $\mathcal{T}_q > 1$ in the non-unity gain regime, it does not suffice to fulfil both criteria simultaneously. This means in the unity-gain regime, $\mathcal{T}_q$ alone provides a necessary and sufficient criterion; however, in the complementary regime, only if both the additional noise and signal transfer were subject to close scrutiny, could one obtain a full picture of the teleportation system.

9.3.4 Heralded CV Quantum Teleportation

We construct and experimentally demonstrate a heralded CV teleporter by incorporating a post-selection function into the classical communication channel of the conventional CV teleporter, as pictured in Fig. 9.4. In contrast to the conventional CV teleporter

where fidelity is intrinsically limited by the amount of accessible EPR correlation, our teleporter permits unit fidelity with a modest level of entanglement. The price to be paid is a finite success probability. Our teleporter works in resemblance to a favourable combination of the DV and CV teleporter, allowing one to tune between high-fidelity and high-success-rate operations. In this section, we provide the theoretical modelling of our teleporter based on the evolution of the system's covariance matrix.

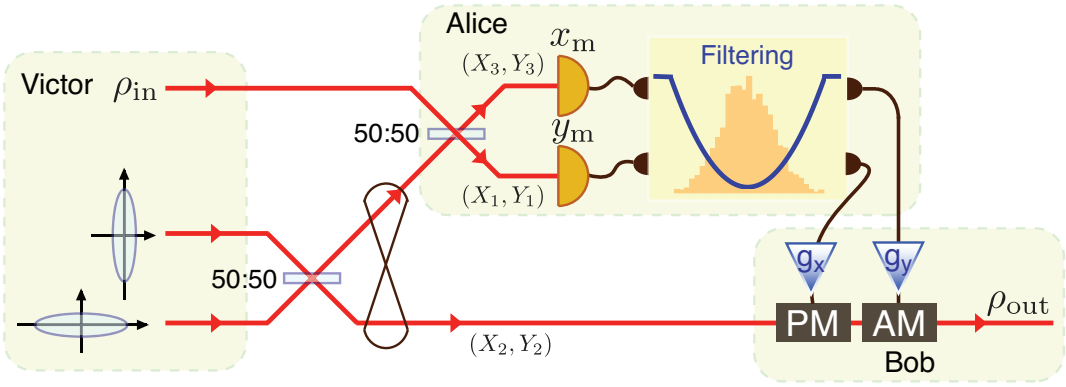

Figure 9.4: Schematic drawing of our heralded high-fidelity quantum teleporter. The notations (X_n, Y_n) refers to the quadrature amplitudes of mode n.

We start with the covariance matrix of the quadrature entanglement that is generated by combining two squeezed states with squeezing parameters $r_{1x(y)}$ and $r_{2x(y)}$, where the subscript $x(y)$ dictates the amplitude (phase) quadrature:

$$\begin{pmatrix} CV_{11} & 0 & CV_{13} & 0 \\ 0 & CV_{22} & 0 & CV_{24} \\ CV_{13} & 0 & CV_{11} & 0 \\ 0 & CV_{24} & 0 & CV_{22} \end{pmatrix}. \tag{9.18}$$

The matrix elements are given by

$$\begin{aligned} CV_{11} &= \frac{e^{-2r_{1x}} + e^{2r_{2x}}}{2}, \quad CV_{22} = \frac{e^{-2r_{2y}} + e^{2r_{1y}}}{2}, \\ CV_{13} &= \frac{e^{2r_{2x}} - e^{-2r_{1x}}}{2}, \quad CV_{24} = \frac{e^{-2r_{2y}} - e^{2r_{1y}}}{2}. \end{aligned} \tag{9.19}$$

In circumstances where the initial squeezed sources are pure and identical, i.e. $r_{1x} = r_{1y} = r_{2x} = r_{2y}$, the covariance matrix in Eq. (9.18) specializes to its more commonly used form, shown in Eq. (2.33). An unknown input state is then inserted into our device and coupled with one arm of the entangled beam on a beam splitter with transmittance

of 50%, giving rise to the combined modes:

$$CV = \begin{pmatrix} CV_{11} & 0 & CV_{13}/\sqrt{2} & 0 & CV_{13}/\sqrt{2} & 0 \\ 0 & CV_{22} & 0 & CV_{24}/\sqrt{2} & 0 & CV_{24}/\sqrt{2} \\ CV_{13}/\sqrt{2} & 0 & (1+CV_{11})/2 & 0 & (CV_{11}-1)/2 & 0 \\ 0 & CV_{24}/\sqrt{2} & 0 & (CV_{22}+1)/2 & 0 & (CV_{22}-1)/2 \\ CV_{13}/\sqrt{2} & 0 & (CV_{11}-1)/2 & 0 & (CV_{11}+1)/2 & 0 \\ 0 & CV_{24}/\sqrt{2} & 0 & (CV_{22}-1)/2 & 0 & (CV_{22}+1)/2 \end{pmatrix}. \tag{9.20}$$

The two outgoing modes of the beam splitter are subject to a dual-quadrature homodyne setup performed by Alice to measure the amplitude and phase quadratures simultaneously. The EPR arm on Bob's side evolves accordingly conditioned upon Alice's measurement outcome $\alpha_m = (x_m + iy_m)/\sqrt{2}$. The variables

$$\begin{aligned} \mu_{X_2|x_m} &= \langle X_2 \rangle + \frac{\langle X_2 X_3 \rangle}{\langle X_3 X_3 \rangle} \left(x_m - \langle X_3 \rangle \right) = \frac{-\sqrt{2} CV_{13}}{1+CV_{11}} \left(x_m - \frac{\langle X_{\text{in}} \rangle}{\sqrt{2}} \right)^T, \\ \Sigma_{X_2|x_m} &= \langle (\delta X_2)^2 \rangle - \frac{\langle X_2 X_3 \rangle \langle X_3 X_2 \rangle}{\langle X_3 X_3 \rangle} = CV_{11} - \frac{CV_{13}^2}{1+CV_{11}} \end{aligned} \tag{9.21}$$

represent, respectively, the conditional mean and variance of the amplitude quadrature, and

$$\begin{aligned} \mu_{Y_2|y_m} &= \langle Y_2 \rangle + \frac{\langle Y_2 Y_1 \rangle}{Y_1 Y_1} \left(y_m - \langle Y_1 \rangle \right) = \frac{\sqrt{2} CV_{24}}{1+CV_{22}} \left(y_m - \frac{\langle Y_{\text{in}} \rangle}{\sqrt{2}} \right)^T, \\ \Sigma_{Y_2|y_m} &= \langle (\delta Y_2)^2 \rangle - \frac{\langle Y_2 Y_1 \rangle \langle Y_1 Y_2 \rangle}{\langle Y_1 Y_1 \rangle} = CV_{22} - \frac{CV_{24}^2}{1+CV_{22}} \end{aligned} \tag{9.22}$$

represent, respectively, the conditional mean and variance of the phase quadrature. $\langle X_n X_m \rangle = \langle \Delta X_n \Delta X_m \rangle$ denotes the covariance between the amplitude quadrature of modes n and m, and for brevity, Δ is omitted in the derivations. It is interesting to note that the unused EPR mode, conditioned on a dual homodyne measurement on the other mode, turns out to be a coherent state if the original squeezed states that comprise the EPR are identical (not necessarily pure), as illustrated in Fig. 9.5. Otherwise, when $r_{2x} > r_{1x}$–implying that the EPR ball in phase space is elongated along the amplitude quadrature–the conditional state is a phase-squeezed state, and vice versa. A remote squeezing gate can be constructed in this way, whereby optimum squeezing is obtained when Victor directly sends one of the initial squeezed states to Bob.

Before transmitting her measurement outcomes to Bob, Alice performs a local post-selection on the measurement records: keeping and discarding data samples based on

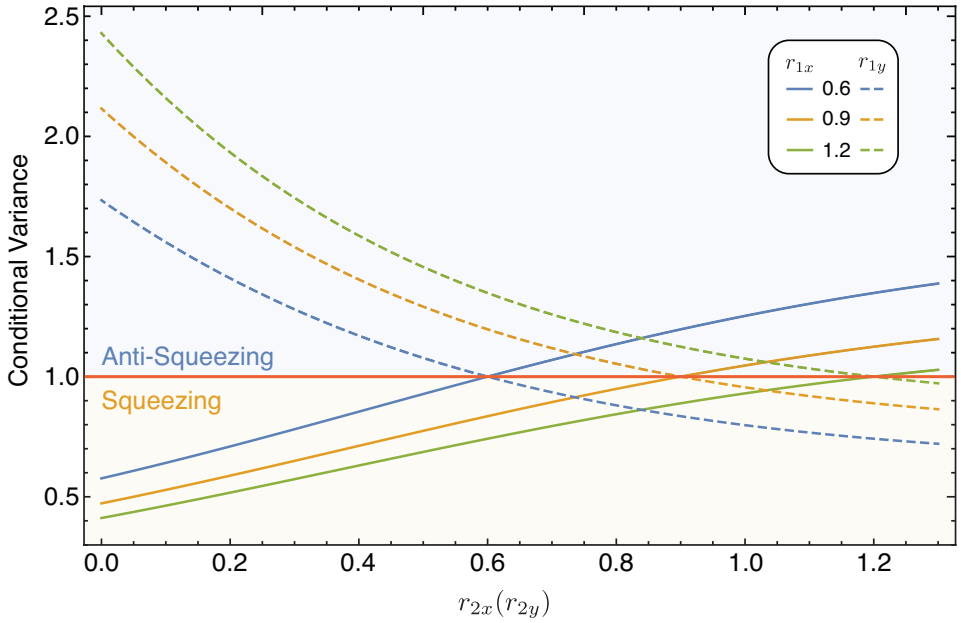

Figure 9.5: Variances of the amplitude (solid curves) and phase quadrature (dashed curves) of the EPR mode on Bob's side conditioned on Alice's dual homodyne measurement for a series of initial squeezing levels.

the inverse-Gaussian filter described in chapter 4:

$$p(\alpha_{\rm m}) = \begin{cases} \exp\left[\left(|\alpha_{\rm m}|^2 - \alpha_{\rm c}^2\right)\left(1 - \frac{1}{g_{\rm f}}\right)\right] & \text{for } |\alpha_{\rm m}| < \alpha_{\rm c}\,, \\ 1 & \text{for } |\alpha_{\rm m}| \geq \alpha_{\rm c}\,. \end{cases} \tag{9.23}$$

α_c is the filter cut-off that determines the operational region of the post-selection, while $g_{\rm f}$ is the filter strength. In a nutshell, the post-selection works analogously to an entanglement distillation: entanglement disguised under noise is distilled by increasing $g_{\rm f}$ and hence the teleportation fidelity is enhanced, at the expense of a finite success probability. The other functionality of this post-selection is to avoid the noise penalty associated with Alice's dual-quadrature measurement. By increasing the filter strength, the conjugate quadratures can be estimated with arbitrarily high accuracy and therefore, perfect reconstruction of the initial input state can be achieved. The post-selected statistics has an amplified mean and variance of the amplitude quadrature (c.f. Sec. 4.2)

$$\langle X_3\rangle \to g_{\rm f}^2\langle X_3\rangle, \quad \langle(\delta X_3)^2\rangle \to g_{\rm f}^2\langle(\delta X_3)^2\rangle = g_{\rm f}^2(1 + CV_{11})/2. \tag{9.24}$$

Similarly, for the phase quadrature,

$$\langle Y_1\rangle \to g_{\rm f}^2\langle Y_1\rangle, \quad \langle(\delta Y_1)^2\rangle \to g_{\rm f}^2\langle(\delta Y_1)^2\rangle = g_{\rm f}^2(1 + CV_{22})/2. \tag{9.25}$$

In accordance with the principle that post-selection should have no impact on the condi-

tional statistical properties of the unused EPR mode, the following relations must hold:

$$\frac{\langle X_2' X_3' \rangle}{\langle X_3' X_3' \rangle} = \frac{\langle X_2 X_3 \rangle}{\langle X_3 X_3 \rangle}, \quad \langle X_2' X_2' \rangle - \frac{\langle X_2' X_3' \rangle \langle X_3' X_2' \rangle}{\langle X_3' X_3' \rangle} = \langle X_2 X_2 \rangle - \frac{\langle X_2 X_3 \rangle \langle X_3 X_2 \rangle}{\langle X_3 X_3 \rangle}. \quad (9.26)$$

$\langle X_n' X_m' \rangle$ refers to the covariance between the variables X_n' and X_m' resulting from the post-selection, with the superscript $'$ implying that the corresponding variable undergoes post-selection. The same relations hold for the phase quadrature as well. The elements of the covariance matrix after post-selection can be deduced from Eq. (9.26), (9.20), and (9.24):

$$\begin{aligned}
\langle X_2' X_3' \rangle &= \frac{\langle X_2 X_3 \rangle \langle X_3' X_3' \rangle}{\langle X_3 X_3 \rangle} = \frac{-CV_{13} g_{\mathrm{f}}^2}{\sqrt{2}}, \quad \langle Y_2' Y_1' \rangle = \frac{\langle Y_2 Y_1 \rangle}{\langle Y_1 Y_1 \rangle \langle Y_1' Y_1' \rangle} = \frac{CV_{24} g_{\mathrm{f}}^2}{\sqrt{2}}, \\
\langle X_2' X_2' \rangle &= \Sigma_{X_2|x_m} + \frac{\langle X_2' X_3' \rangle \langle X_3' X_2' \rangle}{\langle X_3' X_3' \rangle} = \frac{CV_{11} + CV_{11}^2 + CV_{13}^2 (g_{\mathrm{f}}^2 - 1)}{1 + CV_{11}}, \\
\langle Y_2' Y_2' \rangle &= \Sigma_{Y_2|y_m} + \frac{\langle Y_2' Y_1' \rangle \langle Y_1' Y_2' \rangle}{\langle Y_1' Y_1' \rangle} = \frac{CV_{22} + CV_{22}^2 + CV_{24}^2 (g_{\mathrm{f}}^2 - 1)}{1 + CV_{22}},
\end{aligned} \quad (9.27)$$

where we have used the relation $\langle (\delta X_n)^2 \rangle = \langle X_n X_n \rangle, n \in (1, 2, 3)$. The equations on the first row denote the correlation between the statistics owned by Alice and Bob, respectively, while $\langle X_2' X_2' \rangle$ and $\langle Y_2' Y_2' \rangle$ represent the conditional variances in amplitude and phase of the EPR mode at Bob's side after Alice performs the post-selection. We can also derive the conditional mean of the amplitude and phase quadratures following the same methodology:

$$\begin{aligned}
\mu'_{X_2|x_m'} &= \mu_{X_2|x_m} + \frac{\langle X_2' X_3' \rangle}{\langle X_3' X_3' \rangle} \left(g_{\mathrm{f}}^2 x_m - \frac{\langle X_{\mathrm{in}} \rangle}{\sqrt{2}} \right) = \frac{CV_{13} \left(1 - g_{\mathrm{f}}^2\right) \langle X_{\mathrm{in}} \rangle}{1 + CV_{11}}, \\
\mu'_{Y_2|y_m'} &= \mu_{Y_2|y_m} + \frac{\langle Y_2' Y_1' \rangle}{\langle Y_1' Y_1' \rangle} (g_{\mathrm{f}}^2 y_m - \frac{\langle Y_{\mathrm{in}} \rangle}{\sqrt{2}}) = \frac{CV_{24} \left(g_{\mathrm{f}}^2 - 1\right) \langle Y_{\mathrm{in}} \rangle}{1 + CV_{22}}.
\end{aligned} \quad (9.28)$$

The post-selected statistics are sent to Bob subsequently via a classical channel. To accomplish the reconstruction of the unknown input state, Bob first rescales the amplitude and phase data by g_{x} and g_{y}, respectively, and then performs a local displacement on his EPR beam accordingly. The expectation values of the amplitude and phase quadratures of the output state are given by

$$\langle X_{\mathrm{out}} \rangle = \mu'_{X_2|x_m'} + g_{\mathrm{x}} g_{\mathrm{f}}^2 \langle X_{\mathrm{in}} \rangle / \sqrt{2}, \quad \langle Y_{\mathrm{out}} \rangle = \mu'_{Y_2|y_m'} + g_{\mathrm{y}} g_{\mathrm{f}}^2 \langle Y_{\mathrm{in}} \rangle / \sqrt{2}, \quad (9.29)$$

while the quadrature variances are

$$\begin{aligned}
\langle (\delta X_{\mathrm{out}})^2 \rangle &= \langle X_2' X_2' \rangle + 2 g_{\mathrm{x}} \langle X_2' X_3' \rangle + g_{\mathrm{x}}^2 g_{\mathrm{f}}^2 (1 + CV_{11})/2, \\
\langle (\delta Y_{\mathrm{out}})^2 \rangle &= \langle Y_2' Y_2' \rangle + 2 g_{\mathrm{y}} \langle Y_2' Y_1' \rangle + g_{\mathrm{y}}^2 g_{\mathrm{f}}^2 (1 + CV_{22})/2.
\end{aligned} \quad (9.30)$$

We have used Eq. (9.24) and (9.25) in the above derivation. The filter strength, denoted by g_{f}, and the rescaling operation, signified by $g_{\mathrm{x(y)}}$, complement each other to ensure the unity-gain condition discussed in Sec. 9.3.2 is satisfied. As a result, the rescaling factors can be expressed as the function of g_{f}

$$g_{\mathrm{x}} = \frac{\sqrt{2}\left[1 + CV_{11} + CV_{13}(g_{\mathrm{f}}^2 - 1)\right]}{g_{\mathrm{f}}^2(1 + CV_{11})}, \quad g_{\mathrm{y}} = \frac{\sqrt{2}\left[1 + CV_{22} - CV_{24}(g_{\mathrm{f}}^2 - 1)\right]}{g_{\mathrm{f}}^2(1 + CV_{22})}, \tag{9.31}$$

which are independent of the input amplitude. Unlike the conventional teleportation scheme where unity gain corresponds to $g_{\mathrm{x}} = g_{\mathrm{y}} = \sqrt{2}$ in all circumstances, the fulfilment of unity gain in our system does require a prior knowledge of the magnitude of the squeezed sources. Nevertheless, the input-invariant feature of a teleporter is retained, whereby the unity-gain conditional is satisfied irrespectively of the input amplitude.

9.3.5 Fidelity as a Function of the NLA Gains

Figure 9.6 plots the fidelity of Bob's reconstructed state with respect to the unknown input as a function of filter strength. We notice that with the help of post-selection, fidelity that is only obtainable with 20 dB squeezing in the conventional scheme is now achievable with 6 dB squeezing. This significantly surmounts the technical difficulty associated with the generation of high-magnitude squeezing. More remarkably, unit fidelity that would require infinitely squeezed resource conventionally can be achieved with an arbitrary level of squeezing in the present scheme, provided that a sufficient filter strength is adopted.

In Fig. 9.6 (a), we explore the teleportation fidelity if impure squeezed states are utilized for producing the quadrature entanglement. A considerable degradation in fidelity is observed as compared to the pure case, and this discrepancy remains even if infinite filter strength were applied. In contrast, we investigate in Fig. 9.6 (b) how the fidelity is affected if non-identical squeezed states were used to generate entanglement. Although the teleporter behaves inferior in this imperfect situation when the filter strength is small, it shows equivalent performance to the ideal case when the filter strength is sufficiently large. The comparison between Fig. 9.6 (a) and (b) showcases a significant distinction between the effect of the squeezing purity and that of the squeezing disparity on the resultant fidelity: while a higher filter strength can compensate for fidelity degradation due to disparity between the two squeezed sources, it is ineffective to counteract the additional loss attributed to the impurity of the initial squeezed states.

9.3.6 Enhancement in the Distance of Teleportation

Whilst much effort has been devoted to extend the distance of discrete variable telerportation, with a recent achievement of 1400 km that demonstrated the first ground-to-satellite teleportation [334, 304, 335, 310], the distance of continuous variable teleportation is substantially limited. The maximum distance of CV teleporatation so far is 12 m

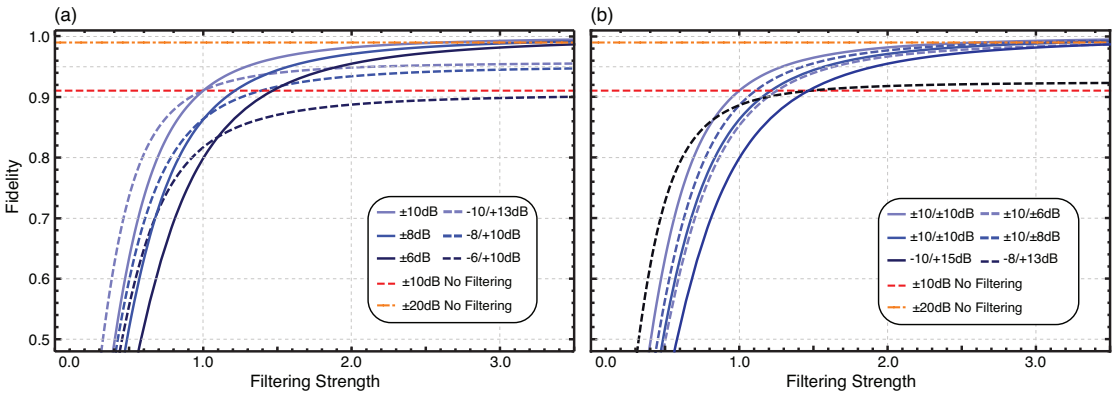

Figure 9.6: Fidelity gradually increases as the post-selection filter strength grows. (a) illustrates how the purity of the squeezed sources impacts the fidelity of Bob's reconstruction, whilst (b) shows that, on the contrary, it is not necessary for the two initial squeezed states to be identical to obtain a reasonable fidelity. For comparison, we plot the achievable fidelity for a conventional CV teleporter with an initial squeezing of 10 dB (red dashed) and 20 dB (orange dash-dotted), respectively.

for a Shrödinger cat state [311], and the state-of-art teleporation for other CV quantum states has been confined to table-top configurations [312, 313, 314, 315, 316, 317, 318]. This has been a long-standing issue in CV quantum information as teleportation serves as a key primitive for a wide variety of quantum communication and computation tasks. The difficulty resides in the fact that the CV entanglement is extremely vulnerable to loss and noise. In practical implementations, long-distance distribution of entanglement would inevitably degrade the EPR correlation and hence the teleportation fidelity. Here we show that this technical hurdle can be perfectly surmounted if the loss is imposed on Bob's EPR arm, and can be alleviated otherwise if the loss is injected on Alice's side. As shown in Fig. 9.7 (a), by increasing the filter strength, a higher fidelity can be achieved compared to the conventional teleporter–when benchmarked on the same channel loss (50%). More remarkably, for loss less than 25% (equivalent to 62 km of optical fiber) on Alice's side, we can obtain a fidelity beyond the best achievable via a conventional setup subject to a perfect channel.

Further advantages of the present scheme lie in its absolute robustness against the loss on Bob's channel as plotted in Fig. 9.7 (b): regardless of the channel transmission, the post-selection always allows us to compensate for the loss and hence obtain unit fidelity by turning up the filter strength. Comparison between Fig. 9.7 (a) and (b) showcases the asymmetric performance of our heralded teleporter, originating from the mechanism of our post-selection filter. Although the post-selection in the present scheme works analogously to a noiseless linear amplifier [22, 94, 336], it does not function equivalently to an NLA in terms of entanglement distillation [81]. The distinction results from the non-commutative nature of the beamsplitter operation and the noiseless linear amplification. An NLA executed before injecting the input state would result

in a unit fidelity despite the asymmetry of the transmission channels. This no longer holds if the NLA is performed the other way around. The enhancement in fidelity in the present teleportation scheme is obtained by circumventing the noise penalty enforced on Alice's measurement on conjugate variables. As an infinite filter strength is applied, this additional noise can be completely avoided so the quadrature amplitudes of an unknown input may be inferred with arbitrarily high accuracy, at the expense of an arbitrarily low success probability.

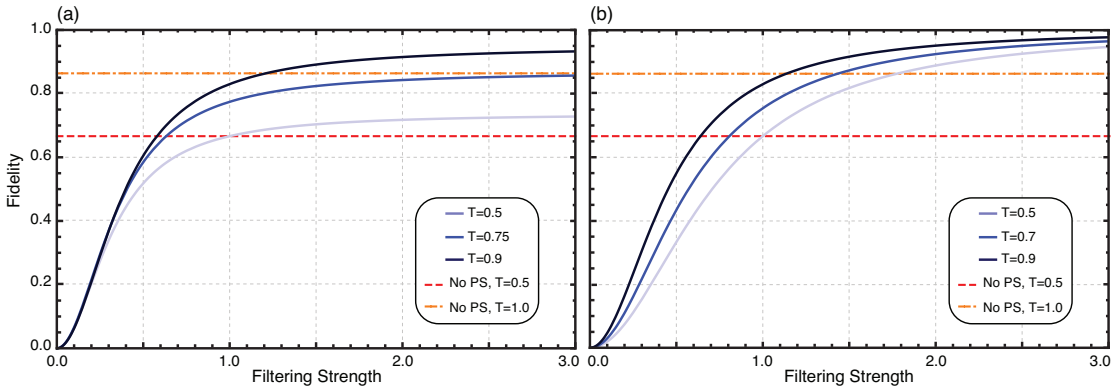

Figure 9.7: Fidelity of teleportation when the distribution of entanglement is subject to an imperfect channel. (a) illustrates the fidelity when different levels of loss, i.e. $T = 0.5$, $T = 0.75$, and $T = 0.9$, are imposed on Alices's EPR mode, while (b) shows the fidelity in situations where Bob's EPR mode undergoes losses of $T = 0.5$, $T = 0.7$, and $T = 0.9$, respectively. The channel loss here is simulated by a partially transmissive beamsplitter. For comparison, the conventional deterministic teleportation when benchmarked by a pure channel (orange dashed-dotted line) and a lossy channel with $T = 0.5$ (red dashed line) are superimposed. 8 dB of pure squeezed sources are assumed in all the plots.

9.4 Experimental Details

In this section, we address the experimental procedure alongside the experimental results for the heralded quantum teleportation. We describe in detail the resultant experimental fidelity that quantifies the faithfulness of Bob's reconstruction of the unknown input and the system T-V diagram that evaluates the teleporter as a communication channel in terms of signal transfer and additional noise.

9.4.1 Experimental Setup

Figure 9.8 and 9.9 plot, respectively, the experimental schematic and the associated electronic servo locking loops for the heralded teleportation experiment.

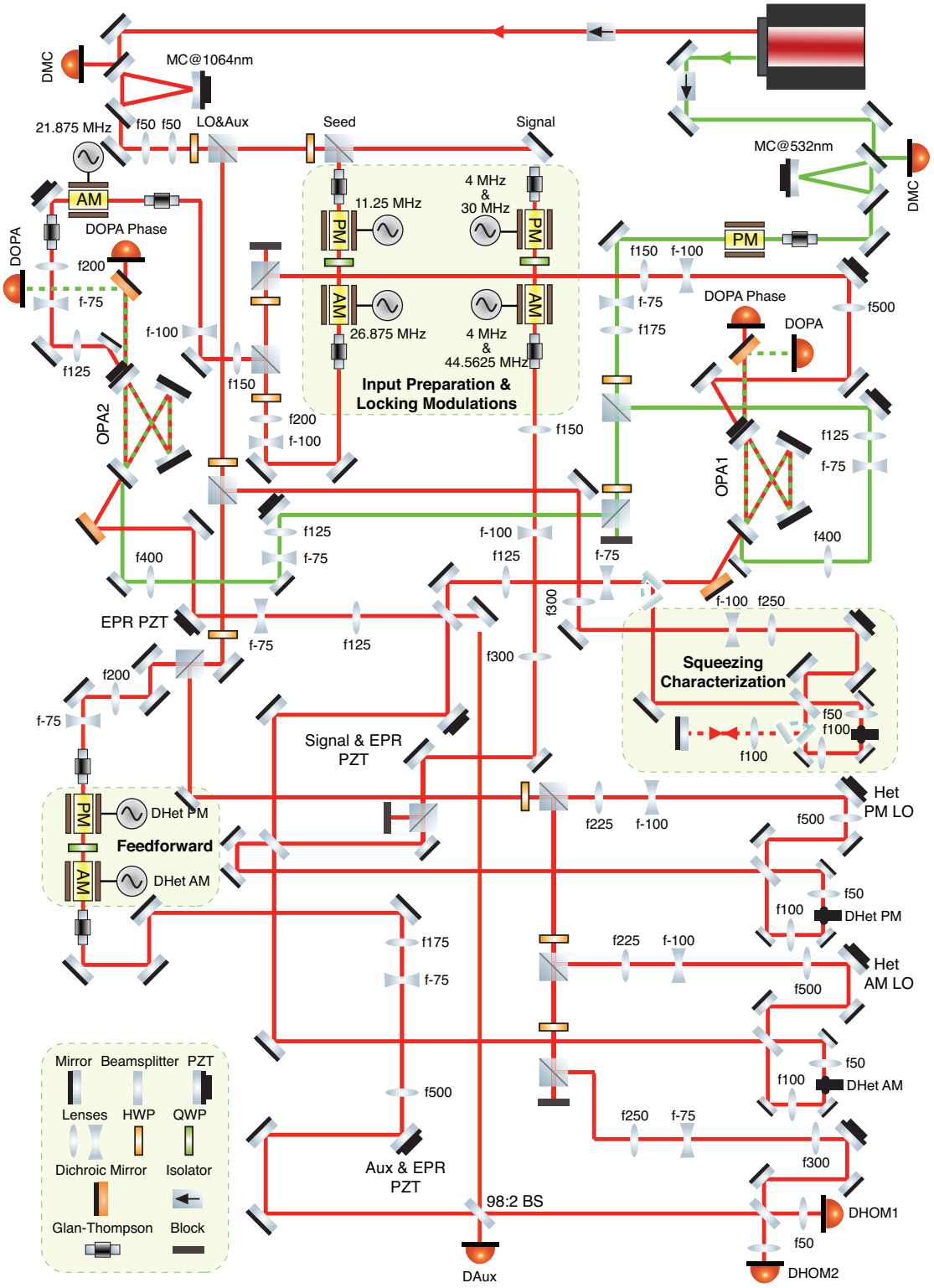

Figure 9.8: Experimental layout of the heralded quantum teleportation experiment. AM/PM: amplitude/phase modulators; PZT: piezo-electric transducer; MC: mode cleaner.

Optical Layout

Two mode cleaners (MC) were inserted into the optical path of the pump and fundamental beams to provide shot-noise limited TEM_{00} Gaussian beam at frequency

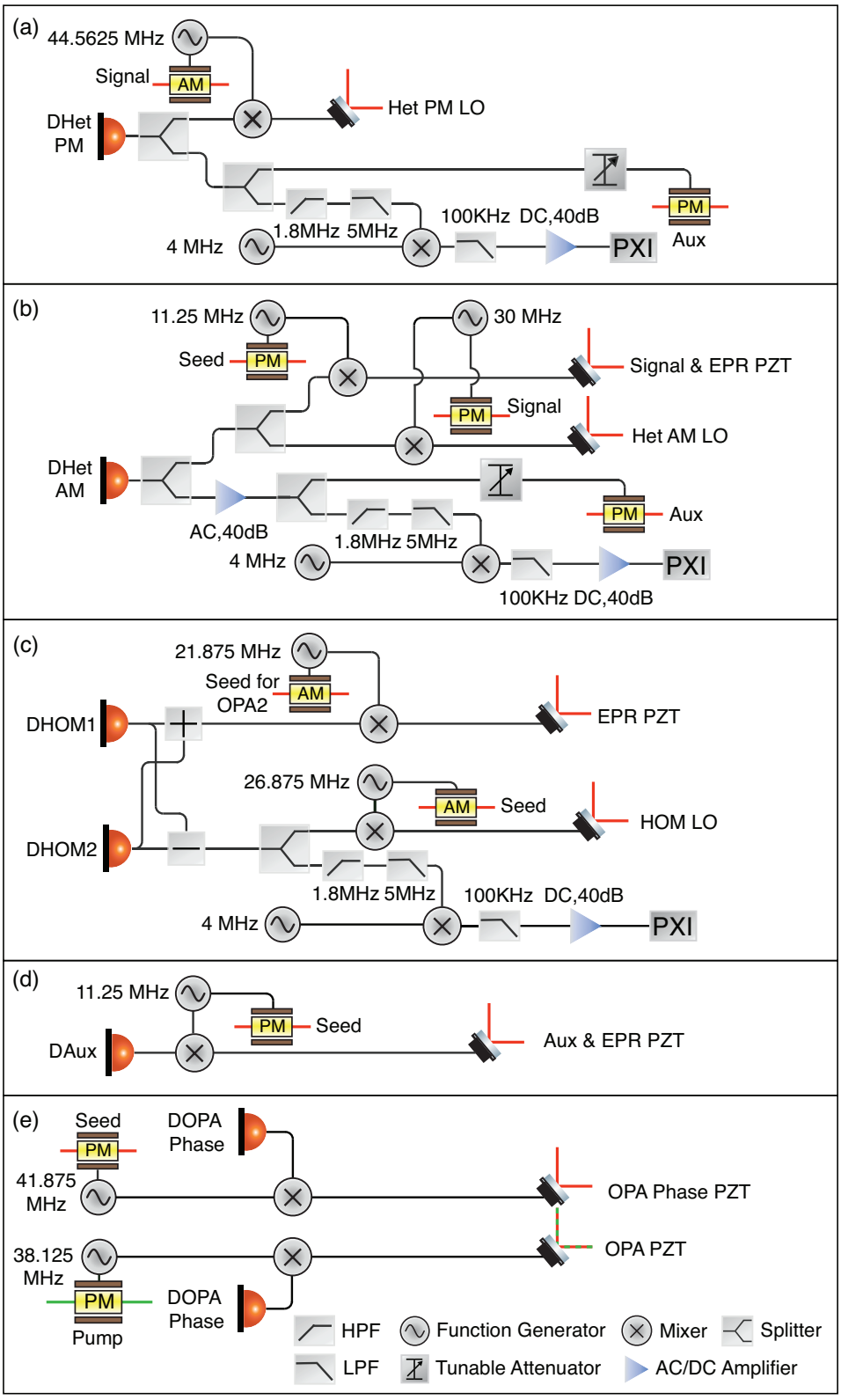

Figure 9.9: Locking arrangement for the heralded quantum teleportation experiment.

higher than the MC bandwidth. Two bow-tie optical parametric amplifiers operating below threshold–as characterized in detail in chapter 5–were utilized as the squeezed

sources for generating quadrature entanglement. Alice's station comprised of two homodyne detections that conduct a simultaneous measurement on the amplitude and phase quadratures of the incident beam, while Bob performs a single homodyne which alternated between probing amplitude and phase of the reconstructed output.

All data samplings were accomplished via a 3-channel digitizer (PXI-5124) with a sampling rate of 200MS/s, maximum bandwidth of 150 MHz, and analog input resolution of 12 bits. An additional low pass filter at 100KHz was implemented subsequently to process the data further in order to get rid of the correlation between consecutive data samples. As addressed in Sec. 8.2.1, we implemented the post-selection off-line by pairing up Alice's and Bob's measurement outcomes during data acquisition. Bob's data samples were either discarded or kept according to the acceptance rate in Eq. (9.23), where $\alpha_{\rm m}$ denotes the measured quadrature amplitude by Alice. The cut-off parameter α_c was carefully chosen to accommodate the input alphabet based on the criterion proposed in [234], which is around 4.5 for all data runs. This was done to ensure no distortion appeared on the output state of the teleportation, and meanwhile to optimize the trade-off between success probability and fidelity.

Electronic Servo Control Loops

The whole experiment involved 14 electronic control loops, among which 13 controls were required to be activated simultaneously. This included five locking loops for the mode cleaner at 1064 nm, the OPA cavity length, and the relative phase between the fundamental and second harmonic fields. Two servo loops were used to stabilize the temperature of the OPA crystals. The remaining servo loops were devoted to ensuring two interfering beams stayed either in-phase or out-of-phase throughout the experiment by employing the relative phase locking technique in Sec. 3.4.1. Modulation signals were generated from two direct digital synthesis (DDS) boards (AD9958) controlled by the LabVIEW FPGA with a built-in clock produced by a frequency generator (NI PXI 5404). To obtain pure error signals and lock to the correct quadratures, special precautions were taken to minimize the cross-talk between amplitude and phase modulations. The resultant PM (AM) cross-talk cancellations for the signal, seed, and auxiliary beams are $55.2(42.5)$, $40(32.5)$, and $41.7(40.3)$, respectively, and we present the best cancellation result in Fig. 9.10 (a) (refer to Fig. 3.4).

Characterization of the Experimental System

Figure 9.10 (b) plots the output noise measured on Bob's homodyne station, where the blue curve illustrates the directly measured thermal noise of Bob's EPR mode, and the yellow trace shows the resultant noise spectrum after implementing the feed-forward. We observe an apparent noise suppression at the frequency of interest (4 MHz) after turning on the feed-forward, owing to the correlation between Alice's and Bob's optical modes. During the experiment, the lengths of the electronic cables used to transmit data

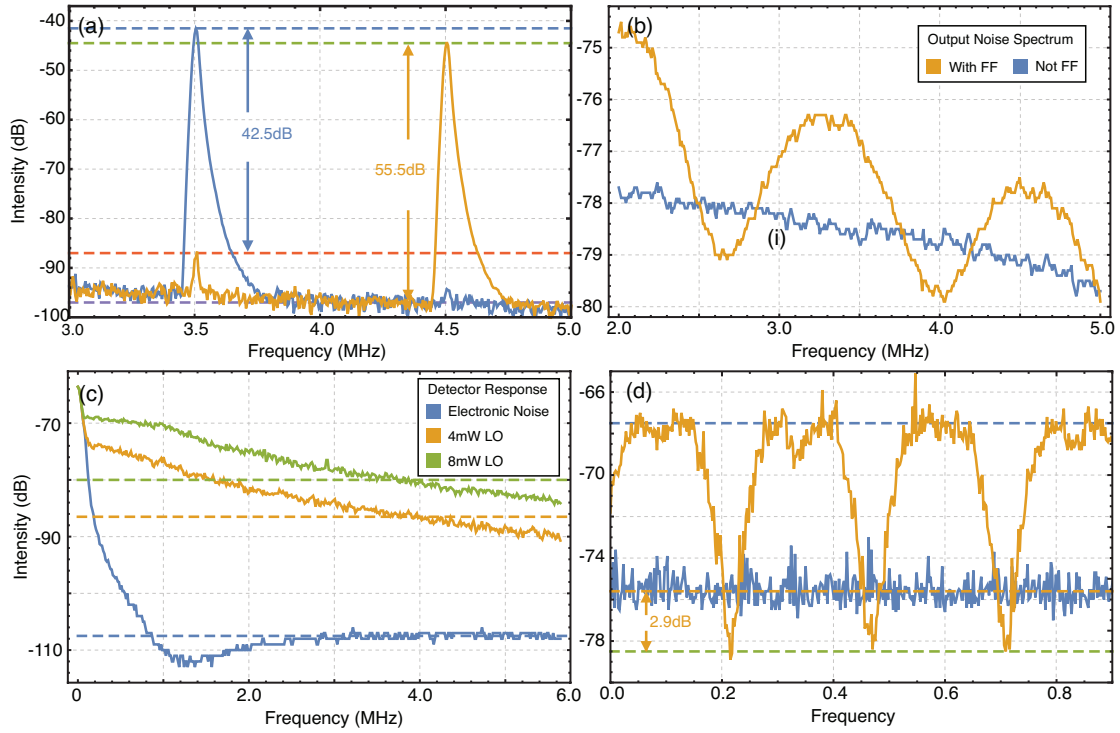

Figure 9.10: Characterization of the experimental system for the heralded teleportation: (a) cross-talk cancellation for the modulators on the signal beam (VBW: 30 kHz, RBW: 30 kHz, sweep time: 8.59×10^{-3} s); (b) noise suppression resulted from feed-forward (VBW: 100 Hz, RBW: 100 kHz, sweep time: 0.244 s); (c) detector noise response (VBW: 100 Hz, RBW: 30 kHz, sweep time: 0.988 s); (d) measurement of the OPA squeezing after a 50:50 beamsplitter (Span: 0 Hz, centre frequency: 2 MHz, VBW: 1 MHz, RBW: 100 KHz, sweep time: 0.926 s). LO: local oscillator for the homodyne measurement; FF: feed-forward.

from Alice to Bob (refer to Fig. 9.4) were adjusted carefully such that the best correlation and hence the largest noise suppression occurs at 4 MHz. To minimize the amount of uncorrelated noise, we used a pair of dual-subtraction homodyne detectors at Alice's station which were customized to have a high dark noise clearance [337]. As shown in Fig. 9.10 (c), up to 27.5 dB dark noise clearance was measured at 4 MHz, and 40 dB clearance was observed at 1.6 MHz.

Furthermore, we characterized the loss of our optical system by measuring the available squeezing at the final homodyne station, as a higher loss would contaminate the entanglement more and hence decrease the teleportation efficiency. We observed ~ 2.9 dB of squeezing (see Fig. 9.10 (d)), of which the maximum possible is 3 dB due to the 50:50 beamsplitter. This shows that the loss in present of our system is reasonably low, so a high fidelity should be achievable. The minimization of loss was ascribed to two main factors: firstly, the minimum amount of optics were placed in the path of the EPR beams, and secondly, all the intereference visibilities were optimized to above 99% (homodyne: 99.5%, in-line homodyne for AM: 99.5%, in-line homodyne for PM: 99.65%, EPR: 99.77%, signal and EPR: 99.3%, and auxiliary beam and EPR: 99.5%).

9.4.2 Experimental Fidelity

We first applied fidelity as our figure of merit to quantify the performance of the heralded teleporter. Two coherent states with different quadrature amplitudes, $(x, y) = (0, 1.05)$ and $(0.70, 0.70)$ as shown in Fig. 9.11 (a) and (e), were injected into the system. Regardless of the different inputs, the resultant fidelities obviously surpass the classical teleportation limit as well as the quantum limit, as evidenced by Fig. 9.11 (b) and (f). We report, in particular, the highest fidelity (90%) ever achieved for CV quantum teleportation. The input state under-interrogation is a coherent state, instead of a vacuum as has been utilized in the previous state-of-the-art (fidelity of 83%) demonstration [316]. The unity-gain condition is verified unambiguously by ensuring the output amplitude coincides with that of the input, which excludes, therefore, any overestimation of the fidelity due to non-unity gain operation.

Note that an artificial improvement of fidelity is possible when an insufficient cut-off is applied during the post-selection [234]. The filtered statistics exhibit an undesirable distortion that departs the output from a Gaussian distribution [336, 234]. In the extreme case where $\alpha_c \ll 1$, the output distribution tends to be a delta function, thereby arbitrarily small output variance and in turn arbitrarily high fidelity can be achieved. In the experiment, the cut-off was chosen with care to preclude such effect. We present the probability distributions of the two output states in Fig. 9.10 (c-d) and (g-h), where, as we can see, both outputs exhibit reasonable Gaussian distributions.

9.4.3 Equivalent T-V Diagram

We analyze the behavior of our teleporter also in terms of signal transfer coefficients and the additional noise during teleportation. As discussed in Sec. 9.3.3, the T-V diagram complements fidelity in a way that provides an avenue to study the information transfer of the system, which is particularly useful in the non-unity gain regime.

We present in Fig. 9.12 (a) the theoretical prediction of the equivalent T-V diagram for our heralded quantum teleporter superimposed with experimental results marked as brown dots. In analogy to the equivalent T-V diagram for a conventional teleporter described in Fig. 9.3, the signal transfer coefficient $\mathcal{T}_q$ measures the amount of information that has been successfully conveyed between the remote stations, while the additional noise V_q' quantifies how much additional noise is induced during the teleportation process, and hence how closely the output resembles the original input. The post-selection enables one to penetrate into the quantum region of a teleporter [328, 331] by increasing the filter strength alone, without requiring a higher EPR correlation. With the same amount of squeezed sources (< 3 dB), teleportation that would have failed in the conventional scheme could succeed using the current system at the price of a finite success probability.

Perhaps the more striking result lies in the possibility to obtain a signal transfer coefficient higher than 2, which is never the case in the conventional quantum teleporter

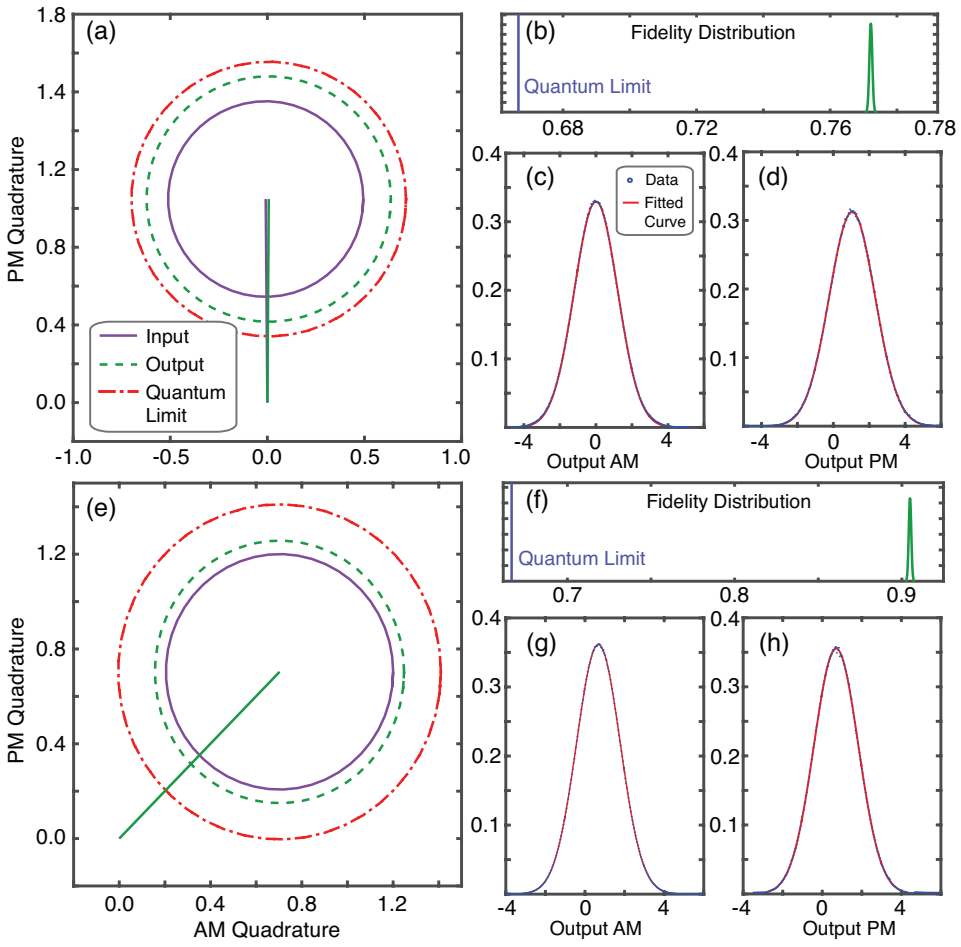

Figure 9.11: Output fidelity for two coherent input states with different quadrature amplitudes. (a) and (e) Noise contours (full width half maximum) of the Wigner functions of the input states (purple circle) and the reconstructed outputs (green dashed circles) alongside the output corresponding to the quantum limit (red dash-dotted, fidelity of 2/3). (b) and (f) The output fidelity distribution benchmarked by the teleportation quantum limit, where the uncertainty is mostly attributed to the finite sample size. (c, d) and (g, h) Quadrature probability distributions of the output states.

even assuming perfect EPR correlation is at our disposal. The heralded teleporter in this regimes operates as a noise-reduced phase-insensitive quantum linear amplifier instead of an identity channel. It not only circumvents completely the noise penalty associated with Alice's dual-quadrature measurement and Bob's reconstruction that is feasible with perfect EPR correlation, but also increases the signal-to-noise ratio of the unknown input state, therefore making the current scheme particularly useful in constructing long-distance quantum networks. This noise-reduced feature culminates with the T-V of a noiseless linear amplifier, shown as purple spades in Fig. 9.12 (a). In contrast to the noise-reduced linear amplifier presented in chapter 6, the realization of noiseless linear amplification does not necessarily leads to a vanishing success probability here. As shown in Fig. 9.12 (a), 3 dB squeezing together with a filter strength of 2 already

suffices to give near-NLA performance. This would give a success probability around 10^{-2} for input with 1 unit of shot noise, initial squeezing of 6 dB, and a cut-off of 4.5. We report the highest experimental signal transfer ever achieved, $\mathcal{T}_s = 1.63$ and $V_q' = 0.05$, for a coherent input with mean quadrature amplitude of $(x, y) = (0.70, 0.70)$. The simultaneous fulfilment of the criteria $\mathcal{T}_s > 1$ and $V_q' < 1$ evidently verifies the success of a quantum teleportation. As depicted in Fig. 9.12 (a), this result also demonstrates the near-NLA performance of our heralded teleporter.

Figure 9.12 (b), on the other hand, displays the equivalent T-V diagram of our heralded teleporter when it operates only in the unity-gain regime. The T-V results for different filter strengths bunch together following the curve representing the unity-gain trace of a conventional teleporter (blue circles), except that $(\mathcal{T}_q, V_q') = (1, 0)$ is reached with less squeezing than the conventional counterpart. It is worthwhile noting that even in the presence of post-selection, $\mathcal{T}_q > 1$ is not achievable in this regime, because the teleporter is constrained to an identity channel. So the best possible performance is $(\mathcal{T}_q, V_q') = (1, 0)$. The grey dots represent our experimental data, which shows good agreement with the theoretical curve, verifying that the unity-gain condition is always satisfied.

9.5 Conclusions and Future Perspectives

In conclusion, we propose and experimentally demonstrate a heralded teleportation scheme that employs a post-selection filter in analogy to a noiseless linear amplifier, which is able to distil entanglement and avoid the noise penalty imposed on the in-line dual-quadrature measurement. The present heralded teleporter combines profitably the advantages of a conventional DV and CV quantum teleporter, allowing one to tune between unit success probability and unit fidelity that is in principle unattainable conventionally. One intriguing feature of the heralded teleporter is its ability to correct any loss on Bob's channel: regardless of the transmission of the receiving channel, unit fidelity is always obtainable with a finite filter strength. This obviates the long-standing hurdle of CV quantum teleporters, enabling teleportation between truly remote stations.

We obtain an experimental fidelity of 0.904 ± 0.001 for a coherent input state. Unity-gain condition is guaranteed by ensuring output amplitude equal to that of the input. This result reports the up-to-date best fidelity for continuous variable quantum teleportation. The improvement in fidelity can be achieved by increasing the filter strength alone without calling for more EPR correlations. Teleportation that would have been certified as a failure conventionally due to a lack of squeezed sources would still be able to succeed ($\mathcal{F} > 2/3$) by allowing for a probabilistic operation.

We further analyze our heralded teleporter in terms of the signal transfer coefficient and additional noise induced during the teleportation process. We report, in particular, the best T-V result ever achieved: $\mathcal{T}_q = 1.63$ and $V_q' = 0.05$. Our teleporter, when operates in the non-unity-gain regime, allows one to access to operational region with $\mathcal{T}_q > 2$

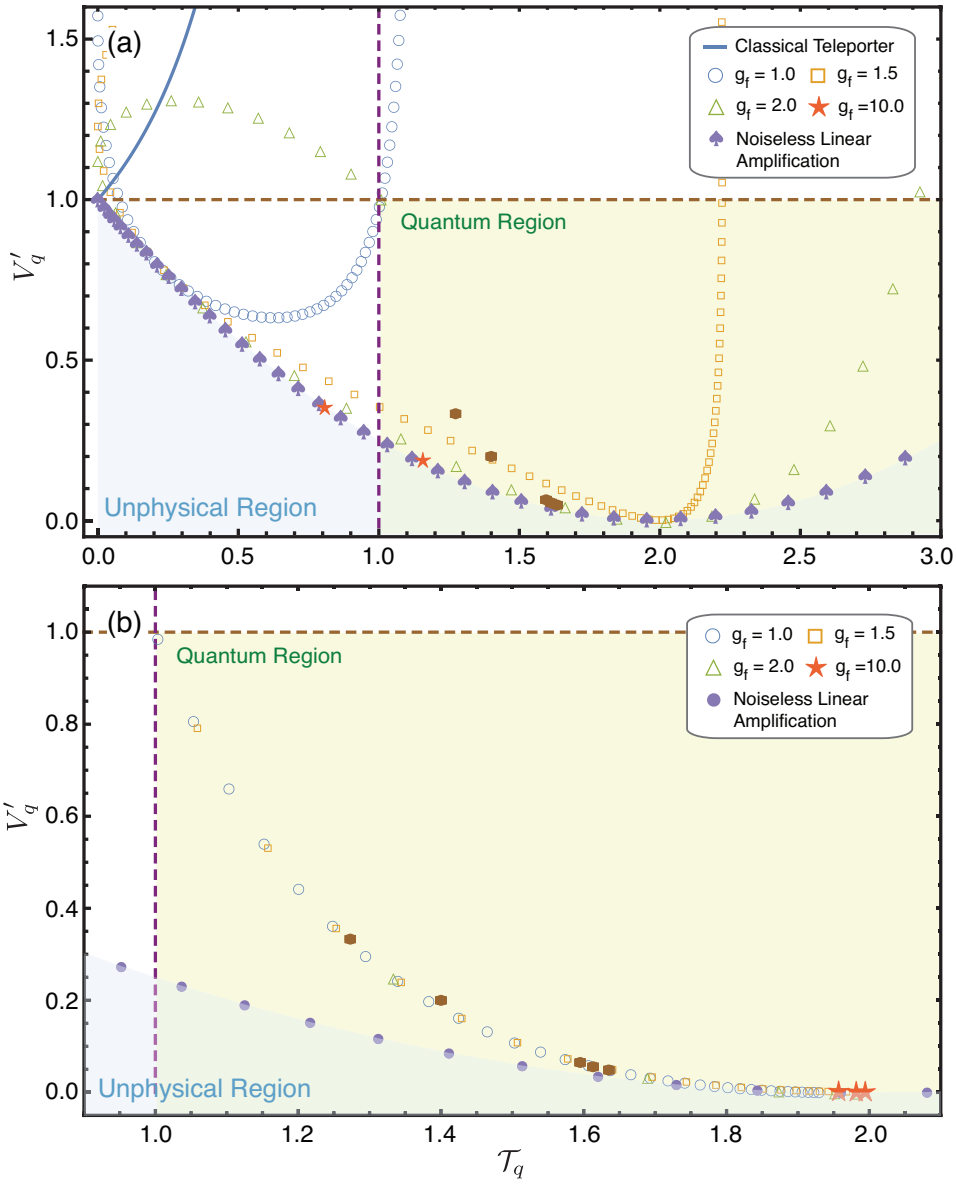

Figure 9.12: Theoretical TV diagram for the heralded teleportation superimposed with experimental data points. We start with 3 dB squeezed sources and implement various filter strengths so as to increase the information transfer while lowering the additional noise. (a) illustrates the equivalent T-V diagram for the tunable gain situation, while (b) presents the T-V diagram when unity-gain condition is satisfied. As analyzed in Sec. 9.3.3 the yellow shaded area represents successful teleportation with both $\mathcal{T}_s > 1$ and $V_q' < 1$. Because the corresponding fidelity exceeds the quantum no-cloning limit, teleporation undertaken in this region thus guarantees no copy of the unknown input has been intercepted by any potential eavesroper [338, 339]. The blue solid curve denotes a classical teleporer with no assistance of EPR correlation where the maximum amount of information transferable between the two remote stations is limited by $\mathcal{T}_q \leq 1$. The purple spades and dots in (a) and (b) show, respectively, the T-V results for a noiseless linear amplifier that is unattainable in the conventional deterministic teleportation. The operational region beyond it constitutes the unphysical regime for both the conventional and the heralded quantum teleporter.

that is inaccessible for a conventional teleporter even with perfect EPR correlation. The heralded teleporter in this regard constitutes a more powerful tool than the noiseless linear amplifier presented in chapter 6 and the references therein. In a post-NLA scheme, the SNR degradation of input occurs due to the additional loss in transmitting it to a remote station, which can not be avoided by the noiseless amplification. A pre-NLA scheme, on the other hand, cannot correct for SNR degradation occurring during signal transmission, albeit with an improved SNR to start with. In the present heralded teleportation scheme, however, the communication channel can be arbitrarily long and one can still benefit from an enhanced SNR of an unknown input, owing to the combined effect of post-selection and the presence of EPR correlation.

Considering the multiple striking benefits our heralded quantum teleporter brings about and the significance of quantum teleportation in quantum communication and computation, we envisage a wide rage of applications of the current teleportation scheme in quantum information processing.

Chapter 10

Conclusions and Outlook

10.1 Summary

This thesis investigated an inverse-Gaussian post-selection filter that was originally conceived to emulate a noiseless linear amplifier (NLA). The exact profile of the filter was engineered such that the statistical properties of the output of an NLA can be fully reproduced by post-processing the outcomes of an information complete measurement acted upon the original input. We found this filter applicable to a wide variety of quantum information protocols, allowing one to either obviate the requirement for non-linear resource to reach a certain benchmark, or realize quantum information tasks that are conventionally impossible. We explored, in particular, its applications to quantum amplification, quantum cloning, quantum squeezing gate, and quantum teleportation. A summary of each application is provided in the following.

10.1.1 Characterization of the Post-selection Filter

The behavior of the filter was placed under close scrutiny in chapter 4, where we compare the performance of the measurement-based implementation of NLA and an optimal physical implementation of NLA via a POVM. We studied their respective probabilities of success and abilities to preserve the Gaussianity of an input Gaussian state. We constructed a 1-to-infinity quantum cloner and an amplifier based on both NLA schemes and examined the properties of the corresponding outputs. These investigations indicate that the equivalence between these two schemes, although has been believed to be absolutely valid, only holds under certain circumstances. The work described in chapter 4 are of instructional importance, for it fosters our understanding of the functionality of such a post-selection filter, and hence provides a guideline for optimizing the filter effective parameters in the remaining projects conducted during my PhD.

10.1.2 Hybrid Noise-Reduced Linear Amplifier and Quantum Cloning

The work presented in chapter 6 exemplifies the possibility of overcoming deterministic bounds by employing the post-selection filter. It has been proved that deterministic

phase-insensitive linear amplifiers inevitably add noise during amplification, and hence deteriorate the signal-to-noise ratio (SNR) of the input state, in compliance with the Heisenberg uncertainty principle. It is this noise penalty that prevents perfect cloning of an arbitrary unknown quantum state, which is normally referred to as the quantum no-cloning theorem. However, this ultimate limit can be circumvented by adopting probabilistic operations. We demonstrated for the first time an enhancement in SNR of an input coherent state with a power gain above ~ 100. Based on this noise-reduced linear amplifier, we further constructed a quantum cloning machine and reported up to five clones with fidelity of each copy surpassing their corresponding no-cloning limit.

10.1.3 Generation of OPA Squeezing and Quadrature Entanglement

In the preceding projects, the post-selection filter was employed in quantum systems, where only measurement and linear optics are involved. It could be more interesting to introduce non-linear sources into the system. Motivated by this idea, we developed a pair of optical parametric amplifiers (OPAs) producing reasonably pure (purity of 1.12) and highly squeezed vacuum (11 dB). The two OPAs also provided the sources to create quadrature entanglement that was utilized in the teleportation experiment in chapter 9. In chapter 5, we put forward considerations with respect to the configuration of the OPA cavities to optimize its performance. Furthermore, the OPA squeezer had been carefully characterized to evaluate its potential for producing high-magnitude of squeezing. We discussed explicitly the experimental results and the theoretical expectations of the pump threshold and the escape efficiency of our squeezer and showed that a rather accurate estimation of the system properties can be obtained from the coating specifications.

10.1.4 High-Fidelity Squeezing Gate for CV Quantum Light Fields

In chapters 7 and 8, we considered an application of our post-selection filter to realize a high-fidelity universal squeezing gate. Such a universal squeezing gate is capable of squeezing arbitrary input states and is an essential component for continuous variable quantum computation. However, in present state-of-the-art techniques, the fidelity of such gate is ultimately limited by the need to synthesize squeezed vacuum modes of unbounded energy. Here we circumvented this fundamental limitation by using a heralded squeezing gate. We proposed and experimentally demonstrated a universal squeezer that can achieve arbitrarily high fidelity for all input states. For a target squeezing of 2.3 dB, we reported a fidelity of up to 98% on a coherent input state. This result cannot be reproduced by conventional schemes even if infinitely squeezed ancilla was available–when benchmarked on identical experimental imperfections. Our technique provides a promising pathway towards high-fidelity gate operations and fault-tolerant quantum computation.

10.1.5 Heralded Quantum Teleportation

A more interesting application was demonstrated in chapter 9, where the post-selection filter was incorporated into a conventional quantum teleportation scheme. Our heralded quantum teleporter reconciles the conventional discrete variable and continuous variable teleportation, allowing one to tune between unit-fidelity and unit-success-probability operations. The significance of the present teleportation scheme is threefold. First, the teleporter works in analogy to an error-corrected channel, where any loss induced on the receiver's transmission line can be completely compensated by turning up the post-selection filter strength. Unit fidelity is obtainable regardless of the channel transmission, rendering the teleporter more resilient to imperfect employment conditions. Second, it obviates the technical difficulty of the conventional CV teleportation, where high-fidelity remains hard to achieve and unit fidelity is in principle impossible. This predicament stems from the intrinsic limit on CV EPR correlation, as perfect correlation would require infinitely squeezed sources. The state-of-the-art fidelity is 83%, reported by Furusawa's group for a vacuum input [316]. We showed that our heralded teleporter allows one to attain high-fidelity teleportation and permits even unit fidelity with a modest level of squeezing and finite success probability. Third, the present teleporter provides access to a signal transfer coefficient $\mathcal{T}_q > 2$, in stark contrast to both the classical teleporter where $\mathcal{T}_q \leq 1$ and the conventional quantum teleporter where $1 < \mathcal{T}_q \leq 2$. As such, via our heralded teleporter, one can benefit from both long-distance communication and SNR enhancement simultaneously owing to the inclusion of EPR correlation.

10.2 Future Work

10.2.1 Potential Characterization of our System and Improvements on Squeezing Generation

We have observed more than 11 dB output squeezing using our bow-tie OPAs, and successfully implemented a quantum teleportation protocol with EPR correlation generated by combing the two squeezed vacuums. There remains much work to be done to fully characterize the entangled state at our disposal. This can be accomplished by conducting dual-quadrature homodyne or heterodyne measurements on both arms of the EPR state, which is sufficient for reconstructing the covariance matrix of the state. Furthermore, the magnitude of available squeezing needs to be improved with the aim of developing entanglement-based quantum network in field deployment settings [283, 319, 2, 8, 320] as well as fault-tolerant and distributed quantum computation [274, 340, 341, 342]. We envisage three possible ways to address this problem. First, material that possesses a higher nonlinear coefficient than PPKTP would potentially promote the parametric non-linear interaction and hence the obtainable squeezing. One promising candidate would be the halide perovskites that has been found to have high

non-linearity [343, 344] and has already been used in a wide variety of device engineerings [345, 346, 347, 348, 349, 350, 351]. Second, the bow-tie geometry of our OPA cavity may be replaced by the hemilithic geometry, where less optical interfaces and hence less intra-cavity loss would be present. This geometry was utilized in the state-of-the-art squeezing generation (15 dB) [186]. Third, a refinement of the present servo locking techniques would reduce any potential additional noise attributed to unstable lockings and enables consequently a constant production of highly squeezed states. We have observed gradually increased detuning of the OPA cavity away from resonance and non-zero offset for the relative phase locking between the pump and fundamental beams in our OPA setup. Although the shift of locking point is fairly small, it could introduce phase mismatching between the two interacting fields, which consequently contaminates the achievable squeezing and may induce spectral splitting of the fundamental mode [352, 254].

In addition, it is worthwhile to explore the miniaturization of squeezing [181, 193, 189] and squeezing on other platforms like atomic and optomechanical systems [178, 184, 179, 174]. Without much reconfiguration of our current experimental setup, we can explore several interesting phenomena arising from the cooperating nonlinearities [353]. Interaction between the second-order up-and-down conversions provides avenues for future research including generation of third-order nonlinear effects [354, 355, 356], optical bistability [357], and optical switching [358, 359]. Conversely, it would be interesting to investigate the competing nonlinearities, as no experiments have successfully demonstrated the predicted signature of such effect that near-perfect squeezing, impossible in the absence of competition, is possible in a quadruply resonant system [360, 361].

Furthermore, we observed an apparent cross-talk degradation for the amplitude and phase modulations on the seed beam as it transmits through the OPA. This issue arises due to multiple reasons, such as the cavity detuning discussed above, the non-ideal phase matching of the pump and seed fields, and the nonlinear interaction between the two fields. To develop a better understanding of how the sidebands evolve in the presence of these effects, more thorough investigations are required on the existing causes and their respective impacts.

10.2.2 Future Directions for Post-selection-based CV Quantum Information

Beyond the aforementioned applications, numerous quantum information tasks can be improved with the inclusion of the inverse-Gaussian post-selection filter. It can be utilized to improve the secure transmission distance of continuous-variable quantum key distribution (QKD) [79, 92, 281, 362, 363]. It may also has the potential to improve the secrete key rate in a pre-amplified QKD configuration [364]. Another interesing extension would be to apply the filter function in remote entanglement generation [365]. While we only concentrated ourselves with noiseless amplification, the filter function can be gen-

eralized to realize noiseless attenuation by setting $g < 1$. Much work needs to be done in characterizing the performance of the attenuator with respect to all effective parameters and the limit on its operational regime. One may also consider to employ the noiseless attenuator to achieve purification of a lossy quantum communication channel [366, 367].

Upon modifications of the filter function, post-selection may open the way for emulating other non-Gaussian operations that are otherwise technically difficult or resource intensive. One possibility is to mimic the photon subtraction and addition operation using post-selection, so that the requirement of non-classical single photon source and single-photon detectors in its conventional implementation is circumvented. The post-selection filter can be constructed following the same methodology in chapter 4. Once the filter is available, it can be adopted to engineer arbitrary single-mode quantum operations [280] or a physical noiseless linear amplifier, for which all of the present experimental demonstrates are extremely challenging [73, 74, 69, 70, 71, 72]. Virtual implementations of various quantum information tasks are enabled with the aid of this filter, including entanglement distillation [368, 369], device-independent QKD [78], and generation and amplification of Shrödinger cat state [370, 371, 74, 372, 373].

An immediate extension of the squeezing gate project in chapters 7 and 8 would be to exploit post-selection to enhance quantum operations that rely on a high-fidelity universal squeezing gate. One such example would be a controlled-Z gate that is essential in the conventional generation of large-scale cluster states [261, 262, 263]. In particular, Menicucci et al. proposed a flexible scheme for cluster state generation based on a single controlled-Z gate and feedback controls [261]. The difficulty of this proposal resides in the implementation of the controlled-Z gate; once this technical hurdle is surmounted, a two-dimensional square-lattice graph state with an arbitrary number of modes can be created. One may also look up the possibility of utilizing post-selection to improve the fidelity of nonlinear operations such as the cubic phase gate [260, 374, 375, 376], the quantum non-demolition gate [264], and quantum error-correction [377], as universal quantum computation demands at least one nonlinear operation together with the full set of linear operations [260]. We anticipate this refinement to be feasible because the filter can be naturally embedded into the measurement-based quantum computing framework [286, 273, 272] by incorporating it into the feed-forward loop present in all gate implementations.

Beyond the characterization of our heralded quantum teleporter in terms of fidelity and T-V diagram in chapter 9, it is worth examining the behavior of our teleporter relative to other figure of merits. One example is to evaluate how effective we harness entanglement to reach a particular teleportation criterion, say secure quantum teleportation certified by a fidelity surpassing the no-cloning limit $2/3$. The magnitude of original squeezing provides a direct indicator of the generated EPR correlations; we have shown that thanks to post-selection, significantly higher fidelity is attainable via the present scheme as compared to its conventional counterpart–when benchmarked on the same squeezed sources. Turn this perspective around, He et al. [249] proved how noiseless

linear amplification helps to relax the requirement of EPR correlation from Tan-Duan inseparability $\delta_{\rm ent} < 1/2$ [338, 378, 43] to two-way steerability [46, 379, 380, 381] to access secure quantum teleportation. An open question is to see if the same improvement retains with regard to other entanglement measures.

Section 9.3.6 has investigated fidelity of our heralded quantum teleporter that accounts for unbalanced channel losses on the sender's and receiver's stations. This analysis may be re-examined in terms of entanglement steerability, because entanglement steering, as opposed to inseparability, offers additional insights into the properties of asymmetric entangled systems. And quantum teleporation subject to unbalanced channel losses describes exactly this type of system [382, 383, 384]. In Section 9.3.6, we have restricted our investigation to pure lossy channel and demonstrated that post-selection is capable of correcting any loss regardless of the transmission rate on the receiver's channel. We have noticed that the result coincided with a recent proposal in [385]. More generally, Tserkis et al. put forth that such an NLA-based quantum teleporter can be used to correct noise not only from pure loss but also from thermal loss channels [386]. Recently, there has been study emerged on using quantum teleporter with limited resources to simulate Gaussian channels [386, 387]. The connections between the new criteria and the equivalent T-V diagram in Sec. 9.3.6 deserve further investigations, and may lead to a complete characterization of our heralded teleporter as a more general Gaussian channel instead of simply an identity channel.

Another more intriguing observation lies in the equivalence between the additional noise V_q' in Fig. 9.3 and 9.12 and the one-way steerability defined in [388, 383, 389]. This gives a new insight into the physical meaning of the equivalent T-V diagram, whereby V_q' signifies not only the additional noise incurred during the teleportation process, but also the quantum correlation between the input and output states. In perspective of input-output correlation, non-separability between the input and output additional noise was manifested in quantum teleportation with $\mathcal{F} > 2/3$ [331]. However, this analysis is constrained to unity-gain regime. The re-evaluation of the equivalent T-V diagram, from the viewpoint of entanglement steering, would aid us to better understand the behavior of the heralded teleporter in more general operational regimes.

The study in Section 9.4.3 has showcased the ability of our heralded quantum teleporter to obtain a signal transfer coefficient $\mathcal{T}_q > 2$, which is impossible conventionally even if perfect EPR correlation was available. This opens up the possibility to realize quantum telecloning [390] with fidelity even surpassing the no-cloning limit and quantum tele-amplification [391] that was useful for coherent-state quantum computing [392, 393].

The phase conjugation on an arbitrary Gaussian state executes the transformation that flips the sign of the phase quadrature of the input while keeping its amplitude quadrature intact [35, 394]. It presents a continuous analogue to the antiunitary universal-NOT gate for qubits [395, 396, 397]. Such a transformation does not conserve the commutation relation and therefore, cannot be performed perfectly. The op-

timal fidelity of phase conjugation was proven to be $1/2$, where two units of shot noise are induced inevitably [394]. The fidelity bound coincides with the maximum accuracy of a dual-quadrature measurement [18, 19, 20], implying, therefore, that the best possible phase conjugator is exactly a measure-and-prepare setup. The deterministic phase conjugator in this regard can be considered as a purely classical process; however, interesting quantum effect occurs when one considers encoding information on phase-conjugated states. Rather counterintuitively, it was discovered that the antiparellel state $|\alpha\rangle \otimes |\alpha^*\rangle$ carries more information than the parallel counterpart $|\alpha\rangle \otimes |\alpha\rangle$. The advantage is attributed to entanglement arising from a joint measurement on the two modes [394, 396]. Through some preliminary studies, we found it is possible to build a probabilistic phase conjugator for coherent states by cascading a conventional CV teleporter with an upfront noiseless linear amplifier and *a posterior* noiseless attenuator. This novel scheme, by renouncing determinism, permits fidelity beyond the quantum limit ($\mathcal{F} > 1/2$) and even unit fidelity, which is in principle unachievable deterministically. It is certainly worthwhile to experimentally demonstrate this possibility upon modifications of our current experimental setup and investigate the many applications this new scheme leads to.

Last but not least, in all experiments in this thesis, the post-selection was implemented off-line for proof-of-principle demonstrations. A truly feasible quantum optical system empowered by post-selection would require it to be performed in real time. To this end, we can design a high-speed nonlinear analogue circuit similar to that has been constructed in [271]. The circuit in [271] was used to apply $\arctan(\kappa)$ and $\sqrt{1+\kappa^2}$, where κ is a sine wave with frequency of 1 MHz. The function of interest here has an inverse-Gaussian profile as discussed in chapter 5. Alternatively, FPGA would have the potential to post-process raw data directly after sampling. This method offers the advantage that both system control, data acquisition, and data processing are integrated in one PXI system; the potential problem, however, lies in the limited speed of data transmission between the digitizers and the FPGAs. Once the post-selection can be carried out in real time, the more appealing investigation would be to implement the teleportation scheme out of laboratory and to pinpoint the technical obstacles associated with post-selection-based quantum network proposals [83, 398].

Part III

Appendix

Appendix A

Layout and Locking for the high-fidelity squeezing gate

This appendix provides supplementary details on the experimental setup as well as the locking scheme for the high-fidelity squeezing gate and teleportatoin projects presented in chapters 7 and 8, and 9, respectively.

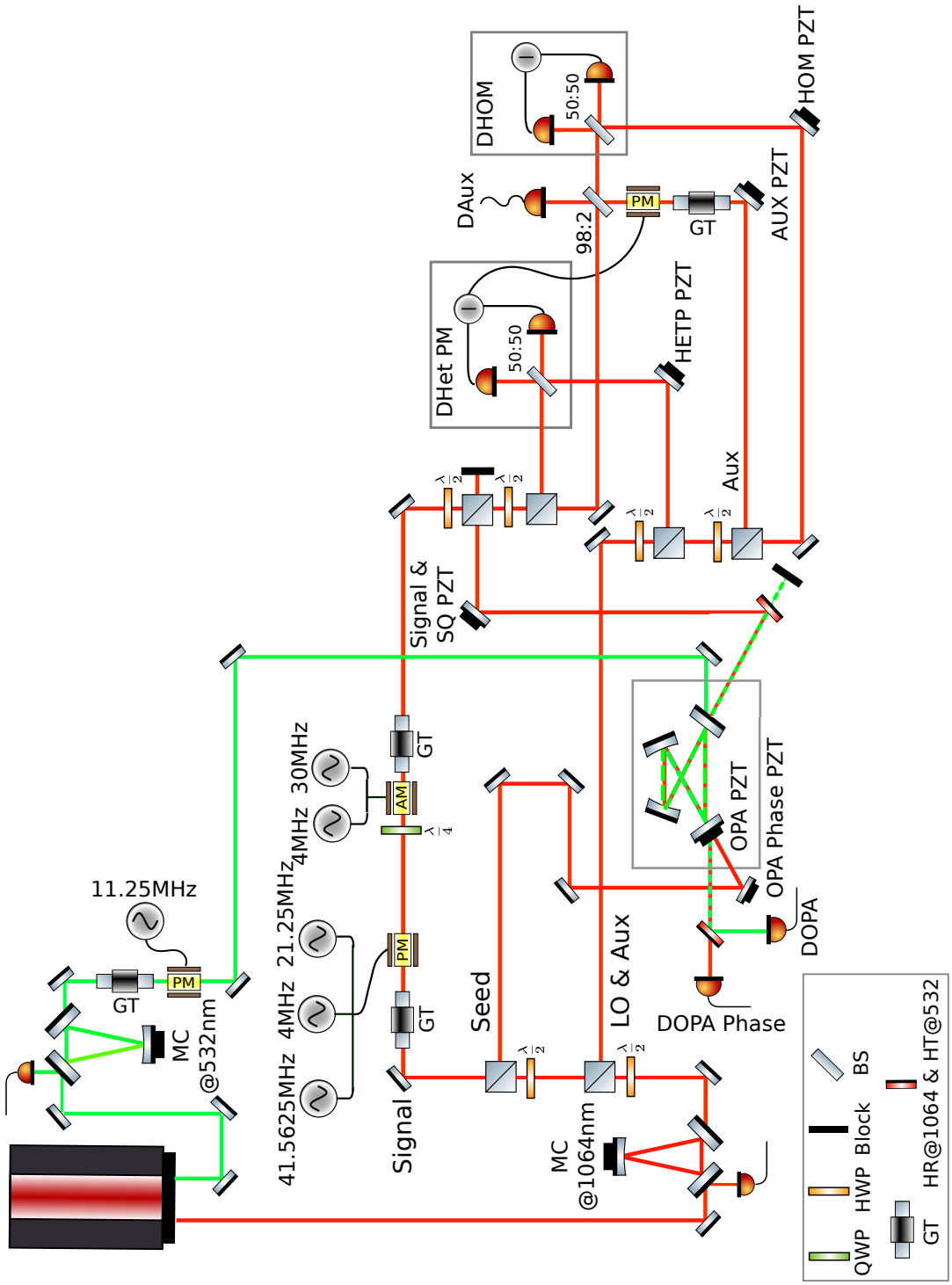

Figure A.1: Experimental layout for the high-fidelity squeezing gate experiment.

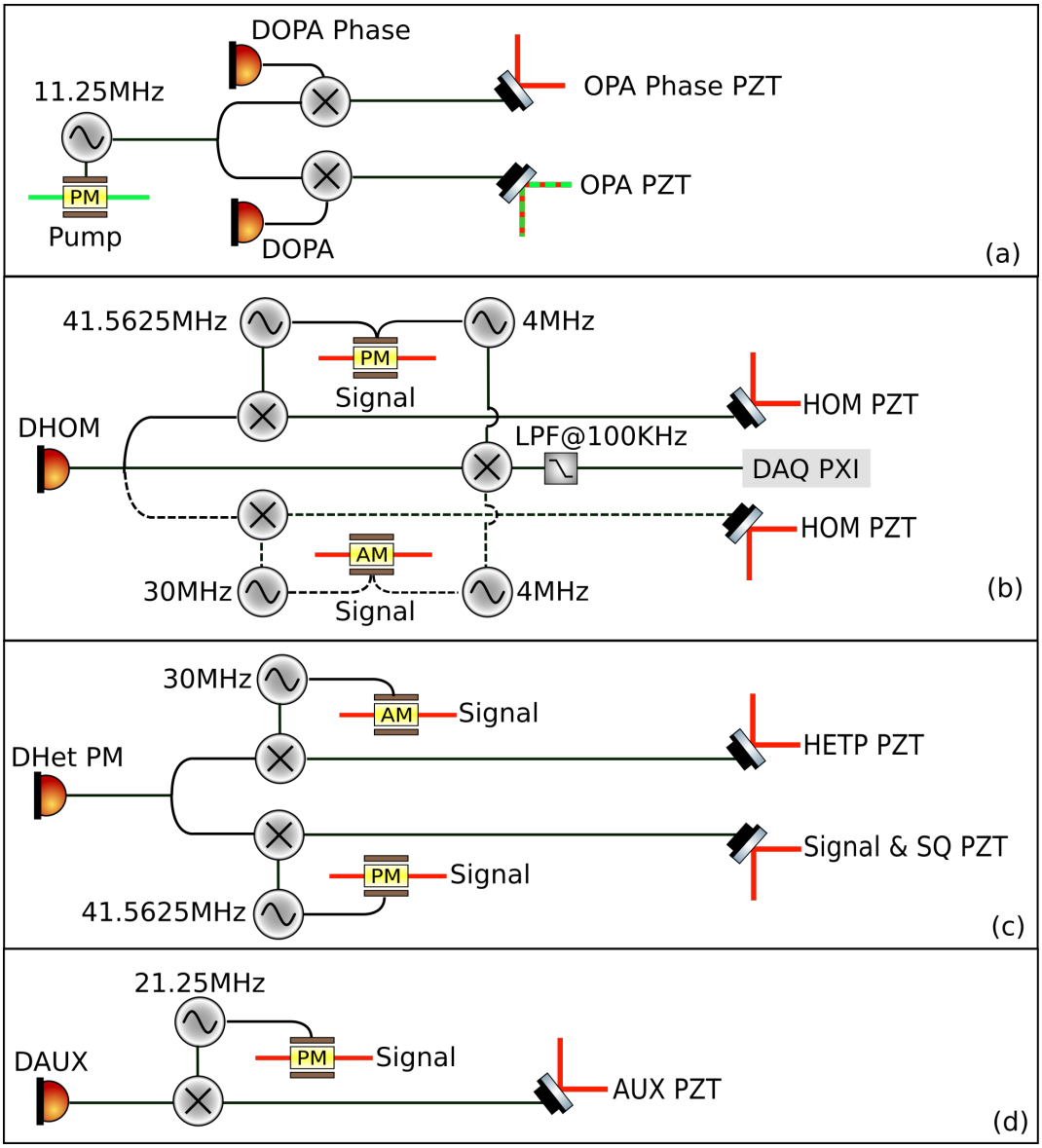

Figure A.2: Locking arrangement for the high-fidelity squeezing gate experiment. Four lockings are involved in total, including the lockings of the mode cleaner for the fundamental laser and the second harmonic laser, respectively, (a) the locking for the OPA cavity length and the relative phase between the pump and seed for the OPA, (b) the locking for the verifying homodyne station consecutively to phase and amplitude, (c) the locking for the in-loop single-quadrature homodyne which is locked to phase and the locking to make signal and the ancillary squeezed vacuum always interfere in phase, (d) the locking for the interference between the bright auxiliary beam and the signal beam that is used to realize the displacement operation. When the verifying homodyne is locked to a particular quadrature, namely phase or amplitude, the output signal is mixed with the corresponding modulation signal for input state generation at 4MHz, which is then fed to the data acquisition card on our PXI chasis (DAQ PXI).

Bibliography

[1] M. A. Nielsen and I. L. Chuang, *Quantum computation and quantum information* (Cambridge university press, 2010).

[2] H. J. Kimble, "The quantum internet," *Nature* **453**, 1023 (2008).

[3] V. Giovannetti, S. Lloyd, and L. Maccone, "Advances in quantum metrology," *Nature Photonics* **5**, 222 (2011).

[4] S. Pirandola, J. Eisert, C. Weedbrook, A. Furusawa, and S. L. Braunstein, "Advances in quantum teleportation," *Nature Photonics* **9**, 641 (2015).

[5] C. H. Bennett and G. Brassard, "Public key distribution and coin tossing," *Proceedings of the IEEE International Conference on Computers, Systems and Signal Processing* , 175 (1984).

[6] C. H. Bennett and G. Brassard, "Quantum cryptography: public key distribution and coin tossing," *Theoretical Computer Science* **560**, 7 (2014).

[7] N. Gisin, G. Ribordy, W. Tittel, and H. Zbinden, "Quantum cryptography," *Rev. Mod. Phys.* **74**, 145 (2002).

[8] N. Gisin and R. Thew, "Quantum communication," *Nature Photonics* **1**, 165 (2007).

[9] C. Simon, "Towards a global quantum network," *Nature Photonics* **11**, 678 (2017).

[10] D. E. Deutsch and R. Penrose, "Quantum computational networks," *Proceedings of the Royal Society of London. A. Mathematical and Physical Sciences* **425**, 73 (1989).

[11] A. Barenco, C. H. Bennett, R. Cleve, D. P. DiVincenzo, N. Margolus, P. Shor, T. Sleator, J. A. Smolin, and H. Weinfurter, "Elementary gates for quantum computation," *Phys. Rev. A* **52**, 3457 (1995).

[12] D. Deutsch and R. Penrose, "Quantum theory, the Church-Turing principle and the universal quantum computer," *Proceedings of the Royal Society of London. A. Mathematical and Physical Sciences* **400**, 97 (1985).

[13] A. Ekert and R. Jozsa, "Quantum computation and Shor's factoring algorithm," *Rev. Mod. Phys.* **68**, 733 (1996).

[14] J. Carolan, C. Harrold, C. Sparrow, E. Martín-López, N. J. Russell, J. W. Silverstone, P. J. Shadbolt, N. Matsuda, M. Oguma, M. Itoh, G. D.

Marshall, M. G. Thompson, J. C. F. Matthews, T. Hashimoto, J. L. O'Brien, and A. Laing, "Universal linear optics," *Science* **349**, 711 (2015) http://science.sciencemag.org/content/349/6249/711.full.pdf.

[15] T. Albash and D. A. Lidar, "Adiabatic quantum computation," *Rev. Mod. Phys.* **90**, 015002 (2018).

[16] H. J. Briegel, D. E. Browne, W. Dür, R. Raussendorf, and M. Van den Nest, "Measurement-based quantum computation," *Nature Physics* **5**, 19 (2009).

[17] W. K. Wootters and W. H. Zurek, "A single quantum cannot be cloned," *Nature* **299**, 802 (1982).

[18] E. Arthurs and J. L. Kelly, "On the simultaneous measurement of a pair of conjugate observables," *The Bell System Technical Journal* **44**, 725 (1965).

[19] S. Massar and S. Popescu, "Optimal Extraction of Information from Finite Quantum Ensembles," *Phys. Rev. Lett.* **74**, 1259 (1995).

[20] S. Stenholm, "Simultaneous measurement of conjugate variables," *Annals of Physics* **218**, 233 (1992).

[21] T. C. Ralph and A. P. Lund, "Nondeterministic Noiseless Linear Amplification of Quantum Systems," *AIP Conference Proceedings* **1110**, 155 (2009).

[22] J. Fiurášek, "Optimal probabilistic cloning and purification of quantum states," *Phys. Rev. A* **70**, 032308 (2004).

[23] W. Vogel and D.-G. Welsch, *Quantum optics* (John Wiley & Sons, 2006).

[24] D. F. Walls and G. J. Milburn, *Quantum Optics*, 2nd ed. ed. (Springer Berlin, 2008).

[25] H.-A. Bachor and T. C. Ralph, *A guide to experiments in quantum optics* (wiley-vch, 2004).

[26] M. M. Wilde, *Quantum Information Theory* (Cambridge University Press, 2013).

[27] T. C. Ralph, "Continuous variable quantum cryptography," *Phys. Rev. A* **61**, 010303 (1999).

[28] M. Hillery, "Quantum cryptography with squeezed states," *Phys. Rev. A* **61**, 022309 (2000).

[29] F. Grosshans and P. Grangier, "Continuous Variable Quantum Cryptography Using Coherent States," *Phys. Rev. Lett.* **88**, 057902 (2002).

[30] F. Grosshans, G. Van Assche, J. Wenger, R. Brouri, N. J. Cerf, and P. Grangier, "Quantum key distribution using gaussian-modulated coherent states," *Nature* **421**, 238 (2003).

[31] T. Symul, S. M. Assad, and P. K. Lam, "Real time demonstration of high bitrate quantum random number generation with coherent laser light," *Applied Physics Letters* **98**, 231103 (2011) https://doi.org/10.1063/1.3597793.

[32] C. Gabriel, C. Wittmann, D. Sych, R. Dong, W. Mauerer, U. L. Andersen, C. Marquardt, and G. Leuchs, "A generator for unique quantum random numbers based on vacuum states," *Nature Photonics* **4**, 711 (2010).

[33] R. J. Glauber, "Coherent and Incoherent States of the Radiation Field," *Phys. Rev.* **131**, 2766 (1963).

[34] E. C. G. Sudarshan, "Equivalence of Semiclassical and Quantum Mechanical Descriptions of Statistical Light Beams," *Phys. Rev. Lett.* **10**, 277 (1963).

[35] C. Weedbrook, S. Pirandola, R. García-Patrón, N. J. Cerf, T. C. Ralph, J. H. Shapiro, and S. Lloyd, "Gaussian quantum information," *Rev. Mod. Phys.* **84**, 621 (2012).

[36] A. Einstein, B. Podolsky, and N. Rosen, "Can Quantum-Mechanical Description of Physical Reality Be Considered Complete?," *Phys. Rev.* **47**, 777 (1935).

[37] B. Hensen, H. Bernien, A. E. Dréau, A. Reiserer, N. Kalb, M. S. Blok, J. Ruitenberg, R. F. L. Vermeulen, R. N. Schouten, C. Abellán, W. Amaya, V. Pruneri, M. W. Mitchell, M. Markham, D. J. Twitchen, D. Elkouss, S. Wehner, T. H. Taminiau, and R. Hanson, "Loophole-free Bell inequality violation using electron spins separated by 1.3 kilometres," *Nature* **526**, 682 (2015).

[38] M. Giustina, M. A. M. Versteegh, S. Wengerowsky, J. Handsteiner, A. Hochrainer, K. Phelan, F. Steinlechner, J. Kofler, J.-A. Larsson, C. Abellán, W. Amaya, V. Pruneri, M. W. Mitchell, J. Beyer, T. Gerrits, A. E. Lita, L. K. Shalm, S. W. Nam, T. Scheidl, R. Ursin, B. Wittmann, and A. Zeilinger, "Significant-Loophole-Free Test of Bell's Theorem with Entangled Photons," *Phys. Rev. Lett.* **115**, 250401 (2015).

[39] L. K. Shalm, E. Meyer-Scott, B. G. Christensen, P. Bierhorst, M. A. Wayne, M. J. Stevens, T. Gerrits, S. Glancy, D. R. Hamel, M. S. Allman, K. J. Coakley, S. D. Dyer, C. Hodge, A. E. Lita, V. B. Verma, C. Lambrocco, E. Tortorici, A. L. Migdall, Y. Zhang, D. R. Kumor, W. H. Farr, F. Marsili, M. D. Shaw, J. A. Stern, C. Abellán, W. Amaya, V. Pruneri, T. Jennewein, M. W. Mitchell, P. G. Kwiat, J. C. Bienfang, R. P. Mirin, E. Knill, and S. W. Nam, "Strong Loophole-Free Test of Local Realism," *Phys. Rev. Lett.* **115**, 250402 (2015).

[40] B. R. Mollow and R. J. Glauber, "Quantum Theory of Parametric Amplification. I," *Phys. Rev.* **160**, 1076 (1967).

[41] S. L. Braunstein and P. van Loock, "Quantum information with continuous variables," *Rev. Mod. Phys.* **77**, 513 (2005).

[42] C. H. Bennett, G. Brassard, S. Popescu, B. Schumacher, J. A. Smolin, and W. K. Wootters, "Purification of Noisy Entanglement and Faithful Teleportation via Noisy Channels," *Phys. Rev. Lett.* **76**, 722 (1996).

[43] L.-M. Duan, G. Giedke, J. I. Cirac, and P. Zoller, "Inseparability Criterion for Continuous Variable Systems," *Phys. Rev. Lett.* **84**, 2722 (2000).

[44] M. M. Wolf, G. Giedke, O. Krüger, R. F. Werner, and J. I. Cirac, "Gaussian entanglement of formation," *Phys. Rev. A* **69**, 052320 (2004).

[45] G. Vidal and R. F. Werner, "Computable measure of entanglement," *Phys. Rev. A* **65**, 032314 (2002).

[46] H. M. Wiseman, S. J. Jones, and A. C. Doherty, "Steering, Entanglement, Nonlocality, and the Einstein-Podolsky-Rosen Paradox," *Phys. Rev. Lett.* **98**, 140402 (2007).

[47] E. Wigner, "On the Quantum Correction For Thermodynamic Equilibrium," *Phys. Rev.* **40**, 749 (1932).

[48] P. D. Drummond and C. W. Gardiner, "Generalised P-representations in quantum optics," *Journal of Physics A: Mathematical and General* **13**, 2353 (1980).

[49] A. Holevo, "Some statistical problems for quantum Gaussian states," *IEEE Transactions on Information Theory* **21**, 533 (1975).

[50] B. Yurke, "Use of cavities in squeezed-state generation," *Phys. Rev. A* **29**, 408 (1984).

[51] S. Reynaud, C. Fabre, E. Giacobino, and A. Heidmann, "Photon noise reduction by passive optical bistable systems," *Phys. Rev. A* **40**, 1440 (1989).

[52] R. J. Glauber, F. Haake, L. M. Narducci, and D. F. Walls, *Coherence, Cooperation and Fluctuations*, 1st ed. ed. (Cambridge University Press, 1985).

[53] P. K. Lam, *"Applications of Quantum Electro-Optic Control and Squeezed Light"*, PhD thesis Australian National University 1998.

[54] J. D. Gibson, *Principles of Digital and Analog Communications*, 2nd ed. ed. (Prentice Hall, 1992).

[55] W. P. Bowen, *"Experiments towards a Quantum Information Network with Squeezed Light and Entanglement"*, PhD thesis Australian National University 2003.

[56] B. E. A. Saleh and M. C. Teich, *Fundamentals of photonics; 2nd ed.*Wiley series in pure and applied optics (Wiley, New York, NY, 2007).

[57] B. J. Cusack, B. S. Sheard, D. A. Shaddock, M. B. Gray, P. K. Lam, and S. E. Whitcomb, "Electro-optic modulator capable of generating simultaneous amplitude and phase modulations," *Appl. Opt.* **43**, 5079 (2004).

[58] M. G. Paris, "Displacement operator by beam splitter," *Physics Letters A* **217**, 78 (1996).

[59] H. Yuen and J. Shapiro, "Optical communication with two-photon coherent states–Part III: Quantum measurements realizable with photoemissive detectors," *IEEE Transactions on Information Theory* **26**, 78 (1980).

[60] K. Vogel and H. Risken, "Determination of quasiprobability distributions in terms of probability distributions for the rotated quadrature phase," *Phys. Rev. A* **40**, 2847 (1989).

[61] U. Leonhardt and H. Paul, "Measuring the quantum state of light," *Progress in Quantum Electronics* **19**, 89 (1995).

[62] A. I. Lvovsky and M. G. Raymer, "Continuous-variable optical quantum-state tomography," *Rev. Mod. Phys.* **81**, 299 (2009).

[63] A. Zavatta, S. Viciani, and M. Bellini, "Non-classical field characterization by high-frequency, time-domain quantum homodyne tomography," *Laser Physics Letters* **3**, 3 (2006).

[64] D. A. Shaddock, *"Advanced Interferometry for Gravitational Wave Detection"*, PhD thesis Australian National University 2000.

[65] G. F. Franklin, D. J. Powell, and A. Emami-Naeini, *Feedback Control of Dynamic Systems*, 4th ed. (Prentice Hall PTR, Upper Saddle River, NJ, USA, 2001).

[66] R. W. P. Drever, J. L. Hall, F. V. Kowalski, J. Hough, G. M. Ford, A. J. Munley, and H. Ward, "Laser phase and frequency stabilization using an optical resonator," *Applied Physics B* **31**, 95 (1983).

[67] E. D. Black, "An introduction to Pound–Drever–Hall laser frequency stabilization," *American Journal of Physics* **69**, 79 (2001).

[68] G. C. Bjorklund, "Frequency-modulation spectroscopy: a new method for measuring weak absorptions and dispersions," *Opt. Lett.* **5**, 15 (1980).

[69] G. Y. Xiang, T. C. Ralph, A. P. Lund, N. Walk, and G. J. Pryde, "Heralded noiseless linear amplification and distillation of entanglement," *Nature Photonics* **4**, 316 (2010).

[70] F. Ferreyrol, M. Barbieri, R. Blandino, S. Fossier, R. Tualle-Brouri, and P. Grangier, "Implementation of a nondeterministic optical noiseless amplifier," *Physical Review Letters* **104**, 123603 (2010).

[71] F. Ferreyrol, R. Blandino, M. Barbieri, R. Tualle-Brouri, and P. Grangier, "Experimental realization of a nondeterministic optical noiseless amplifier," *Physical Review A* **83**, 063801 (2011).

[72] S. Kocsis, G. Xiang, T. Ralph, and G. Pryde, "Heralded noiseless amplification of a photon polarization qubit," *Nat Phys* **9**, 23 (2013).

[73] A. Zavatta, J. Fiurášek, and M. Bellini, "A high-fidelity noiseless amplifier for quantum light states," *Nature Photon* **5**, 52 (2011).

[74] A. E. Ulanov, I. A. Fedorov, A. A. Pushkina, Y. V. Kurochkin, T. C. Ralph, and L. I., "Undoing the effect of loss on quantum entanglement," *Nat Photon* **9**, 764 (2015).

[75] M. A. Usuga, C. R. Müller, C. Wittmann, P. Marek, R. Filip, C. Marquardt, G. Leuchs, and U. L. Andersen, "Noise-powered probabilistic concentration of phase information," *Nat Phys* **6**, 767 (2010).

[76] C. Caves, "Quantum limits on noise in linear amplifiers," *Physical Review D* **26**, 1817 (1982).

[77] R. Blandino, A. Leverrier, M. Barbieri, J. Etesse, P. Grangier, and R. Tualle-Brouri, "Improving the maximum transmission distance of continuous-variable quantum key distribution using a noiseless amplifier," *Phys. Rev. A* **86**, 012327 (2012).

[78] N. Gisin, S. Pironio, and N. Sangouard, "Proposal for Implementing Device-Independent Quantum Key Distribution Based on a Heralded Qubit Amplifier," *Phys. Rev. Lett.* **105**, 070501 (2010).

[79] J. Fiurśšek and N. J. Cerf, "Gaussian postselection and virtual noiseless amplification in continuous-variable quantum key distribution," *Phys. Rev. A* **86**, 060302 (2012).

[80] C. R. Müller, C. Wittmann, P. Marek, R. Filip, C. Marquardt, G. Leuchs, and U. L. Andersen, "Probabilistic cloning of coherent states without a phase reference," *Phys. Rev. A* **86**, 010305 (2012).

[81] H. M. Chrzanowski, N. Walk, S. M. Assad, J. Janousek, S. Hosseini, T. C. Ralph, T. Symul, and P. K. Lam, "Measurement-based noiseless linear amplification for quantum communication," *Nature Photonics* **8**, 333 (2014).

[82] J. Bernu, S. Armstrong, T. Symul, T. C. Ralph, and P. K. Lam, "Theoretical analysis of an ideal noiseless linear amplifier for Einstein-Podolsky-Rosen entanglement distillation," *Journal of Physics B: Atomic, Molecular and Optical Physics* **47**, 215503 (2014).

[83] J. Dias and T. C. Ralph, "Quantum repeaters using continuous-variable teleportation," *Phys. Rev. A* **95**, 022312 (2017).

[84] T. C. Ralph, "Quantum error correction of continuous-variable states against Gaussian noise," *Phys. Rev. A* **84**, 022339 (2011).

[85] V. Dunjko and E. Andersson, "Truly noiseless probabilistic amplification," *Phys. Rev. A* **86**, 042322 (2012).

[86] J. Jeffers, "Nondeterministic amplifier for two-photon superpositions," *Phys. Rev. A* **82**, 063828 (2010).

[87] J. Fiurášek, "Engineering quantum operations on traveling light beams by multiple photon addition and subtraction," *Phys. Rev. A* **80**, 053822 (2009).

[88] P. Marek and R. Filip, "Coherent-state phase concentration by quantum probabilistic amplification," *Phys. Rev. A* **81**, 022302 (2010).

[89] S. Pandey, Z. Jiang, J. Combes, and C. M. Caves, "Quantum limits on probabilistic amplifiers," *Phys. Rev. A* **88**, 033852 (2013).

[90] N. A. McMahon, A. P. Lund, and T. C. Ralph, "Optimal architecture for a nondeterministic noiseless linear amplifier," *Phys. Rev. A* **89**, 023846 (2014).

[91] J. Combes, N. Walk, A. P. Lund, T. C. Ralph, and C. M. Caves, "Models of reduced-noise, probabilistic linear amplifiers," *Phys. Rev. A* **93**, 052310 (2016).

[92] N. Walk, T. C. Ralph, T. Symul, and P. K. Lam, "Security of continuous-variable quantum cryptography with Gaussian postselection," *Phys. Rev. A* **87**, 020303 (2013).

[93] R. Blandino, N. Walk, A. P. Lund, and T. C. Ralph, "Channel purification via continuous-variable quantum teleportation with Gaussian postselection," *Phys. Rev. A* **93**, 012326 (2016).

[94] J. Y. Haw, J. Zhao, J. Dias, S. M. Assad, M. Bradshaw, R. Blandino, T. Symul, T. C. Ralph, and P. K. Lam, "Surpassing the no-cloning limit with a heralded hybrid linear amplifier for coherent states," *Nature Communication* **7**, 13222 (2017).

[95] N. J. Cerf and S. Iblisdir, "Optimal N -to-M cloning of conjugate quantum variables," *Phys. Rev. A* **62**, 040301 (2000).

[96] R. E. Slusher, L. W. Hollberg, B. Yurke, J. C. Mertz, and J. F. Valley, "Observation of Squeezed States Generated by Four-Wave Mixing in an Optical Cavity," *Phys. Rev. Lett.* **55**, 2409 (1985).

[97] S. Machida and Y. Yamamoto, "Observation of sub-poissonian photoelectron statistics in a negative feedback semiconductor laser," *Optics Communications* **57**, 290 (1986).

[98] L.-A. Wu, H. J. Kimble, J. L. Hall, and H. Wu, "Generation of Squeezed States by Parametric Down Conversion," *Phys. Rev. Lett.* **57**, 2520 (1986).

[99] R. M. Shelby, M. D. Levenson, S. H. Perlmutter, R. G. DeVoe, and D. F. Walls, "Broad-Band Parametric Deamplification of Quantum Noise in an Optical Fiber," *Phys. Rev. Lett.* **57**, 691 (1986).

[100] L.-A. Wu, M. Xiao, and H. J. Kimble, "Squeezed states of light from an optical parametric oscillator," *J. Opt. Soc. Am. B* **4**, 1465 (1987).

[101] B. Gazdy and J. M. Bowman, "Novel decomposition of the multichannel scattering matrix at resonances," *Phys. Rev. Lett.* **59**, 3 (1987).

[102] P. Grangier, R. E. Slusher, B. Yurke, and A. LaPorta, "Squeezed-light–enhanced polarization interferometer," *Phys. Rev. Lett.* **59**, 2153 (1987).

[103] A. Heidmann, R. J. Horowicz, S. Reynaud, E. Giacobino, C. Fabre, and G. Camy, "Observation of Quantum Noise Reduction on Twin Laser Beams," *Phys. Rev. Lett.* **59**, 2555 (1987).

[104] R. E. Slusher, P. Grangier, A. LaPorta, B. Yurke, and M. J. Potasek, "Pulsed Squeezed Light," *Phys. Rev. Lett.* **59**, 2566 (1987).

[105] S. Machida, Y. Yamamoto, and Y. Itaya, "Observation of amplitude squeezing in a constant-current–driven semiconductor laser," *Phys. Rev. Lett.* **58**, 1000 (1987).

[106] S. F. Pereira, M. Xiao, H. J. Kimble, and J. L. Hall, "Generation of squeezed light by intracavity frequency doubling," *Phys. Rev. A* **38**, 4931 (1988).

[107] C. D. Nabors and R. M. Shelby, "Two-color squeezing and sub-shot-noise signal recovery in doubly resonant optical parametric oscillators," *Phys. Rev. A* **42**, 556 (1990).

[108] A. Sizmann, R. Horowicz, G. Wagner, and G. Leuchs, "Observation of amplitude squeezing of the up-converted mode in second harmonic generation," *Optics Communications* **80**, 138 (1990).

[109] K. Bergman and H. A. Haus, "Squeezing in fibers with optical pulses," *Opt. Lett.* **16**, 663 (1991).

[110] W. H. Richardson and Y. Yamamoto, "Quantum correlation between the junction-voltage fluctuation and the photon-number fluctuation in a semiconductor laser," *Phys. Rev. Lett.* **66**, 1963 (1991).

[111] M. Rosenbluh and R. M. Shelby, "Squeezed optical solitons," *Phys. Rev. Lett.* **66**, 153 (1991).

[112] E. S. Polzik, J. Carri, and H. J. Kimble, "Atomic spectroscopy with squeezed light for sensitivity beyond the vacuum-state limit," *Applied Physics B* **55**, 279 (1992).

[113] S. Inoue, H. Ohzu, S. Machida, and Y. Yamamoto, "Quantum correlation between longitudinal-mode intensities in a multimode squeezed semiconductor laser," *Phys. Rev. A* **46**, 2757 (1992).

[114] E. S. Polzik, J. Carri, and H. J. Kimble, "Spectroscopy with squeezed light," *Phys. Rev. Lett.* **68**, 3020 (1992).

[115] P. Kürz, R. Paschotta, K. Fiedler, A. Sizmann, G. Leuchs, and J. Mlynek, "Squeezing by second-harmonic generation in a monolithic resonator," *Applied Physics B* **55**, 216 (1992).

[116] O. Aytür and P. Kumar, "Squeezed-light generation with a mode-locked Q-switched laser and detection by using a matched local oscillator," *Opt. Lett.* **17**, 529 (1992).

[117] M. J. Freeman, H. Wang, D. G. Steel, R. Craig, and D. R. Scifres, "Wavelength-tunable amplitude-squeezed light from a room-temperature quantum-well laser," *Opt. Lett.* **18**, 2141 (1993).

[118] P. Kürz, R. Paschotta, K. Fiedler, and J. Mlynek, "Bright Squeezed Light by Second-Harmonic Generation in a Monolithic Resonator," *EPL (Europhysics Letters)* **24**, 449 (1993).

[119] P. D. Drummond, R. M. Shelby, S. R. Friberg, and Y. Yamamoto, "Quantum solitons in optical fibres," *Nature* **365**, 307 (1993).

[120] C. Kim and P. Kumar, "Quadrature-Squeezed Light Detection Using a Self-Generated Matched Local Oscillator," *Phys. Rev. Lett.* **73**, 1605 (1994).

[121] R. Paschotta, M. Collett, P. Kürz, K. Fiedler, H. A. Bachor, and J. Mlynek, "Bright squeezed light from a singly resonant frequency doubler," *Phys. Rev. Lett.* **72**, 3807 (1994).

[122] G. Breitenbach, T. Müller, S. F. Pereira, J.-P. Poizat, S. Schiller, and J. Mlynek, "Squeezed vacuum from a monolithic optical parametric oscillator," *J. Opt. Soc. Am. B* **12**, 2304 (1995).

[123] H. Tsuchida, "Generation of amplitude-squeezed light at 431 nm from a singly resonant frequency doubler," *Opt. Lett.* **20**, 2240 (1995).

[124] T. C. Ralph, M. S. Taubman, A. G. White, D. E. McClelland, and H.-A. Bachor, "Squeezed light from second-harmonic generation: experiment versus theory," *Opt. Lett.* **20**, 1316 (1995).

[125] D. C. Kilper, D. G. Steel, R. Craig, and D. R. Scifres, "Polarization-dependent noise in photon-number squeezed light generated by quantum-well lasers," *Opt. Lett.* **21**, 1283 (1996).

[126] K. Schneider, R. Bruckmeier, H. Hansen, S. Schiller, and J. Mlynek, "Bright squeezed-light generation by a continuous-wave semimonolithic parametric amplifier," *Opt. Lett.* **21**, 1396 (1996).

[127] S. R. Friberg, S. Machida, M. J. Werner, A. Levanon, and T. Mukai, "Observation of Optical Soliton Photon-Number Squeezing," *Phys. Rev. Lett.* **77**, 3775 (1996).

[128] G. Breitenbach, S. Schiller, and J. Mlynek, "Measurement of the quantum states of squeezed light," *Nature* **387**, 471 (1997).

[129] J. Gao, F. Cui, C. Xue, C. Xie, and K. Peng, "Generation and application of twin beams from an optical parametric oscillator including an α-cut KTP crystal," *Opt. Lett.* **23**, 870 (1998).

[130] K. Schneider, M. Lang, J. Mlynek, and S. Schiller, "Generation of strongly squeezed continuous-wave light at 1064 nm," *Opt. Express* **2**, 59 (1998).

[131] D. Krylov and K. Bergman, "Amplitude-squeezed solitons from an asymmetric fiber interferometer," *Opt. Lett.* **23**, 1390 (1998).

[132] S. Schmitt, J. Ficker, M. Wolff, F. König, A. Sizmann, and G. Leuchs, "Photon-Number Squeezed Solitons from an Asymmetric Fiber-Optic Sagnac Interferometer," *Phys. Rev. Lett.* **81**, 2446 (1998).

[133] S. Spälter, M. Burk, U. Strößner, A. Sizmann, and G. Leuchs, "Propagation of quantum properties of sub-picosecond solitons in a fiber," *Opt. Express* **2**, 77 (1998).

[134] P. K. Lam, T. C. Ralph, B. C. Buchler, D. E. McClelland, H.-A. Bachor, and J. Gao, "Optimization and transfer of vacuum squeezing from an optical parametric oscillator," *Journal of Optics B: Quantum and Semiclassical Optics* **1**, 469 (1999).

[135] S. Lahti, K. Tanaka, T. Morita, S. Inoue, H. Kan, and Y. Yamamoto, "Transverse-junction-stripe GaAs-AlGaAs lasers for squeezed light generation," *IEEE J. Quantum Electron.* **35**, 387 (1999).

[136] M. Fiorentino, J. E. Sharping, P. Kumar, D. Levandovsky, and M. Vasilyev, "Soliton squeezing in a Mach-Zehnder fiber interferometer," *Phys. Rev. A* **64**, 031801 (2001).

[137] S. Lorenz, C. Silberhorn, N. Korolkova, R. Windeler, and G. Leuchs, "Squeezed light from microstructured fibres: towards free-space quantum cryptography," *Applied Physics B* **73**, 855 (2001).

[138] K. McKenzie, D. A. Shaddock, D. E. McClelland, B. C. Buchler, and P. K. Lam, "Experimental Demonstration of a Squeezing-Enhanced Power-Recycled Michelson Interferometer for Gravitational Wave Detection," *Phys. Rev. Lett.* **88**, 231102 (2002).

[139] M. Fiorentino, J. E. Sharping, P. Kumar, A. Porzio, and R. S. Windeler, "Soliton squeezing in microstructure fiber," *Opt. Lett.* **27**, 649 (2002).

[140] W. P. Bowen, R. Schnabel, N. Treps, H.-A. Bachor, and P. K. Lam, "Recovery of continuous wave squeezing at low frequencies," *Journal of Optics B: Quantum and Semiclassical Optics* **4**, 421 (2002).

[141] J. Laurat, T. Coudreau, N. Treps, A. Maître, and C. Fabre, "Conditional Preparation of a Quantum State in the Continuous Variable Regime: Generation of a sub-Poissonian State from Twin Beams," *Phys. Rev. Lett.* **91**, 213601 (2003).

[142] J. Ries, B. Brezger, and A. I. Lvovsky, "Experimental vacuum squeezing in rubidium vapor via self-rotation," *Phys. Rev. A* **68**, 025801 (2003).

[143] K. McKenzie, N. Grosse, W. P. Bowen, S. E. Whitcomb, M. B. Gray, D. E. McClelland, and P. K. Lam, "Squeezing in the Audio Gravitational-Wave Detection Band," *Phys. Rev. Lett.* **93**, 161105 (2004).

[144] J. Laurat, T. Coudreau, G. Keller, N. Treps, and C. Fabre, "Compact source of Einstein-Podolsky-Rosen entanglement and squeezing at very low noise frequencies," *Phys. Rev. A* **70**, 042315 (2004).

[145] J. Heersink, V. Josse, G. Leuchs, and U. L. Andersen, "Efficient polarization squeezing in optical fibers," *Opt. Lett.* **30**, 1192 (2005).

[146] K. Hirosawa, H. Furumochi, A. Tada, F. Kannari, M. Takeoka, and M. Sasaki, "Photon Number Squeezing of Ultrabroadband Laser Pulses Generated by Microstructure Fibers," *Phys. Rev. Lett.* **94**, 203601 (2005).

[147] S. Chelkowski, H. Vahlbruch, B. Hage, A. Franzen, N. Lastzka, K. Danzmann, and R. Schnabel, "Experimental characterization of frequency-dependent squeezed light," *Phys. Rev. A* **71**, 013806 (2005).

[148] S. Suzuki, H. Yonezawa, F. Kannari, M. Sasaki, and A. Furusawa, "7dB quadrature squeezing at 860nm with periodically poled KTiOPO4," *Applied Physics Letters* **89**, 061116 (2006).

[149] H. Vahlbruch, S. Chelkowski, B. Hage, A. Franzen, K. Danzmann, and R. Schnabel, "Coherent Control of Vacuum Squeezing in the Gravitational-Wave Detection Band," *Phys. Rev. Lett.* **97**, 011101 (2006).

[150] Y. Takeno, M. Yukawa, H. Yonezawa, and A. Furusawa, "Observation of -9 dB quadrature squeezing with improvement of phase stability in homodyne measurement," *Opt. Express* **15**, 4321 (2007).

[151] H. Vahlbruch, S. Chelkowski, K. Danzmann, and R. Schnabel, "Quantum engineering of squeezed states for quantum communication and metrology," *New Journal of Physics* **9**, 371 (2007).

[152] C. F. McCormick, V. Boyer, E. Arimondo, and P. D. Lett, "Strong relative intensity squeezing by four-wave mixing in rubidium vapor," *Opt. Lett.* **32**, 178 (2007).

[153] Y. Zhang, T. Furuta, R. Okubo, K. Takahashi, and T. Hirano, "Experimental generation of broadband quadrature entanglement using laser pulses," *Phys. Rev. A* **76**, 012314 (2007).

[154] Y. Eto, T. Tajima, Y. Zhang, and T. Hirano, "Observation of squeezed light at 1.535 μm using a pulsed homodyne detector," *Opt. Lett.* **32**, 1698 (2007).

[155] K.-i. Yoshino, T. Aoki, and A. Furusawa, "Generation of continuous-wave broadband entangled beams using periodically poled lithium niobate waveguides," *Applied Physics Letters* **90**, 041111 (2007).

[156] H. Vahlbruch, M. Mehmet, S. Chelkowski, B. Hage, A. Franzen, N. Lastzka, S. Goßler, K. Danzmann, and R. Schnabel, "Observation of Squeezed Light with 10-dB Quantum-Noise Reduction," *Phys. Rev. Lett.* **100**, 033602 (2008).

[157] C. F. McCormick, A. M. Marino, V. Boyer, and P. D. Lett, "Strong low-frequency quantum correlations from a four-wave-mixing amplifier," *Phys. Rev. A* **78**, 043816 (2008).

[158] K. Goda, E. E. Mikhailov, O. Miyakawa, S. Saraf, S. Vass, A. Weinstein, and N. Mavalvala, "Generation of a stable low-frequency squeezed vacuum field with periodically poled KTiOPO4 at 1064 nm," *Opt. Lett.* **33**, 92 (2008).

[159] M. Pysher, R. Bloomer, C. M. Kaleva, T. D. Roberts, P. Battle, and O. Pfister, "Broadband amplitude squeezing in a periodically poled KTiOPO4 waveguide," *Opt. Lett.* **34**, 256 (2009).

[160] K. Hirosawa, Y. Ito, H. Ushio, H. Nakagome, and F. Kannari, "Generation of squeezed vacuum pulses using cascaded second-order optical nonlinearity of periodically poled lithium niobate in a Sagnac interferometer," *Phys. Rev. A* **80**, 043832 (2009).

[161] T. Eberle, S. Steinlechner, J. Bauchrowitz, V. Händchen, H. Vahlbruch, M. Mehmet, H. Müller-Ebhardt, and R. Schnabel, "Quantum Enhancement of the Zero-Area Sagnac Interferometer Topology for Gravitational Wave Detection," *Phys. Rev. Lett.* **104**, 251102 (2010).

[162] M. Mehmet, H. Vahlbruch, N. Lastzka, K. Danzmann, and R. Schnabel, "Observation of squeezed states with strong photon-number oscillations," *Phys. Rev. A* **81**, 013814 (2010).

[163] H. Yonezawa, K. Nagashima, and A. Furusawa, "Generation of squeezed light with a monolithic optical parametric oscillator: Simultaneous achievement of phase matching and cavity resonance by temperature control," *Opt. Express* **18**, 20143 (2010).

[164] H. Vahlbruch, A. Khalaidovski, N. Lastzka, C. Gräf, K. Danzmann, and R. Schnabel, "The GEO600 squeezed light source," *Classical and Quantum Gravity* **27**, 084027 (2010).

[165] I. H. Agha, G. Messin, and P. Grangier, "Generation of pulsed and continuous-wave squeezed light with 87Rb vapor," *Opt. Express* **18**, 4198 (2010).

[166] M. Mehmet, S. Ast, T. Eberle, S. Steinlechner, H. Vahlbruch, and R. Schnabel, "Squeezed light at 1550 nm with a quantum noise reduction of 12.3 dB," *Opt. Express* **19**, 25763 (2011).

[167] J. Dias and T. Ralph, "Continuous Variable Quantum Repeaters," *arXiv preprint arXiv:1505.03626* (2015).

[168] Q. Glorieux, L. Guidoni, S. Guibal, J.-P. Likforman, and T. Coudreau, "Quantum correlations by four-wave mixing in an atomic vapor in a nonamplifying regime: Quantum beam splitter for photons," *Phys. Rev. A* **84**, 053826 (2011).

[169] S. S. Y. Chua, M. S. Stefszky, C. M. Mow-Lowry, B. C. Buchler, S. Dwyer, D. A. Shaddock, P. K. Lam, and D. E. McClelland, "Backscatter tolerant squeezed light source for advanced gravitational-wave detectors," *Opt. Lett.* **36**, 4680 (2011).

[170] Y. Eto, A. Koshio, A. Ohshiro, J. Sakurai, K. Horie, T. Hirano, and M. Sasaki, "Efficient homodyne measurement of picosecond squeezed pulses with pulse shaping technique," *Opt. Lett.* **36**, 4653 (2011).

[171] N. Corzo, A. M. Marino, K. M. Jones, and P. D. Lett, "Multi-spatial-mode single-beam quadrature squeezed states of light from four-wave mixing in hot rubidium vapor," *Opt. Express* **19**, 21358 (2011).

[172] S. Barreiro, P. Valente, H. Failache, and A. Lezama, "Polarization squeezing of light by single passage through an atomic vapor," *Phys. Rev. A* **84**, 033851 (2011).

[173] J. U. Fürst, D. V. Strekalov, D. Elser, A. Aiello, U. L. Andersen, C. Marquardt, and G. Leuchs, "Quantum Light from a Whispering-Gallery-Mode Disk Resonator," *Phys. Rev. Lett.* **106**, 113901 (2011).

[174] A. Ourjoumtsev, A. Kubanek, M. Koch, C. Sames, P. W. H. Pinkse, G. Rempe, and K. Murr, "Observation of squeezed light from one atom excited with two photons," *Nature* **474**, 623 (2011).

[175] M. S. Stefszky, C. M. Mow-Lowry, S. S. Y. Chua, D. A. Shaddock, B. C. Buchler, H. Vahlbruch, A. Khalaidovski, R. Schnabel, P. K. Lam, and D. E. McClelland, "Balanced homodyne detection of optical quantum states at audio-band frequencies and below," *Classical and Quantum Gravity* **29**, 145015 (2012).

[176] S. Ast, A. Samblowski, M. Mehmet, S. Steinlechner, T. Eberle, and R. Schnabel, "Continuous-wave nonclassical light with gigahertz squeezing bandwidth," *Opt. Lett.* **37**, 2367 (2012).

[177] S. Ast, M. Mehmet, and R. Schnabel, "High-bandwidth squeezed light at 1550 nm from a compact monolithic PPKTP cavity," *Opt. Express* **21**, 13572 (2013).

[178] T. P. Purdy, P.-L. Yu, R. W. Peterson, N. S. Kampel, and C. A. Regal, "Strong Optomechanical Squeezing of Light," *Phys. Rev. X* **3**, 031012 (2013).

[179] A. H. Safavi-Naeini, S. Gröblacher, J. T. Hill, J. Chan, M. Aspelmeyer, and O. Painter, "Squeezed light from a silicon micromechanical resonator," *Nature* **500**, 185 (2013).

[180] A. M. Pérez, T. S. Iskhakov, P. Sharapova, S. Lemieux, O. V. Tikhonova, M. V. Chekhova, and G. Leuchs, "Bright squeezed-vacuum source with 1.1 spatial mode," *Opt. Lett.* **39**, 2403 (2014).

[181] G. Masada, K. Miyata, A. Politi, T. Hashimoto, J. L. O'Brien, and A. Furusawa, "Continuous-variable entanglement on a chip," *Nature Photonics* **9**, 316 (2015).

[182] M. A. Finger, T. S. Iskhakov, N. Y. Joly, M. V. Chekhova, and P. S. J. Russell, "Raman-Free, Noble-Gas-Filled Photonic-Crystal Fiber Source for Ultrafast, Very Bright Twin-Beam Squeezed Vacuum," *Phys. Rev. Lett.* **115**, 143602 (2015).

[183] A. Dutt, K. Luke, S. Manipatruni, A. L. Gaeta, P. Nussenzveig, and M. Lipson, "On-Chip Optical Squeezing," *Phys. Rev. Applied* **3**, 044005 (2015).

[184] J.-M. Pirkkalainen, E. Damskägg, M. Brandt, F. Massel, and M. A. Sillanpää, "Squeezing of Quantum Noise of Motion in a Micromechanical Resonator," *Phys. Rev. Lett.* **115**, 243601 (2015).

[185] C. H. H. Schulte, J. Hansom, A. E. Jones, C. Matthiesen, C. Le Gall, and M. Atatüre, "Quadrature squeezed photons from a two-level system," *Nature* **525**, 222 (2015).

[186] H. Vahlbruch, M. Mehmet, K. Danzmann, and R. Schnabel, "Detection of 15 dB Squeezed States of Light and their Application for the Absolute Calibration of Photoelectric Quantum Efficiency," *Phys. Rev. Lett.* **117**, 110801 (2016).

[187] T. Serikawa, J. ichi Yoshikawa, K. Makino, and A. Frusawa, "Creation and measurement of broadband squeezed vacuum from a ring optical parametric oscillator," *Opt. Express* **24**, 28383 (2016).

[188] E. Oelker, G. Mansell, M. Tse, J. Miller, F. Matichard, L. Barsotti, P. Fritschel, D. E. McClelland, M. Evans, and N. Mavalvala, "Ultra-low phase noise squeezed vacuum source for gravitational wave detectors," *Optica* **3**, 682 (2016).

[189] A. Brieussel, Y. Shen, G. Campbell, G. Guccione, J. Janousek, B. Hage, B. C. Buchler, N. Treps, C. Fabre, F. Z. Fang, X. Y. Li, T. Symul, and P. K. Lam, "Squeezed light from a diamond-turned monolithic cavity," *Opt. Express* **24**, 4042 (2016).

[190] F. Kaiser, B. Fedrici, A. Zavatta, V. D'Auria, and S. Tanzilli, "A fully guided-wave squeezing experiment for fiber quantum networks," *Optica* **3**, 362 (2016).

[191] W. Yang, S. Shi, Y. Wang, W. Ma, Y. Zheng, and K. Peng, "Detection of stably bright squeezed light with the quantum noise reduction of 12.6 dB by mutually compensating the phase fluctuations," *Opt. Lett.* **42**, 4553 (2017).

[192] S. Shi, Y. Wang, W. Yang, Y. Zheng, and K. Peng, "Detection and perfect fitting of 13.2 dB squeezed vacuum states by considering green-light-induced infrared absorption," *Opt. Lett.* **43**, 5411 (2018).

[193] F. Lenzini, J. Janousek, O. Thearle, M. Villa, B. Haylock, S. Kasture, L. Cui, H.-P. Phan, D. V. Dao, H. Yonezawa, P. K. Lam, E. H. Huntington, and M. Lobino, "Integrated photonic platform for quantum information with continuous variables," *Science Advances* **4** (2018) http://advances.sciencemag.org/content/4/12/eaat9331.full.pdf.

[194] V. V. Dodonov, "'Nonclassical' states in quantum optics: a 'squeezed' review of the first 75 years," *Journal of Optics B: Quantum and Semiclassical Optics* **4**, R1 (2002).

[195] J. N. Hollenhorst, "Quantum limits on resonant-mass gravitational-radiation detectors," *Phys. Rev. D* **19**, 1669 (1979).

[196] C. M. Caves, "Quantum-mechanical noise in an interferometer," *Phys. Rev. D* **23**, 1693 (1981).

[197] L. Mandel, "Squeezing and photon antibunching in harmonic generation," *Optics Communications* **42**, 437 (1982).

[198] U. L. Andersen, T. Gehring, C. Marquardt, and G. Leuchs, "30 years of squeezed light generation," *Physica Scripta* **91**, 053001 (2016).

[199] M. J. Collett and C. W. Gardiner, "Squeezing of intracavity and traveling-wave light fields produced in parametric amplification," *Phys. Rev. A* **30**, 1386 (1984).

[200] P. D. Drummond and Z. Ficek, *Quantum Squeezing*, 1st ed. ed. (Springer-Verlag Berlin Heidelberg, 2004).

[201] B. Robert, *Nonlinear Optics*, 3rd ed. ed. (Academic Press, 2008).

[202] M. S. Stefszky, *"Low-Frequency Squeezing for Gravitational-Wave Detection"*, PhD thesis Australian National University 2012.

[203] J. A. Armstrong, N. Bloembergen, J. Ducuing, and P. S. Pershan, "Interactions between Light Waves in a Nonlinear Dielectric," *Phys. Rev.* **127**, 1918 (1962).

[204] K. McKenzie, *"Squeezing in the Audio Gravitational Wave Detection Band"*, PhD thesis Australian National University 2002.

[205] H. TAKAHASI, *Information Theory of Quantum-Mechanical Channels*volume 1 of *Advances in Communication Systems* (Elsevier, 1965).

[206] B. R. Mollow and R. J. Glauber, "Quantum Theory of Parametric Amplification. II," *Phys. Rev.* **160**, 1097 (1967).

[207] G. Milburn and D. Walls, "Production of squeezed states in a degenerate parametric amplifier," *Optics Communications* **39**, 401 (1981).

[208] A. G. White, *"Classical and quantum dynamics of optical frequency conversion"*, PhD thesis Australian National University 1997.

[209] F. D. Valle, E. Milotti, A. Ejlli, U. Gastaldi, G. Messineo, L. Piemontese, G. Zavattini, R. Pengo, and G. Ruoso, "Extremely long decay time optical cavity," *Opt. Express* **22**, 11570 (2014).

[210] P. Drummond, K. McNeil, and D. Walls, "Non-equilibrium Transitions in Sub/Second Harmonic Generation," *Optica Acta: International Journal of Optics* **27**, 321 (1980).

[211] P. Drummond, K. McNeil, and D. Walls, "Non-equilibrium Transitions in Sub/second Harmonic Generation," *Optica Acta: International Journal of Optics* **28**, 211 (1981).

[212] G. D. Boyd and D. A. Kleinman, "Parametric Interaction of Focused Gaussian Light Beams," *Journal of Applied Physics* **39**, 3597 (1968).

[213] S. Wang, V. Pasiskevicius, and F. Laurell, "Dynamics of green light-induced infrared absorption in KTiOPO4 and periodically poled KTiOPO4," *Journal of Applied Physics* **96**, 2023 (2004).

[214] Y. Furukawa, K. Kitamura, A. Alexandrovski, R. K. Route, M. M. Fejer, and G. Foulon, "Green-induced infrared absorption in MgO doped LiNbO3," *Applied Physics Letters* **78**, 1970 (2001).

[215] S. Wang, *"Fabrication and Characterization of Periodically-poled KTP andRb-doped KTP for Applications in the Visible and UV"*, PhD thesis Royal Institute of Technology 2005.

[216] H. Kogelnik, "Imaging of optical modes - resonators with internal lenses," *The Bell System Technical Journal* **44**, 455 (1965).

[217] H. Kogelnik and T. Li, "Laser Beams and Resonators," *Appl. Opt.* **5**, 1550 (1966).

[218] M. Dietrich, *Light Transmission Optics*, 2nd ed. ed. (Krieger Pub Co, 1989).

[219] R. W. Boyd, "Intuitive explanation of the phase anomaly of focused light beams," *J. Opt. Soc. Am.* **70**, 877 (1980).

[220] S. Feng and H. G. Winful, "Physical origin of the Gouy phase shift," *Opt. Lett.* **26**, 485 (2001).

[221] G. Y. Xiang, T. C. Ralph, A. P. Lund, N. Walk, and G. J. Pryde, "Heralded noiseless linear amplification and distillation of entanglement," *Nature Photonics* **4**, 316 (2010).

[222] H. A. Haus and J. A. Mullen, "Quantum Noise in Linear Amplifiers," *Phys. Rev.* **128**, 2407 (1962).

[223] B. Yurke, "Use of cavities in squeezed-state generation," *Physical Review A* **29**, 408 (1984).

[224] G. J. Milburn, M. L. Steyn-Ross, and D. F. Walls, "Linear amplifiers with phase-sensitive noise," *Phys. Rev. A* **35**, 4443 (1987).

[225] J. A. Levenson, I. Abram, T. Rivera, and P. Grangier, "Reduction of quantum noise in optical parametric amplification," *J. Opt. Soc. Am. B* **10**, 2233 (1993).

[226] J. A. Levenson, I. Abram, T. Rivera, P. Fayolle, J. C. Garreau, and P. Grangier, "Quantum optical cloning amplifier," *Phys. Rev. Lett.* **70**, 267 (1993).

[227] E. Goobar, A. Karlsson, G. Björk, and O. Nilsson, "Low-noise optoelectronic photon number amplifier and quantum-optical tap," *Opt. Lett.* **19**, 922 (1994).

[228] P. K. Lam, T. C. Ralph, E. H. Huntington, and H.-A. Bachor, "Noiseless Signal Amplification using Positive Electro-Optic Feedforward," *Phys. Rev. Lett.* **79**, 1471 (1997).

[229] N. Walk, A. P. Lund, and T. C. Ralph, "Nondeterministic noiseless amplification via non-symplectic phase space transformations," *New Journal of Physics* **15**, 073014 (2013).

[230] Z. Y. Ou, "Quantum amplification with correlated quantum fields," *Phys. Rev. A* **48**, R1761 (1993).

[231] J. Kong, F. Hudelist, Z. Y. Ou, and W. Zhang, "Cancellation of Internal Quantum Noise of an Amplifier by Quantum Correlation," *Phys. Rev. Lett.* **111**, 033608 (2013).

[232] F. Hudelist, J. Kong, C. Liu, J. Jing, Z. Ou, and W. Zhang, "Quantum metrology with parametric amplifier-based photon correlation interferometers," *Nature communications* **5**, 3049 (2014).

[233] V. Josse, M. Sabuncu, N. Cerf, G. Leuchs, and U. Andersen, "Universal Optical Amplification without Nonlinearity," *Physical Review Letters* **96** (2006).

[234] J. Zhao, J. Y. Haw, T. Symul, P. K. Lam, and S. M. Assad, "Characterization of a measurement-based noiseless linear amplifier and its applications," *Phys. Rev. A* **96**, 012319 (2017).

[235] L.-M. Duan and G.-C. Guo, "Probabilistic cloning and identification of linearly independent quantum states," *Phys. Rev. Lett.* **80**, 4999 (1998).

[236] T. C. Ralph, A. Gilchrist, G. J. Milburn, W. J. Munro, and S. Glancy, "Quantum computation with optical coherent states," *Phys. Rev. A* **68**, 042319 (2003).

[237] H. Chen, D. Lu, B. Chong, G. Qin, X. Zhou, X. Peng, and J. Du, "Experimental Demonstration of Probabilistic Quantum Cloning," *Phys. Rev. Lett.* **106**, 180404 (2011).

[238] J. Y. Haw, J. Zhao, J. Dias, S. M. Assad, M. Bradshaw, R. Blandino, T. Symul, T. C. Ralph, and P. K. Lam, "Surpassing the no-cloning limit with a heralded hybrid linear amplifier for coherent states," *Nature Communications* **7**, 13222 (2016).

[239] V. Scarani, S. Iblisdir, N. Gisin, and A. Acín, "Quantum cloning," *Rev. Mod. Phys.* **77**, 1225 (2005).

[240] P. Jouguet, S. Kunz-Jacques, A. Leverrier, P. Grangier, and E. Diamanti, "Experimental demonstration of long-distance continuous-variable quantum key distribution," *Nature Photonics* **7**, 378 (2013).

[241] M. Sabuncu, U. L. Andersen, and G. Leuchs, "Experimental demonstration of continuous variable cloning with phase-conjugate inputs," *Phys. Rev. Lett.* **98**, 170503 (2007).

[242] S. Olivares, M. G. Paris, and U. L. Andersen, "Cloning of Gaussian states by linear optics," *Phys. Rev. A* **73**, 062330 (2006).

[243] C. Weedbrook, N. B. Grosse, T. Symul, P. K. Lam, and T. C. Ralph, "Quantum cloning of continuous-variable entangled states," *Phys. Rev. A* **77**, 052313 (2008).

[244] S. Koike, H. Takahashi, H. Yonezawa, N. Takei, S. L. Braunstein, T. Aoki, and A. Furusawa, "Demonstration of quantum telecloning of optical coherent states," *Phys. Rev. Lett.* **96**, 060504 (2006).

[245] M. F. Sacchi, "Phase-covariant cloning of coherent states," *Phys. Rev. A* **75**, 042328 (2007).

[246] M. Sabuncu, G. Leuchs, and U. L. Andersen, "Experimental continuous-variable cloning of partial quantum information," *Phys. Rev. A* **78**, 052312 (2008).

[247] P. Cochrane, T. C. Ralph, and A. Dolińska, "Optimal cloning for finite distributions of coherent states," *Physical Review A* **69**, 042313 (2004).

[248] R. Blandino, N. Walk, A. P. Lund, and T. C. Ralph, "Channel purification via continuous-variable quantum teleportation with Gaussian postselection," *Phys. Rev. A* **93**, 012326 (2016).

[249] Q. He, L. Rosales-Zárate, G. Adesso, and M. D. Reid, "Secure Continuous Variable Teleportation and Einstein-Podolsky-Rosen Steering," *Phys. Rev. Lett.* **115**, 180502 (2015).

[250] S. Makovejs et al., "Record-low (0.1460 dB/km) attenuation ultra-large Aeff optical fiber for submarine applications," in *Optical Fiber Communications Conference and Exhibition (OFC), 2015* pp. 1–3 IEEE 2015.

[251] Y. Miwa, J.-i. Yoshikawa, N. Iwata, M. Endo, P. Marek, R. Filip, P. van Loock, and A. Furusawa, "Exploring a New Regime for Processing Optical Qubits: Squeezing and Unsqueezing Single Photons," *Phys. Rev. Lett.* **113**, 013601 (2014).

[252] F. A. M. de Oliveira and P. L. Knight, "Bright Squeezing," *Phys. Rev. Lett.* **61**, 830 (1988).

[253] A. La Porta, R. E. Slusher, and B. Yurke, "Back-Action Evading Measurements of an Optical Field Using Parametric Down Conversion," *Phys. Rev. Lett.* **62**, 28 (1989).

[254] J. Zhang, C. Ye, F. Gao, and M. Xiao, "Phase-Sensitive Manipulations of a Squeezed Vacuum Field in an Optical Parametric Amplifier inside an Optical Cavity," *Phys. Rev. Lett.* **101**, 233602 (2008).

[255] J. L. O'Brien, A. Furusawa, and J. Vučković, "Photonic quantum technologies," *Nature Photonics* **3**, 687 (2009).

[256] V. Giovannetti, S. Lloyd, and L. Maccone, "Quantum-Enhanced Measurements: Beating the Standard Quantum Limit," *Science* **306**, 1330 (2004).

[257] J. Aasi et al., "Enhanced sensitivity of the LIGO gravitational wave detector by using squeezed states of light," *Nature Photonics* **7**, 613 (2013).

[258] M. A. Taylor, J. Janousek, V. Daria, J. Knittel, B. Hage, H.-A. Bachor, and W. P. Bowen, "Biological measurement beyond the quantum limit," *Nature Photonics* **7**, 229 (2013).

[259] J. B. Clark, F. Lecocq, R. W. Simmonds, J. Aumentado, and J. D. Teufel, "Sideband cooling beyond the quantum backaction limit with squeezed light," *Nature* **541**, 191 (2017).

[260] S. Lloyd and S. L. Braunstein, "Quantum Computation over Continuous Variables," *Phys. Rev. Lett.* **82**, 1784 (1999).

[261] N. C. Menicucci, X. Ma, and T. C. Ralph, "Arbitrarily Large Continuous-Variable Cluster States from a Single Quantum Nondemolition Gate," *Phys. Rev. Lett.* **104**, 250503 (2010).

[262] S. L. Braunstein, "Squeezing as an irreducible resource," *Phys. Rev. A* **71**, 055801 (2005).

[263] B. Yurke, "Optical back-action-evading amplifiers," *J. Opt. Soc. Am. B* **2**, 732 (1985).

[264] J.-i. Yoshikawa, Y. Miwa, A. Huck, U. L. Andersen, P. van Loock, and A. Furusawa, "Demonstration of a Quantum Nondemolition Sum Gate," *Phys. Rev. Lett.* **101**, 250501 (2008).

[265] S. Puri and A. Blais, "High-Fidelity Resonator-Induced Phase Gate with Single-Mode Squeezing," *Phys. Rev. Lett.* **116**, 180501 (2016).

[266] H. Le Jeannic, A. Cavaillès, K. Huang, R. Filip, and J. Laurat, "Slowing Quantum Decoherence by Squeezing in Phase Space," *Phys. Rev. Lett.* **120**, 073603 (2018).

[267] M. Takeoka and M. Sasaki, "Discrimination of the binary coherent signal: Gaussian-operation limit and simple non-Gaussian near-optimal receivers," *Phys. Rev. A* **78**, 022320 (2008).

[268] X. Su, S. Hao, X. Deng, L. Ma, M. Wang, X. Jia, C. Xie, and K. Peng, "Gate sequence for continuous variable one-way quantum computation," *Nature Communications* **4**, 2828 (2013).

[269] J.-i. Yoshikawa, T. Hayashi, T. Akiyama, N. Takei, A. Huck, U. L. Andersen, and A. Furusawa, "Demonstration of deterministic and high fidelity squeezing of quantum information," *Phys. Rev. A* **76**, 060301 (2007).

[270] A. M. Lance, H. Jeong, N. B. Grosse, T. Symul, T. C. Ralph, and P. K. Lam, "Quantum-state engineering with continuous-variable postselection," *Phys. Rev. A* **73**, 041801 (2006).

[271] K. Miyata, H. Ogawa, P. Marek, R. Filip, H. Yonezawa, J.-i. Yoshikawa, and A. Furusawa, "Experimental realization of a dynamic squeezing gate," *Phys. Rev. A* **90**, 060302 (2014).

[272] R. Ukai, N. Iwata, Y. Shimokawa, S. C. Armstrong, A. Politi, J.-i. Yoshikawa, P. van Loock, and A. Furusawa, "Demonstration of Unconditional One-Way Quantum Computations for Continuous Variables," *Phys. Rev. Lett.* **106**, 240504 (2011).

[273] M. Gu, C. Weedbrook, N. C. Menicucci, T. C. Ralph, and P. van Loock, "Quantum computing with continuous-variable clusters," *Phys. Rev. A* **79**, 062318 (2009).

[274] N. C. Menicucci, "Fault-Tolerant Measurement-Based Quantum Computing with Continuous-Variable Cluster States," *Phys. Rev. Lett.* **112**, 120504 (2014).

[275] R. Filip, "Gaussian quantum adaptation of non-Gaussian states for a lossy channel," *Phys. Rev. A* **87**, 042308 (2013).

[276] D. Menzies and R. Filip, "Gaussian-optimized preparation of non-Gaussian pure states," *Phys. Rev. A* **79**, 012313 (2009).

[277] R. Jozsa, "Fidelity for Mixed Quantum States," *J. Mod. Opt.* **41**, 2315 (1994) https://doi.org/10.1080/09500349414552171.

[278] A. Uhlmann, "The "transition probability" in the state space of a *-algebra," *Rev. Math. Phys* **9**, 273 (1976).

[279] R. Filip, P. Marek, and U. L. Andersen, "Measurement-induced continuous-variable quantum interactions," *Phys. Rev. A* **71**, 042308 (2005).

[280] J. Fiurášek, "Engineering quantum operations on traveling light beams by multiple photon addition and subtraction," *Phys. Rev. A* **80**, 053822 (2009).

[281] Z. Li, Y. Zhang, X. Wang, B. Xu, X. Peng, and H. Guo, "Non-Gaussian postselection and virtual photon subtraction in continuous-variable quantum key distribution," *Phys. Rev. A* **93**, 012310 (2016).

[282] J. Fiurášek, R. García-Patrón, and N. J. Cerf, "Conditional generation of arbitrary single-mode quantum states of light by repeated photon subtractions," *Phys. Rev. A* **72**, 033822 (2005).

[283] H.-J. Briegel, W. Dür, J. I. Cirac, and P. Zoller, "Quantum Repeaters: The Role of Imperfect Local Operations in Quantum Communication," *Phys. Rev. Lett.* **81**, 5932 (1998).

[284] H. Yonezawa, T. Aoki, and A. Furusawa, "Demonstration of a quantum teleportation network for continuous variables," *Nature* **431**, 430 (2004).

[285] R. J. Schoelkopf and S. M. Girvin, "Wiring up quantum systems," *Nature* **451**, 664 (2008).

[286] R. Raussendorf and H. J. Briegel, "A One-Way Quantum Computer," *Phys. Rev. Lett.* **86**, 5188 (2001).

[287] C. H. Bennett, G. Brassard, C. Crépeau, R. Jozsa, A. Peres, and W. K. Wootters, "Teleporting an unknown quantum state via dual classical and Einstein-Podolsky-Rosen channels," *Phys. Rev. Lett.* **70**, 1895 (1993).

[288] D. Bouwmeester, J.-W. Pan, K. Mattle, M. Eibl, H. Weinfurter, and A. Zeilinger, "Experimental quantum teleportation," *Nature* **390**, 575 (1997).

[289] D. Boschi, S. Branca, F. De Martini, L. Hardy, and S. Popescu, "Experimental Realization of Teleporting an Unknown Pure Quantum State via Dual Classical and Einstein-Podolsky-Rosen Channels," *Phys. Rev. Lett.* **80**, 1121 (1998).

[290] X.-L. Wang, X.-D. Cai, Z.-E. Su, M.-C. Chen, D. Wu, L. Li, N.-L. Liu, C.-Y. Lu, and J.-W. Pan, "Quantum teleportation of multiple degrees of freedom of a single photon," *Nature* **518**, 516 (2015).

[291] M. A. Nielsen, E. Knill, and R. Laflamme, "Complete quantum teleportation using nuclear magnetic resonance," *Nature* **396**, 52 (1998).

[292] J. F. Sherson, H. Krauter, R. K. Olsson, B. Julsgaard, K. Hammerer, I. Cirac, and E. S. Polzik, "Quantum teleportation between light and matter," *Nature* **443**, 557 (2006).

[293] Y.-A. Chen, S. Chen, Z.-S. Yuan, B. Zhao, C.-S. Chuu, J. Schmiedmayer, and J.-W. Pan, "Memory-built-in quantum teleportation with photonic and atomic qubits," *Nature Physics* **4**, 103 (2008).

[294] M. D. Barrett, J. Chiaverini, T. Schaetz, J. Britton, W. M. Itano, J. D. Jost, E. Knill, C. Langer, D. Leibfried, R. Ozeri, and D. J. Wineland, "Deterministic quantum teleportation of atomic qubits," *Nature* **429**, 737 (2004).

[295] M. Riebe, H. Häffner, C. F. Roos, W. Hänsel, J. Benhelm, G. P. T. Lancaster, T. W. Körber, C. Becher, F. Schmidt-Kaler, D. F. V. James, and R. Blatt, "Deterministic quantum teleportation with atoms," *Nature* **429**, 734 (2004).

[296] S. Olmschenk, D. N. Matsukevich, P. Maunz, D. Hayes, L.-M. Duan, and C. Monroe, "Quantum Teleportation Between Distant Matter Qubits," *Science* **323**, 486 (2009).

[297] C. Nölleke, A. Neuzner, A. Reiserer, C. Hahn, G. Rempe, and S. Ritter, "Efficient Teleportation Between Remote Single-Atom Quantum Memories," *Phys. Rev. Lett.* **110**, 140403 (2013).

[298] W. B. Gao, P. Fallahi, E. Togan, A. Delteil, Y. S. Chin, J. Miguel-Sanchez, and A. Imamoğlu, "Quantum teleportation from a propagating photon to a solid-state spin qubit," *Nature Communications* **4**, 2744 (2013).

[299] F. Bussières, C. Clausen, A. Tiranov, B. Korzh, V. B. Verma, S. W. Nam, F. Marsili, A. Ferrier, P. Goldner, H. Herrmann, C. Silberhorn, W. Sohler, M. Afzelius, and N. Gisin, "Quantum teleportation from a telecom-wavelength photon to a solid-state quantum memory," *Nature Photonics* **8**, 775 (2014).

[300] L. Steffen, Y. Salathe, M. Oppliger, P. Kurpiers, M. Baur, C. Lang, C. Eichler, G. Puebla-Hellmann, A. Fedorov, and A. Wallraff, "Deterministic quantum teleportation with feed-forward in a solid state system," *Nature* **500**, 319 (2013).

[301] W. Pfaff, B. J. Hensen, H. Bernien, S. B. van Dam, M. S. Blok, T. H. Taminiau, M. J. Tiggelman, R. N. Schouten, M. Markham, D. J. Twitchen, and R. Hanson, "Unconditional quantum teleportation between distant solid-state quantum bits," *Science* **345**, 532 (2014).

[302] Q.-C. Sun, Y.-L. Mao, S.-J. Chen, W. Zhang, Y.-F. Jiang, Y.-B. Zhang, W.-J. Zhang, S. Miki, T. Yamashita, H. Terai, X. Jiang, T.-Y. Chen, L.-X. You, X.-F. Chen, Z. Wang, J.-Y. Fan, Q. Zhang, and J.-W. Pan, "Quantum teleportation with independent sources and prior entanglement distribution over a network," *Nature Photonics* **10**, 671 (2016).

[303] R. Valivarthi, M. G. Puigibert, Q. Zhou, G. H. Aguilar, V. B. Verma, F. Marsili, M. D. Shaw, S. W. Nam, D. Oblak, and W. Tittel, "Quantum teleportation across a metropolitan fibre network," *Nature Photonics* **10**, 676 (2016).

[304] X.-S. Ma, T. Herbst, T. Scheidl, D. Wang, S. Kropatschek, W. Naylor, B. Wittmann, A. Mech, J. Kofler, E. Anisimova, V. Makarov, T. Jennewein, R. Ursin, and A. Zeilinger, "Quantum teleportation over 143 kilometres using active feed-forward," *Nature* **489**, 269 (2012).

[305] J.-G. Ren, P. Xu, H.-L. Yong, L. Zhang, S.-K. Liao, J. Yin, W.-Y. Liu, W.-Q. Cai, M. Yang, L. Li, K.-X. Yang, X. Han, Y.-Q. Yao, J. Li, H.-Y. Wu, S. Wan, L. Liu, D.-Q. Liu, Y.-W. Kuang, Z.-P. He, P. Shang, C. Guo, R.-H. Zheng, K. Tian, Z.-C. Zhu, N.-L. Liu, C.-Y. Lu, R. Shu, Y.-A. Chen, C.-Z. Peng, J.-Y. Wang, and J.-W. Pan, "Ground-to-satellite quantum teleportation," *Nature* **549**, 70 (2017).

[306] H. Weinfurter, "Experimental Bell-State Analysis," *Europhysics Letters (EPL)* **25**, 559 (1994).

[307] S. L. Braunstein and A. Mann, "Measurement of the Bell operator and quantum teleportation," *Phys. Rev. A* **51**, R1727 (1995).

[308] J. Calsamiglia and N. Lütkenhaus, "Maximum efficiency of a linear-optical Bell-state analyzer," *Applied Physics B* **72**, 67 (2001).

[309] S. L. Braunstein and H. J. Kimble, "Teleportation of Continuous Quantum Variables," *Phys. Rev. Lett.* **80**, 869 (1998).

[310] R. Valivarthi, M. G. Puigibert, Q. Zhou, G. H. Aguilar, V. B. Verma, F. Marsili, M. D. Shaw, S. W. Nam, D. Oblak, and W. Tittel, "Quantum teleportation across a metropolitan fibre network," *Nature Photonics* **10**, 676 (2016).

[311] N. Lee, H. Benichi, Y. Takeno, S. Takeda, J. Webb, E. Huntington, and A. Furusawa, "Teleportation of Nonclassical Wave Packets of Light," *Science* **332**, 330 (2011).

[312] A. Furusawa, J. L. Sørensen, S. L. Braunstein, C. A. Fuchs, H. J. Kimble, and E. S. Polzik, "Unconditional Quantum Teleportation," *Science* **282**, 706 (1998) http://science.sciencemag.org/content/282/5389/706.full.pdf.

[313] T. C. Zhang, K. W. Goh, C. W. Chou, P. Lodahl, and H. J. Kimble, "Quantum teleportation of light beams," *Phys. Rev. A* **67**, 033802 (2003).

[314] W. P. Bowen, N. Treps, B. C. Buchler, R. Schnabel, T. C. Ralph, H.-A. Bachor, T. Symul, and P. K. Lam, "Experimental investigation of continuous-variable quantum teleportation," *Phys. Rev. A* **67**, 032302 (2003).

[315] N. Takei, T. Aoki, S. Koike, K.-i. Yoshino, K. Wakui, H. Yonezawa, T. Hiraoka, J. Mizuno, M. Takeoka, M. Ban, and A. Furusawa, "Experimental demonstration of quantum teleportation of a squeezed state," *Phys. Rev. A* **72**, 042304 (2005).

[316] M. Yukawa, H. Benichi, and A. Furusawa, "High-fidelity continuous-variable quantum teleportation toward multistep quantum operations," *Phys. Rev. A* **77**, 022314 (2008).

[317] U. L. Andersen and T. C. Ralph, "High-Fidelity Teleportation of Continuous-Variable Quantum States Using Delocalized Single Photons," *Phys. Rev. Lett.* **111**, 050504 (2013).

[318] S. Takeda, T. Mizuta, M. Fuwa, P. van Loock, and A. Furusawa, "Deterministic quantum teleportation of photonic quantum bits by a hybrid technique," *Nature* **500**, 315 (2013).

[319] L. S. Madsen, V. C. Usenko, M. Lassen, R. Filip, and U. L. Andersen, "Continuous variable quantum key distribution with modulated entangled states," *Nature Communications* **3**, 1083 (2012).

[320] A. Zeilinger, "Quantum teleportation, onwards and upwards," *Nature Physics* **14**, 3 (2018).

[321] D. Gottesman and I. L. Chuang, "Demonstrating the viability of universal quantum computation using teleportation and single-qubit operations," *Nature* **402**, 390 (1999).

[322] T. D. Ladd, F. Jelezko, R. Laflamme, Y. Nakamura, C. Monroe, and J. L. O'Brien, "Quantum computers," *Nature* **464**, 45 (2010).

[323] S. L. Braunstein, C. A. Fuchs, and H. J. Kimble, "Criteria for continuous-variable quantum teleportation," *Journal of Modern Optics* **47**, 267 (2000).

[324] J.-W. Pan, D. Bouwmeester, H. Weinfurter, and A. Zeilinger, "Experimental Entanglement Swapping: Entangling Photons That Never Interacted," *Phys. Rev. Lett.* **80**, 3891 (1998).

[325] X. Jia, X. Su, Q. Pan, J. Gao, C. Xie, and K. Peng, "Experimental Demonstration of Unconditional Entanglement Swapping for Continuous Variables," *Phys. Rev. Lett.* **93**, 250503 (2004).

[326] S. Takeda, M. Fuwa, P. van Loock, and A. Furusawa, "Entanglement Swapping between Discrete and Continuous Variables," *Phys. Rev. Lett.* **114**, 100501 (2015).

[327] M. Fuwa, S. Toba, S. Takeda, P. Marek, L. Mišta, R. Filip, P. van Loock, J.-i. Yoshikawa, and A. Furusawa, "Noiseless Conditional Teleportation of a Single Photon," *Phys. Rev. Lett.* **113**, 223602 (2014).

[328] T. C. Ralph and P. K. Lam, "Teleportation with Bright Squeezed Light," *Phys. Rev. Lett.* **81**, 5668 (1998).

[329] T. C. Ralph, P. K. Lam, and R. E. S. Polkinghorne, "Characterizing teleportation in optics," *Journal of Optics B: Quantum and Semiclassical Optics* **1**, 483 (1999).

[330] P. Grangier, J. A. Levenson, and J.-P. Poizat, "Quantum non-demolition measurements in optics," *Nature* **396**, 537 (1998).

[331] G. Philippe and G. F., "Quantum teleportation criteria for continuous variables," *arXiv preprint arXiv:quant-ph/0009079* (2000).

[332] Poizat, J.-Ph., Roch, J.-F., and Grangier, P., "Characterization of quantum non-demolition measurements in optics," *Ann. Phys. Fr.* **19**, 265 (1994).

[333] M. D. Reid, "Demonstration of the Einstein-Podolsky-Rosen paradox using non-degenerate parametric amplification," *Phys. Rev. A* **40**, 913 (1989).

[334] J.-G. Ren, P. Xu, H.-L. Yong, L. Zhang, S.-K. Liao, J. Yin, W.-Y. Liu, W.-Q. Cai, M. Yang, L. Li, K.-X. Yang, X. Han, Y.-Q. Yao, J. Li, H.-Y. Wu, S. Wan, L. Liu, D.-Q. Liu, Y.-W. Kuang, Z.-P. He, P. Shang, C. Guo, R.-H. Zheng, K. Tian, Z.-C. Zhu, N.-L. Liu, C.-Y. Lu, R. Shu, Y.-A. Chen, C.-Z. Peng, J.-Y. Wang, and J.-W. Pan, "Ground-to-satellite quantum teleportation," *Nature* **549**, 70 (2017).

[335] Q.-C. Sun, Y.-L. Mao, S.-J. Chen, W. Zhang, Y.-F. Jiang, Y.-B. Zhang, W.-J. Zhang, S. Miki, T. Yamashita, H. Terai, X. Jiang, T.-Y. Chen, L.-X. You, X.-F. Chen, Z. Wang, J.-Y. Fan, Q. Zhang, and J.-W. Pan, "Quantum teleportation with independent sources and prior entanglement distribution over a network," *Nature Photonics* **10**, 671 (2016).

[336] J. Zhao, J. Dias, J. Y. Haw, T. Symul, M. Bradshaw, R. Blandino, T. Ralph, S. M. Assad, and P. K. Lam, "Quantum enhancement of signal-to-noise ratio with a heralded linear amplifier," *Optica* **4**, 1421 (2017).

[337] X. Jin, J. Su, Y. Zheng, C. Chen, W. Wang, and K. Peng, "Balanced homodyne detection with high common mode rejection ratio based on parameter compensation of two arbitrary photodiodes," *Opt. Express* **23**, 23859 (2015).

[338] F. Grosshans and P. Grangier, "Quantum cloning and teleportation criteria for continuous quantum variables," *Phys. Rev. A* **64**, 010301 (2001).

[339] N. J. Cerf, A. Ipe, and X. Rottenberg, "Cloning of Continuous Quantum Variables," *Phys. Rev. Lett.* **85**, 1754 (2000).

[340] K. Fukui, A. Tomita, A. Okamoto, and K. Fujii, "High-Threshold Fault-Tolerant Quantum Computation with Analog Quantum Error Correction," *Phys. Rev. X* **8**, 021054 (2018).

[341] R. N. Alexander, N. C. Gabay, P. P. Rohde, and N. C. Menicucci, "Measurement-Based Linear Optics," *Phys. Rev. Lett.* **118**, 110503 (2017).

[342] J. Zhang and S. L. Braunstein, "Continuous-variable Gaussian analog of cluster states," *Phys. Rev. A* **73**, 032318 (2006).

[343] R. Zhang, J. Fan, X. Zhang, H. Yu, H. Zhang, Y. Mai, T. Xu, J. Wang, and H. J. Snaith, "Nonlinear Optical Response of Organic–Inorganic Halide Perovskites," *ACS Photonics* **3**, 371 (2016).

[344] F. O. Saouma, C. C. Stoumpos, J. Wong, M. G. Kanatzidis, and J. I. Jang, "Selective enhancement of optical nonlinearity in two-dimensional organic-inorganic lead iodide perovskites," *Nature Communications* **8**, 742 (2017).

[345] Y. Jia, R. A. Kerner, A. J. Grede, B. P. Rand, and N. C. Giebink, "Continuous-wave lasing in an organic–inorganic lead halide perovskite semiconductor," *Nature Photonics* **11**, 784 (2017).

[346] M. Abdi-Jalebi, Z. Andaji-Garmaroudi, S. Cacovich, C. Stavrakas, B. Philippe, J. M. Richter, M. Alsari, E. P. Booker, E. M. Hutter, A. J. Pearson, S. Lilliu, T. J. Savenije, H. Rensmo, G. Divitini, C. Ducati, R. H. Friend, and S. D. Stranks, "Maximizing and stabilizing luminescence from halide perovskites with potassium passivation," *Nature* **555**, 497 (2018).

[347] B. R. Sutherland and E. H. Sargent, "Perovskite photonic sources," *Nature Photonics* **10**, 295 (2016).

[348] F. P. García de Arquer, A. Armin, P. Meredith, and E. H. Sargent, "Solution-processed semiconductors for next-generation photodetectors," *Nature Reviews Materials* **2**, 16100 (2017).

[349] S. D. Stranks and H. J. Snaith, "Metal-halide perovskites for photovoltaic and light-emitting devices," *Nature Nanotechnology* **10**, 391 (2015).

[350] W. Zhang, G. E. Eperon, and H. J. Snaith, "Metal halide perovskites for energy applications," *Nature Energy* **1**, 16048 (2016).

[351] Q. A. Akkerman, G. Rainò, M. V. Kovalenko, and L. Manna, "Genesis, challenges and opportunities for colloidal lead halide perovskite nanocrystals," *Nature Materials* **17**, 394 (2018).

[352] G. S. Agarwal, "Interferences in Parametric Interactions Driven by Quantized Fields," *Phys. Rev. Lett.* **97**, 023601 (2006).

[353] A. E. Siegman, "Nonlinear Optical Effects: An Optical Power Limiter," *Appl. Opt.* **1**, 127 (1962).

[354] Z. Ou, "Observation of nonlinear phase shift in CW harmonic generation," *Optics Communications* **124**, 430 (1996).

[355] G. I. Stegeman, M. Sheik-Bahae, E. V. Stryland, and G. Assanto, "Large nonlinear phase shifts in second-order nonlinear-optical processes," *Opt. Lett.* **18**, 13 (1993).

[356] G. Assanto, G. I. Stegeman, M. Sheik-Bahae, and E. VanStryland, "Coherent interactions for all-optical signal processing via quadratic nonlinearities," *IEEE Journal of Quantum Electronics* **31**, 673 (1995).

[357] A. G. White, J. Mlynek, and S. Schiller, "Cascaded second-order nonlinearity in an optical cavity," *Europhysics Letters* **35**, 425 (1996).

[358] G. Assanto, G. Stegeman, M. Sheik-Bahae, and E. Van Stryland, "All optical switching devices based on large nonlinear phase shifts from second harmonic generation," *Applied Physics Letters* **62**, 1323 (1993).

[359] M. L. Sundheimer, C. Bosshard, E. W. V. Stryland, G. I. Stegeman, and J. D. Bierlein, "Large nonlinear phase modulation in quasi-phase-matched KTP waveguides as a result of cascaded second-order processes," *Opt. Lett.* **18**, 1397 (1993).

[360] M. A. M. Marte, "Nonlinear dynamics and quantum noise for competing $\chi(2)$ nonlinearities," *J. Opt. Soc. Am. B* **12**, 2296 (1995).

[361] M. A. M. Marte, "Sub-Poissonian Twin Beams via Competing Nonlinearities," *Phys. Rev. Lett.* **74**, 4815 (1995).

[362] J. Fang, Y. Lu, P. Huang, G. He, and G. Zeng, "Discretely modulated continuous-variable quantum key distribution with a nondeterministic noiseless amplifier," *International Journal of Quantum Information* **11**, 1350037 (2013).

[363] Y. Zhang, S. Yu, and H. Guo, "Application of practical noiseless linear amplifier in no-switching continuous-variable quantum cryptography," *Quantum Information Processing* **14**, 4339 (2015).

[364] S. Fossier, E. Diamanti, T. Debuisschert, R. Tualle-Brouri, and P. Grangier, "Improvement of continuous-variable quantum key distribution systems by using optical preamplifiers," *Journal of Physics B: Atomic, Molecular and Optical Physics* **42**, 114014 (2009).

[365] M. Silveri, E. Zalys-Geller, M. Hatridge, Z. Leghtas, M. H. Devoret, and S. M. Girvin, "Theory of remote entanglement via quantum-limited phase-preserving amplification," *Phys. Rev. A* **93**, 062310 (2016).

[366] M. Mičuda, I. Straka, M. Miková, M. Dušek, N. J. Cerf, J. Fiurášek, and M. Ježek, "Noiseless Loss Suppression in Quantum Optical Communication," *Phys. Rev. Lett.* **109**, 180503 (2012).

[367] G. Meng, S. Yang, X. Zou, S. Zhang, B. Shi, and G. Guo, "Noiseless suppression of losses in optical quantum communication with conventional on-off photon detectors," *Phys. Rev. A* **86**, 042305 (2012).

[368] S. Zhang, Y. Dong, X. Zou, B. Shi, and G. Guo, "Continuous-variable-entanglement distillation with photon addition," *Phys. Rev. A* **88**, 032324 (2013).

[369] H. Takahashi, J. S. Neergaard-Nielsen, M. Takeuchi, M. Takeoka, K. Hayasaka, A. Furusawa, and M. Sasaki, "Entanglement distillation from Gaussian input states," *Nature Photonics* **4**, 178 (2010).

[370] M. Dakna, T. Anhut, T. Opatrný, L. Knöll, and D.-G. Welsch, "Generating Schrödinger-cat-like states by means of conditional measurements on a beam splitter," *Phys. Rev. A* **55**, 3184 (1997).

[371] A. P. Lund, H. Jeong, T. C. Ralph, and M. S. Kim, "Conditional production of superpositions of coherent states with inefficient photon detection," *Phys. Rev. A* **70**, 020101 (2004).

[372] A. Laghaout, J. S. Neergaard-Nielsen, I. Rigas, C. Kragh, A. Tipsmark, and U. L. Andersen, "Amplification of realistic Schrödinger-cat-state-like states by homodyne heralding," *Phys. Rev. A* **87**, 043826 (2013).

[373] D. V. Sychev, A. E. Ulanov, A. A. Pushkina, M. W. Richards, I. A. Fedorov, and A. I. Lvovsky, "Enlargement of optical Schrödinger's cat states," *Nature Photonics* **11**, 379 (2017).

[374] P. Marek, R. Filip, and A. Furusawa, "Deterministic implementation of weak quantum cubic nonlinearity," *Phys. Rev. A* **84**, 053802 (2011).

[375] K. Marshall, R. Pooser, G. Siopsis, and C. Weedbrook, "Repeat-until-success cubic phase gate for universal continuous-variable quantum computation," *Phys. Rev. A* **91**, 032321 (2015).

[376] K. Miyata, H. Ogawa, P. Marek, R. Filip, H. Yonezawa, J.-i. Yoshikawa, and A. Furusawa, "Implementation of a quantum cubic gate by an adaptive non-Gaussian measurement," *Phys. Rev. A* **93**, 022301 (2016).

[377] S. L. Braunstein, "Error Correction for Continuous Quantum Variables," *Phys. Rev. Lett.* **80**, 4084 (1998).

[378] S. M. Tan, "Confirming entanglement in continuous variable quantum teleportation," *Phys. Rev. A* **60**, 2752 (1999).

[379] S. J. Jones, H. M. Wiseman, and A. C. Doherty, "Entanglement, Einstein-Podolsky-Rosen correlations, Bell nonlocality, and steering," *Phys. Rev. A* **76**, 052116 (2007).

[380] E. G. Cavalcanti, S. J. Jones, H. M. Wiseman, and M. D. Reid, "Experimental criteria for steering and the Einstein-Podolsky-Rosen paradox," *Phys. Rev. A* **80**, 032112 (2009).

[381] Y. Xiang, B. Xu, L. Mišta, T. Tufarelli, Q. He, and G. Adesso, "Investigating Einstein-Podolsky-Rosen steering of continuous-variable bipartite states by non-Gaussian pseudospin measurements," *Phys. Rev. A* **96**, 042326 (2017).

[382] E. G. Cavalcanti, M. J. W. Hall, and H. M. Wiseman, "Entanglement verification and steering when Alice and Bob cannot be trusted," *Phys. Rev. A* **87**, 032306 (2013).

[383] V. Händchen, T. Eberle, S. Steinlechner, A. Samblowski, T. Franz, R. F. Werner, and R. Schnabel, "Observation of one-way Einstein–Podolsky–Rosen steering," *Nature Photonics* **6**, 596 (2012).

[384] S. Armstrong, M. Wang, R. Y. Teh, Q. Gong, Q. He, J. Janousek, H.-A. Bachor, M. D. Reid, and P. K. Lam, "Multipartite Einstein-Podolsky-Rosen correlations steering and genuine tripartite entanglement with optical networks," *Nature Physics* **11**, 167 (2015).

[385] J. Dias and T. C. Ralph, "Quantum error correction of continuous-variable states with realistic resources," *Phys. Rev. A* **97**, 032335 (2018).

[386] S. Tserkis, J. Dias, and T. C. Ralph, "Simulation of Gaussian channels via teleportation and error correction of Gaussian states," *Phys. Rev. A* **98**, 052335 (2018).

[387] P. Liuzzo-Scorpo, A. Mari, V. Giovannetti, and G. Adesso, "Optimal Continuous Variable Quantum Teleportation with Limited Resources," *Phys. Rev. Lett.* **119**, 120503 (2017).

[388] S. L. W. Midgley, A. J. Ferris, and M. K. Olsen, "Asymmetric Gaussian steering: When Alice and Bob disagree," *Phys. Rev. A* **81**, 022101 (2010).

[389] K. Wagner, J. Janousek, V. Delaubert, H. Zou, C. Harb, N. Treps, J. F. Morizur, P. K. Lam, and H. A. Bachor, "Entangling the Spatial Properties of Laser Beams," *Science* **321**, 541 (2008).

[390] M. Murao, D. Jonathan, M. B. Plenio, and V. Vedral, "Quantum telecloning and multiparticle entanglement," *Phys. Rev. A* **59**, 156 (1999).

[391] J. S. Neergaard-Nielsen, Y. Eto, C.-W. Lee, H. Jeong, and M. Sasaki, "Quantum tele-amplification with a continuous-variable superposition state," *Nature Photonics* **7**, 439 (2013).

[392] T. C. Ralph, A. Gilchrist, G. J. Milburn, W. J. Munro, and S. Glancy, "Quantum computation with optical coherent states," *Phys. Rev. A* **68**, 042319 (2003).

[393] H. Jeong and M. S. Kim, "Efficient quantum computation using coherent states," *Phys. Rev. A* **65**, 042305 (2002).

[394] N. J. Cerf and S. Iblisdir, "Phase conjugation of continuous quantum variables," *Phys. Rev. A* **64**, 032307 (2001).

[395] V. Bužek, M. Hillery, and R. F. Werner, "Optimal manipulations with qubits: Universal-NOT gate," *Phys. Rev. A* **60**, R2626 (1999).

[396] N. Gisin and S. Popescu, "Spin Flips and Quantum Information for Antiparallel Spins," *Phys. Rev. Lett.* **83**, 432 (1999).

[397] F. De Martini, V. Bužek, F. Sciarrino, and C. Sias, "Experimental realization of the quantum universal NOT gate," *Nature* **419**, 815 (2002).

[398] L.-K. Chen, H.-L. Yong, P. Xu, X.-C. Yao, T. Xiang, Z.-D. Li, C. Liu, H. Lu, N.-L. Liu, L. Li, T. Yang, C.-Z. Peng, B. Zhao, Y.-A. Chen, and J.-W. Pan, "Experimental nested purification for a linear optical quantum repeater," *Nature Photonics* **11**, 695 (2017).